Étude de la production de méson neutre léger dans la voie de désintégration dimuonique en collision proton-proton à sqrt(s) = 13 TeV en rapidité vers l'avant dans ALICE au LHC du CERN

Boris Teyssier

N° d'ordre NNT : 2017LYSE1240

THÈSE DE DOCTORAT DE L'UNIVERSITÉ DE LYON
opérée au sein de
l'Université Claude Bernard Lyon 1

École Doctorale ED52
Physique & Astrophysique de Lyon

Spécialité de doctorat : Physique Hadronique
Discipline : Physique Expérimentale

Soutenue publiquement le 24/11/2017, par :
TEYSSIER Boris

Light-neutral meson production in pp collisions at $\sqrt{s} = 13$ TeV at forward rapidity in ALICE at the CERN LHC

Devant le jury composé de :

ERAZMUS Barbara, DR-HDR, CNRS–SUBATECH	Présidente
ARNALDI Roberta, Chercheur, INFN–Torino	Rapporteure
CROCHET Philippe, DR-HDR, CNRS–LPC	Rapporteur
BALDISSERI Alberto, DR-HDR, CEA–Saclay	Examinateur
HANSEN Hubert, MC-HDR, UCBL–IPNL	Examinateur
CHEYNIS Brigitte, CR-HDR, CNRS–IPNL	Directrice de thèse
URAS Antonio, CR, CNRS–IPNL	Co-directeur de thèse

Abstract: The ordinary matter surrounding us is made of hadrons which in turn are composed of quarks and gluons. These latter are elementary constituents which cannot be observed in a free state. However it is at present recognized that this matter confined within hadrons can undergo, under extreme conditions of high temperature and/or high net baryonic density, a transition to a state of deconfined quarks and gluons which is called quark gluon plasma.

The conditions required to form this quark gluon plasma can be experimentally achieved using a machine capable of colliding nuclei at very high energies: this is particularly the case at CERN where is located the world's largest and most powerful particle accelerator, the Large Hadron Collider, which collided Pb ions at a center-of-mass energy of 2.76 to 5.02 TeV per nucleon pair and protons of 0.9 to 13 TeV. Pb-Pb collisions at such relativistic energies definitely allow for the suitable density conditions to form the quark gluon plasma phase.

This thesis work contributes to this physics program by studying the production of neutral light mesons in collisions of proton-proton at 13 TeV, which provides the necessary reference to understand further observations done in Pb-Pb collisions. This study has been performed in the dimuon decay channel by analyzing the dimuon invariant mass spectrum in the region of masses lower than 1.5 GeV/c^2, giving access to the measurement of the cross sections of η, ρ/ω and ϕ meson.

Keywords: CERN, LHC, ALICE, QGP, Chirality, Muon, Meson, Strangeness, Hadronic Physics, High Energy Physics

Étude de la production de mésons neutres légers dans la voie de désintégration dimuonique en collisions proton-proton à $\sqrt{s} = 13$ TeV à rapidité vers l'avant dans ALICE au LHC du CERN

Résumé : La matière qui nous entoure est formée de hadrons, eux-mêmes constitués de quarks et de gluons. Ces derniers sont des composants élémentaires qui n'existent pas sous forme libre. Cependant nous savons à l'heure actuelle que la matière confinée dans des hadrons peut, dans des conditions de haute température et/ou de haute densité baryonique, se retrouver sous une forme déconfinée de plasma de quarks et de gluons.

Pour réaliser expérimentalement les conditions permettant de former ce plasma de quarks et de gluons, nous avons besoin d'une machine capable de faire entrer en collisions des noyaux à des énergies très élevées: cela est notamment possible au CERN, où se situe le plus grand accélérateur de particules du monde, le Large Hadron Collider, qui a permis de faire entrer en collisions des noyaux de Plomb à une énergie par paire de nucléons de 2.76 et 5.02 TeV, et des protons à des énergies allant de 0.9 à 13 TeV. Les collisions entre noyaux de Plomb permettent, en particulier, d'atteindre les conditions de densité d'énergie nécessaires à la formation de la phase de plasma de quarks et de gluons.

Ce travail de thèse contribue à ce programme de physique par l'étude de la production de mésons neutres légers en collisions proton-proton à 13 TeV, référence nécessaire pour comprendre les observations en collisions Plomb-Plomb. L'étude des mésons neutres légers a été menée dans le canal dimuonique par l'analyse du spectre de masse invariante des dimuons de masse inférieure à 1.5 GeV/c^2, permettant notamment de mesurer les sections efficaces des mésons η, ρ/ω et ϕ.

Mots clés : CERN, LHC, ALICE, QGP, Chiralité, Muon, Méson, Étrangeté, Physique Hadronique, Physique des hautes énergies

---

Remerciements

Je tiens tout d'abord à remercier l'IPNL sous la direction de Guy Chanfray ainsi que le groupe ALICE de Lyon, sous la direction de Brigitte Cheynis, pour m'avoir accueilli pendant ces trois années. Je tiens aussi à remercier le CNRS pour m'avoir permis de faire cette thèse grâce à leur financement ainsi que le LAVEX LIO (Lyon Institute of Origins) de l'université de Lyon pour le serveur de calcul du groupe théorie que j'ai eu l'opportunité d'utiliser.

Je voudrais remercier Barbara Erazmus qui a bien voulu être la présidente de mon jury de thèse, Roberta Arnaldi et Philippe Crochet pour avoir été mes rapporteurs qui grâce à leurs commentaires, ont permis d'améliorer la qualité de ce manuscrit. Merci aussi à Alberto Baldisseri et Hubert Hansen qui ont bien voulu être examinateurs de cette thèse ce qui a contribuée à l'amélioration du document. Je voudrais aussi vous remercier d'avoir fait le trajet sur Lyon pour avoir assisté à ma soutenance.

Le groupe ALICE de Lyon m'a permis de réaliser cette thèse dans une bonne ambiance. Je remercie Brigitte Cheynis, ma directrice de thèse, avec qui j'ai pu avoir de nombreuses discussions, que ce sois sur le VZERO pour ma tâche de service au sein de la collaboration ALICE, sur des aspects scientifiques de mon analyse ou tous simplement sur l'actualité ainsi que pour les nombreuses corrections orthographiques que ce sois en anglais ou en français qu'elle a apportées à mon travail. Je tiens aussi à remercier Antonio, mon co-encadrant de thèse qui m'a appris la ponctualité italienne, avec qui j'ai beaucoup appris sur l'analyse de données de ma thèse et avec qui j'ai eu de nombreux échanges/discussions que se sois scientifiques ou non. Je voudrais aussi remercier Cvetan, pour toutes les discussions que j'ai pu avoir, que ce sois sur le VZERO en lien avec ma tâche de service ou sur la physique hadronique et l'expérience ALICE. Ces discussions m'ont permis d'élargir ma vision du domaine. Merci aussi à Laurent Ducroux pour les échanges en lien avec l'enseignement ainsi que les conseils après mes différentes présentations au laboratoire. Merci aussi à Raphaël pour les divers échanges ainsi que sur l'aide apporté durant la préparation de l'oral et à Massimiliano, pour ces quelques mois au laboratoire en tant que nouveau post-doc du groupe, où tes conseils et points relevés durant ma préparation d'oral ont été utile. En plus des permanents et post-doc, le groupe à accueilli des stagiaires durant ma présence dans le groupe et j'aimerai les remercier pour la bonne humeur et ambiance qu'ils sont apportés, tous particulièrement ceux qui ont côtoyé mon bureau, que ce sois pour deux ou six mois, merci à Thibault, Pierre Demongodin, Samuel et Alexandre Thyvollet ainsi que Pierre-Etienne et Satya pour leur bonne humeur et leur motivation pour participer au tournoi de volley de l'APPN.

Je souhaiterais aussi remercier Hubert et Alexandre Biguet pour leur échanges sur la QCD et la physique hadronique théorique que j'ai pu avoir.

Je souhaiterai aussi remercier les membres de l'observatoire des sciences de l'univers qui m'ont permis de réaliser une tâche d'enseignement pendant deux ans de ma thèse.

Merci à Jean-Philippe Perrillat, Jean-François Gonzalez et Laurent Ducroux pour m'avoir pris dans leur équipe d'enseignement, cela a été une expérience très enrichissante.

I would like to thank all the ALICE collaboration that allowed me to do this thesis and especially, I thank all the collaborators who contributed at the lmmumu PAG, in particular Alessandro Di Falco and Ester Casula from the INFN of Cagliari for their help and advice given during the thesis, Satoshi Yano from the Hiroshima university for his contribution of the pp at 13 TeV. In addition to the PAG collaborator, I would like to thanks all the DQ people and in particular Diego, Laurent Aphecetch and Philippe Pillot for their help in the evaluation of the muon arms systematics, Martino for all the enriching exchanges on the operation of the ALICE trigger system and the luminosity, Evgeny for his response concerning the physics selection and David for the response on the multiplicity evaluation. I would like to thanks Andreas, Elena and Marie, quality assurance coordinator, with whom I was in contact for my service task, for their kindness and efficiency during the two and a half years or I participated in the QA as well as for their understanding on the delays.

Cette thèse m'a permis de m'immerger dans la communauté française de la physique hadronique notamment grâce aux rencontre QGP France et je voudrais remercier toutes les personnes avec qui j'ai pu avoir de bonnes discussions lors de ces rencontres, notamment les doctorants et post-doc que j'ai pu rencontrer : Antoine, Astrid, Audrey, Benjamin, Emilie, Gabriel, Gabriele, Jana, Julien, Lucile, Maxime, Michael et Mohamad. Cette thèse m'a permis aussi de faire des rencontres enrichissantes durant les diverses écoles que j'ai réalisés et je souhaiterai remercier les doctorants qui y ont participé pour les bons moments passés dans ces diverses écoles.

Bien sûr je souhaite aussi remercier les doctorants qui ont côtoyé l'IPNL durant ces trois années, notamment Alexandre Biguet, Anne-Laure, Bertrand, Cécile, Elvire, Emeline, François, Guillaume Garilot, Guillaume Victor, Jean-Baptiste, Joffrey, Lola, Nicolas Baillot, Nicolas Deutschmann, Nicolas Galy, Pierre Becker, Rémi et Solène. En plus des doctorants que j'ai côtoyés, je souhaiterai aussi remercier Alain, Clément, David, Geoffrey, Hubert, Martin, Sylvie et Yoan pour les nombreuses pauses café pris ensemble durant ces trois années ainsi qu'Antoine pour avoir accepté d'être mon parrain pour ma thèse.

Merci aussi à Aurélie, Camille, Éloïse, Florian et Laurine pour tous les bons moments, que ce sois les midis, en soirée, durant des films ou des sessions jeux. Merci aussi à Claire pour toutes ces discussions et soutiens mutuel pour nos thèses malgré le décalage entre la France et le Brésil.

Enfin, j'aimerais remercier ma famille pour leur soutiens durant toute ma formation universitaire ainsi que durant ma thèse. Je suis sûr que mes grands-parents paternel aurai été très fière de me voir arriver jusqu'à ce diplôme, eux qui étaient inquiets de savoir si j'y arriverai, ainsi que Christian et Thierry, mes oncles, auraient été fière et auraient aimé me voir à ce niveau.

Résumé

Ce manuscrit sur mon travail de thèse commence par un premier chapitre sur les motivations physiques du sujet étudié, tant sur le plan théorique qu'expérimental. Dans le deuxième chapitre, je traiterai du collisionneur de particules ayant produit les collisions dans l'expérience ALICE, utilisées durant l'analyse présentée dans ce manuscrit. La seconde partie de ce chapitre est justement dédiée à l'appareillage ALICE. Le troisième chapitre porte sur la caractérisation du jeu de données que j'ai exploité, ainsi que sur l'évaluation de la luminosité intégrée correspondant à cet échantillon. Le quatrième chapitre, quant à lui, porte sur les simulations Monte-Carlo qui ont du être faites pour mener à bien cette analyse. Le cinquième chapitre sur la méthodologie utilisée pour extraire de nos données les signaux d'intérêt. Dans l'avant-dernier chapitre, le sixième, nous traiterons de l'évaluation des quatre sources de systématiques qui impactent notre analyse. Le dernier chapitre traitera des résultats que nous avons pu obtenir en termes de sections efficaces de production de mésons neutres légers.

Cadre Physique (chapitre 1)

Le cadre théorique englobant le travail présenté dans ce document est la chromodynamique quantique, décrivant l'interaction forte, l'une des quatre interactions fondamentales que nous connaissons à l'heure actuelle, agissant sur les quarks et les gluons par échange de gluons. On verra que cette théorie peut s'exprimer mathématiquement en termes de densité Lagrangienne. De ce Lagrangien, peut être extraite une symétrie particulièrement intéressante pour l'étude des mésons légers neutres, la symétrie chirale, qui sera traitée en détails dans ce chapitre introductif. De la chromodynamique quantique, peut être extrait un diagramme thermodynamique de la matière hadronique, dans lequel deux principales phases sont visibles, la phase où la matière hadronique se condense sous forme de hadrons et la phase partonique où est créé un plasma de quarks et de gluons (QGP).

Expérimentalement ce diagramme de phases peut être étudié grâce à des accélérateurs de particules permettant de faire des collisions cible fixe et/ou en mode collisionneur. Dans la seconde partie de ce chapitre, je commencerai par introduire quelques variables cinématiques d'intérêt pour le domaine ainsi que deux concepts géométriques qui sont la centralité de la collision, déterminée par la distance qui sépare les centres des deux noyaux et le plan de réaction de la collision. Une collision entre deux noyaux comporte plusieurs étapes chronologiques, notamment la phase de QGP, suivie par deux phases hadroniques dominées respectivement par des collisions inélastiques et élastiques: cela engendre des productions de particules très diverses. Dans la suite du chapitre, seront parcourus tous les types de sondes intéressantes pour l'étude des collisions d'ions lourds: j'en profiterai pour faire un petit état de l'art des mesures faites dans les différentes voies d'observation. Bien sûr, les résultats montrés le sont seulement à titre d'exemple et pas de manière exhaustive.

La dernière section sur les résultats expérimentaux est focalisée sur la production de dimuons de basses masses dans ALICE, qui fait l'objet de l'étude rapportée dans ce

manuscrit. Dans les précédentes études, l'accent était mis sur le méson ϕ qui est à l'origine du signal le plus facilement observable dans la région des basses masses. Dans notre cas, l'étude a été portée sur les mésons η, ρ/ω et ϕ car la statistique disponible dans le lot de données étudié est suffisante pour extraire les signaux correspondants.

LHC et ALICE (chapitre 2)

La première partie du chapitre 2 sera consacrée au LHC, notamment au complexe d'accélérateurs permettant d'injecter au sein du LHC des noyaux ou des protons. On en profitera pour évoquer les scénarios futurs à relativement court terme pour le LHC et, pour finir cette courte partie, les programmes d'ions lourds au CERN et plus généralement dans le monde.

La seconde partie du chapitre est dédiée au détecteur ALICE. Cette partie peut être grossièrement coupée en deux parties, la première dédiée au détecteur actuel et son fonctionnement, la seconde au programme d'amélioration qui doit débuter à la fin du Run 2 du LHC.

Luminosité et Jeu de Données (chapitre 3)

Dans ce chapitre, deux points seront évoqués. Le premier porte sur les conditions expérimentales pour les données proton-proton à 13 TeV prises en 2016, utilisées dans l'analyse décrite dans ce manuscrit. Le second porte sur l'évaluation de la luminosité intégrée. Cette mesure nous permet d'évaluer des sections efficaces de production à partir des taux de production connaissant la section efficace associée à la condition de déclenchement de biais minimal de l'expérience et le nombre d'événements de biais minimal équivalent au jeu de données considéré dans l'analyse. Ce chapitre ne traitera pas de l'évaluation de cette section efficace de biais minimal, qui fait l'objet d'une étude à part entière, non discuté dans ce manuscrit, et qui sert à toutes les analyses. Cette section traitera en détails de la procédure permettant d'avoir le facteur de conversion entre le nombre d'événements analysés et le nombre équivalent d'événements de biais minimal.

Simulations Monte-Carlo (chapitre 4)

Ce chapitre est structuré en deux parties, la première se focalisant sur les mésons neutres légers et la deuxième sur les simulations des processus de charme et beauté ouverte.

Dans la partie sur les mésons, on commencera par donner quelques généralités sur ces particules ainsi que sur le générateur employé dans les simulations. Puis on traitera deux cas d'intérêt. Le premier cas concerne les processus faisant intervenir trois particules dans l'état final de la désintégration (désintégration Dalitz), en mettant l'accent sur leur facteur de forme. Le second cas, quandt à lui, correspond aux désintégrations à deux corps dans les canaux dileptoniques, et plus particulièrement dans celui dimuonique.

La seconde partie du chapitre est consacrée aux dimuons venant des désintégrations des saveurs lourdes ouvertes. Un dimuon venant des saveurs lourdes ouvertes est défini

comme deux muons produits durant les chaînes de désintégration d'une paire quark anti-quark charmés ou beaux. On verra dans cette section qu'un impact visible sur le spectre en masse découle de la distribution cinématique initiale du quark beau ou charmé, grâce aux comparaisons que nous avons faites avec des simulations utilisant les distributions cinématiques de PYTHIA6 et de FONLL. Le dernier point évoqué dans ce chapitre concerne la longueur de chaîne de désintégration des hadrons charmés et beaux, car nous sommes intéressés à reproduire les dimuons venant des paires de charme ou de beauté qui sont corrélés. Une hypothèse que nous pouvons faire est que, plus une chaîne de désintégration est longue, plus la corrélation résultante de la paire est amoindrie. On montrera que le profil de longueur de chaîne de désintégration possède une structure relativement complexe et qu'il y a un impact sur le spectre en masse en ne considérant qu'un certain intervalle de longueur de désintégration.

Extraction du Signal (chapitre 5)

Dans ce chapitre, deux points seront évoqués, le premier sera l'évaluation et la soustraction du bruit combinatoire, le second portera sur la procédure utilisée pour extraire le signal.

La composante de bruit combinatoire dans les dimuons de signes opposés, aussi appelé bruit non-corrélé, provient de la méthode de construction des dimuons. Cette méthode nécessite la création de toutes les paires de dimuons possibles dans un événement. Pour évaluer cette composante, nous employons la technique du mixage d'événements, c'est-à-dire que nous créons, à l'aide des données, un lot de dimuons qui par construction seront non-corrélés, en formant chaque dimuon par combinaison d'un muon d'un événement avec un muon d'un autre événement. La distribution ainsi obtenue est normalisée à partir des distributions de dimuons de mêmes signes. Cette procédure à été validée à l'aide de simulations Monte-Carlo. Une fois la soustraction du bruit faite pour chaque intervalle en p_{T} et y considéré dans notre analyse, nous pouvons passer à l'extraction du signal.

Pour extraire le signal d'intérêt de notre spectre de dimuons corrélés, nous utilisons une procédure d'ajustement par minimisation du χ^2. Cette procédure est basée sur une fonction, servant à l'ajustement, qui est composée des distributions en masse des processus hadroniques composant notre cocktail hadronique. Nous verrons notamment par quel moyen nous arrivons à réduire le nombre de degrés de liberté de notre fonction en asservissant certaines composantes à d'autres. Une grande partie de ce point est consacrée au traitement du continuum corrélé et aux méthodes permettant de décrire la forme de la fonction modélisant le continuum corrélé.

Évaluation des Systématiques (chapitre 6)

Ce chapitre est divisé en quatre parties, une pour chaque contribution à la systématique de notre analyse.

La première partie traitera de la systématique sur l'extraction du signal, et notamment sur l'évaluation de la systématique sur tous les choix que nous avons faits pour réaliser notre ajustement. Pour cela, un ou plusieurs tests sont faits en modifiant à chaque fois un seul paramètre par rapport à notre ajustement de référence. Une fois tous les tests

réalisés pour un intervalle en p_{T}-y considéré dans cette analyse, on évalue par la méthode de déviation standard l'erreur systématique qui en résulte.

Les autres parties traiteront de la systématique liée à l'estimation du produit de l'acceptante géométrique et de l'efficacité de reconstruction, notamment le choix de l'input cinématique pour les simulations Monte-Carlo, l'incertitude sur l'efficacité du système de déclenchement et sur l'efficacité du système de trajectographie.

Résultats (chapitre 7)

Dans ce dernier chapitre, avant de parler des résultats, nous discuterons la correction du signal extrait des distributions de masse invariante reconstruit, pour l'estimation de la section efficace de production. Nous passerons ensuite aux résultats, en présentant et en discutant la dépendance en p_{T} et y de la section efficace de production des mésons η, ρ/ω et ϕ. Les résultats obtenus dans cette analyse seront comparés aux prédictions des modèles `PYTHIA` et `PHOJET` et aux résultats disponibles dans ALICE à d'autres énergies.

Table of contents

Chapter 1

Physics Motivations

Summary

1.1 Theoretical Baseline

The theoretical framework underlying the subject of the present thesis is the Standard Model of particle physics (SM). The SM gathers the theories describing the electromagnetic, weak, and strong interactions as well as Higgs sector, providing at the same time a classification of all the subatomic particles known in terms of matter constituents and gauge bosons, see figure 1.1. It was developed throughout the latter half of the 20^{th} century, the current formulation having been finalized in the mid-1970s upon experimental confirmation of the existence of quarks. Since then, discoveries of the $W^{\pm}$ and Z^0 bosons (1983), the top quark (1995), the tau neutrino (2000), and the Higgs boson (2012) have given further credence to the Standard Model [1].

Each elementary interaction in the SM is characterized by an interaction range and a set of gauge bosons carrying the interaction charge. It should be noted that the SM describes the weak and electromagnetic interactions as two different aspects of a single electroweak interaction.

- The weak interaction has a very small range, of the order of 10^{-18} m, and is mediated by the Z^0, W^+ and W^- bosons. This interaction affects all known elementary fermions.

- The electromagnetic interaction is characterized by an infinite range and affects any particle having a non-zero electric charge. The associated gauge boson is the photon.

- The strong interaction acts at small distances, having a range of the order of 10^{-15} m: at this range, the strong interaction dominates over the other elementary interactions. The strong interaction is mediated by the exchange of massless gauge bosons called gluons that interact with quarks, anti-quarks, and other gluons, via a charge called color charge. The theoretical framework for the strong interaction is given by the theory of Quantum Chromodynamics, described in more details in the next section.

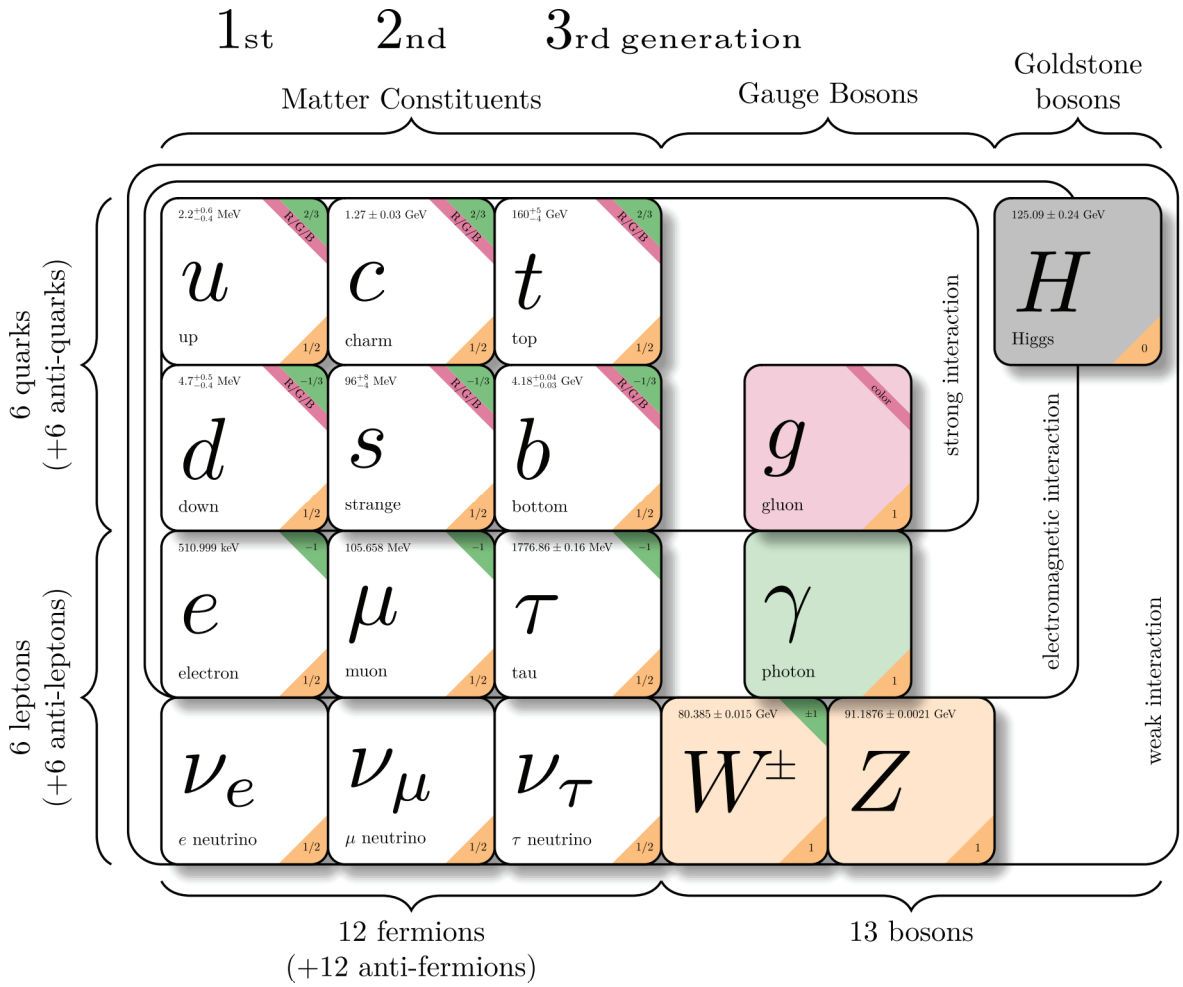

Figure 1.1: Standard Model of particle physics and the different families of matter

1.1.1 Quantum ChromoDynamics (QCD)

The Quantum ChromoDynamics (QCD) is the theory describing the hadronic physics phenomena in the framework of the SM. For this reason, QCD is needed to correctly describe and interpret the observations in experiments involving high-energy hadronic interactions like ALICE at the LHC.

The color charge of the QCD can have three different values (red, green and blue) as well as the corresponding anti-colors. This determines a part of the mathematical structure of QCD, based on the special unitary group of degree 3 — the Lie group $\mathrm{SU(N_c{=}3)}_c$. The complete mathematical structure of QCD is based on: the Lorentz group $L = \mathrm{SO}(1,3)$ for the space-time transformations (gluons are in the vector representation and quarks in the spinor one); a gauge symmetry $\mathrm{SU}(N_c = 3)_c$; an approximate light flavor symmetry $\mathrm{SU}(N_f = 3)_f$ (this symmetry is not relevant even approximately for the remaining 3 heavy flavors). The introduction of a three-color charge allowed, at the beginning of the development of the QCD, for the reconciliation of the observation of the spin-$\frac{3}{2}$ Δ^{++} baryon, composed of three up quarks in the same spin state, with the Pauli exclusion principle.

The QCD Lagrangian $\mathscr{L}_{\mathrm{QCD}}$

In the Quantum Field Theory formalism of particle physics, any theory can be expressed in terms of a Lagrangian. The mathematical expression of the Lagrangian density of QCD[1] is:

$$\begin{aligned}\mathscr{L}_{\mathrm{QCD}} = &\sum_{f}^{\text{flavors}} \bar{q}_f^{c_1} \left(i\partial_\mu \gamma^\mu \delta_{c_1 c_2} - m_f \delta_{c_1 c_2}\right) q_f^{c_2} \\ &+ \sum_{f}^{\text{flavors}} \bar{q}_f^{c_1} g_s A_\mu^a t_{c_1 c_2}^a \gamma^\mu q_f^{c_2} - \frac{1}{4} G_a^{\mu\nu} G_{\mu\nu}^a + \mathscr{L}_{\mathrm{CP}},\end{aligned} \tag{1.1}$$

(Besides the explicit flavor summation, each index, when repeated twice, indicates a summation on this index). In equation (1.1) μ, ν are Minkowski indexes ranging from 0 to 3, the q_f^c spinor represents the quark field of flavor f and color c (the Dirac index of quark fields and γ-matrices are not written explicitly for convenience), m_f is the mass of a quark of flavor f, g_s is linked to the coupling constant of the theory $\alpha_s = g_s^2/4\pi$ (after quantification and renormalization, α_s becomes a running coupling constant, also quantification requires the introduction of ghost fields), the gluon fields A_μ^a are Lorentz vectors, $G_a^{\mu\nu}$ is the gluon strength tensor, and the t^a matrices (generators of $\mathrm{SU(N_c{=}3)}_c$) are defined after the Gell-Mann matrices: $t^a = \lambda^a/2$.

The first term of $\mathscr{L}_{\mathrm{QCD}}$:

$$\mathscr{L}_{\text{free } q} = \sum_{f}^{\text{flavors}} \bar{q}_f^{c_1} \left(i\partial_\mu \gamma^\mu \delta_{c_1 c_2} - m_f \delta_{c_1 c_2}\right) q_f^{c_2} = \bar{q}\left(i\not{\partial} - \hat{m}_f\right) q, \tag{1.2}$$

is a free Lagrangian, representing the propagation of free quarks, $\hat{m}$ representing the diagonal quark mass matrix.

[1] By language abuse, the QCD Lagrangian density is simply named QCD Lagrangian.

The second term :

$$\mathscr{L}_{\text{int}} = \sum_{f}^{\text{flavors}} \bar{q}_f^{c_1} g_s A_\mu^a t_{c_1 c_2}^a \gamma^\mu q_f^{c_2} = g_s \bar{q} \not{A} q \tag{1.3}$$

encodes the minimal (or Yukawa) coupling describing the interaction of the quark fields with the gluons.

The third term of $\mathscr{L}_{\text{QCD}}$ involves $G_{\mu\nu}^a$, the gluon strength tensor which can be expressed as

$$G_{\mu\nu}^a = \partial_\mu A_\nu^a - \partial_\nu A_\mu^a + g_s f^{abc} A_\mu^b A_\nu^c. \tag{1.4}$$

The f^{abc} coefficients are the structure constants of SU(3). The first part of the tensor in equation (1.4), $\partial_\mu A_\nu^a - \partial_\nu A_\mu^a$, describes the gluon kinematics, in analogy to the kinematics description of photons in quantum electrodynamics (QED). The last term $g_s f^{abc} A_\mu^b A_\nu^c$ is specific to QCD and describes the gluon auto-coupling due to the fact the QCD is a non-Abelian theory.

The last term in equation (1.1), $\mathscr{L}_{\text{CP}}$, is related to a possible violation of the CP-symmetry (due to a breaking of T symmetry and the conservation of the CPT symmetry) in the QCD sector. This term is defined as:

$$\mathscr{L}_{\text{CP}} = \theta \frac{g_s^2}{32\pi^2} \tilde{G}_{\mu\nu}^a G^{\mu\nu a}, \tag{1.5}$$

where $\tilde{G}$ is the dual of G:

$$\tilde{G}_{\mu\nu}^a = \frac{1}{2} \varepsilon_{\mu\nu\alpha\beta} G^{\alpha\beta a}, \tag{1.6}$$

and $\varepsilon_{\mu\nu\alpha\beta}$ is the antisymmetric Levi-Civita pseudo-tensor. The θ parameter, which would take a non-zero value in case of CP-violation of $\mathscr{L}_{\text{QCD}}$, can be experimentally accessed by measuring the electric dipole momentum of the neutron. Its value compatible with zero is currently not explained by the theory [2, 3].

The QCD Running Coupling Constant α_s

By using the perturbative-QCD (pQCD) and the renormalization group equation [4], it is possible to extract a running coupling constant α_s depending on the momentum transfer Q and on a parameter Λ_{QCD} establishing the scale at which the perturbatively-defined coupling would diverge. At first order of perturbation theory, α_s can be expressed as:

$$\alpha_s(Q^2) = \frac{12\pi}{(11N_c - 2N_f) \ln\left(\frac{Q^2}{\Lambda_{\text{QCD}}^2}\right)}, \tag{1.7}$$

where N_c is the number of colors (3), N_f is the number of light flavors respecting $m_q \ll Q$ and $\Lambda_{\text{QCD}} \approx 200$ MeV.

Figure 1.2 shows the excellent agreement between available measurements of $\alpha_s(Q^2)$ and the pQCD theoretical prediction beyond first order. According to the value of the transfer momentum Q, two regimes of QCD can be defined: for values of the transfer momentum Q above $Q \approx 1$ GeV (of the order of the nucleon mass), implying $Q \gg \Lambda_{\text{QCD}}$ (or for distances well below 1 fm corresponding to the nucleon size) QCD is in the regime of asymptotic freedom; for $Q \lesssim 1$ GeV, QCD behavior is dominated by the color confinement mechanism.

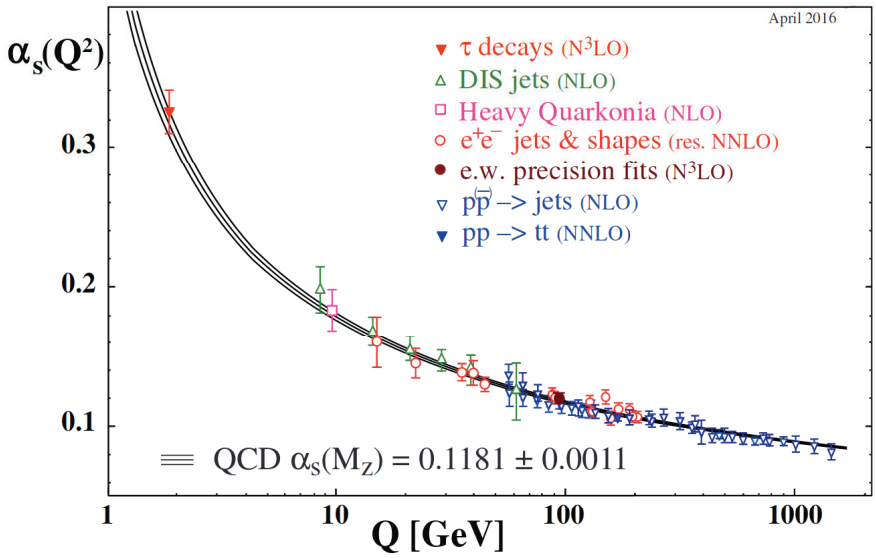

Figure 1.2: Summary of measurements of α_s as a function of the momentum transfer Q and the pQCD prediction [4].

Asymptotic Freedom

In the large momentum transfer region $Q \gg \Lambda_{\mathrm{QCD}}$, or at small distance, the decreasing of the coupling constant α_s reflects the fact that the particles, interacting over short distances $\ll 1$ fm (the typical size of the nucleon), can be treated asymptotically as quasi-free particles. This allows one to use a perturbative approach in performing calculations based on series of α_s powers. Let us notice that asymptotic freedom does not mean that quarks are not interacting at all in high-energy collisions (the freedom is only asymptotic). Indeed it has been shown that at RHIC energy a strongly interacting QGP (s-QGP) is created.

Color Confinement

In the small momentum transfer region, or large distance, the coupling constant perturbatively diverges. The physical interpretation for this phenomenon is the color confinement. A schematic explanation of this phenomenon is the following: if it was possible to hold two color charges (for example two quarks) and pull them part, the energy density would concentrate into a flux tube due to the non-Abelian characteristics of QCD (differently to QED). The energy would increase with the separation until it reaches a threshold above which pair creation is possible. Figure 1.3 sketches this effect known as string breaking. This is the reason why in vacuum it is not possible to observe directly one isolated quark and all of them are found in composite particles named hadrons: the color charge of hadrons is zero (hadrons are "colorless" or "white") as the colored flux tube wraps within the hadron itself and can be observed.

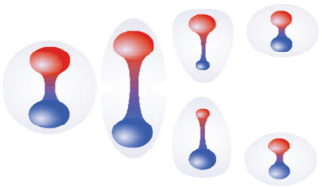

Figure 1.3: Sketch of two quark separation

A simple modelisation of the potential $V(r)$ between two quarks is given by the Cornell potential [5]:

$$V(r) = -\frac{\alpha_s}{r} + \sigma r. \tag{1.8}$$

In equation (1.8), the first term models the asymptotic freedom with a Coulomb potential (this term is dominating at $r \to 0$) and the second term (dominating when $r \to \infty$) is called the string potential with the string tension $\sigma \sim (260\ \mathrm{MeV}^2)$.

Hadrons can be classified as:

- mesons, composed of one quark and one anti-quark
- baryons, composed of three quarks
- exotic states like the recently observed tetra-quark, etc.

1.1.2 Chiral Symmetry

The chiral symmetry is one of the two fundamental symmetries of QCD, governing low-energy QCD (low-hadronic masses) and the properties of the transition between the partonic and the hadronic phases observed in heavy-ion collisions.

The chiral symmetry can be conveniently introduced and discussed considering the way Lorentz transformations act on bosons and fermions. To start this discussion, let us consider a massless universe. To understand the properties of the Lorentz transformation of any quantum state one can decompose it into its fundamental building blocks called chiral fermions: χ_R (the right chiral fermion) and χ_L (the left chiral fermion). Physically, χ_R and χ_L are spinor fields (spin ½) and the R and L indices denote the helicities of the states. In a massless universe the helicity is a good quantum number: there is no Lorentz transformation that can change the "orientation" of the spin hence for any inertial observers the measured helicity would be the same. Since χ_R and χ_L are fundamental states when Lorentz transformations are considered, one can build any spin state by mixing these building blocks: mathematically, the Lorentz group can then be described as a $\mathrm{SU}(2)_R \otimes \mathrm{SU}(2)_L$ group whose fundamental representations[2] are χ_R and χ_L.

Let us now consider a massive fermion state: obviously now two observers with different speed relative to the fermion will measure different projections of the spin along the momentum of the particle: the helicity is no more a good quantum number. The chiral fermions χ_R and χ_L can now transform into one another: this mechanism is called the breaking of the chiral symmetry. As anticipated in the introduction of this section, this symmetry is crucial to understand the low-mass sector of QCD since it is dominated by hadronic states composed of almost massless quarks (namely u, d, s, composing the light

[2] To see why the SO(1,3) Lorentz group L can be described by the combination of two SU(2) groups, one has to remember that L contains three rotations (that gives one SU(2) group) and three boosts (that can be seen as rotation involving the time direction and an imaginary angle that gives another SU(2) group). Those two algebras are not independent (e.g. boost and rotation do not commute) but they can be decoupled into $\mathrm{SU}(2)_R \otimes \mathrm{SU}(2)_L$ independent algebras.

neutral meson studied in this thesis) compared to the typical scale of QCD, Λ_{QCD} (see table 1.1).

u:	$m = 2.2^{+0.6}_{-0.4}$ MeV/c^2	c:	$m = 1.27 \pm 0.03$ GeV/c^2	t:	$m = 160^{+5}_{-4}$ GeV/c^2
d:	$m = 4.7^{+0.5}_{-0.4}$ MeV/c^2	s:	$m = 96^{+6}_{-4}$ MeV/c^2	b:	$m = 4.18^{+0.4}_{-0.3}$ GeV/c^2

Table 1.1: Quark masses [4].

In the following, we will explain with a very simple quark model, some observable phenomena linked to the fundamental QCD chiral symmetry: the non observation of degeneration in mass between the scalar and pseudo-scalar octet as well as the spontaneous chiral symmetry breaking related to the phase transition, observed e.g. in LHC, around a temperature of 170 MeV.

a A Lagrangian for a free massless quark

For one chiral quark χ_R the free Lagrangian is[3]:

$$\mathscr{L}_{\text{free } q,R} = i\chi_R^\dagger \partial_0 \chi_R + i\chi_R^\dagger \overrightarrow{\sigma} \cdot \overrightarrow{\partial} \chi_R, \tag{1.9}$$

the form of the Lagrangian being dictated by the usual constraints (Lorentz invariance, hermiticity, conservation laws), but for one quark flavor, the state with opposite helicity also exists in nature: for one quark flavor, one can write $\mathscr{L}_{\text{free } q} = \mathscr{L}_{\text{free } q,R} + \mathscr{L}_{\text{free } q,L}$. This can be conveniently written:

$$\mathscr{L}_{\text{free } q} = \overline{q} i \not{\partial} q, \tag{1.10}$$

where q is a Weyl spinor (4 component spinor):

$$q = \begin{bmatrix} \chi_R \\ \chi_L \end{bmatrix}, \tag{1.11}$$

and the usual notation $\overline{q} = q^\dagger \gamma^0$ (see chapter 3.2 of [1]):

b Explicit breaking of the chiral symmetry in presence of a mass term

The Lagrangian of a free quark of mass m is

$$\mathscr{L}_{\text{free } q} = \overline{q}\left(i\not{\partial} - m\right) q = \mathscr{L}_0 + \mathscr{L}_m, \tag{1.12}$$

This Lagrangian contains a mass term which is explicitly written as

$$\mathscr{L}_m = m\overline{q}q = m\left(\chi_R^\dagger \chi_L + \chi_L^\dagger \chi_R\right). \tag{1.13}$$

The number of R (L) quarks in this system is given by:

$$N_{R,L} = \chi_R^\dagger \chi_R \qquad \left(\chi_L^\dagger \chi_L\right). \tag{1.14}$$

[3] We do not consider Majorana fermions in this manuscript.

Let us define a transformation belonging to the symmetry group $\mathrm{U}(1)_R \otimes \mathrm{U}(1)_L$:

$$\left.\begin{array}{rl} \chi_R \to & \mathrm{e}^{i\theta_R}\chi_R \\ \chi_L \to & \mathrm{e}^{i\theta_L}\chi_L \end{array}\right\} \mathscr{L}_{\text{free } q} \to \mathscr{L}_0 + m\left(\mathrm{e}^{i(\theta_L-\theta_R)}\chi_R^\dagger\chi_L + \mathrm{e}^{i(\theta_R-\theta_L)}\chi_L^\dagger\chi_R\right); \tag{1.15}$$

this symmetry is broken by the mass term, as discuss previously when considering the case of the boost of a massive fermion: the number of R or L quarks is not the same for all observers. However, this symmetry, restricted to the case of $\theta_R = \theta_L \equiv \theta_V$, is not broken, and is associated to the conservation of the fermion number. This result in the $\mathrm{U}_V(1)$ symmetry:

$$q \to \mathrm{e}^{i\theta_V} q \iff \begin{bmatrix}\chi_R \\ \chi_L\end{bmatrix} \to \mathrm{e}^{i\theta_V}\begin{bmatrix}\chi_R \\ \chi_L\end{bmatrix} \quad , \quad \mathscr{L}_{\text{free } q} \to \mathscr{L}_{\text{free } q}. \tag{1.16}$$

The V stands for Vector (it is the conservation of the so-called vector current $V^\mu = \overline{q}\gamma^\mu q$). For further convenience, we also define $\mathrm{U}_A(1)$ as the symmetry group with transformation given by $\theta_R = -\theta_L \equiv \theta_A$, the A stands for Axial (a transformation in $\mathrm{U}_A(1)$ is thus given by $q \to \mathrm{e}^{i\theta_A\gamma_5} q$).

c **For more than one flavor:**

Finally, let us consider the Lagrangian of a system composed by the two lightest flavors u and d, giving $\mathrm{N}_f = 2$ (but this discussion could also be extended to a system including a third flavor s, light enough compared to Λ_{QCD})

$$\mathscr{L}_{\text{free light } q} = i\overline{q_u}\partial_\mu\gamma^\mu q_u + i\overline{q_d}\partial_\mu\gamma^\mu q_d - m_u\overline{q_u}q_u - m_d\overline{q_d}q_d. \tag{1.17}$$

In this case, one can introduce for convenience the iso-spinor $\psi = \begin{pmatrix} q_u \\ q_d \end{pmatrix}$

$$\mathscr{L}_{\text{free light } q} = \overline{\psi}\left(i\partial\!\!\!/ - \hat{m}_0\right)\psi \tag{1.18}$$

$$= i\overline{\psi}\partial_\mu\gamma^\mu\psi - \frac{m_u + m_d}{2}\overline{\psi}\psi - \frac{m_u - m_d}{2}\overline{\psi}\tau_3\psi\,, \tag{1.19}$$

where $\hat{m}_0$ is the quark masses matrix, τ_3 is the iso-spin Pauli matrix (noted τ not to confuse it with σ_3 that acts on spinor index). For convenience let us also use

$$\psi_R \equiv \begin{bmatrix} q_{uR} \\ q_{dR} \end{bmatrix} \equiv \begin{bmatrix} q_{uR} \\ 0 \\ q_{dR} \\ 0 \end{bmatrix} \equiv P_R\psi, \tag{1.20}$$

where

$$P_R = \frac{1+\gamma_5}{2}, \tag{1.21}$$

and the same for ψ_L where

$$P_L = \frac{1-\gamma_5}{2}. \tag{1.22}$$

The symmetry we discussed in paragraph b is extended by adding a mixing of the flavor states. This is what is usually called in the literature "chiral symmetry": $\mathrm{SU}_R(\mathrm{N}_f)\times\mathrm{SU}_L(\mathrm{N}_f)$.

The iso-spinor $\psi = \psi_R + \psi_L$, transforms under the chiral symmetry as

$$\psi \;\rightarrow\; \mathrm{e}^{i\overrightarrow{\theta_R}\,\cdot\,\overrightarrow{t}}\,\psi_R + \mathrm{e}^{i\overrightarrow{\theta_L}\,\cdot\,\overrightarrow{t}}\,\psi_L, \tag{1.23}$$

where $\overrightarrow{t} = \dfrac{\vec{\tau}}{2}$ and $\overrightarrow{\theta_R}, \overrightarrow{\theta_L} \in (\mathbb{R}^3)^2$.

As in the one flavor case, the kinetic term

$$\mathscr{L}_k = i\overline{\psi_L}\partial_\mu\gamma^\mu\psi_L + i\overline{\psi_R}\partial_\mu\gamma^\mu\psi_R, \tag{1.24}$$

is chiral invariant while the mass term is not. However when the mass difference is zero (the so-called exact isospin limit) the $\mathrm{SU}_V(\mathrm{N}_f)$ symmetry is exact.

d The symmetry of the quark sector of QCD — the eightfold way

Let us consider only massless quarks (a good approximation for u, d, and s) giving $\mathrm{N}_f = 3$, and the light sector only:

$$\mathscr{L}_{\mathrm{QCD}} = \mathscr{L}_{\text{free light } q} + \mathscr{L}_r, \tag{1.25}$$

where $\mathscr{L}_r$ incorporates the terms appearing in the second line of equation (1.1), as well as any term relative to heavy quark, $\mathscr{L}_r$ transforms trivially or in the same way as a $\mathscr{L}_{\text{free light } q}$. For this reason, the chiral transformation of $\mathscr{L}_{\mathrm{QCD}}$ can be studied considering $\mathscr{L}_{\text{free } q}$ only. In this massless scenario, the largest symmetry group for $\mathscr{L}_{\mathrm{QCD}}$ can be expressed as: $\mathrm{G}{=}\mathrm{U}_R(1)\otimes\mathrm{U}_L(1)\otimes\mathrm{SU}_R(\mathrm{N}_f)\otimes\mathrm{SU}_L(\mathrm{N}_f) = \mathrm{U}_R(\mathrm{N}_f)\otimes\mathrm{U}_L(\mathrm{N}_f)$. A transformation of this group is given by:

$$\psi \rightarrow \mathrm{e}^{i\tilde{\theta_R}\tilde{t}}\,\psi_R + \mathrm{e}^{i\tilde{\theta_L}\tilde{t}}\,\psi_L, \tag{1.26}$$

where $\tilde{t} = \left(\mathbb{1}, \vec{t}\right)$ and $\tilde{\theta} = \left(\theta, \vec{\theta}\right)$. This symmetry would allow one to classify light hadronic states into double $\mathrm{U}(\mathrm{N}_f = 3)$ multiplets (one for left-handed and one for right-handed), where scalar and pseudo-scalar members would be invariant under $\mathrm{U}(\mathrm{N}_f = 3)$ rotation in the flavor space, which implies the same mass. This is not what is observed. At most, one sees multiplets (approximately) invariant under vector symmetry $\mathrm{SU}_V(\mathrm{N}_f = 3)$ rotation (see paragraph b): for example the octet of pseudo-scalar mesons π, K, η and the decuplet of baryons n, p, Λ, etc.

The chiral partner of the cited pseudoscalar meson octet, is the scalar octet of the a_0, κ and σ meson: the fact that no degeneracy in mass is observed between the members of the pseudoscalar octet and the members of the scalar one is linked to the G symmetry breaking. For convenience one can rewrite $\mathrm{G} = \mathrm{U}_R(\mathrm{N}_f = 3)\times\mathrm{U}_L(\mathrm{N}_f = 3)$ as

$$\mathrm{G} = \mathrm{U}_V(1) \otimes \mathrm{U}_A(1) \otimes \mathrm{SU}_V(3) \otimes \mathrm{SU}_A(3), \tag{1.27}$$

where:

- $\mathrm{U}_V(1)$ is the symmetry already discussed in paragraph b: it is the conservation of the individual flavor quark number.

- $U_A(1)$ was also introduced in paragraph b. This group should be a symmetry in the massless scenario leading to the observation of $m_\eta = m_{\eta'}$ (one should see a nonet, instead of an octet, of degenerated pseudoscalar mesons) [6]. This is, however, not the case. The more generally accepted explanation is that the gluon part $\mathscr{L}_r$ of $\mathscr{L}_{\text{QCD}}$ generates an explicit breaking of the $U_A(1)$ symmetry due to non-zero quantum fluctuations in the gluon strength tensor $\sim \langle G^2 \rangle$.

$$G^2 = G_{\mu\nu}\tilde{G}^{\mu\nu}. \tag{1.28}$$

- $SU_V(3)$: this is the observed (approximate) symmetry between the masses of the members of a multiplet[4]. This means that the $SU_V(3)$ symmetry is good enough to classify hadronic states: this corresponds to "the eightfold way".

- $SU_A(3)$: this group should be again a symmetry in a massless scenario, one would then observe a degeneracy between the scalar and the pseudoscalar meson octet. This is not the case because the chiral symmetry $SU_V(N_f) \otimes SU_A(N_f)$ is spontaneously broken (Goldstone mechanism) to $SU_V(N_f = 3)$. The π, K, η are the (almost) massless Goldstone bosons of this mechanism.

e Spontaneous breaking of the chiral symmetry and phase transition

The Goldstone mechanism just mentioned when discussing the $SU_A(3)$ group can be understood in the framework of a quark model, the Nambu-Jona-Lasinio model [7,8] with massless quarks. For two light flavors, one has:

$$\mathscr{L}_{\text{NJL}} = \overline{\psi}\left(i\not{\partial}\right)\psi + G_s\left[\left(\overline{\psi}\psi\right)^2 + \left(\overline{\psi}i\gamma_5\vec{\tau}\psi\right)^2\right], \tag{1.29}$$

where G_s is a coupling constant for four-quark contact interactions. It mimics the short range strong interaction as a contact interaction. This Lagrangian is chirally invariant since the interaction term is built from a scalar $\overline{\psi}\psi$ and its pseudoscalar counterpart so as to be invariant.

If the interaction term is sufficiently large ($G_s{\Lambda_{\text{QCD}}}^2 \sim 1$) quarks can condense ($\langle\overline{\psi}\psi\rangle \neq 0$) and equation (1.29) can be rewritten as:

$$\mathscr{L}_{\text{NJL}} \simeq \overline{\psi}\left(i\not{\partial} + 2G_s\langle\overline{\psi}\psi\rangle\right)\psi + \cdots \tag{1.30}$$

The quantity $m_D \equiv -2G_s\langle\overline{\psi}\psi\rangle$ acts exactly as a mass term (it is the so-called dynamical mass) and spontaneously breaks the chiral symmetry.

If temperature increases, generally there will be a screening of the interaction and $\langle\overline{\psi}\psi\rangle(T) = 0$ for $T > T_c$, where T_c is called the phase transition temperature: the chiral symmetry is said to be restored. At approximately the same temperature, the deconfinement occurs, hence the high temperature phase is also known as the Quark Gluon Plasma (or QGP) phase. The fact that chiral symmetry restoration and deconfinement are occurring at almost the same temperature, happens because in low-energy QCD there is basically one scale only, Λ_{QCD}.

[4] The observed mass differences are not exactly zero because the u, d, s mass differences are not exactly zero (isospin limit).

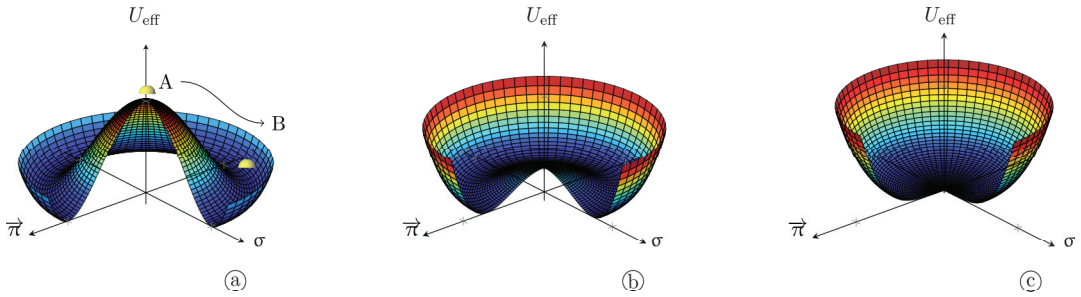

Figure 1.4: Effective potential as a function of $\vec{\pi}$–σ, left to right going towards fully chirality restoration.

If one takes $\sigma \sim \overline{\psi}\psi$ and $\vec{\pi} \sim \overline{\psi} i\gamma_5 \vec{\tau}\psi$ the chiral symmetry restoration can be described in the same way as the Goldstone mechanism related to the Higgs mechanism. At low temperature one has a Goldstone effective potential U_{eff} (see figure 1.4 a) that has the well-known Mexican hat shape: the "vacuum" (relative to the expectation value $\langle\vec{\pi}\rangle = 0 = \langle\sigma\rangle$) is in fact unstable. The physical vacuum is located at the bottom of the potential on the so-called chiral circle. As the temperature increases, the chiral circle shrinks until the state $\langle\vec{\pi}\rangle = 0 = \langle\sigma\rangle$ is stable (see figure 1.4 c): this is the restoration of the chiral symmetry.

The chiral symmetry restoration has an impact on the in-medium spectral functions of hadrons: the most easily accessible experimental observable related to this mechanism is the ρ meson, thanks to its short life-time (1.3 fm/c), allowing it to be produced and decay inside the volume of the QGP typically obtainable in heavy-ion collisions.

1.1.3 Hadronic Matter — Quark-Gluon Plasma (QGP)

As already remarked, low-energy QCD mechanisms are driven by the same scale parameter, Λ_{QCD}: this is the reason why chiral symmetry restoration and color deconfinement happen under the same thermodynamical conditions, identifiable in the QCD phase diagram shown in figure 1.5.

This schematic diagram presents two main regions. The first one is the region at low temperature and density where quarks and gluons are confined inside hadrons and the chiral symmetry is broken. The second region is characterized by large values of temperature and / or net baryon density where the relevant degrees of freedom are quark and gluon and is a new state of matter, the Quark Gluon Plasma (QGP). These two regions are separated by a phase transition. At vanishing net baryonic density (from 0 to an hypothetical critical point), this frontier is a smooth phase ("cross-over") transition. At increasing value of net baryonic density beyond an hypothetical critical point, the frontier becomes a first order phase transition. At extreme values of the net baryonic density and low temperature, other hadron phases of the hadronic matter can be possible as the hypothetic color superconducting phase proposed by some theoretical speculations.

The only way to get experimental access to the QCD phase diagram in the region of deconfinement, under controlled conditions, is to perform ultra-relativistic heavy-ion collisions. Different regions of the phase diagram can be covered by changing the center-

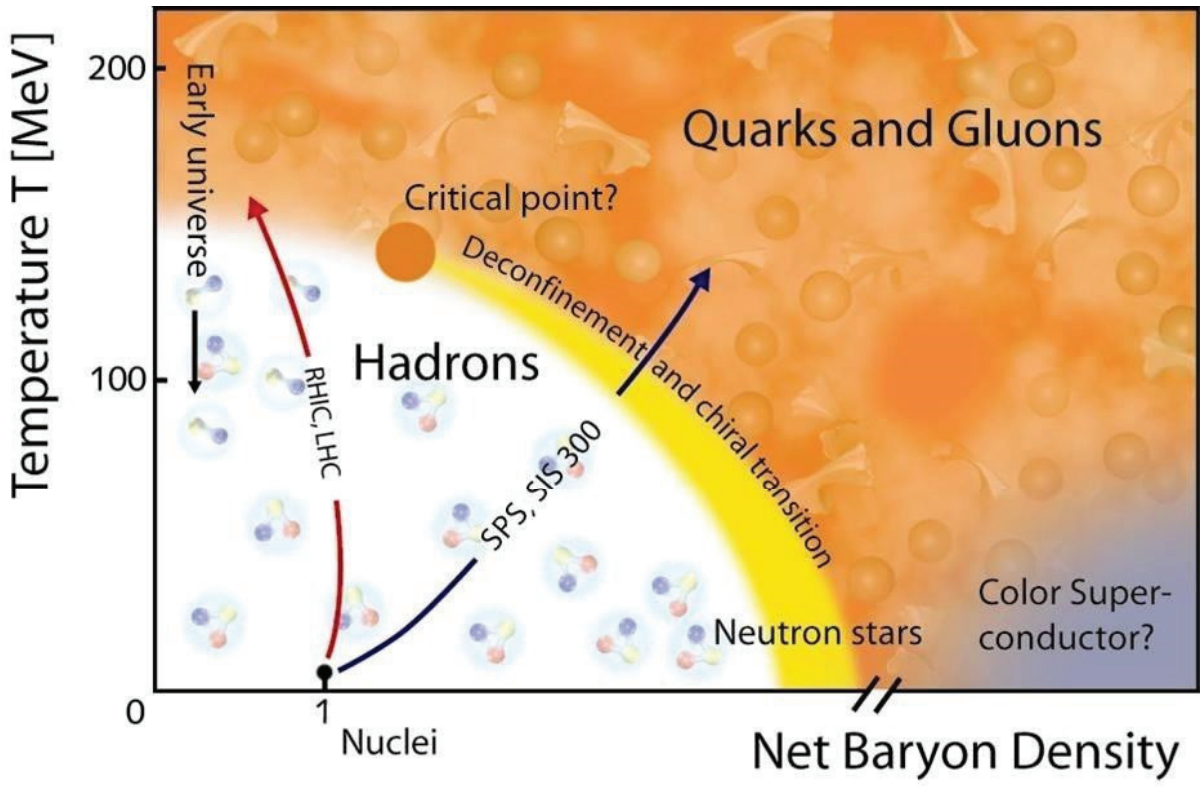

Figure 1.5: Schematic QCD phase diagram as a function of temperature and net baryon density.

of-mass energy of the collision: as the energy increases, the initial temperature of the system increases and its net baryonic density decreases. At the high-energy frontier, the experiments carried at the Large Hadron Collider (LHC) at CERN and the Relativistic Heavy-Ion Collider (RHIC) at the BNL are suited to reproduce the conditions of high temperature and low-net baryonic density present in the early Universe.

In this QCD phase diagram there is a hypothetical Critical Point and this point provides a major research focus both theoretically and experimentally. On the theory side, lattice QCD (LQCD) gives accurate results only at zero density. It can be extrapolated at finite density. Another technique is the use of effective models as the NJL one [7]. On the experimental side, studies of heavy-ion collisions are done with several energies and ion species (NA61, STAR, PHENIX) and they probe different density regimes. Finally compact star observation may also give results about the zero temperature, high density phase of QCD.

1.2 Heavy-Ion Physics: Experimental Program

The experimental study of QGP needs this state of matter to be recreated in laboratory. As we have seen in the previous section, high density and/or temperature are needed in order to reach the conditions for the creation of the QGP state: these conditions are met in ultra-relativistic heavy-ion collisions. This experimental tool allows one to change the energy density of the system by varying the size and the energy of the colliding nuclei.

Several probes of the QGP exist, which will be described later in this chapter: the design of a heavy-ion detector directly depends on the probes chosen for the experimental program.

The relativistic heavy-ion experimental program started in the early 1980s at the BNL AGS [9] and CERN SPS [10] (collision energy per nucleon pair up to $\sqrt{s_{\mathrm{NN}}} \approx 20$ GeV) and continues today both at the SPS and at the RHIC [11] and LHC [12] colliders, where energies up to $\sqrt{s_{\mathrm{NN}}} = 0.2$ TeV and 5 TeV are reached, respectively.

1.2.1 Relevant Kinematic Variables

Before discussing collision geometry and QGP probes, we briefly introduced the main kinematic variables of interest for heavy-ion physics and particularly for the study presented in this manuscript.

Transverse Momentum (p_{T}): The kinematics of a particle can be described by an energy-momentum quadrivector. In the context of a high-energy experiment where a privileged axis is defined by the beams, the 3-momentum can be conveniently decomposed into its longitudinal (p_z) and transverse (p_{T}) components. The transverse momentum is interesting for two reasons: firstly, the transverse degree of freedom is created during the collision, since the initial state is characterized only by the longitudinal degree of freedom of the colliding particles; secondly, the transverse momentum is invariant under Lorentz boosts along the z-axis, allowing one to directly compare the p_{T} distributions measured in fixed-target and collider experiments.

Rapidity (y): The longitudinal degree of freedom of a particle kinematics can be conveniently expressed in terms of the rapidity variable y, defined as:

$$y = \frac{1}{2} \ln \left(\frac{E + p_z c}{E - p_z c} \right). \tag{1.31}$$

It can be shown that the rapidity is additive under Lorentz boosts along the z-axis: this allows one to directly compare the shape of the rapidity distributions measured in fixed-target and collider experiments.

Pseudo-Rapidity (η): In the ultra-relativistic regime, where $p \gg m$ and $E \approx p$, the rapidity can be approximated by the pseudo-rapidity η:

$$y = \frac{1}{2} \ln \left(\frac{E + cp\cos\theta}{E - cp\cos\theta} \right) \approx \frac{1}{2} \ln \left(\frac{1 + \cos\theta}{1 - \cos\theta} \right) = -\ln \left[\tan \left(\frac{\theta}{2} \right) \right] \equiv \eta. \tag{1.32}$$

The pseudo-rapidity is especially useful whenever the energy and the longitudinal momentum p_z are not available at the same time: in this case, the pseudo-rapidity provides an approximation of the rapidity based on the measurement of the polar angle θ only (the angle between the z-axis and the particle direction).

Invariant Mass: In case the particle of interest for a given analysis is not directly observable (because of its short life time), its kinematics can still be reconstructed by identifying and measuring its decay products: the quadrivectors of the daughters can be composed to obtain the quadrivector of the mother particle, from which can be easily obtained its invariant mass $m^2c^4 = E^2 - p^2c^2$. In the specific case of the analysis presented in this thesis, the ϕ meson (as well as the other low-mass neutral mesons η, ρ, ω) has been identified through its decay into two muons.

1.2.2 Collision Geometry

To clearly interpret the observables in a heavy-ion collision, one also needs to characterize its geometry. The two main geometric parameters characterizing a heavy-ion collision are the centrality and the event plane.

Centrality — The centrality is a concept related to the finite size of the colliding nuclei: in fact, heavy nuclei (like the lead nuclei accelerated at the LHC) can be regarded as extended objects consisting of several nucleons. Some of these nucleons participate to the collision and are called participants, while the remnants do not interact and are called spectators, see figure 1.6-left.

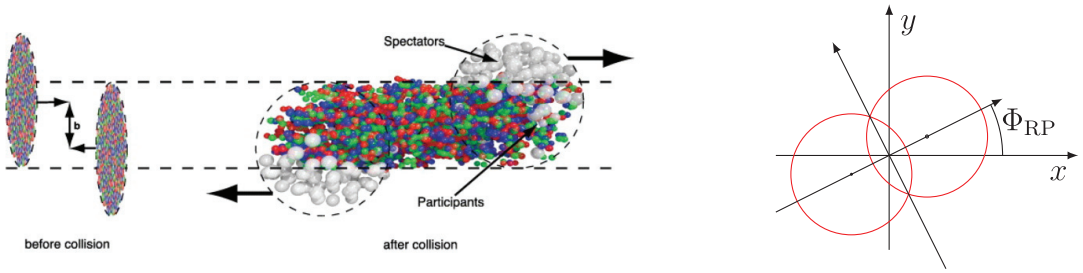

Figure 1.6: Schematic representation of a lead-lead collision.

As it can be also seen in figure 1.6-left, an impact parameter b can be identified when looking at a nucleus-nucleus collision in the transverse plane. If this parameter is null, the overlap between the two nuclei and the energy available in the overlapping volume is maximal: these collisions are classified as most central. For larger impact parameters, the overlap region between the two nuclei and the energy available in the overlapping volume become smaller: these collisions are classified as semi-central, semi-peripheral and peripheral for increasing values of b. If the impact parameter is larger then two nuclear radii, the collision is called ultra-peripheral and there is no hadronic interaction between the two nuclei.

The impact parameter, in a heavy-ion collision, is not directly measurable due to its femtoscopic size. Yet, b (so, the centrality of the collision) can be estimated by quantifying the produced particle multiplicity, since the two quantities are strongly correlated [13]. An effective way to establish this correlation is provided by the Glauber Model [14].

In smaller collision systems like pp and p-Pb, the measurement of the produced particle multiplicity is still possible, giving insight into the energy of the partonic interactions

involved in the collision (the so-called "event activity"). However, due to the loose correlation between this quantity and the geometry of the collision in such small systems [13], no geometrical interpretation can be established in this case.

Event plane — In case the collision is not head-on, it is possible to define the event plane, as a plane formed by the beam direction and the impact parameter. The transverse profile of this plane in non-central nucleus-nucleus collisions is represented in the right panel of figure 1.6. The determination of the event plane orientation, event-by-event, is important to characterize the azimuthal anisotropies observed in the measurement of the particles produced in the collisions.

1.2.3 Evolution of a Heavy-Ion Collision

Figure 1.7 illustrates the evolution of the hadronic collision in the two cases where the QGP is created (right side) or not (left side).

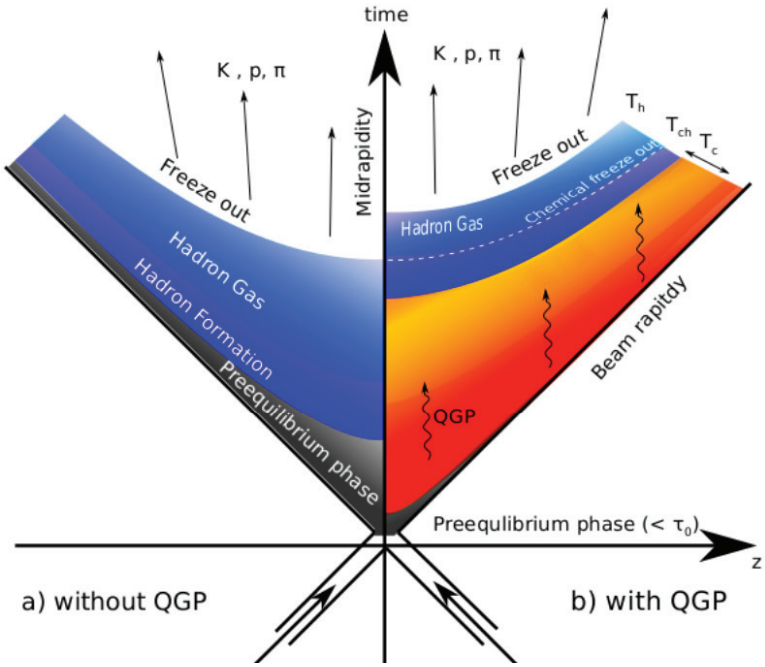

Figure 1.7: Space time evolution, left-side without QGP, right-side with QGP.

Collisions with creation of QGP — In this case, a dense and hot system of free partons is created in the collision; the typical size of the system is such that a thermodynamical approach can be adopted, and a medium temperature defined. This system of deconfined quarks and gluons undergoes multiple interactions and the expansion characterized by a hydrodynamic-like collective expansion. During this expansion, the hadronization starts and there is a cooling of the system until the critical temperature of the transition between the partonic and hadronic phases (T_c) is reached. The cooling continues, the medium is a hadronic gas, until the temperature of chemical freeze-out (T_{ch}) is reached (from above): beyond this point, the inelastic interactions stop and the

composition of hadronic species is fixed. The cooling continues until the kinetic freeze-out is reached: beyond this point the elastic interactions also stop and the hadrons fly to the detectors with kinematic distributions characterized by a temperature T_{h}.

Collisions without creation of QGP — In this case, the collision starts by a pre-equilibrium partonic phase which directly leads to the hadronic phase, without passing through any significant hydrodynamic or thermodynamic evolution. After the elastic interactions between the hadrons stop, the species and their kinematics are fixed.

1.2.4 Experimental Observables of the QGP

A variety of observables exists, giving insight into the properties of the QGP, each observable providing a complementary piece of information.

Bulk physics: light-flavor radiation

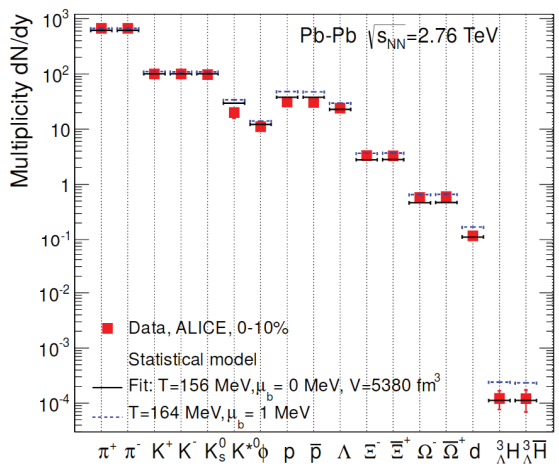

Figure 1.8: Hadron yields from ALICE at the LHC and fit with the statistical hadronization model [15].

The bulk radiation is mainly composed of light-flavored hadrons (u, d, s quarks). Having a typical scale of 1 fm $\simeq 1/(200\ \mathrm{MeV})$, these hadrons cannot exist inside the deconfined medium. For this reason, the light-flavor radiation measured by the detector is formed at the transition between the QGP and the physical vacuum, taking place at the critical temperature $T_{\mathrm{c}} \simeq 160 - 180$ MeV. This fact is confirmed by the good agreement between the measured relative abundances of the main light hadron species (including light hypernuclei) and the prediction of a statistical hadronization model with fixed thermodynamical parameters at the transition phase, see figure 1.8.

The global hydrodynamical flow driving the expansion of the deconfined medium induces the radial flow characterizing the light-flavor radiation p_{T} spectrum. Experimentally, it is possible to observe this radial flow by measuring the p_{T} dependence of the yield for the various species of the bulk radiation: an example is given in figure 1.9.

Moreover, if the initial conditions are not spherically symmetric, as it is in fact the case in non-central heavy-ion collisions, the difference in pressure in different spatial directions will lead to a further "directed" or "elliptic" flow (characterized by the v_2 parameters in the Fourier expansion of the azimuthal particle distribution). Since the elliptic flow depends on the initial conditions of the expending medium (like the geometry and the shear viscosity) the flow studies of hadron spectra can provide information about the earlier, pre-hadronic stages of the collisions. For example, figure 1.10 illustrates how the

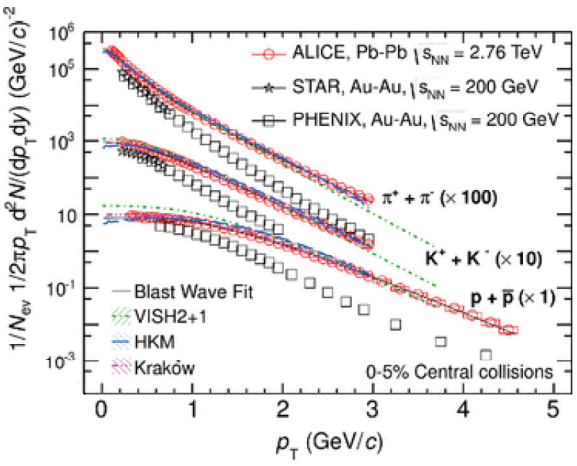

Figure 1.9: Transverse momentum distributions of the sum of positive and negative particles as measured by ALICE, fitted individually with a blast wave function, compared to RHIC data and hydrodynamic models [16].

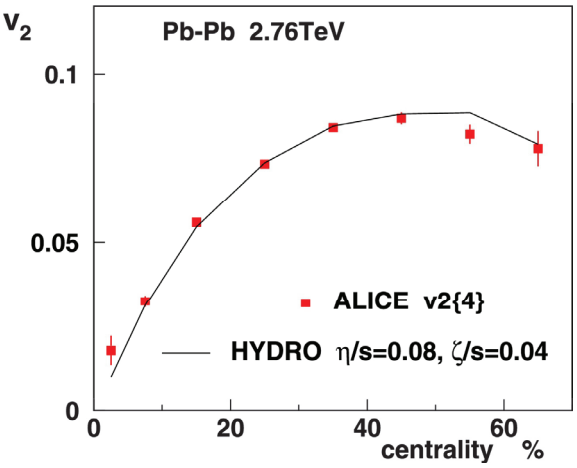

Figure 1.10: Elliptic flow coefficient of charged particle in Pb–Pb collisions as a function of centrality compared to viscous hydrodynamic results [17, 18]

shear viscosity (η/s) of the medium can be estimated by the analysis of the centrality dependence of the v_2 parameter.

Strangeness production

Within the light-flavor radiation, strangeness production plays a peculiar role, since there are no strange valence quarks in the initial state of the collision as opposed to u and d quarks, yet they are sufficiently light to be abundantly created in the course of the collisions. High-p_T strangeness production happens either at the early stages of high-energy collisions in hard partonic scattering processes by flavor creation and flavor excitation (see Feynman diagrams in figure 1.11), or during the subsequent partonic evolution via gluon splittings. Low-p_T strangeness production is dominated by non-perturbative processes like string fragmentation: however, due to the heavier mass of the strange quark (95 ± 5 MeV/c^2) than the u and d quarks, the production of strange hadrons in fragmentation processes is suppressed in comparison to the production of hadrons containing only u and d quarks.

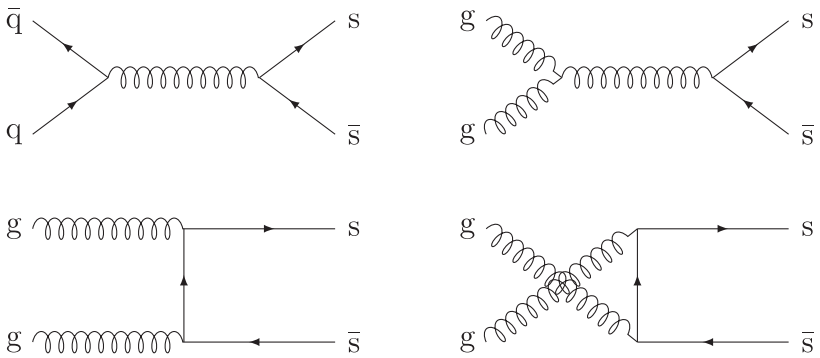

Figure 1.11: Feynman diagrams in pQCD at first order for the strangeness production inside QGP.

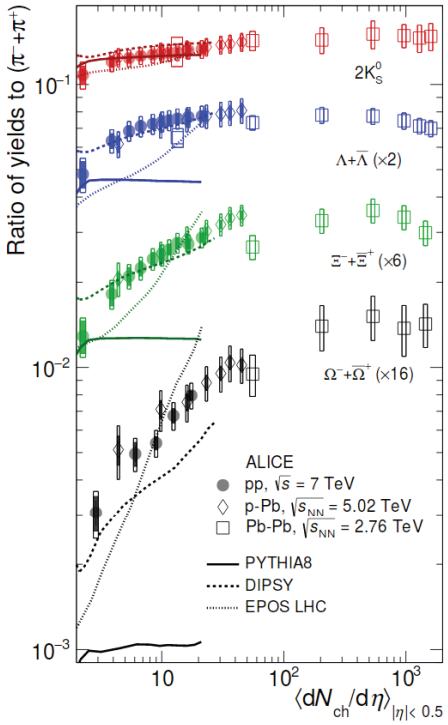

Figure 1.12: p_{T}-integrated yield ratios of strange and multi-strange hadrons to $(\pi^+ + \pi^-)$ as a function of $\langle \mathrm{d}N_{\mathrm{ch}}/\mathrm{d}\eta \rangle$ measured in the rapidity interval $|y| < 0.5$ [20].

An enhancement of strange hadron production was historically proposed [19] as an indication of the QGP formation: the argument is that strangeness production would be enhanced by the large energy density available in the medium, the enhancement scaling with the strangeness content of each hadron. Figure 1.12 shows the ratio of strange hadrons over pions as a function of event multiplicity for pp, p-Pb and Pb-Pb collisions. In this figure, one can appreciate the difference of the measured enhancement for strange hadrons containing different numbers of strange quarks: K_s mesons and Λ baryons containing one strange quark, Ξ baryons containing two strange quarks, and Ω baryons containing three strange quarks.

Jets

In high-energy collisions, a significant production of hard partons is observed: the hadronization of these partons produces a narrow cone of hadrons and other particles correlated together, named jet. In heavy-ion collisions, jet measurements offer the possibility to probe the deconfined medium by measuring the energy loss of the initial hard parton (jet quenching), and the modification of the jet cone structure and composition (jet broadening). Due to the high energy involved in the production of hard partons, jet physics in heavy-ion collision basically started at RHIC in 2000', where $\sqrt{s_{\mathrm{NN}}}$ values of the order of 100 GeV became available for the first time. Today, jet physics in heavy-ion collisions profits from the larger energies available at the LHC, implying larger cross-sections for hard scattered partons, and an extended range of jet energies.

In figure 1.13 and 1.14 two examples of jet physics results in heavy-ion collisions are

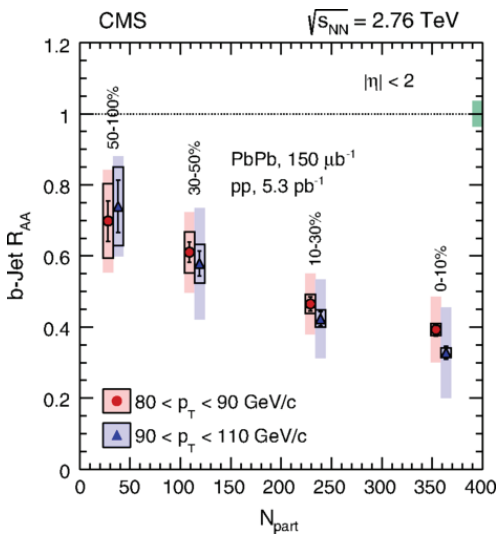

Figure 1.13: The b-tagged jet R_{AA}, as a function of N_{part} for two jet p_{T} selections in Pb-Pb at $\sqrt{s_{\mathrm{NN}}} = 2.76$ TeV in CMS [21].

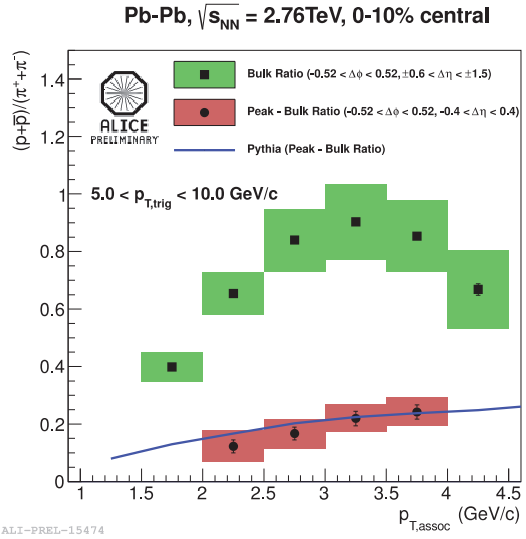

Figure 1.14: Ratio of proton to pion spectra as function of p_{T} for the "bulk" and "peak-bulk" [22]

shown. In figure 1.13 the nuclear modification factor (R_{AA}) of b-tagged jets is shown as a function of N_{part}, as measured by the CMS experiment at the LHC in Pb-Pb collisions at $\sqrt{s_{\mathrm{NN}}} = 2.76$ TeV. A clear decreasing trend for R_{AA} is observed for increasing values of N_{part}, interpreted as a manifestation of the jet-quenching mechanism. In figure 1.14 the proton-over-pion ratios in the bulk and in jet are shown as a function of p_{T}, measured by ALICE in Pb-Pb collisions at $\sqrt{s_{\mathrm{NN}}} = 2.76$ TeV. The comparison of the measured proton-over-pion ratio in jets ("peak-bulk") with the prediction from `PYTHIA` suggests that no significant medium-induced modification of particle ratios is at play in jets.

Heavy flavors

The abundant production of c and b quarks at LHC offers a unique possibility to understand the details of the energy loss, thermalization and hadronization mechanisms characterizing the interaction of heavy quarks with the medium.

The energy loss can be studied through the measurement of the p_{T}-dependence of the nuclear modification factor R_{AA} for the various heavy flavor hadron species. In figures 1.15 and 1.16 the R_{AA} averaged over the main non-strange D-meson species is compared with the R_{AA} of light-flavored mesons and (non-prompt) J/ψ from B decays, respectively, probing the suppression hierarchy $R_{\mathrm{AA}}^{\mathrm{B}} > R_{\mathrm{AA}}^{\mathrm{D}} \gtrsim R_{\mathrm{AA}}^{\text{light quarks}}$ reflecting the different energy loss of light, charm and beauty quarks. Despite the large uncertainties, the data suggest a similar energy loss for the charm and light quark, a scenario also supported by some theoretical models [23]. The heavy quark hadronization mechanism in the medium can be studied by comparing the production of various species of heavy flavor hadrons [24, 25].

Quarkonia

Quarkonia are resonance states of charm-anticharm (charmonia) or bottom-antibottom (bottomonia) pairs. Quarkonium measurements provide information on the properties of

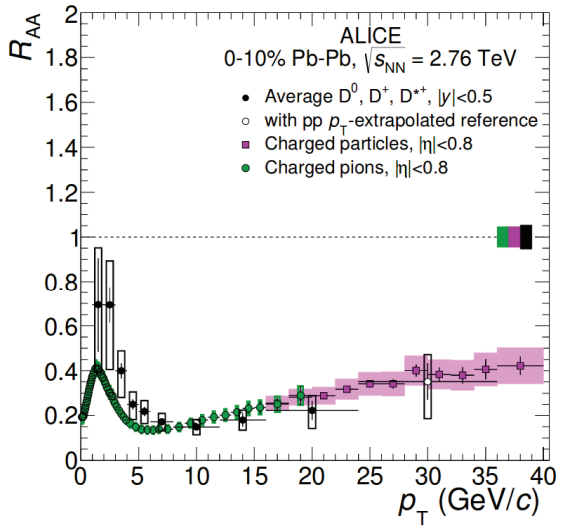

Figure 1.15: Prompt D-meson R_{AA} as a function of p_T compared to the pion and charged particles R_{AA} in the 0-10% centrality classes [26].

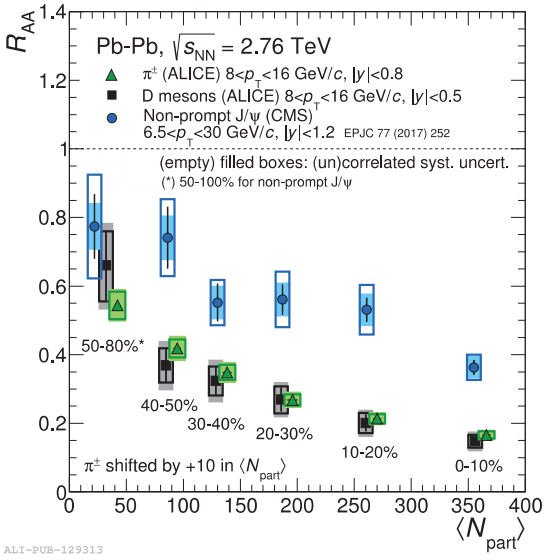

Figure 1.16: Comparison of the average D-meson R_{AA} in 8<p_T <16 GeV/c with charged pions in the same p_T range and J/ψ from B decays in 6.5<p_T <30 GeV/c [27].

the medium in the early stages of heavy-ion collisions, being sensitive to the in-medium dissociation and recombination mechanisms for the various quarkonium states. Quarkonium dissociation was indeed proposed as a signature of the production of QGP in heavy-ion collisions due to a color-screening effect [28, 29], in analogy to the Debye-screening in electrostatics, coupled to a dynamical interaction of the heavy-quark pair with the surrounding partons [30, 31].

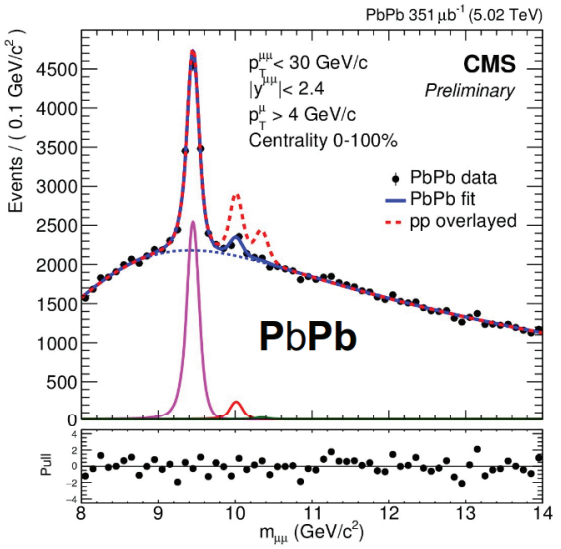

Figure 1.17: Dimuon mass spectrum in the ϒ region in Pb-Pb collisions at $\sqrt{s_{NN}} = 5.02$ TeV with CMS experiment [32].

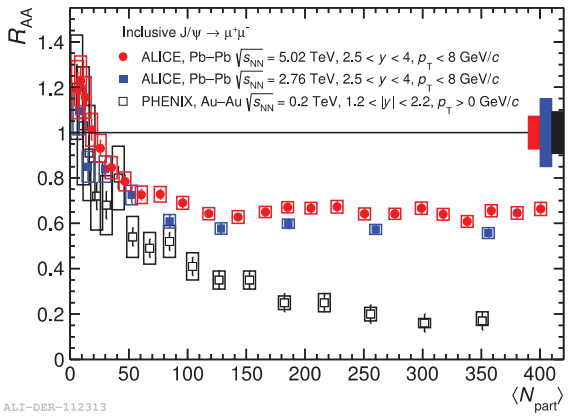

Figure 1.18: The participant number dependence of R_{AA} for inclusive J/ψ in ALICE in Pb-Pb collisions at $\sqrt{s_{NN}} = 5.02$ and 2.76 TeV and in PHENIX at forward rapidity in Au-Au at $\sqrt{s_{NN}} = 200$ GeV

The dissociation mechanism, resulting in the suppression of the less bound quarkonium states, is best illustrated in figure 1.17, showing the dimuon mass spectrum in the Υ region measured by the CMS experiment, with the Pb-Pb data at $\sqrt{s_{\rm NN}} = 5.02$ TeV compared to the expected yield in pp. One can observe that the suppression of the Υ(3S) state is stronger than the one of the Υ(2S), with respect to the Υ(1S), due to the different binding energy of the two resonance states (sequential melting of quarkonium).

For the charmonium states, a statistical recombination mechanism is expected to compete with dissociation for sufficiently large values of the $c\bar{c}$ cross-section, expected for instance in Pb-Pb collisions at the LHC energies. The interplay of the suppression and recombination mechanisms has indeed been proposed to explain the ALICE data for the centrality dependence of the J/ψ $R_{\rm AA}$ in Pb-Pb at $\sqrt{s_{\rm NN}} = 5.02$ and 2.76 TeV, shown in figure 1.18 together with the PHENIX results in Au-Au collisions at $\sqrt{s_{\rm NN}} = 200$ GeV. For $\langle N_{\rm part} \rangle > 120$, the ALICE J/$\psi$ $R_{\rm AA}$ shows no significant centrality dependence and is almost a factor of 3 larger than the PHENIX data for the most central points, no sizable recombination mechanism being at play at RHIC energy. Further insight on the role of statistical recombination in charmonium production at the LHC could come from the comparison of the J/ψ elliptic flow measurements with the theoretical models.

Electromagnetic probes

Electromagnetic radiation (real photons and dileptons from virtual photons) is emitted from a variety of processes: prompt photons from initial hard scatterings, thermal photons and medium-modified ρ dileptons from the QGP phase, real and dileptons from radiative decays after hadronization. The fact that electromagnetic radiation is emitted during the whole evolution of the collision, represents at the same time an advantage (for instance, the possibility of probing the entire lifetime of the fireball) and a drawback (the various components being hard to disentangle). Another advantage of electromagnetic radiation is that, whenever emitted, it is not affected during its propagation by the strong interaction dominating inside the deconfined medium, providing a clean probe of hadronic interactions.

Figure 1.19 shows the $p_{\rm T}$ spectrum of real photons in Pb-Pb collisions at $\sqrt{s_{\rm NN}} = 2.76$ TeV measured by ALICE for three centrality classes. In all centrality classes, no evidence for medium influence is observed at high $p_{\rm T}$. At low $p_{\rm T}$ ($\lesssim 2$ GeV/c), on the contrary, an excess of real photons with respect to pQCD real photon production is observed for mid- and central collisions, with a temperature of $T_{\rm eff} \approx 300$ MeV extracted in central collisions [33]. This excess might be related, indeed, to the production of thermal photons from the QGP phase.

Figure 1.20 shows the excess in the dimuon mass spectrum, with respect to the expected hadronic sources, measured by NA60 in semi-central In-In collisions at $\sqrt{s_{\rm NN}} = 17.3$ GeV, compared to various theoretical scenarios. This excess is dominated by the medium-modified ρ line shape at low mass ($\lesssim 1$ GeV/c^2), and by a thermal contribution at intermediate mass ($\gtrsim 1$ GeV/c^2), and its study allows one to shed light on the relevant properties of QGP equation of state [34, 35].

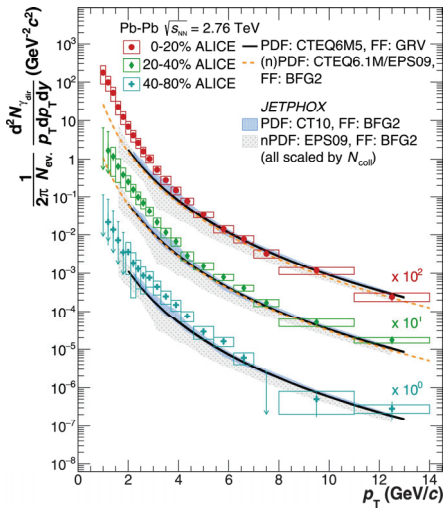

Figure 1.19: Direct photon spectra in Pb–Pb collisions at $\sqrt{s_{\rm NN}} = 2.76$ TeV for three centrality classes compared to model in pp collisions at the same energy, scaled by the number of binary nucleon collisions for each centrality class [33].

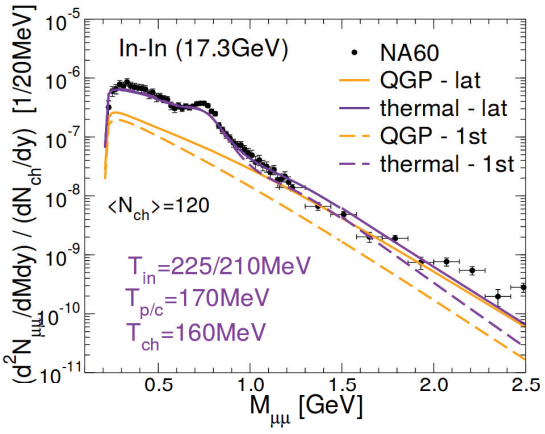

Figure 1.20: Dimuon invariant-mass in semi-central In-In collisions with NA60 [34].

1.2.5 Proton-Proton Collisions

Proton-proton collisions present various aspects of interest in the context of heavy-ion physics, namely as a reference for heavy-ion observations, test for pQCD calculations, input for phenomenological non-perturbative models, and environment for collectivity in small systems.

As a reference for heavy-ion collisions, pp measurements are needed in order hot and cold nuclear matter effects to be properly disentangled respectively in nucleus-nucleus and proton-nucleus collisions. This implies two necessities: collecting pp reference data at the same $\sqrt{s_{\rm NN}}$ energy as more complex collision systems, and finding appropriate variables which could relate pp, pA and AA observations. A primary example is given by the nuclear modification factor ($R_{\rm AA}$), defined as the direct ratio of production cross-sections in AA or pA, over the corresponding pp reference scaled by the number of binary collisions, for example to study the charged-particle production [36].

Proton-proton collisions are also an ideal environment for the study of hard and soft processes in vacuum. In the first case (jets, J/ψ, Υ, ...) one has the possibility to test pQCD calculations; in the second case, constraints on phenomenological models can be derived, in terms of kinematic distributions and production cross-sections [37, 38].

Finally, it is possible to use pp collisions for studying the emergence of collective effects in small systems. This study is typically performed analyzing the data in classes of charged particle multiplicity, the onset of collectivity being driven by the event activity. In this context, the observation of collective effects in large-activity pp and p-Pb collisions, showing striking similarities with those observed in Pb-Pb collisions, represents an intriguing challenge for theoretical models [39].

1.3 Low-Mass Dimuon Measurements in ALICE

This thesis work is focused on low-mass dimuon measurements in pp collisions at $\sqrt{s} = 13$ TeV. For this reason, it is interesting to report here about low-mass dimuon results and currently ongoing analyses in the other collision systems and energies available. Low-mass dimuon production is studied in ALICE in Pb-Pb collisions at $\sqrt{s_{\rm NN}} = 2.76$ and 5.02 TeV, in p-Pb collisions at $\sqrt{s_{\rm NN}} = 5.02$ and 8.16 TeV, as well as in pp collisions at $\sqrt{s} = 2.76$, 5.02, 7 and 8 TeV. Due to the favorable position of its two-body decay in the low-mass dimuon region, with no significant competing sources beyond the smooth correlated continuum from open heavy flavors, the ϕ-meson has been the privileged subject of the low-mass dimuon analyses in the first years of LHC operation.

Pb-Pb collisions

The LHC provided Pb-Pb collisions in Run 1 at $\sqrt{s_{\rm NN}} = 2.76$ TeV and in Run 2 at $\sqrt{s_{\rm NN}} = 5.02$ TeV.

Due to the limited statistics of the Run 1 data, the ϕ-meson study is limited to the $p_{\rm T}$ range from 2.0 to 5.0 GeV/c for the dimuons in Pb-Pb collisions at $\sqrt{s_{\rm NN}} = 2.76$ TeV, see figure 1.21, where the lower limit is imposed by the hardware trigger condition on single muons ($p_{\rm T} \gtrsim 1$ GeV/c), and the upper limit is defined by the available statistics. The analysis of the Run 1 low-mass dimuon data allowed the measurement of the nuclear modification factor $R_{\rm AA}$ of the ϕ-meson at forward rapidity in Pb-Pb collisions at $\sqrt{s_{\rm NN}} = 2.76$ TeV, shown in figure 1.22 together with the corresponding ALICE measurement at mid-rapidity and the PHENIX measurement at mid-rapidity in Au-Au and Cu-Cu collisions at $\sqrt{s_{\rm NN}} = 200$ GeV. As can be seen from the comparison of the two ALICE sets of points, the $R_{\rm AA}$ does not exhibit any significant dependence on the rapidity region considered; on the contrary, the PHENIX points seem systematically higher than the ALICE ones, although still compatible with the latter within the total uncertainties. All the data sets agree on the general decreasing trend of $R_{\rm AA}$ as a function of $\langle N_{\rm part} \rangle$.

The larger statistics available from the first Pb-Pb data taking at $\sqrt{s_{\rm NN}} = 5.02$ TeV of Run 2 (2015, a second one being foreseen for 2018) allows the analysis of ϕ-meson production to be performed up to 7 GeV/c, starting again from 2 GeV/c due to the hardware trigger condition. The $p_{\rm T}$ dependence of the ϕ-meson yield could be studied in several centrality classes, as shown in figure 1.23, where the data points are fitted with the power-law function

$$\frac{{\rm d}N}{{\rm d}p_{\rm T}} \propto \frac{p_{\rm T}}{\left[1 + \left(\frac{p_{\rm T}}{p_0}\right)^2\right]^n} \quad , \tag{1.33}$$

where n and p_0 are the free parameters of the fit. The centrality dependence of ϕ-meson production is also studied by looking at the central-to-peripheral ratio $R_{\rm AA}$ as a function of $\langle N_{\rm part} \rangle$: as shown in figure 1.24, this dependence suggests a general decreasing trend of $R_{\rm AA}$ as a function of centrality.

p-Pb collisions

The LHC provided in Run 1 p-Pb collisions at $\sqrt{s_{\rm NN}} = 5.02$ TeV and in Run 2 at

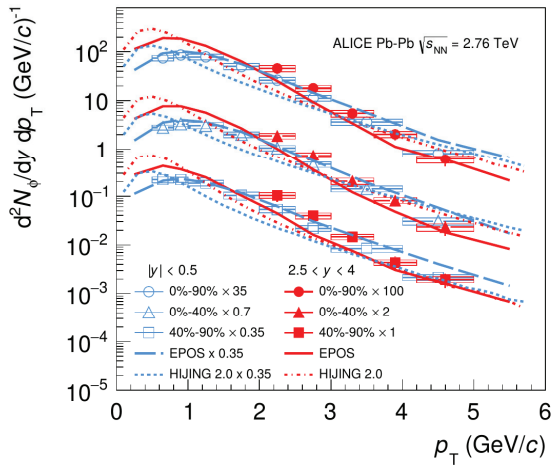

Figure 1.21: ϕ-meson yield as a function of p_{T} in Pb-Pb collisions at $\sqrt{s_{\mathrm{NN}}} = 2.76$ TeV in three centrality classes and two rapidity regions [40].

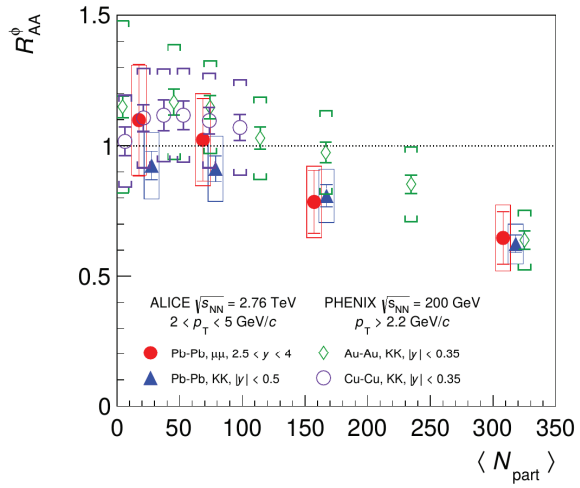

Figure 1.22: ϕ-meson R_{AA} as function of $\langle N_{\mathrm{part}} \rangle$, in Pb-Pb collision at $\sqrt{s_{\mathrm{NN}}} = 2.76$ TeV, and Au-Au and Cu-Cu collisions at $\sqrt{s_{\mathrm{NN}}} = 200$ GeV [40].

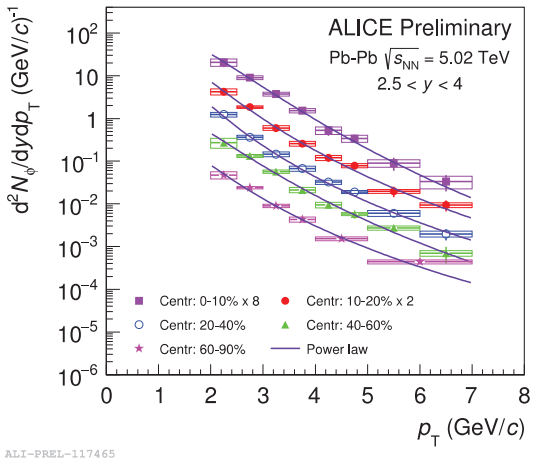

Figure 1.23: ϕ yield as a function of p_{T} for five centrality classes in Pb-Pb collisions at $\sqrt{s_{\mathrm{NN}}} = 5.02$ TeV [41].

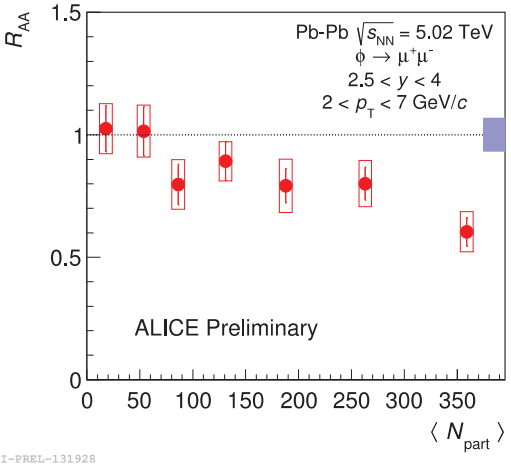

Figure 1.24: ϕ nuclear modification factor R_{cp} as a function of N_{part} in Pb-Pb collisions at $\sqrt{s_{\mathrm{NN}}} = 5.02$ TeV [41].

$\sqrt{s_{\rm NN}}$ = 8.16 TeV. Because of the different energy of the proton and Pb beams, in p-Pb collisions the nucleon-nucleon center-of-mass moves in the laboratory with a positive rapidity in the direction of the proton beam. The directions of the proton and Pb beam orbits can be inverted during the p-Pb data taking periods, allowing the ALICE muon spectrometer to access a forward rapidity region when the proton beam is directed towards the muon spectrometer ($2.03 < y < 3.53$), and a backward rapidity region when the Pb beam is directed towards the muon spectrometer ($-4.46 < y < -2.96$).

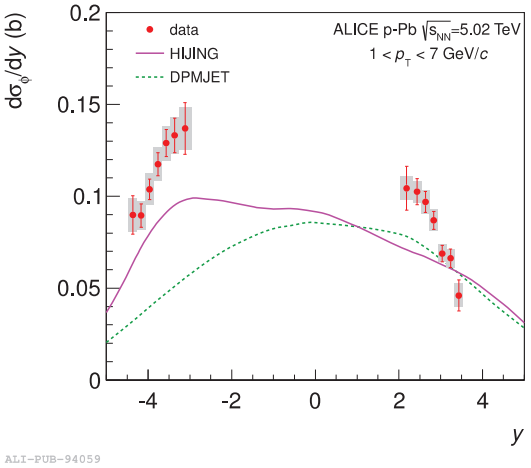

Figure 1.25: ϕ-meson cross-section as a function of y in p-Pb collisions at $\sqrt{s_{\rm NN}} = 5.02$ TeV and $1.0 < p_{\rm T} < 7.0$ GeV/c. Predictions from HIJING and DPMJET are also shown for comparison.

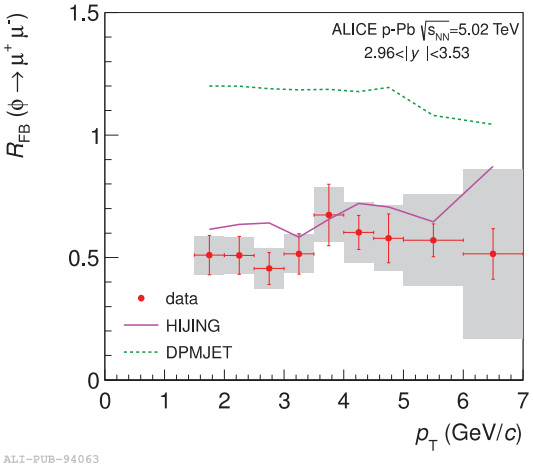

Figure 1.26: ϕ-meson forward-backward cross-section ratio as a function of $p_{\rm T}$, for $2.96 < |y| < 3.53$, in p-Pb collisions at $\sqrt{s_{\rm NN}} = 5.02$ TeV. Predictions from HIJING and DPMJET are also shown for comparison.

Figure 1.25 reports the ϕ-meson cross-section as a function of y for p-Pb collisions at $\sqrt{s_{\rm NN}} = 5.02$ TeV, showing a clear asymmetry between the forward and backward regions, not reproduced by the predictions of `HIJING` and `DPMJET`, also shown. To establish a more direct comparison of the ϕ-meson cross-section in the forward and backward regions, the cross-section was extracted as a function of $p_{\rm T}$ in the common $|y|$ range $2.96 < |y| < 3.53$, in terms of the ratio $R_{\rm FB}$ between the forward and backward cross-section, shown in figure 1.26. The observation of $R_{\rm FB}$ values significantly different than 1 is consistent with the observation of the asymmetry in the y dependence of the cross-section reported in figure 1.25. No significant $p_{\rm T}$ dependence of $R_{\rm FB}$ is visible within statistical and systematic uncertainties.

p-Pb data have also been taken in 2016 at $\sqrt{s_{\rm NN}} = 8.16$ TeV, with a total integrated luminosity larger than the one of the $\sqrt{s_{\rm NN}} = 5.02$ TeV data taking (see table 2.2). The analysis of this data is currently ongoing and is expected to produce the first preliminary results in 2018.

pp collisions

Low-mass dimuon data in pp collisions are available at several center-of-mass energies: $\sqrt{s} = 2.76$, 7 and 8 TeV (data taken during the LHC Run 1); 5.02 and 13 TeV (data taken during the LHC Run 2).

pp results at $\sqrt{s} = 2.76$ TeV [13] are used as a reference for Pb-Pb collisions at the same $\sqrt{s_{\rm NN}}$. Figure 1.27 shows the opposite-sign dimuon signal (after combinatorial background subtraction) integrated over the available $p_{\rm T}$ and y ranges, compared to the result of the hadronic cocktail fit: the good quality of the data-MC comparison leads to a robust extraction of the ϕ-meson signal. Figure 1.28 shows the ϕ-meson differential cross-section as a function of $p_{\rm T}$ compared to the Levy-Tsallis function [42]

$$\frac{1}{p_{\rm T}}\frac{{\rm d}N}{{\rm d}p_{\rm T}} \propto \left(1 + \frac{\sqrt{{p_{\rm T}}^2 + m_{\phi}^2} - m_{\phi}}{n\,T}\right)^{-n}, \tag{1.34}$$

with n and T as free parameters. In figure 1.28, data are also compared to the predictions by PHOJET and PYTHIA tunes ATLAS-CSC, D6T, Perugia0 and Perugia11. As one can see, a good agreement is found between predictions and data, except for PYTHIA tunes Perugia0 and Perugia11 which underestimate the cross-section measurement.

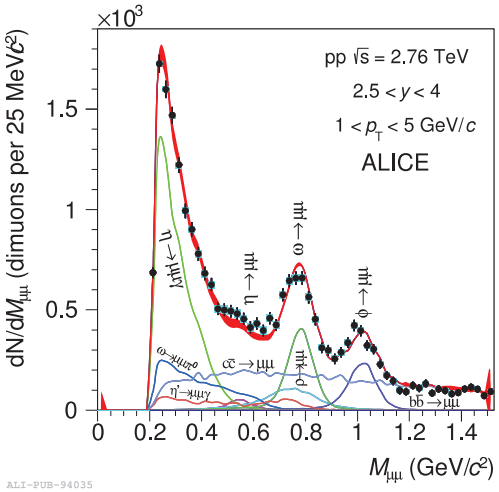

Figure 1.27: Dimuon opposite-sign mass spectrum in pp collisions at $\sqrt{s} = 2.76$ TeV after combinatorial background subtraction: $p_{\rm T}$- and y-integrated data, compared to the hadronic cocktail fit [13].

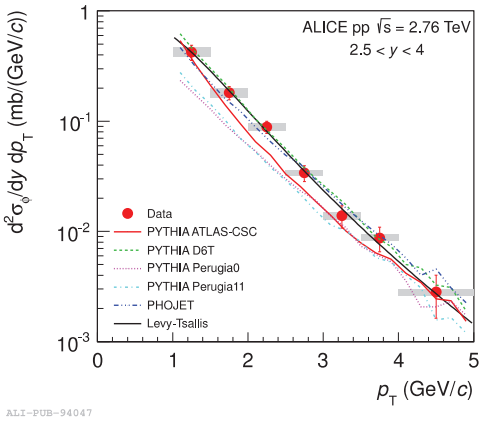

Figure 1.28: ϕ-meson cross-section as a function of $p_{\rm T}$ in pp collisions at $\sqrt{s} = 2.76$ TeV. Predictions from PHOJET and PYTHIA are also shown for comparison, as well as the result of a fit with a Levy-Tsallis function [13].

Low-mass dimuon data taken in 2015 in pp collisions at $\sqrt{s} = 5.02$ TeV offer the possibility to establish a data-based reference for Pb-Pb and p-Pb data at the same energy. The opposite-sign dimuon signal in pp collisions at $\sqrt{s} = 5.02$ TeV is shown in figure 1.29, integrated over the available $p_{\rm T}$ and y ranges, compared to the result of the hadronic cocktail fit: the good quality of the data-MC comparison allows for a robust extraction of the ϕ-meson signal. The $p_{\rm T}$-differential ϕ-meson cross-section could be extracted up to 6 GeV/c, as shown in figure 1.30 compared to different theoretical models.

Low-mass dimuon data in pp collisions at $\sqrt{s} = 7$ TeV allowed for the study of the $p_{\rm T}$-differential ω and ϕ cross-sections. The hadronic cocktail fit on the isolated opposite-sign dimuon signal is shown in figure 1.31. The identification of the ω and the ϕ meson signals

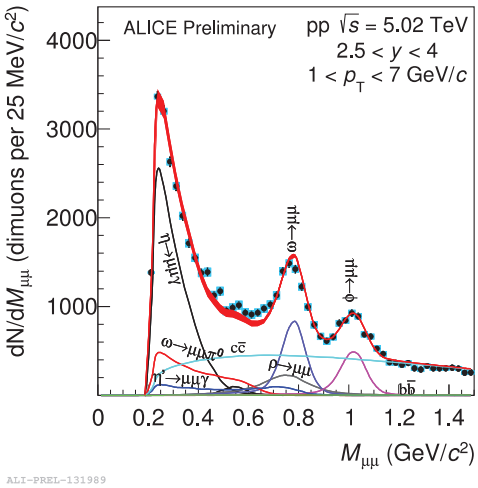

Figure 1.29: Dimuon opposite-sign mass spectrum in pp collisions at $\sqrt{s} = 5.02$ TeV after combinatorial background subtraction: p_{T}- and y-integrated data, compared to the hadronic cocktail fit [41].

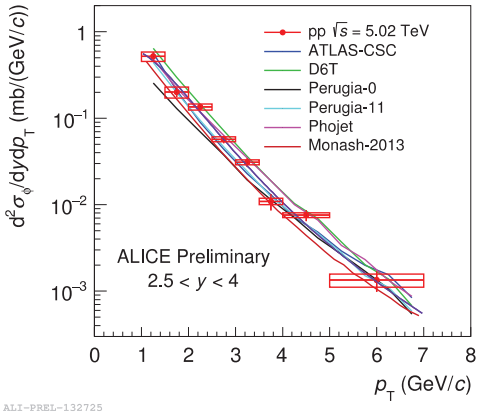

Figure 1.30: ϕ-meson cross-section as a function of p_{T} in pp collisions at $\sqrt{s} = 5.02$ TeV [41].

resulted in the measurements of the p_{T} differential cross-section shown in figure 1.32 for the ω-meson only: calculation based of PHOJET and PYTHIA with ATLAS-CSC and D6T tunes fairly agree with the data while the Perugia0 and Perugia11 PYTHIA tunes underestimate the cross-section by about a factor of 2 and 2.5 respectively (the same conclusions stand for ϕ-meson).

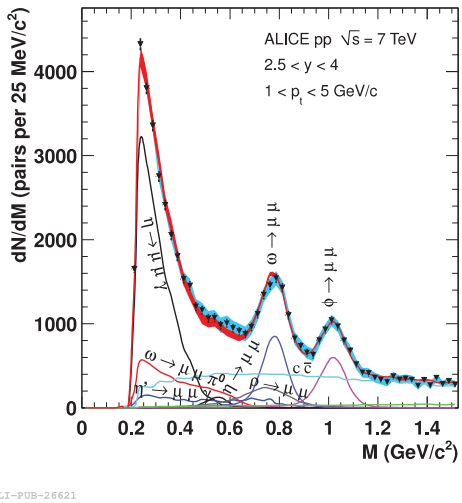

Figure 1.31: Dimuon opposite-sign mass spectrum for pp collisions at $\sqrt{s} = 7$ TeV after combinatorial background subtraction: p_{T}- and y-integrated sample, compared to the result of the hadronic cocktail fit [43].

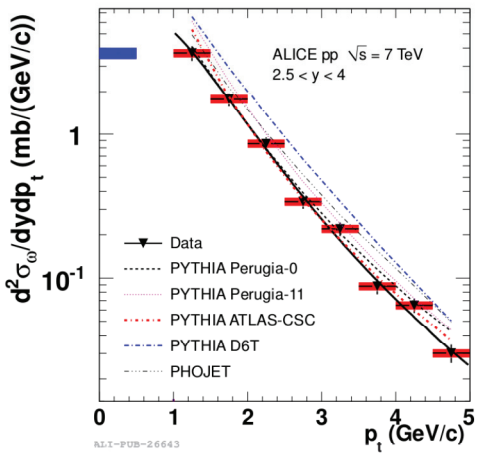

Figure 1.32: ω-meson cross-section as a function of p_{T} in pp collisions at $\sqrt{s} = 7$ TeV compared to the predictions of various phenomenological models [43].

Finally, low-mass dimuon data are also available in pp collisions at $\sqrt{s} = 8$ TeV. This

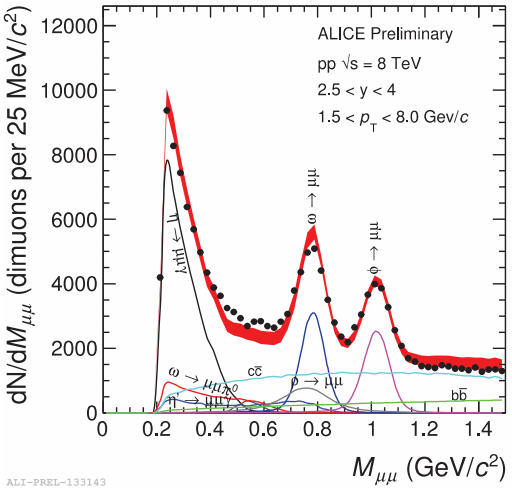

Figure 1.33: Dimuon opposite-sign mass spectrum in pp collisions at $\sqrt{s} = 8$ TeV after combinatorial background subtraction: p_{T}- and y-integrated data, compared to the hadronic cocktail fit [41].

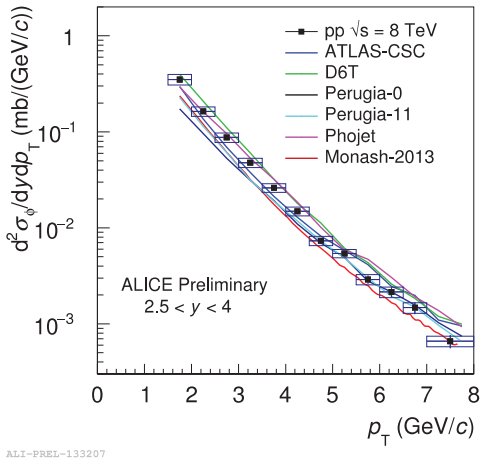

Figure 1.34: ϕ-meson cross-section as a function of p_{T} in pp collisions at $\sqrt{s} = 8$ TeV [41].

offers the possibility to enrich the study of light neutral meson production in pp collisions as a function of $\sqrt{s}$ providing at a same time a useful reference for the p-Pb data at the same $\sqrt{s_{\mathrm{NN}}}$ energy. The available statistics, larger than the one in pp collisions at $\sqrt{s} = 7$ TeV, allows to extract the low-mass dimuon analysis up to $p_{\mathrm{T}} = 8.0$ GeV/c. On the other side the higher single muon threshold implies that the analysis could only start from $p_{\mathrm{T}} = 1.5$ GeV/c. The p_{T}- and y-integrated opposite-sign dimuon signal is shown in figure 1.33 with the associated hadronic cocktail fit. Figure 1.34 shows the extracted ϕ cross-section as a function of p_{T}, compared to three predictions of `EPOS-LHC` and `PYTHIA-8` with and without multiple parton interactions. As one can see, the `EPOS-LHC` prediction overestimates the ϕ cross-section, while the comparison to the `PYTHIA-8` predictions seems to favor a scenario including multiple parton interactions.

Chapter 2

ALICE at the CERN LHC

Summary

2.1 The Large Hadron Collider

The Large Hadron Collider (LHC) straddling the French/Swiss border in average 100 meter underground in a circular tunnel of some 27 km of circumference is, as for now, the world's largest and most powerful particle collider. It operates at the TeV energy scale, with nominal energy of 14 TeV (in pp collision) and 5.5 TeV/nucleon pair (in Lead-Lead) foreseen to be achieved in 2018. To carry out this technical challenge, the CERN machine engineers developed a new accelerating technique based on superconducting magnets (NbTi) cooled down to a temperature below 2 K, which can generate magnetic fields up to 8 T. Four main experiments have been installed within the LHC ring, namely ATLAS (A Toroidal LHC ApparatuS), CMS (Compact Muon Solenoid), LHCb (LHC-beauty) and ALICE (A Large Ion Collider Experiment). ALICE will be described in more details in section 2.2.

2.1.1 The CERN accelerator complex

Figure 2.1 displays the LHC ring and the full complex of accelerators upstream the LHC. Following a complete trip from the proton source to the final output within the LHC, protons are produced in the LINAC 2 and then injected in the BOOSTER (PSB for Proton Synchroton Booster) first accelerator ring. This accelerating stage increases the

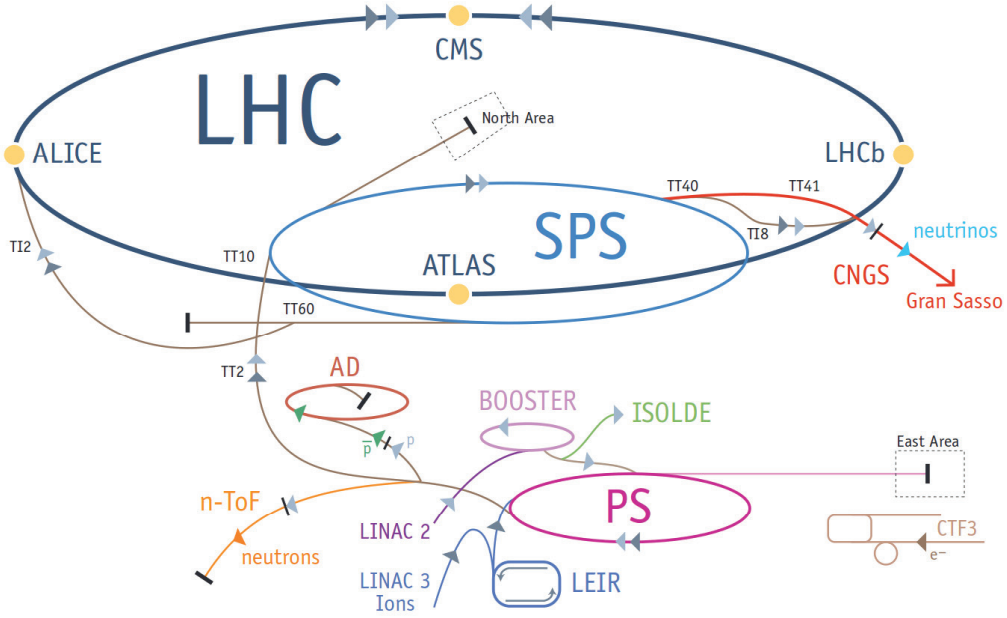

Figure 2.1: The LHC and the CERN accelerator complex [44]

proton energy from 50 MeV to 1.4 GeV. Once protons have reached the top PSB energy, they are injected into the Proton Synchroton (PS) where their energy is ramped up to 25 GeV and then into the Super Proton Synchrotron (SPS) (7 km in circumference) to the nominal energy of 450 GeV. The latter is the LHC injector and is used in parallel to provide particle beam to other CERN experiments (for example NA61/SHINE).

In the case of the LHC heavy ions runs, the lead ions are firstly accelerated in a LINAC 3, then further accelerated in the Low Energy Ion Ring (LEIR) which increases the lead energy from 4.2 MeV to 72 MeV/nucleon before injection in the PS. The lead ions are then accelerated and injected in the SPS, and from there to the LHC.

2.1.2 The LHC schedule

During the first LHC run (Run 1, 2009–2013), several energies and three collision systems (pp, p-Pb, Pb-Pb) have been explored. In pp collisions, five different center-of-mass energies have been considered: 0.9, 2.36, 2.76, 7, and 8 TeV; p-Pb and Pb-Pb collisions have been measured at $\sqrt{s_{\rm NN}} = 5.02$ TeV and $\sqrt{s_{\rm NN}} = 2.76$ TeV, respectively. Run 1 was followed by a first Long Shutdown (LS1), mainly dedicated to the upgrade of the accelerator system — resulting in an increase of the collision energy from $7 - 8$ TeV to $13 - 14$ TeV in proton-proton collisions (from 2.76 TeV to 5.02 TeV in Pb-Pb collisions) — and the completion of the detectors of some of LHC experiment (in the case of ALICE, the electromagnetic calorimeter and the Transition Radiation Detector were updated). Run 2 started in mid-2016 and is planned to last until the end of 2018, with pp collisions delivered at 5.02 and 13 TeV, Pb-Pb collisions delivered at $\sqrt{s_{\rm NN}} = 5.02$ TeV and p-Pb collision delivered at $\sqrt{s_{\rm NN}} = 5.02 - 8$ TeV. LS2 is foreseen to start at the beginning of 2019, ending in late 2020: during LS2, the installation phase of the ALICE upgrade

program will take place. During Run 3, pp and Pb-Pb collisions will be delivered at the nominal LHC energy (14 TeV for pp and $\sqrt{s_{\mathrm{NN}}} = 5.5$ TeV for Pb-Pb) and the first Pb-Pb data taking at high-luminosity will take place. LS3 will be mainly devoted to the installation of the High-Luminosity LHC (HL-LHC) providing unprecedented luminosities in pp collisions at the designed LHC energy. During LS3, the CMS and ATLAS upgrade programs will be finalize. Run 4 will see the beginning of the HL-LHC program in pp collisions and the continuation of the high-luminosity heavy ion program.

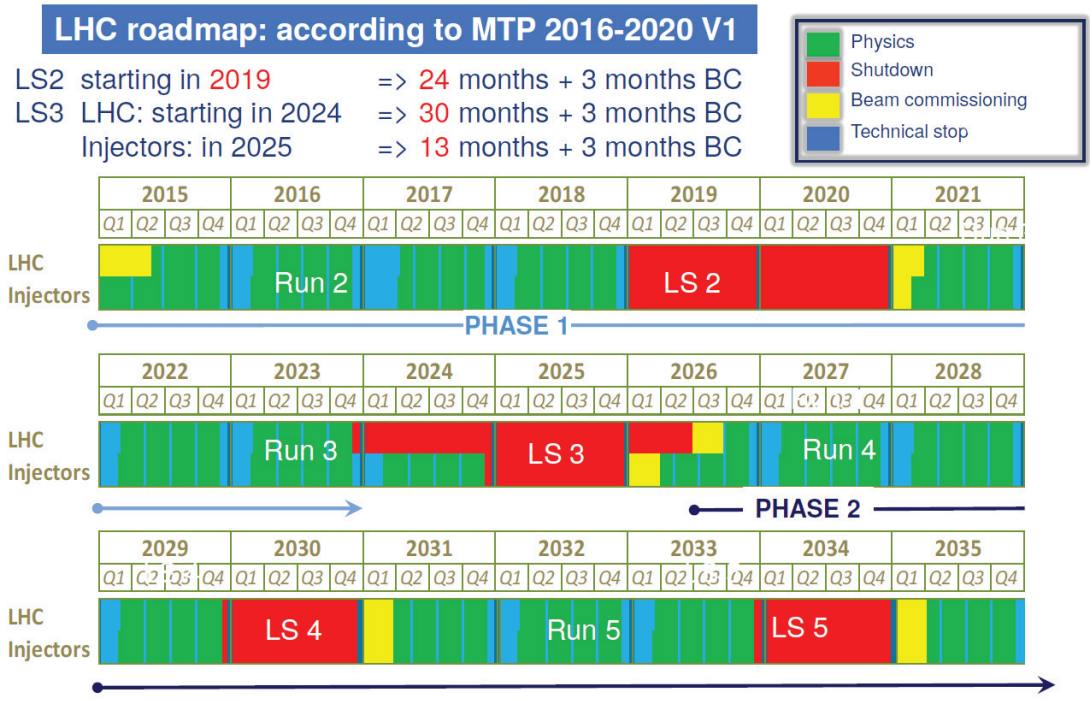

Figure 2.2: LHC schedule for 2015 to 2035 [45]

a Delivered Luminosity Measurement in ALICE

In high energy physics, the luminosity is an essential concept, expressing the interaction rate normalized to the intensity of the interacting fluxes of particles. In the specific case of a collider with beam pulsing, the luminosity is defined by equation (2.1), where N_b is the number of particles per bunch, n_b is the number of bunches per beam, f_{rev} the revolution frequency, γ is the relativistic gamma factor, ε_n the normalized transverse beam emittance, β^* the beam beta function at the interaction point (for more details, see chapter 4 of [46]), and F the geometric luminosity reduction factor due to the crossing angle at the interaction point (IP) [47].

$$\mathscr{L} = \frac{N_b^2 n_b f_{\mathrm{rev}} \gamma}{4\pi \varepsilon_n \beta^*} F \tag{2.1}$$

The luminosity determination in ALICE is based on visible cross section measurements performed during van der Meer (vdM) scans [48, 49]. In standard vdM scans, the two beams are moved across each other in transverse directions x and y. The two scans are

performed separately and the visible cross section is given by the detectors used for the definition of the minimum bias triggering conditions, typically the V0 and T0 in ALICE.

2.1.3 The Experimental Heavy-Ion Program

The goal of the LHC heavy-ion program is to produce the hottest, the largest and the longest-lived volumes of QGP in laboratory, and to provide a precise characterization of this new state of matter. For that, nucleus-nucleus collisions (A-A) are delivered at energies up to $\sqrt{s_{\rm NN}} = 5.5$ TeV. Proton-proton and proton-nucleus collisions are also part of the LHC heavy-ion program, providing the needed baseline (in terms of vacuum-like cross-sections and cold nuclear matter effects) allowing for a correct interpretation of the observations in A-A collisions.

In addition to the LHC, there are other experimental complexes developing specific heavy-ion programs. The most important one is the experimental program implemented at the Relativistic Heavy Ion Collider (RHIC) [50] hosted at the Brookhaven National Laboratory (BNL) in Long Island (New York, US). RHIC is a dedicated heavy-ion facility and it has a large flexibility in the choice of both the nuclear species accelerated (from protons to Uranium) and the center-of-mass energy (in the range $\sqrt{s_{\rm NN}} = 7.5 - 200$ GeV). Four detectors are installed at RHIC: one of them, STAR, still operates today, while PHOBOS, BRAHMS and PHENIX completed there operations respectively in 2005, 2006 and 2016. At CERN, a fixed-target heavy-ion program complementary to the LHC one is also running at the SPS, with the NA61/SHINE experiment [51] currently performing a systematic scan both in beam energy ($\sqrt{s_{\rm NN}} = 4.5 - 17.3$ GeV) and colliding system size.

In addition to the upgrade of some of the existing experiments, several new heavy-ion programs are under discussion or already in preparation [52]:

- The NICA[1] facility at JINR [53] will operate in collider mode in the center-of-mass energy range $\sqrt{s_{\rm NN}} = 4 - 11$ GeV, and in fixed-target mode in the center-of-mass energy range $\sqrt{s_{\rm NN}} = 1.9 - 2.4$ GeV.
- The FAIR[2] [54] facility at GSI[3] will provide fixed-target collisions in the center-of-mass energy range $\sqrt{s_{\rm NN}} = 2 - 29$ GeV.
- The AFTER[4] project [55] aiming at running a fixed-target heavy-ion program with the LHC beams, at a center-of-mass energy of $\sqrt{s_{\rm NN}} \approx 72$ GeV.
- The NA60+ [56,57] is a project of fixed-target experiment based at the SPS, focusing on dimuon observables at a center-of-mass energy range $\sqrt{s_{\rm NN}} = 6.3 - 17.3$ GeV.

[1] Nuclotron-based Ion Collider fAcility
[2] Facility for Antiproton and Ion Research
[3] Gesellschaft für Schwerionenforschung mbH
[4] A Fixed Target ExpeRiment at LHC

2.2 A Large Ion Collider Experiment (ALICE)

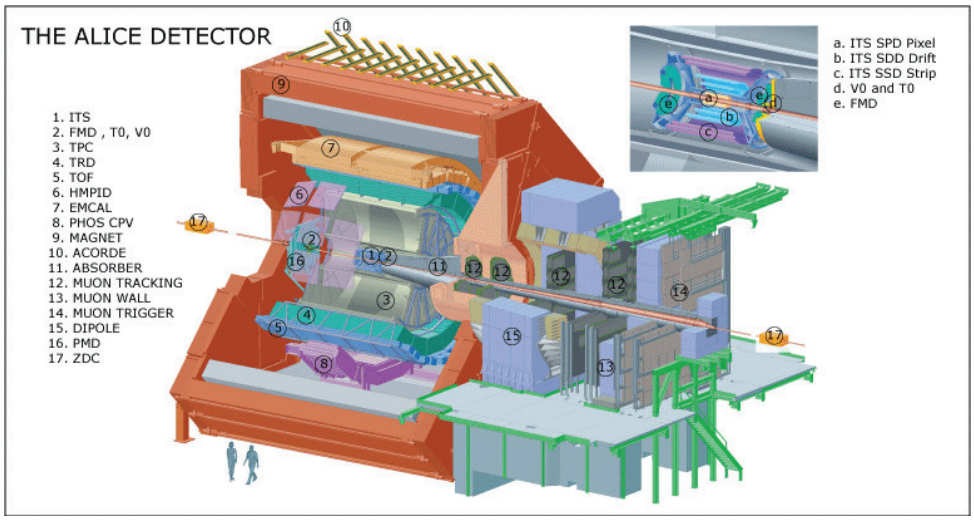

Figure 2.3: Scheme of the ALICE detector

ALICE is an experiment optimized for the study of the physics of strongly interacting matter at extremely high energy density, focusing in particular on the investigation of the QGP state and the characterization of its properties. A key design consideration driving the developement of the ALICE detector is the possibility to study the most energetic Pb-Pb collisions delivered by the LHC. This is done by measuring the particles emerging from the interaction region: it is achieved by ALICE by exploiting a rich variety of sub-detectors, see figure 2.3, based on different technologies, described in the following sections [58]. Beyond the heavy-ion program, ALICE is also interested in collecting data in proton-proton (pp) and proton-Lead (p-Pb) collisions, where no large volumes of deconfined matter are supposed to be produced, to be used as a reference for the Pb-Pb ones.

In table 2.1 and table 2.2 the ALICE running conditions in the LHC Run 1 and Run 2, respectively, are summarized.

System	E_{CM} [TeV]	Year	Delivered luminosity
pp	0.9	2009	19.6 μb^{-1}
	2.36	2009	0.87 μb^{-1}
	2.76	2011	46 nb^{-1}
		2013	129 nb^{-1}
	7	2010	0.5 pb^{-1}
		2011	4.9 pb^{-1}
	8	2012	9.7 pb^{-1}
p-Pb	5.02	2012	1.5 μb^{-1}
		2013	0.891 nb^{-1} and 14.0 nb^{-1}
Pb-Pb	2.76	2010	9 μb^{-1}
		2011	146 μb^{-1}

Table 2.1: Summary of Run 1 ALICE data taking considered for published or ongoing analyses [59]

System	E_{CM} [TeV]	Year	Delivered luminosity
pp	5.02	2015	149.51 nb^{-1}
	13	2015	6.94 pb^{-1}
		2016	13.35 pb^{-1}
		2017	19.2 pb^{-1}
p-Pb	5.02	2016	
	8.16	2016	8.68 nb^{-1} and 12.4 nb^{-1}
Pb-Pb	5.02	2015	280 μb^{-1}

Table 2.2: Summary of Run 2 ALICE data taking considered for published or ongoing analyses [59]

2.2.1 The Central Barrel

The ALICE central barrel refers to the assembly of detectors installed around the interaction point inside the L3 magnet. These detectors are dedicated to the tracking and identification of isolated charged particles and photons, as well as to the reconstruction of jets.

Inner Tracking System (ITS)

The Inner Tracking System (ITS) is the internal tracker of ALICE. It is formed by six cylindrical layers of silicon detector, the innermost one having an internal radius of 3.9 cm, limited by the external radius of the beam pipe. The radius of the outermost layer is 43.0 cm. The geometric parameters of the ITS are summarized in table 2.3.

sub-system name	layer	technology	r(cm)	$\pm z$(cm)
SPD	1	Pixel	3.9	14.1
	2	Pixel	7.6	14.1
SDD	3	Drift	15.0	22.2
	4	Drift	23.9	29.7
SSD	5	Strip	38.0	43.1
	6	Strip	43.0	48.9

Table 2.3: ITS Geometric features

The pseudo-rapidity coverage of the ITS is $|\eta| < 0.9$. The six layers are grouped into six groups of two layers each, differing by the adopted technology. The two innermost layers are composed of silicon pixel detectors (SPD), the central one of silicon drift detectors (SDD), the two outermost are composed of silicon strip detectors (SSD). The ITS allows the position of the primary and secondary (from strange and charmed particles) vertices to be determined with a resolution better than 200 µm in $r\phi$ and 300 µm in z direction. Furthermore, it contributes to the particle identification, complementing the information provided by the TPC especially for the low momentum particles ($p < 200$ MeV/c).

Time Projection Chamber (TPC)

The Time Projection Chamber (TPC) is the main detector of the central barrel. It is composed of a 5.1 m long cylindrical drift volume of 90 m^3, developing between an inner radius of 85 cm and an outer radius of 247 cm. This volume is filled with Ne–CO_2 and is divided into two parts by the central cathode, which is kept at −100 kV. The end plates are equipped with multiwire proportional chambers (MWPC). As the ITS, the pseudo rapidity coverage is $|\eta| < 0.9$. In addition to tracking, the TPC provides charged-particle identification via measurement of the specific ionization energy loss $\mathrm{d}E/\mathrm{d}x$. Due to the adopted technology and the large size, the TPC is the slowest detector of ALICE, thus limiting the interaction rate that can be supported.

Transition Radiation Detector (TRD)

The Transition Radiation Detector (TRD) is composed of eighteen super-modules, divided into thirty modules arranged in six radial layers and five sectors along the beam direction. The TRD has full azimuth coverage and spans the pseudo-rapidity region $|\eta| < 0.9$. This sub-detector provides particle identification for electrons of momentum larger than 1 GeV/c.

Time-Of-Flight (TOF)

The Time Of Flight (TOF) detector allows the particle time-of-flight to be measured. The TOF coverage is $|\eta| < 0.9$ in full azimuth. It has a modular structure organized into eighteen sectors in azimuth and five modules along the beam axis. The whole detector is inscribed in a cylindrical volume with an internal radius of 370 cm and an external one of 399 cm. The TOF has an intrinsic time resolution of about 50 ps thanks to the technology of Multi-Resistive Plate Chambers (MRPC).

High-Momentum Particle Identification Detector (HMPID)

The ALICE HMPID is based on proximity focusing Ring Imaging Cherenkov (RICH) counters and consists of seven modules mounted in an independent support cradle, fixed to the space frame at the radial distance of 490 cm from the interaction point. The pseudo-rapidity acceptance is $|\eta| < 0.6$ and an azimuthal coverage develops between 1 and 59°, corresponding to 5% of the central barrel acceptance. The HMPID allows one to extend the particle identification for π and K up to $p_{\mathrm{T}} \approx 3$ GeV/c and $p_{\mathrm{T}} \approx 5$ GeV/c for protons.

PHOton Spectrometer (PHOS)

The PHOton Spectrometer (PHOS) is a high resolution electromagnetic spectrometer, covering the pseudo-rapidity range $|\eta| < 0.13$ and the azimuth between 220 to 320°, and installed at the radial distance of 460 cm. The detector technology is based on lead-tungstate ($PbWO_4$) crystals. The PHOS is used to detect photons in the transverse momentum range between 0.5 to 10 GeV/c, including diphotons coming from the decay of the light pseudoscalar neutral mesons.

ElectroMagnetic Calorimeter (EmCal)

The ElectroMagnetic Calorimeter (EMCal) and its extension the Di-jet Calorimeter (DCal) are sampling electromagnetic calorimeters with the pseudo-rapidity coverage $|\eta| < 0.7$ and azimuth coverage from 80 to 187° (for the EMCal) and 260 to 327° (for the DCal). Specific allowance is made in the DCal acceptance for the space occupied by the PHOS detector. The combined information of the EmCal and the DCal allows to study jets and di-jets, providing trigger signals for hard jets, photons and electrons.

2.2.2 The Forward Detectors

In this section, the ALICE sub-detectors covering the forward/backward acceptance region are presented. These detectors are used to measure global observables, especially the centrality/activity of the collisions and the event plane.

Forward Multiplicity Detector (FMD)

The Forward Multiplicity Detector (FMD) is based on the silicon strip technology. It is divided in seven disks perpendicular to the beam pipe located at distances between 42 and 225 cm from the interaction point. The goal of this sub-detector is to study the charged particle multiplicity in the pseudo-rapidity ranges $-3.4 < \eta < -1.7$ and $1.7 < \eta < 5.1$, complementary to the one of the ITS.

T0

The T0 is composed of two arrays of Cherenkov counters circularly arranged around the beam pipe, with a time resolution better than 50 ps. The forward and backward parts of this sub-detector are located at 375 cm and −72.7 cm, covering a pseudo-rapidity range of $4.61 < \eta < 4.92$ and $-3.28 < \eta < -2.97$, respectively. It participates to the trigger decision and to the estimation of the luminosity.

V0

The V0 is composed of two scintillator disks installed around the beam axis, on each side of the interaction point. The V0-A (for A-side, corresponding to positive values of z) is installed at 329 cm from the interaction point, it has a diameter of 100 cm, and covers the pseudo-rapidity range $2.8 < \eta < 5.1$. The V0-C (for C-side, corresponding to negative values of z) is installed at −90 cm from the interaction point, it has a diameter of 74 cm, and covers the pseudo-rapidity range $-3.7 < \eta < -1.7$.

The V0 measures the charged particle multiplicity, and by the measurement of the time-of-flight difference between the A and C scintillators, makes possible to identify and reject the beam-gas[5] events. This technique is illustrated in figure 2.4: beam-beam and beam-gas events can be easily discriminated on the basis of the time correlation of the two signals reported on the x and y axes.

[5] A beam-gas event corresponds to an interaction between a beam ion and a nucleus of the residual gas in the beam pipe vacuum.

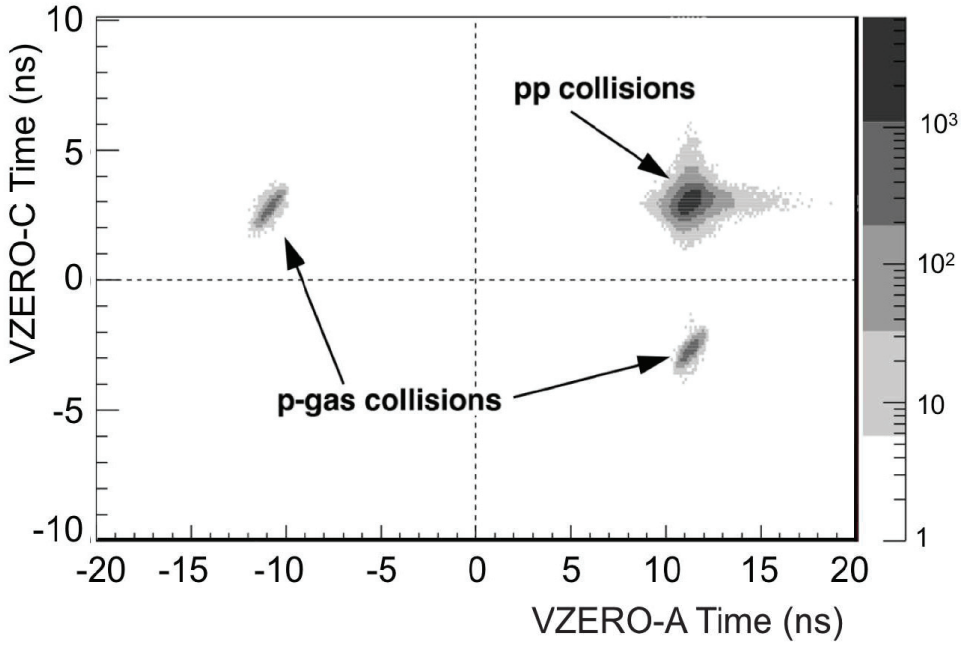

Figure 2.4: Weighted average time-of-flight of the particles detected in V0-C versus V0-A. The dashed line intersection represents the time of the collisions at the interaction point, or the crossing time of the background tracks at the vertical plane $z = 0$. [60]

The V0 participates in the minimum-bias trigger decision and in the estimation of the luminosity. Furthermore, this sub-detector is involved in the centrality measurement in Pb-Pb collisions.

Photon Multiplicity Detector (PMD)

The Photon Multiplicity Detector (PMD) consists of two identical planes of detectors, made of gas proportional counters with honeycomb structure and wire readout with Lead converter in between, located at 360 cm from the interaction point in opposite side of muon spectrometer. The PMD covers the pseudo-rapidity region ($2.3 < \eta < 3.7$). It measures the multiplicity and spatial distribution of photons, and estimates the transverse electromagnetic energy and the reaction plane event-by-event.

ALICE Diffractive Detector (AD)

The ALICE Diffractive detector (AD) is a ALICE sub-detector which was installed during the Long Shutdown 2 (2013-2014). The goal of this sub-detector is to increase the pseudo-rapidity coverage (from 8.8 to 13.2 units) and to enhance trigger efficiency for light particles produced in diffractive events. This sub-detector also participates in the estimation of the multiplicity event-by-event. It is composed of two double layers of scintillator counters, one on each side of ALICE, sensitive to charged particles with p_{T} down to 20 MeV/c. In the A-side, AD is installed at $z = 17.0$ m and covers the pseudo-rapidity range $4.9 < \eta < 6.3$. In the C-side, the sub-detector is installed at $z = -19.5$ m and covers the pseudo-rapidity range $-7.0 < \eta < -4.8$.

Zero Degree Calorimeter (ZDC)

The Zero Degree Calorimeter (ZDC) is composed of two identical sets of quartz spaghetti calorimeters located on both sides of the ALICE detector, in fully horizontal position, 112.5 m from the interaction point. Each set of detectors consists of a neutron and a proton calorimeter. Each of the neutron calorimeters has dimensions 7x7x100 cm^3 while the proton calorimeters have dimensions 22.8x12x150 cm^3. The ZDC detector is completed by two small electromagnetic calorimeter (ZEM) placed at 7.35 m from the interaction point, on one side, detecting the energy of particles emitted in the pseudo-rapidity range $4.8 < \eta < 5.7$. The ZDC is used to estimate the centrality in Lead-Lead collisions.

2.2.3 The Muon Spectrometer

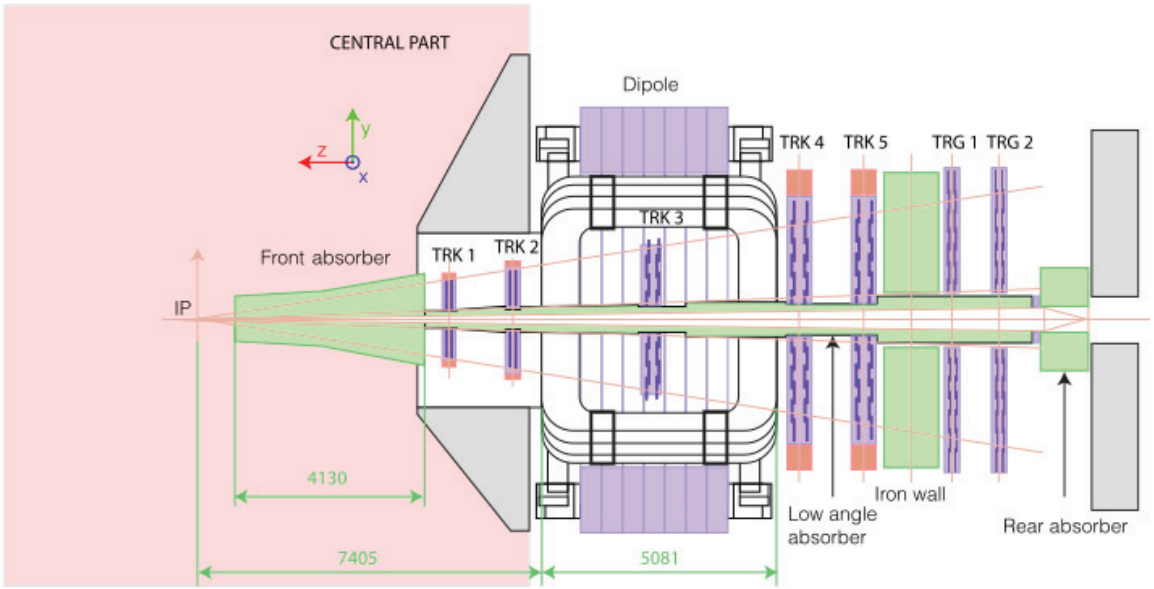

Figure 2.5: The ALICE muon spectrometer layout. [61]

The ALICE muon spectrometer (represented in figure 2.5) is 17 m long. The pseudo-rapidity coverage is $-4.0 < \eta < -2.5$, corresponding to the angular range $171° < \theta < 178°$. The muon spectrometer was designed to study quarkonia (J/ψ and Υ families) and light vector meson production (η, ρ, ω and ϕ) through their dimuon decays, and open charm and beauty production (B and D hadrons) in the single-muon channel. The spectrometer is composed of several elements, described in the following sections.

a Front Absorber

The first element of the ALICE muon spectrometer starting from the interaction point is the front absorber (or hadron absorber). The hadron absorber suppresses all particles except muons coming from the interaction vertex (mainly $\pi^{\pm}$ and $K^{\pm}$). It is made of

carbon and concrete (cf figure 2.6) in order to limit the multiple scattering and the energy loss of the muons. The inner beam shield protects the tracking chambers from background originating from particles at small angles. It is made of tungsten, lead and stainless steel to minimize the background arising from primary particles emitted in the collision and from their showers produced in the beam pipe and in the shield itself.

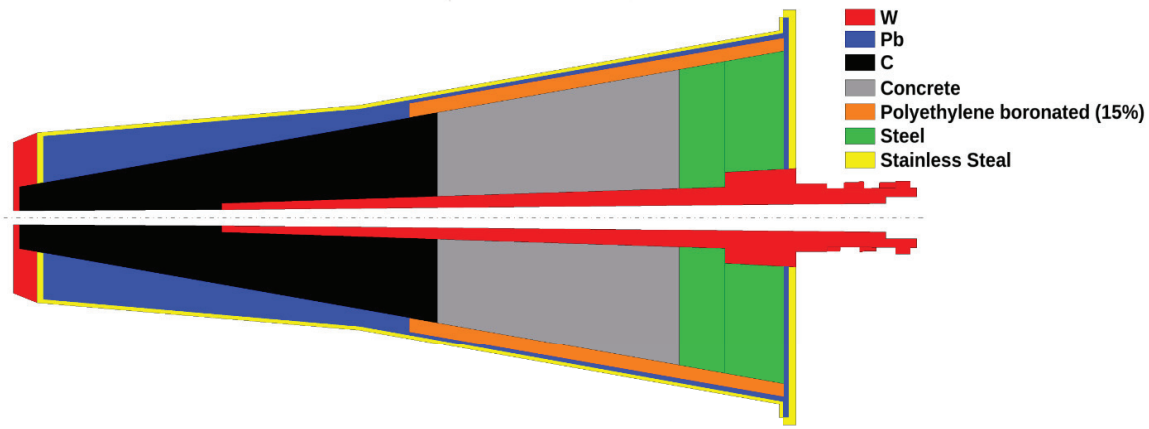

Figure 2.6: The ALICE front absorber structure [62]

The absorber is located 90 cm away from the interaction point, just after the V0-C, and is 413 cm long.

b Dipole Magnet

The dipole magnet provides a maximum magnetic field of 0.7 T, and an integral field of 3 T · m. It is a warm magnet (one of the largest warm dipoles in the world) and it is cooled with a demineralized water-cooling system, ensuring operating temperatures between 15 to 25 °C. Its dimensions are 5 m in length, 7.1 m in width and 9 m in height. The dipole is centered at 9.94 m from the interaction point and the free gap between poles has a diameter of approximately 3 m. The dipole is designed to provide a horizontal magnetic field perpendicular to the beam axis, and its polarity can be reverted. The magnetic field is defined by requirements on the mass resolution for the heavy Υ states.

c Tracking Chambers

The tracking system of the muon spectrometer is composed of five stations, each station made of two chambers. The distance between two chambers of a same station is between 10 and 20 cm. The chambers are based on a Multiwire Proportional Chamber (MWPC) technology with pad-segmented cathodes [63]. The tracking system was designed to achieve the spatial resolution of 100 µm in the bending plane, needed for obtaining an invariant mass resolution of $\sim 100\ \mathrm{MeV}/c^2$ at the Υ mass. The segmentation of the cathodes allows the spectrometer to operate with maximum hit densities of about $5 \cdot 10^{-2}\ \mathrm{cm}^{-2}$, sufficiently large to cope with the observed multiplicity in central Pb-Pb collisions.

d Iron Wall

The iron wall complements the hadron absorber. It is 1.2 m thick and covers a transverse surface of 5.6×5.6 m^2. It is located 15 m away from the interaction point, before the trigger chambers. The goal of this element is to suppress all hadrons emerging from the front absorber. The combined action of the iron wall and the front absorber imposes the muons to have a minimum momentum of ~ 4 GeV/c in order to reach the trigger chambers.

e Trigger Chambers

The ALICE muon spectrometer is equipped with two trigger stations, allowing events of interest for the muon physics to be selected. Each station is composed of two chambers based on the Resistive Plate Chamber (RPC) technology, ensuring the time resolution of 2 ns necessary for the identification of the bunch crossing. The first station is located at 16 m, just after the iron wall, and the second station at 17 m.

Several trigger conditions are hard-coded in the trigger electronics: The electronics provides the possibility to use two p_{T} thresholds used for different physics and the list of triggers is:

- MSL : at least one muon with p_{T} larger than the low-p_{T} threshold;
- MSH : at least one muon with p_{T} larger than the high-p_{T} threshold;
- MLL : at least two muons of same charge with p_{T} larger than the low-p_{T} threshold;
- MUL : at least two muons of opposite charge with p_{T} larger than the low-p_{T} threshold.

In addition to these trigger conditions, the A-p_{T} trigger condition can also be defined, it is the minimum-p_{T} trigger threshold for which a muon is firing the trigger and the value of this trigger is 0.5 GeV/c.

In LHC Run 2, the single-muon high-p_{T} threshold was set to 4.2 GeV/c while the value of the single-muon low-p_{T} threshold depended on the data taking periods. In the pp data taking during Run 2, two different values have been considered for the single-muon low-p_{T} threshold: 1 GeV/c, allowing one to access ϕ meson p_{T} down to ~ 1.5 GeV/c, and 0.5 GeV/c, allowing one to access ϕ meson p_{T} down to almost 0 GeV/c.

2.2.4 The ALICE software framework

The ALICE software (`AliRoot` [64] and `AliPhysics` [65]) is based on `ROOT` [66], a software originally designed at CERN for particle physics data analysis. `ROOT`, `AliRoot` and `AliPhysics` are written in `C++` and are used to handle the online-offline data. The software also manages the Monte-Carlo simulation framework, by interfacing several MC generators (`PYTHIA` [67], `HIJING` [68]) and particle transport codes which simulate the detector response (`GEANT3` [69], `GEANT4` [70] and `FLUKA` [71]).

The working flow of the ALICE software is represented in figure 2.7, where the main structures of the online-offline handling are shown. The reconstruction steps are the

same for the raw data and MC data. At the end of the reconstruction chain, the data are available in the `AOD` format (Analysis Object Data). From the `AOD` data, further data formats can be derived, designed for any specific analysis. In the case of the analysis performed in this thesis, the `AOD` events are reduced to the `AliLMREvent` format, containing the information of interest for the study of light-neutral meson production decaying into muons.

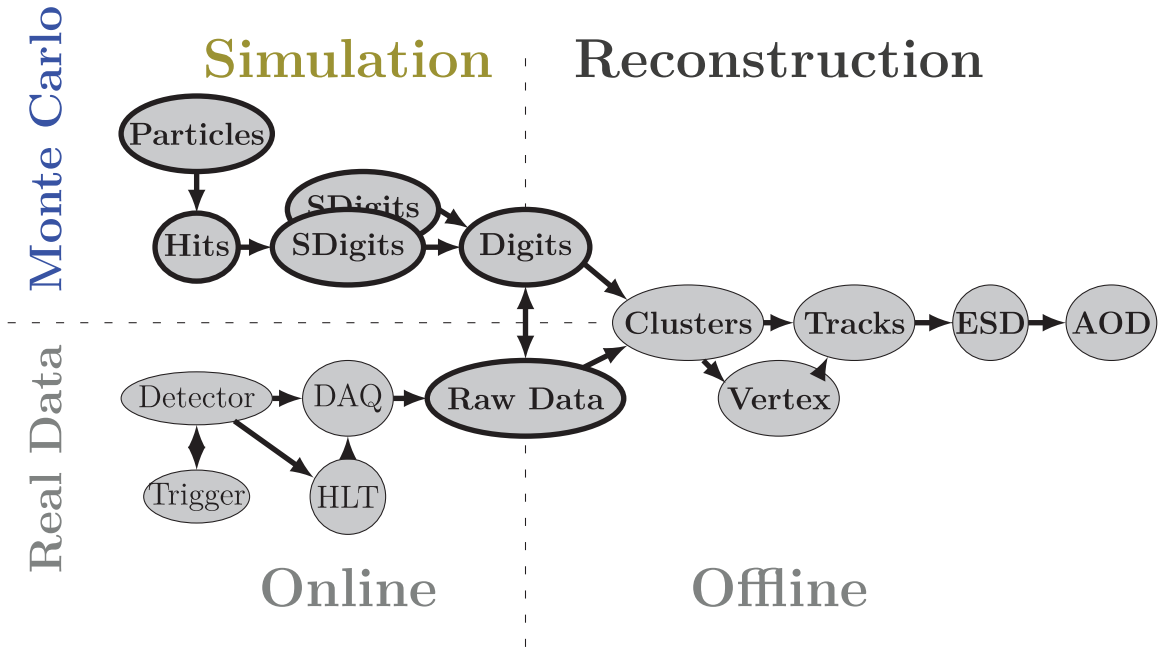

Figure 2.7: Schema of the reconstruction chain for data and simulation.

2.2.5 The ALICE Upgrade

During LHC Run 1 and Run 2 the goal of ALICE is to explore the unprecedented energy regime available in heavy ion collisions, see section 1.2.4. In the LHC Run 3 and Run 4 ALICE we move from the exploration phase to a precision-measurement phase. For this reason, ALICE is undertaking a complex upgrade program of its detectors, with the installation of the upgraded sub-detectors to take place in 2019–2020 during the LHC Long Shutdown 2.

Physics Motivations

The ALICE upgrade will preserve the specificities of the ALICE physics program with respect to the other LHC experiments. The track reconstruction performance will be improved, in terms of spatial precision and efficiency, in particular for low-momentum particles, in order to select more efficiently the decay vertices of heavy-flavor mesons and baryons. The particle identification capabilities of the apparatus will be consolidated: they represent a crucial tool for the selection of heavy-flavor, quarkonium and dilepton signals at low momentum. In the following, the main items of the foreseen physics program are shortly reviewed

- **Heavy Flavors:** characterization of the parton energy loss, study of the transport of heavy quarks in the medium and the hadronization of heavy flavors. In ALICE the focus is placed on the low-momentum region, down to zero p_{T} and the reconstruction of heavy-flavor hadrons (mesons and baryons) and the possibility to measure the flavor-dependence in low-momentum jets using light flavor, strange and charmed hadrons reconstructed within jets.

- **Quarkonia:** study of the quarkonia dissociation (and possible regeneration) as probe of the deconfined nature and temperature of the medium. In ALICE the emphasis is in the low-momenta region and the possibility to study J/ψ, ψ(2S) and ϒ in central and forward rapidity. At forward rapidity, in particular, the Muon Forward Tracker (MFT) will allow the prompt J/ψ component to be statistically separated from the displaced production, and the ψ(2S) to be observed even in the most central Pb–Pb collisions thanks to a strong reduction of the non-prompt background.

- **Low-Mass Dileptons and Thermal Photons:** estimation of the initial temperature of the medium and investigation of the chiral nature of the phase transition. ALICE will access this physics both in the dielectron and dimuon channels down to zero p_{T}.

- **Beyond Standard Model:** specific studies are also undergoing to assess the sensitivity of ALICE to the measurement of possible low-mass dark matter bosons decaying into electron or muon pairs, thanks to the improvement of the discrimination between prompt and non-prompt dileptons.

Inner Tracking System (ITS)

The current ALICE Inner Tracking System (ITS) will be totally dismounted at the end of the LHC Run 2, to be replaced by a new detector during Long Shutdown 2. The new ITS [72] will be composed of seven cylindrical layers of Monolithic Active Pixel Sensors (MAPS), the innermost one having an internal radius of 22.4 mm, limited by the external radius of the future beam pipe. The internal radius of the outermost layer is 391.8 mm.

The hit resolution of the detector will be of about 5 μm and the material budget of the three innermost layers will be reduced from the present 1.1% to 0.3% of the radiation length per layer; these features provide an improvement by a factor about three for the track impact parameter resolution in the transverse plane. The new ITS would have a pseudo-rapidity coverage of $|\eta| < 1.22$. This upgrade will improve the precision in the secondary vertex separation (from beauty, charm and strange particle decays).

Muon Forward Tracker

The Muon Forward Tracker (MFT) [73] will be a new sub-detector of ALICE, made of five disks of the same MAPS used in the upgraded ITS. The MFT will provide precise tracking and secondary vertex reconstruction for muon tracks in the pseudo-rapidity region $-3.6 < \eta < -2.5$, within the acceptance of the muon spectrometer.

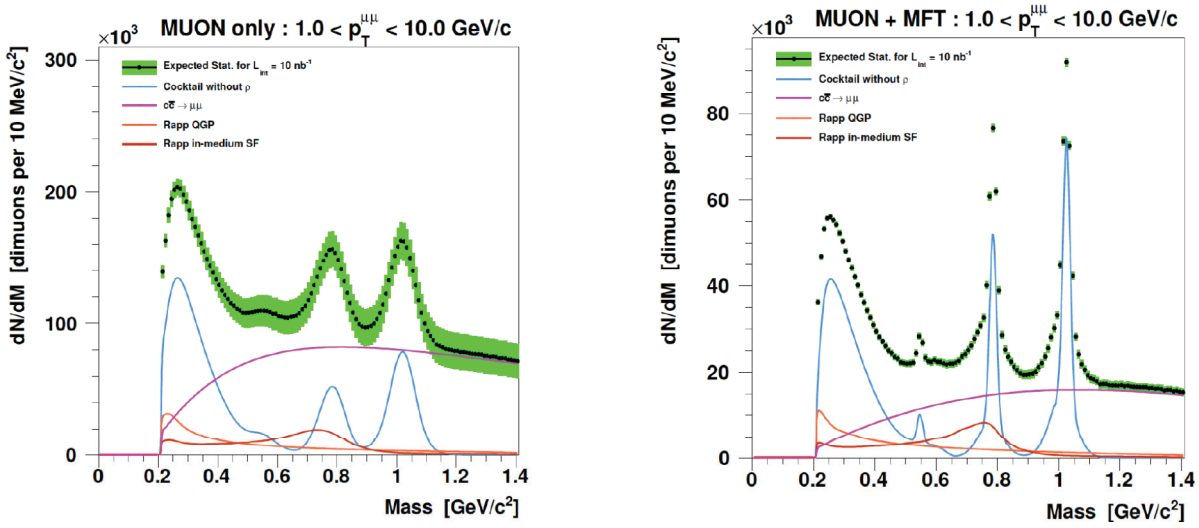

Figure 2.8: Simulation of low-mass dimuons with and without ALICE upgrade

The measurement of prompt dimuon sources in the low-mass region will strongly benefit from the addition of the MFT to the muon spectrometer. A significant improvement, up to a factor of about 4, is expected for the mass resolution of the narrow resonances η, ω and ϕ, for which resolutions of $\sim 15\,\mathrm{MeV}/c^2$ are expected (to be compared with the current $\sim 50\,\mathrm{MeV}/c^2$ resolution at the mass of the ϕ meson, see figure 2.8): this will translate into a significant improvement of the measurements involving these particles, allowing at the same time a reliable identification of the underlying thermal dimuon continuum and the measurement of the in-medium modified line shape of the short-lived ρ meson. A precision of about 20 % is expected for the observation of these sources, currently not feasible due to the very small signal-over-background ratio affecting the measurement with the present muon spectrometer.

TPC

The expected increase of the LHC luminosity after LS2, corresponding to an interaction rate about 50 kHz in Pb–Pb implies that TPC operation with a gating grid is no longer possible. This motivates the choice of GEMs for the new readout chambers, since they feature intrinsic ion blocking capabilities that avoid massive charge accumulation in the drift volume from back-drifting ions, and prevent excessive space-charge distortions. The present particle identification (PID) capability via the measurement of the specific ionization $\mathrm{d}E/\mathrm{d}x$ and the combined momentum resolution of the central barrel tracking system must be retained by the TPC upgrade [74], preserving the excellent performance of the current detector.

Fast Interaction Trigger (FIT)

The Fast Interaction Trigger (FIT) [75] will be a new sub-detector of ALICE, expected to match and even exceed the functionality and performance (fast event triggering, minimum bias luminosity and charged-particle multiplicity measurements) currently secured

by three ALICE sub-detectors: the T0, the V0 and the FMD detectors. The location of FIT will be similar to that of the current V0 and T0 modules with sensors on both sides of the Interaction Point (IP). The restrictions imposed by the desired functionality, tight space requirements, and the need to minimize the material in the vicinity of the interaction point have narrowed the choice of detector technologies for FIT to either plastic scintillator- and/or Cherenkov radiator.

ALICE O^2 (ALICE Online-Offline)

After the LHC LS2, the Pb-Pb collision interaction rate will be approximately 50 kHz. Since the ALICE physics program will focus on untriggerable signals, a continuous readout will be required in order for all events to be recorded. The resulting data throughput from the detector has been estimated to be larger than 1 TB/s for Pb−Pb events, roughly two orders of magnitude more than in Run 1 and Run 2. To minimize the costs and the requirements of the computing system needed for data processing and storage, ALICE is developing a new Computing Framework for Runs 3 and 4, called ALICE Online-Offline (ALICE O^2) [76]. This framework is designed for a maximal reduction of the data volume read out from the detector as early as possible during the data-flow.

Chapter 3

Data Sample Selection and Integrated Luminosity Evaluation

Summary

3.1 Data Sample, Event and Track Selection

The analysis presented in this thesis is based on a data sample collected by ALICE in 2016 in pp collisions at $\sqrt{s} = 13$ TeV, amounting to $\approx 2.6 \times 10^8$ events recorded with a dimuon trigger. This is the largest data sample recorded with the low-p_{T} threshold at ~ 0.5 GeV/c as of today (September 2017).

The ALICE data taking is organized into two levels: at the first level, data are organized into periods, each one characterized by the same detector and beam configurations; at the second level, data within a given period are further organized into runs, each one spanning the interval of two consecutive stops in the data acquisition[1]. Runs retained for the analysis are selected on the basis of the quality assurance conditions defined for the muon spectrometer. These conditions imply the good operation of all detectors involved in the analysis of the muon data (muon tracking chambers, muon trigger chambers, SPD layers of the ITS, V0 and T0). The full list of runs used for the present analysis is reported in appendix A.

The Minimum-Bias (MB) trigger condition for the considered data sample is given by the logical AND of the signals given by the two V0 detectors (`VOAND`) [48]. Events containing a muon pair are selected by means of a specific dimuon trigger, based on the detection of two muon candidate tracks in the trigger system of the muon spectrometer, in coincidence with the MB condition. Due to the intrinsic momentum cut imposed by the detector, only muons with $p_{\mathrm{T},\mu} \gtrsim 0.5$ GeV/c manage to leave a signal in the trigger chambers. Both unlike-sign and like-sign dimuon triggers were collected; the like-sign

[1] The data acquisition can be stopped either because of beam-related or detector-related issues.

trigger sample was downscaled by a factor that varied from run to run according to the instantaneous luminosity.

Background events not coming from beam-beam interactions are rejected by performing an offline selection, based on the timing information from the V0 detectors. Moreover, it is requested that at least one SPD tracklet contributes to the vertex reconstructed by the ITS.

Track reconstruction in the muon spectrometer is based on a Kalman filter algorithm [43, 77, 78]. Muon identification is performed by requiring the candidate track to match a track segment in the trigger chambers (trigger tracklet). This request selects muons with $p_{\mathrm{T},\mu} \gtrsim 0.5$ GeV/c and, as a consequence, significantly affects the collected statistics for dimuons with invariant mass $\lesssim 1$ GeV/c^2 and $p_{\mathrm{T}} \lesssim 1$ GeV/c. A harder programmable p_{T} threshold can be imposed on single muons when defining the trigger conditions, according to the specific physics target; it was not the case for the data considered in the present analysis, for which the trigger condition was based on any trigger-matched muon. Due to the geometrical acceptance of the muon spectrometer, the pseudo-rapidity selection $-4.00 < \eta_\mu < -2.50$ on the muon tracks is imposed, where η_μ is defined in the laboratory frame, in order to remove the tracks close to the acceptance borders of the spectrometer, where the acceptance drops abruptly. Muon pairs are built combining two muon tracks that satisfy the cuts mentioned above.

The invariant mass spectrum was obtained both for Opposite-Sign (OS) and Like-Sign (LS) muon pairs, the latter being considered for background subtraction related purpose. It should be noted that the OS component coming from the LS triggers was safely neglected in the analysis, so that only LS pairs were extracted from the LS-triggered events: they were upscaled, run by run, by the inverse of the downscaling factor applied in the data taking.

3.2 Integrated Luminosity Evaluation

The integrated luminosity for the considered data sample was evaluated as $L_{\mathrm{int}} = N_{\mathrm{MB}}/\sigma_{\mathrm{MB}}$, where N_{MB} is the equivalent number of MB events for the analyzed event sample, and σ_{MB} the MB trigger cross section. The value of N_{MB} was obtained by using the following formula:

$$N_{\mathrm{MB}} = \sum_{i=\mathrm{run}} F^i_{\mathrm{norm}} \times N^i_{\mathrm{MUL}}, \tag{3.1}$$

where the N^i_{MUL} is the number of events fulfilling the unlike-sign dimuon trigger condition (MUL, given by the presence of at least two tracklets in the muon trigger system, of opposite sign, both satisfying the single-muon p_{T}-trigger condition) and F^i_{norm} is the normalization factor to convert the number of MUL events in the analyzed sample to the equivalent number of MB events. In the present analysis, two conditions are considered to estimate the number of MB events:

- The first condition (in the following, referred to as "V0") is the `CINT7-B-NOPF-MUFAST` one. This condition is defined by the coincidence of two signals in the V0-A and -C sub-detectors, with the requirement that the

coincidence actually comes from a valid beam-beam interaction (B-NOPF). It is also required that the detectors implied in the definition of the MUL trigger condition are also included in the readout for the considered M B events: this is guaranteed by the composition of the specific MUFAST trigger cluster, containing the SPD, MUON_TRK, MUON_TRG, T0, V0, and AD detectors.

- The second condition (in the following, referred to as "T0") is based on the coincidence of the above condition CINT7-B-NOPF-MUFAST and the level-0 trigger condition 0TVX defined by the coincidence of two signals in the T0-A and -C sub-detectors.

3.2.1 F^i_{norm} Calculation

Three methods are usually considered to compute the F_{norm} factor run by run, one based on the counting scaler information (online method) and two based on the reconstructed data (offline methods).

Pile-Up correction

Regardless of the method, one needs to estimate the pile-up contribution, in order to properly correct the estimation of N_{MB}. The pile-up correction factor (PU) is defined for a given run i as:

$$\begin{aligned} PU^i &= \frac{\mu^i}{1-\mathrm{e}^{-\mu^i}}, \\ \mu^i &= -\ln\left(1-\frac{F^{\text{MB},i}_{\text{purity}}\times L0b^i_{\text{MB}}}{D^i\times N^i_{\text{colliding}}\times f_{\text{LHC}}}\right), \end{aligned}$$

where

- f_{LHC} is the frequency of one bunch in the LHC (11245 Hz),
- $N^i_{\text{colliding}}$ is the number of colliding bunches,
- D^i is the run duration as given by the Central Trigger Processor (CTP),
- $L0b^i_{\text{MB}}$ is the scaler input of the level-0 trigger for the considered MB condition,
- $F^{\text{MB},i}_{\text{purity}}$ is the purity factor associated to the considered MB condition.

The purity factor for a generic trigger condition X is computed offline as the fraction of physics-selected (PS) X-trigged events [79] divided by the total number of X-trigged events:

$$F^{X,i}_{\text{purity}} = \frac{N^i_X(\text{PS})}{N^i_X(\text{ALL})}, \tag{3.2}$$

In the case of the "T0" MB condition, the purity factor is considered equal to 1. Figure 3.1 shows the evolution of the purity factor for all the periods involved in this analysis and for the MUL and the "V0" MB trigger conditions.

Figure 3.2 shows the evolution of the pile-up correction factor for the periods involved in this analysis and for the two conditions considered for the estimate of the number of MB events.

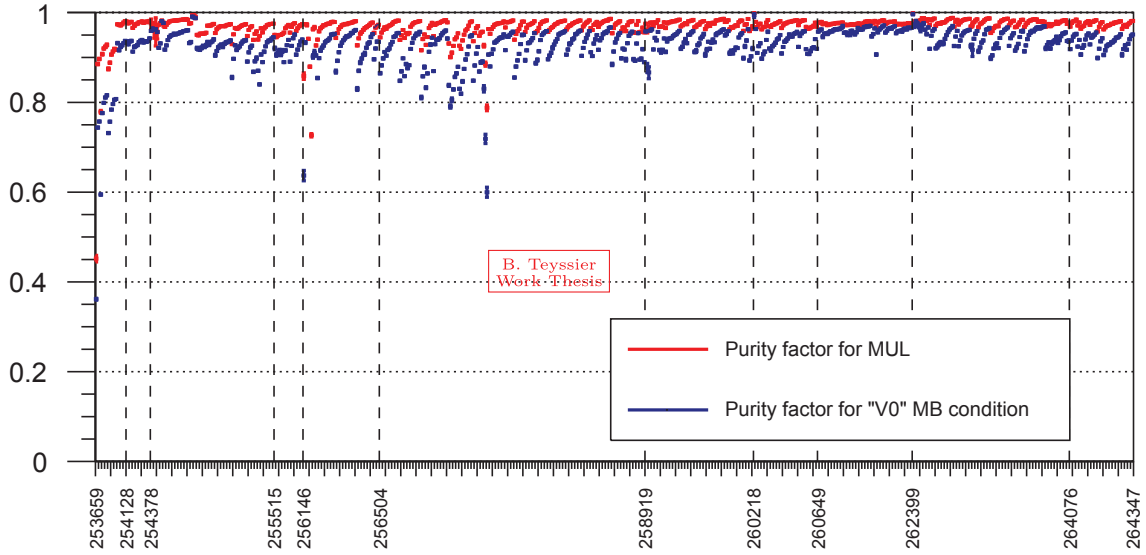

Figure 3.1: Purity factor for the periods f to p in chronological order.

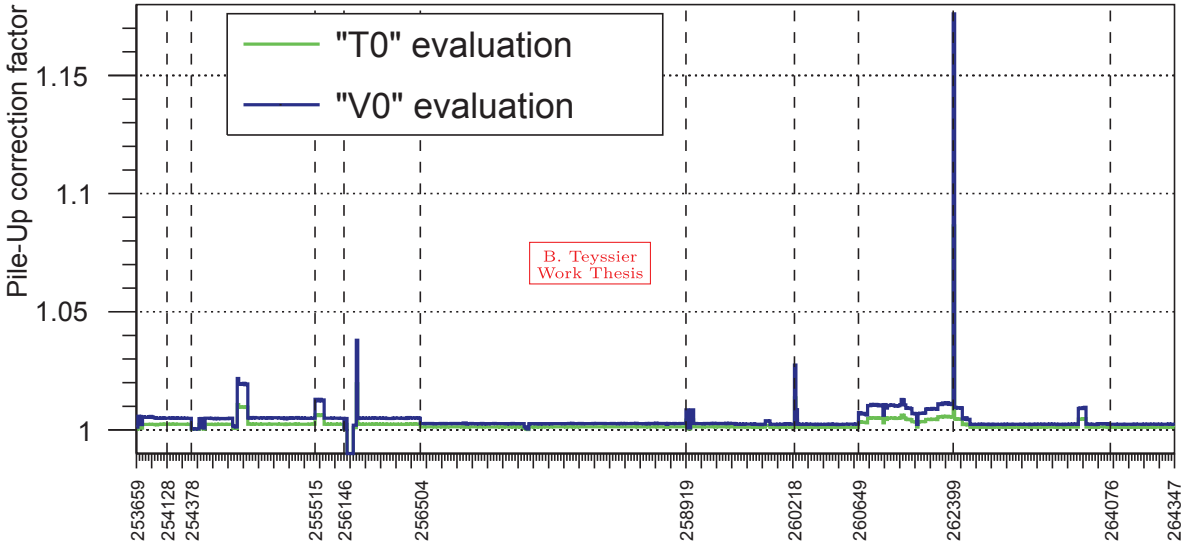

Figure 3.2: Pile-Up correction for the periods f to p in chronological order.

F_{norm} Evaluation with Online Method

The online method for the evaluation of the F_{norm} factor is based on the information of the $L0b$ scaler inputs for the MUL and MB triggers conditions. In this case, F^i_{norm} is computed for a given run i as:

$$F^i_{\text{norm}} = PU^i \times \frac{F^{\text{MB},i}_{\text{purity}} \times L0b^i_{\text{MB}}}{F^{\text{MUL},i}_{\text{purity}} \times L0b^i_{\text{MUL}}} \tag{3.3}$$

where $F^{X,i}_{\text{purity}}$ is the purity factor associated to the events selected by the trigger condition X. This method does exploit the full event sample in the analyzed data. The run-by-run

evolution of the F^i_{norm} factor evaluated with this method is given in figure 3.3 both for the "V0" and "T0" MB conditions.

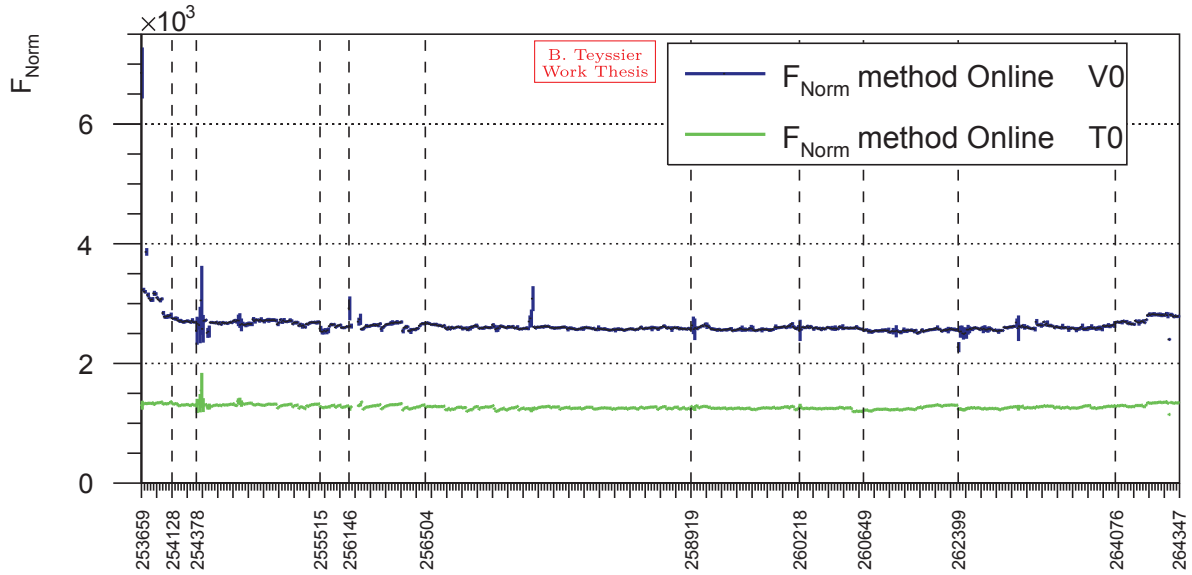

Figure 3.3: Normalization factor for the periods f to p in chronological order, evaluated with the online method both for the "V0" and "T0" MB conditions.

Offline Methods

The offline methods are based on the comparison between the number of minimum bias events in a given data sample, and the number of minimum bias events in the same data sample satisfying at the same time the trigger condition of the analyzed events at the level-0. For the first offline method, the following formula is used for a given run i:

$$F^i_{\text{norm}} = PU^i \times \frac{\text{MB}^i}{(\text{MB\&0MUL})^i}\,, \tag{3.4}$$

where

- MB^i is the number of physics-selected MB events,
- $(\text{MB\&0MUL})^i$ is the number of physics-selected MB events also fulfilling the MUL trigger condition at the level-0.

The run-by-run evolution of the F^i_{norm} factor evaluated with this method is given in figure 3.4 both for the "V0" and "T0" MB conditions.

The second offline method is based on the formula:

$$F^i_{\text{norm}} = PU^i \times \frac{\text{MB}^i}{(\text{MB\&0MSL})^i} \times \frac{\text{MSL}^i}{(\text{MSL\&0MUL})^i}, \tag{3.5}$$

where

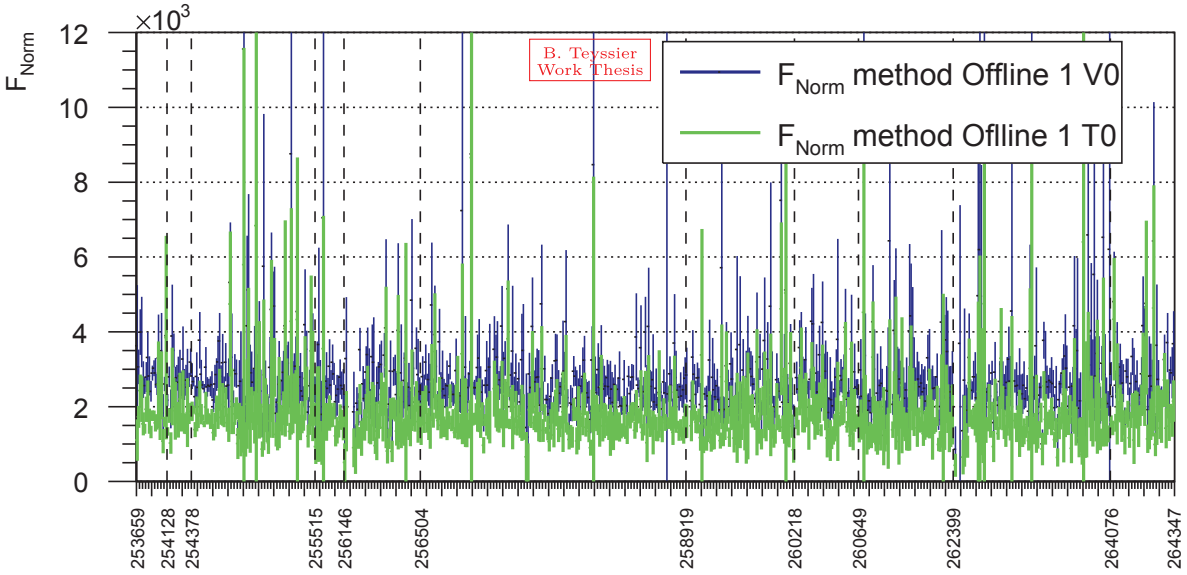

Figure 3.4: Normalization factor for the periods f to p in chronological order, evaluated with the first offline method both for the "V0" and "T0" MB conditions.

- MSL^i is the number of physics-selected events satisfying the single-muon trigger condition (MSL, given by the presence of at least one tracklet in the muon trigger system, passing the all-p_T single-muon threshold) in coincidence with the "V0" MB condition,
- $(\mathrm{MSL}\&\texttt{0MUL})^i$ is the number of physics-selected MSL events (see above) also satisfying the MUL trigger condition at the level-0,
- $(\mathrm{MB}\&\texttt{0MSL})^i$ is the number of physics-selected MB events also satisfying the MSL trigger condition at the level-0.

The run-by-run evolution of the F^i_norm factor evaluated with this method is given in figure 3.5 both for the "V0" and "T0" MB conditions.

The relative rate of the MSL trigger condition relative to the MB and the MUL ones is larger than the relative rate of the MUL trigger condition to the MB one: this guarantees this second offline method to profit from a larger event sample, resulting in a smaller statistical uncertainty. As expected, the results from the two offline methods agree within the error bars.

3.2.2 The MB Trigger Cross Section

The "MB" cross section σ_MB was measured with a van der Meer scan for both the "V0" and "T0" MB condition and found to be 57.8 ± 1.2 mb for the "V0" condition and 30.1 ± 0.6 mb for the "T0" condition [80]. As reported in [80], "when the LHC is operated with isolated-bunch-based filling schemes, the two detectors provide independent measurements of the luminosity, with a total uncertainty of 2.3%. When the LHC is operated with bunch trains the V0-based luminosity is affected by non-trivial systematic effects; in this case, the total uncertainty on the luminosity, measured with T0, is 3.4%."

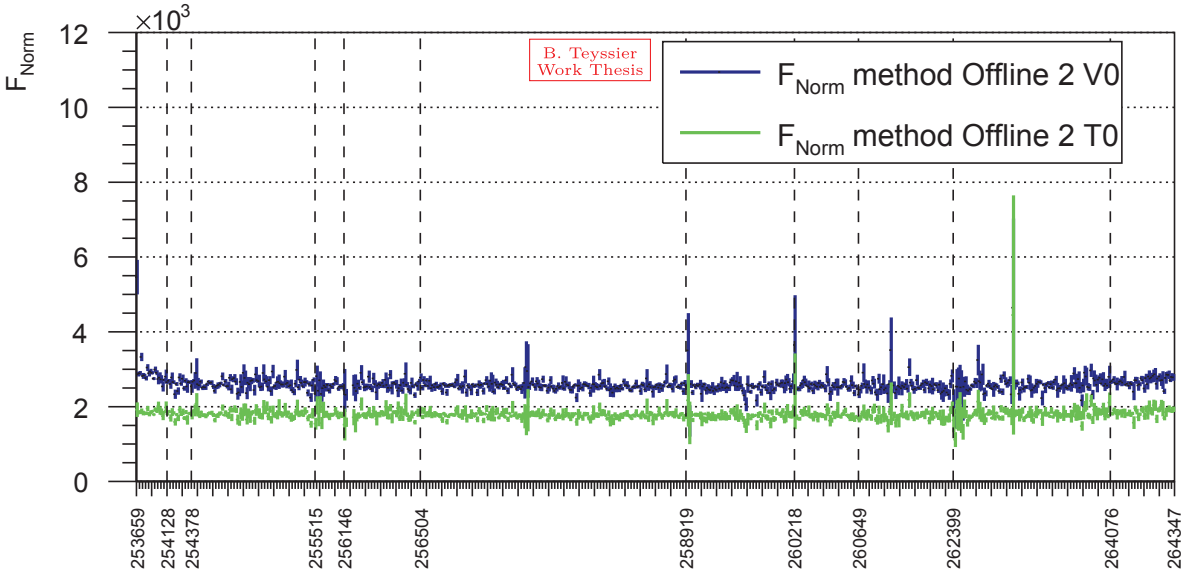

Figure 3.5: Normalization factor for the periods f to p in chronological order, evaluated with the second offline method both for the "V0" and "T0" MB conditions.

It should be noted that these values refer to the pp data taking of 2015, since the corresponding results from the van der Meer scan of 2016 (when the data considered in the present analysis were taken) is not available yet. We thus currently assume a 5 % additional systematic uncertainty on σ_{MB}, accounting for any possible difference between the efficiency of the detectors involved in the MB trigger conditions between 2015 and 2016.

3.2.3 L_{int} Evaluation

To obtain the value of L_{int} for the data taking periods considered in this present analysis, one has to assume a reference MB condition and a reference method for the evaluation of F_{norm}. From equation (3.1) one can expect that, for a given MB condition, the values of F_{norm} coming from the online and offline methods discussed above agree between each other to give the same estimation of N_{MB}. Moreover, the definition of the integrated luminosity $L_{\mathrm{int}} = N_{\mathrm{MB}}/\sigma_{\mathrm{MB}}$ implies that the ratio between the $N_{\mathrm{MB}}(\mathrm{V0})$ and $N_{\mathrm{MB}}(\mathrm{T0})$, and then the ratio between $F_{\mathrm{norm}}(\mathrm{V0})$ and $F_{\mathrm{norm}}(\mathrm{T0})$, should be consistent with the ratio between $\sigma_{\mathrm{MB}}(\mathrm{V0})$ and $\sigma_{\mathrm{MB}}(\mathrm{T0})$. As one can see by comparing figures 3.3 to 3.5, the three evaluation methods give compatible estimations for F_{norm}. However, the expected ratio between the "V0" and "T0" estimations of F_{norm} is only observed with the online method. For this reason, the online method (which also profits from the smaller statistical uncertainties) is retained for the evaluation of the L_{int} value to be used for the present analysis.

The resulting values of L_{int} are $8.44 \pm 0.00(\mathrm{stat.}) \pm 0.42(\mathrm{syst.})\ \mathrm{pb}^{-1}$ and $9.04 \pm 0.00(\mathrm{stat.}) \pm 4.52(\mathrm{syst.})\ \mathrm{pb}^{-1}$, respectively when the "T0" and "V0" MB conditions are considered. The "T0" MB condition, assuring the most stable reference, is finally retained and considered in the present analysis.

Chapter 4

Monte Carlo Simulations

Summary

This thesis work is devoted to the study of light-meson production decaying in two-muon (dimuon) channel. The dimuon mass range of interest for this study goes from the production threshold ($M_{\mu\mu} = 2m_{\mu}$) to 1.5 GeV/c^2 and is named Low-Mass Region (LMR). This region gives access to the dimuon decays of the light vector (ρ, ω and ϕ) and pseudo-scalar (η and η') mesons, discussed in section 4.1. In addition to these decays, a correlated dimuon continuum is also present in the LMR: this contribution is treated in section 4.2 in terms of open charm and beauty processes.

For each process discussed in the following, the underlying physics is reviewed and the main details of the corresponding MC simulations are given. All the MC simulations performed in this thesis used GEANT3 as transport code.

4.1 Light-Meson Decays

The properties of the light mesons contributing to the LMR through their dimuon decays are reported in table 4.1. These mesons contribute to the LMR with two types of decays: the two-body decays and the three-body (Dalitz) decays, which will be discussed separately in the following section. All the light-meson decays involved in the LMR are simulated with the AliGenMUONLMR parametric generator.

As can be seen from the quark composition reported in table 4.1, the ρ and ω mesons can be used as reference for particle production in the (u,d) quark sector, while strangeness production can be accessed via ϕ meson (and, to a lesser extent, η and η' mesons) measurement. The physical width of the ρ meson, significantly larger than one of the other particles contributing to the LMR, corresponds to the life time of ~ 1.3 fm/c: this makes the ρ an ideal probe of in-medium modifications in the case of QGP production, given that a large fraction of the observed ρ mesons would decay inside the hot medium.

Particle	Pole Mass [MeV/c^2]	Width [MeV/c^2]	Quark Composition
η	547.862 ± 0.018	$(1.31 \pm 0.05) \cdot 10^{-3}$	$\frac{1}{\sqrt{6}}\left(u\bar{u} + d\bar{d} - 2s\bar{s}\right)$
ρ	775.26 ± 0.25	149.1 ± 0.8	$\frac{1}{2}\left(u\bar{u} - d\bar{d}\right)$
ω	782.65 ± 0.12	8.49 ± 0.08	$\frac{1}{2}\left(u\bar{u} + d\bar{d}\right)$
η'	957.78 ± 0.06	0.198 ± 0.009	$\frac{1}{\sqrt{3}}\left(u\bar{u} + d\bar{d} + s\bar{s}\right)$
ϕ	1019.461 ± 0.019	4.266 ± 0.031	$s\bar{s}$

Table 4.1: Property of light-mesons involved in the dimuon mass spectrum, values taken from [4]

4.1.1 Kinematical Distributions

The kinematics parametrization of the light mesons in the `AliGenMUONLMR` generator are provided by a p_T-y distribution estimated by `PHOJET` [81, 82] (based on a Dual Parton Model combined with perturbative QCD).

4.1.2 Dalitz Decays

Among the light mesons reported in table 4.1, the η, ω and η' mesons give a sizable Dalitz decay contribution to the LMR. The involved decay channels are summarized in table 4.2.

Process	Branching Ratio (BR)
$\eta \to \mu^+\mu^-\gamma$	$(3.1 \pm 0.4) \cdot 10^{-4}$
$\omega \to \mu^+\mu^-\pi^0$	$(1.3 \pm 0.6) \cdot 10^{-4}$
$\eta' \to \mu^+\mu^-\gamma$	$(1.08 \pm 0.27) \cdot 10^{-4}$

Table 4.2: Dalitz decay processes in the LMR and the branching ratios used in the analysis

The Feynman diagram corresponding to the Dalitz decay under discussion are shown in figure 4.1. In the considered processes the parent mesons decay electromagnetically into one virtual photon with mass M and a third body (real photon or π^0) with the virtual photon converting into a muon pair.

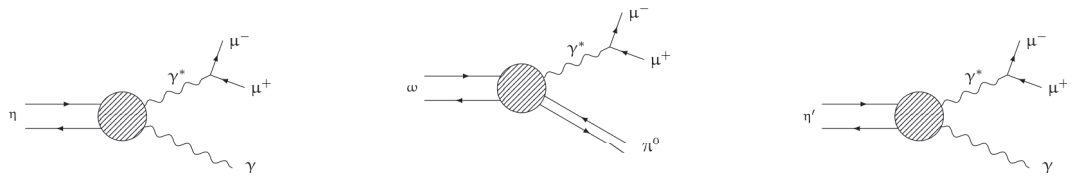

(a) $\eta \to \mu^+\mu^-\gamma$ (b) $\omega \to \mu^+\mu^-\pi^0$ (c) $\eta' \to \mu^+\mu^-\gamma$

Figure 4.1: Feynman diagrams of the Dalitz decays of interest for the dimuon LMR

The ALICE muon spectrometer is not equipped for detecting neither the real photon nor the π^0 emitted within the Dalitz decays discussed here: these decays are identified by

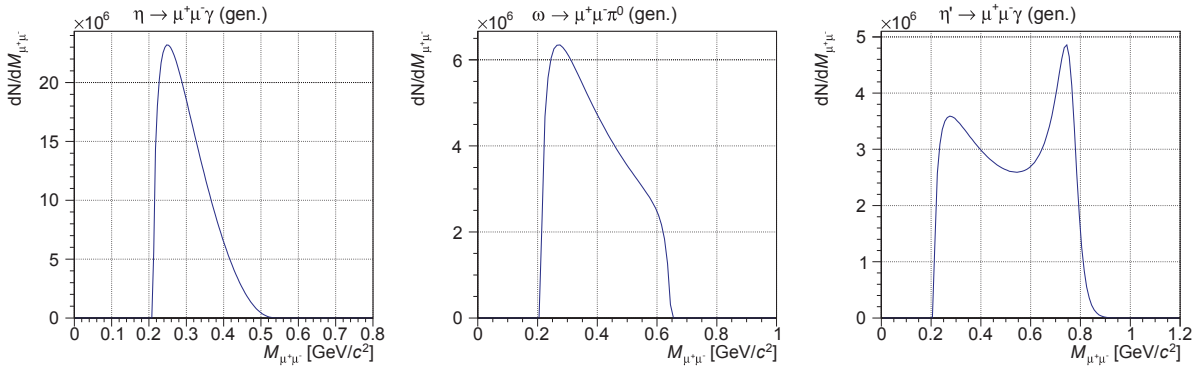

(a) η (b) ω (c) η′

Figure 4.2: Generated dimuon mass distribution of Dalitz decay integrated in full phase space.

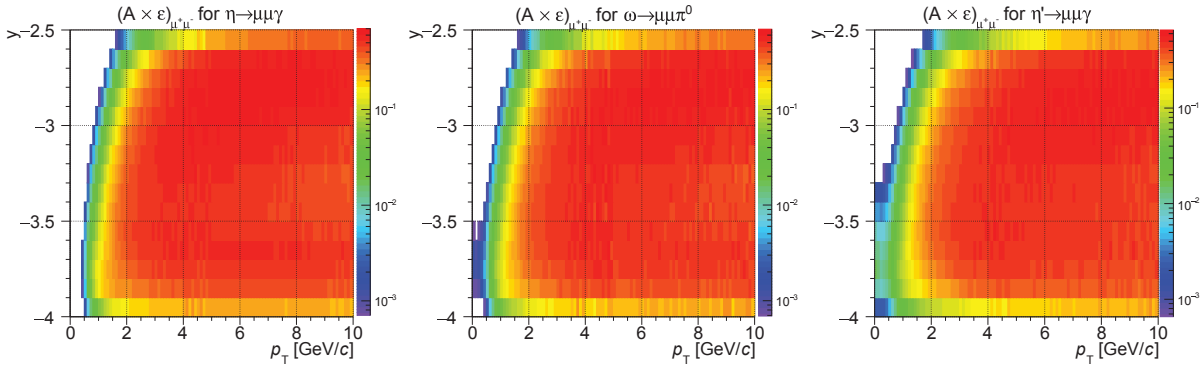

(a) η (b) ω (c) η′

Figure 4.3: Acceptance times efficiency of Dalitz decay.

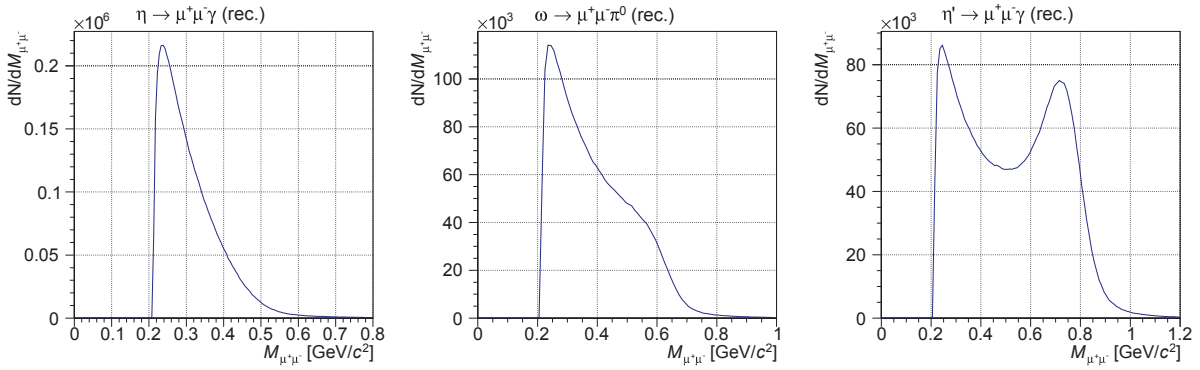

(a) η (b) ω (c) η′

Figure 4.4: Reconstructed dimuon mass distribution of Dalitz decay integrated in full phase space.

looking at the mass distribution of the dimuons coming from the virtual photon conversion. For this reason, it is important to have a theoretical description of the shape of such mass distributions: they can be computed in pure QED under the hypothesis of a point-like electromagnetic transition vertex, with the deviation from the real transition vertex quantified by a form factor $|F(M^2)|^2$, see Equations (4.1) to (4.3).

$$\begin{aligned}\frac{\mathrm{d}\Gamma(\eta\to\mu\mu\gamma)}{\mathrm{d}M} &= 2M\frac{2}{3}\frac{\alpha}{\pi}\frac{\Gamma(\eta\to\gamma\gamma)}{M^2}\left(1-\frac{M^2}{m_\eta^2}\right)^3\left(1+\frac{2m_\mu^2}{M^2}\right)\\ &\quad\times\sqrt{\left(1-\frac{4m_\mu^2}{M^2}\right)}\left|F_\eta\left(M^2\right)\right|^2,\end{aligned} \tag{4.1}$$

$$\begin{aligned}\frac{\mathrm{d}\Gamma(\omega\to\mu\mu\pi^0)}{\mathrm{d}M} &= 2M\frac{\alpha}{3\pi}\frac{\Gamma(\omega\to\gamma\pi^0)}{M^2}\left(1+\frac{2m_\mu^2}{M^2}\right)\sqrt{\left(1-\frac{4m_\mu^2}{M^2}\right)}\\ &\quad\times\left[\left(1+\frac{M^2}{m_\omega^2-m_{\pi^0}^2}\right)^2-\frac{4m_\omega^2M^2}{\left(m_\omega^2-m_{\pi^0}^2\right)^2}\right]^{3/2}\left|F_\omega\left(M^2\right)\right|^2,\end{aligned} \tag{4.2}$$

$$\begin{aligned}\frac{\mathrm{d}\Gamma(\eta'\to\mu\mu\gamma)}{\mathrm{d}M} &= 2M\frac{2}{3}\frac{\alpha}{\pi}\frac{\Gamma(\eta'\to\gamma\gamma)}{M^2}\left(1-\frac{M^2}{m_{\eta'}^2}\right)^3\left(1+\frac{2m_\mu^2}{M^2}\right)\\ &\quad\times\sqrt{\left(1-\frac{4m_\mu^2}{M^2}\right)}\left|F_{\eta'}\left(M^2\right)\right|^2,\end{aligned} \tag{4.3}$$

where the π^0, η, ω and η' pole masses are taken from the PDG tables [4] and the form factors are expressed by the pole-parametrization for the η and ω mesons and from a Breit-Wigner form for the η' meson:

$$\left|F_\eta\left(M^2\right)\right|^2=\frac{1}{\left(1-\frac{M^2}{\Lambda_\eta^2}\right)^2}, \tag{4.4}$$

$$\left|F_\omega\left(M^2\right)\right|^2=\frac{1}{\left(1-\frac{M^2}{\Lambda_\omega^2}\right)^2}, \tag{4.5}$$

$$\left|F_{\eta'}\left(M^2\right)\right|^2=\frac{m_0^4}{\left(m_0^2-M^2\right)^2+m_0^2\Gamma_0^2}. \tag{4.6}$$

For the η and ω form factors the corresponding Λ parameter is taken from a recent analysis on p-A NA60 data [83], while for the η' form factor the parameters $m_0 = 0.764\ \mathrm{GeV}/c^2$ and $\Gamma_0 = 0.102\ \mathrm{GeV}/c^2$ are extracted from a fit on the Lepton-G data [84]. The invariant mass distributions Equations (4.1) to (4.3) are implemented in the description of the Dalitz decays in the `AliGenMUONLMR` generator, together with the definition of the form factors Equations (4.4) to (4.6). This allows one to extract a properly distributed value of the virtual photon invariant mass, to be used to simulate the decays $\eta\to\gamma^*\gamma$, $\omega\to\gamma^*\gamma$ and $\eta'\to\gamma^*\gamma$; from here, the full kinematics of the virtual photon can be extracted, allowing in turn the kinematics of the muon pair to be evaluated.

Figure 4.2 shows the generated dimuon mass distribution for the three Dalitz decays of interest here. The η' mass distribution (figure 4.2c) shows a characteristic enhancement corresponding to the ρ/ω peak, given by the transition form factor, which can be easily interpreted in terms of the Vector Meson Dominance model [84]. For each decay, the p_T and y dependence of the product of geometrical acceptance and reconstruction efficiency ($A \times \varepsilon$) is shown in figure 4.3. As expected, the phase space coverage at low-p_T is more important for the Dalitz decays allowing for larger values of the dimuon invariant mass. For the $\eta \to \mu^+\mu^-\gamma$ decay, which is the reference process for the extraction of the η-meson signal, $(A \times \varepsilon)_{\mu^+\mu^-}$ is negligible for $p_T{}^{\mu\mu} \lesssim 0.5$ GeV/c, putting a strong constraint in the available phase space for the η-meson measurement.

Figure 4.4 shows the reconstructed dimuon mass distribution for each Dalitz decay, integrated over $-4.00 < y < -2.50$ and $0.0 < p_T < 10.0$ GeV/c. These shapes enter as ingredients in the hadronic cocktail fit (discussed in section 5.2), imposing their profiles to be sufficiently smooth for each phase space interval considered in the analysis: since these shapes extend over a large mass range and are not easily parameterizable, a significantly large MC statistics is needed especially when $(A \times \varepsilon)_{\mu^+\mu^-}$ is particularly low.

4.1.3 Two-Body Decays

The two-body decays of interest for the present thesis work are listed in table 4.3 with the corresponding branching ratios. For the $\omega \to \mu^+\mu^-$ and $\phi \to \mu^+\mu^-$ decays the branching ratios are taken as the average (weighted by the corresponding uncertainty) of the available measurements of BR($\mu^+\mu^-$) and BR(e^+e^-) assuming lepton universality in order to reduce the final uncertainty.

Process	Branching Ratio (BR)
$\eta \to \mu^+\mu^-$	$(5.8 \pm 0.8) \cdot 10^{-6}$
$\rho \to \mu^+\mu^-$	$(4.55 \pm 0.28) \cdot 10^{-5}$
[a] $\omega \to \mu^+\mu^-$	$(7.28 \pm 0.14) \cdot 10^{-5}$
[b] $\phi \to \mu^+\mu^-$	$(2.954 \pm 0.030) \cdot 10^{-4}$

[a] The value reported in this table for the ω is the weighted average measurement of BR($\omega \to l^+l^-$). The BR($\mu^+\mu^-$) is $(9.0 \pm 3.1) \cdot 10^{-5}$

[b] The value reported in this table for the ϕ is the weighted average measurement of BR($\phi \to l^+l^-$). The BR($\mu^+\mu^-$) is $(2.87 \pm 0.19) \cdot 10^{-4}$

Table 4.3: Two-body decay processes in the LMR and the branching ratios used in the analysis

The decay of the vector mesons ρ, ω and ϕ into two muons is mediated by a virtual photon: $V \to \gamma^* \to \mu^+\mu^-$ (see figures 4.5b to 4.5d). The decay of the pseudo-scalar η meson into two muons is a 4^{th} order electromagnetic process (see figure 4.5a) mediated by two virtual photons, where the μ^+ coming from one γ^* and the μ^- coming from the other γ^* are contracted.

The two-body decays are implemented in the `AliGenMUONLMR` generator approximating the narrow mass line shapes of the η, ω and ϕ mesons with a Dirac delta distribution defined at the resonance pole mass, since their physical widths are negligible with respect

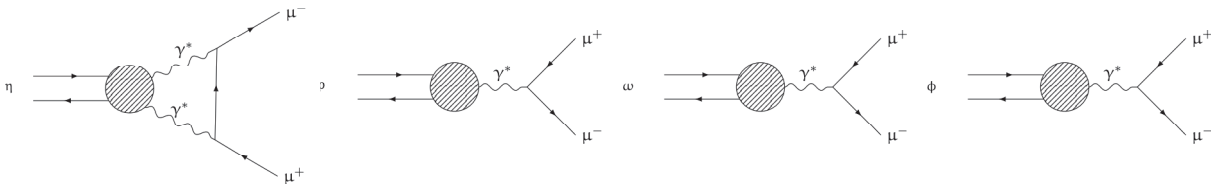

(a) $\eta \to \mu^+\mu^-$ (b) $\rho \to \mu^+\mu^-$ (c) $\omega \to \mu^+\mu^-$ (d) $\phi \to \mu^+\mu^-$

Figure 4.5: Feynman diagrams of two-body decays of the light neutral meson η, ρ, ω and ϕ.

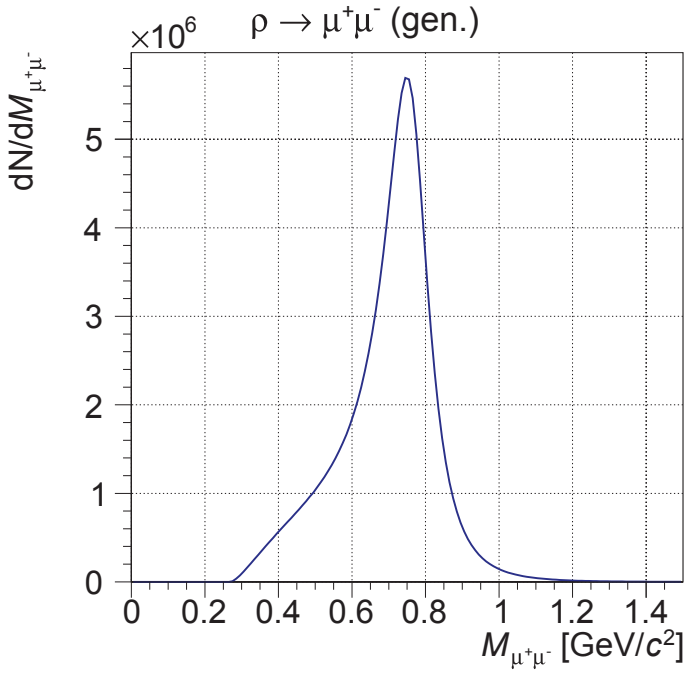

Figure 4.6: Generated mass distribution for the $\rho \to \mu^+\mu^-$ process, see equation (4.7)

to the detector mass resolution. On the contrary, for the ρ meson, due to its natural large mass distribution, the following parametrization is used [83, 85]:

$$\frac{\mathrm{d}N}{\mathrm{d}M} = \frac{\alpha^2 m_\rho^4}{3\,(2\pi)^4} \frac{\sqrt{1-\frac{4m_\mu^2}{M2}}\left(1+\frac{2m_\mu^2}{M^2}\right)\left(1-\frac{4m_\pi^2}{M^2}\right)^{3/2}}{\left(m_\rho^2 - M^2\right)^2 + m_\rho^2\Gamma_\rho^2(M)} (2\pi MT)^{3/2}\,\mathrm{e}^{-\frac{M}{T_\rho}}\,, \tag{4.7}$$

with a mass-dependent width:

$$\Gamma_\rho(M) = \Gamma_{0\rho}\frac{m_\rho}{M}\left(\frac{\frac{M^2}{4}-m_\mu^2}{\frac{m_\rho^2}{4}-m_\mu^2}\right)^{3/2} = \Gamma_{0\rho}\frac{m_\rho}{M}\left(\frac{q}{q_0}\right)^3, \tag{4.8}$$

where the $\Gamma_{0\rho}$ is the full resonance width and m_ρ the resonance mass pole taken from [4]. This distribution is shown in figure 4.6, one can appreciate the peculiar profile of this line shape, covering practically the whole LMR.

For each decay, the p_T and y dependence of $A \times \varepsilon$ is shown in figure 4.7. As expected, the phase space coverage at low-p_T becomes larger as the mass of the meson increases.

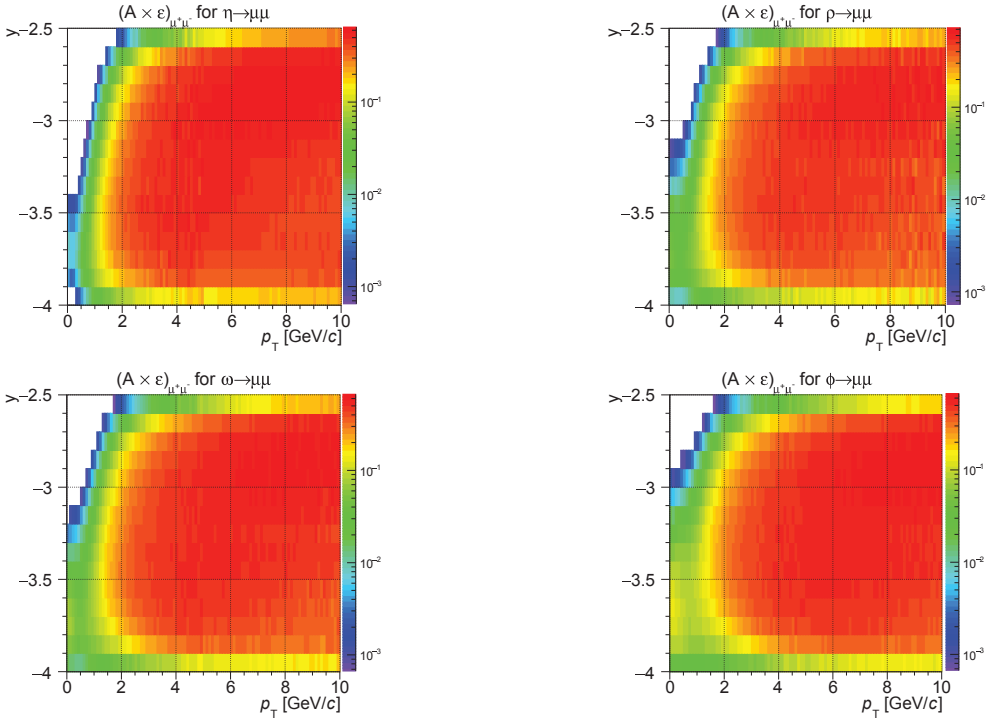

Figure 4.7: Acceptance times efficiency of two body decay.

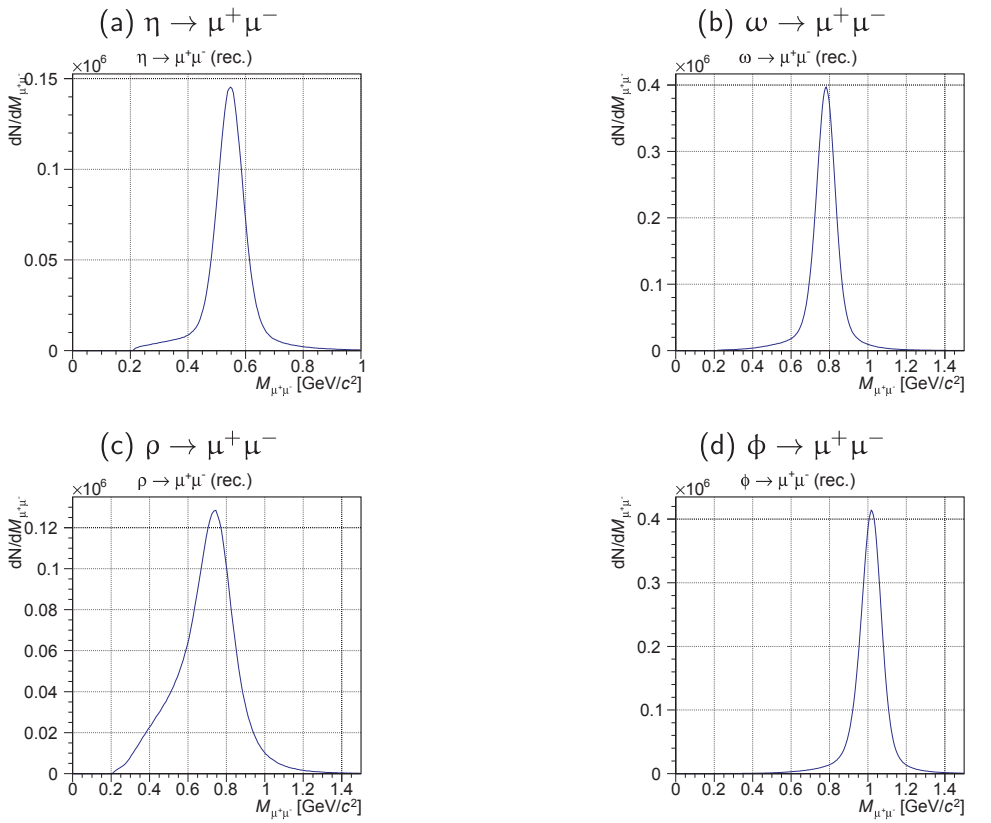

Figure 4.8: Reconstructed dimuon mass distribution of two body decays integrated in full phase space.

For the $\omega \to \mu^+\mu^-$ decay, which is the reference process for the extraction of the ω-meson signal, $(A \times \varepsilon)_{\mu^+\mu^-}$ is significant down to $p_T = 0.0$ GeV/c in the rapidity range $-4.00 < y < -3.25$ and down to $p_T \approx 2.0$ GeV/c towards the $y = -2.50$ limit. For the $\phi \to \mu^+\mu^-$ decay, from which ϕ-meson signal can be extracted, $(A \times \varepsilon)_{\mu^+\mu^-}$ is significant down to $p_T = 0.0$ GeV/c in the rapidity range $-4.00 < y < -3.00$ and down to $p_T \approx 2.0$ GeV/c towards the $y = -2.50$ limit.

Figure 4.8 shows the reconstructed dimuon mass distribution for each two-body decay, integrated over $-4.00 < y < -2.50$ and $0.0 < p_T < 10.0$ GeV/c. These shapes enter, together with the Dalitz one discussed in the previous section, as ingredients in the hadronic cocktail fit. From the mass distributions in figure 4.8, the detector mass resolution for the narrow η, ω and ϕ mesons can be estimated, performing a Gaussian fit on the central part of the peaks: the value are found to be $\sigma_\eta \approx 45.8$ MeV/c^2, $\sigma_\omega \approx 48.9$ MeV/c^2 and $\sigma_\phi \approx 52.0$ MeV/c^2.

4.2 Dimuons from Open Heavy-Flavor Decays

In the low mass region, in addition to the Dalitz and two-body decays of light neutral mesons, two other processes may contribute namely the so-called open charm and open beauty processes. In these processes, a correlated muon pair comes from the simultaneous semi-muonic decay of two correlated heavy-flavor hadrons coming from the hadronization of a heavy $q\bar{q}$ pair. These processes are illustrated in figure 4.9 for the open charm and beauty.

Figure 4.9: Illustration of open heavy-flavor decays.

The open charm and beauty processes are generated with the PYTHIA6 MC generator: PYTHIA generates the primary $c\bar{c}$ (or $b\bar{b}$) quark pairs, performs the corresponding hadronization as well as the decay of the heavy flavor hadrons. The decays of the long-lived particles possibly appearing in the decay chains of the heavy-flavor hadrons are performed by the transport code GEANT3. To save CPU time, the PYTHIA6-based parametric generator (AliGenCorrHF) is used, developed within the AliRoot framework, generating one heavy-flavor pair per event; to further optimize the simulation, the first heavy hadron pair is produced in the rapidity hemisphere of the muon spectrometer.

The simulation of the open charm and beauty processes depends of the knowledge of the kinematic distributions of the primary $c\bar{c}$ (or $b\bar{b}$) quark pairs, determining the

kinematics of the first hadron pair and thus the shape of the mass distribution of final muon pairs. The $c\bar{c}$ and $b\bar{b}$ kinematic distributions are known with large uncertainties at forward rapidity at the LHC energies, due to the lack of measurements of heavy flavor hadrons in this kinematic range. For this reason, we also considered a second model, FONLL [86] (for Fixed-Order plus Next-to-Leading Log), giving an alternative description of the $c\bar{c}$ and $b\bar{b}$ kinematic distributions based on some perturbative calculation made possible by the large mass of the charm and beauty quarks. To optimize the CPU time for the simulations based on the FONLL predictions, a reweighting is applied on the existing simulations, based on the ratio between the $(p_T - y)$ parton distributions given by PYTHIA and FONLL. The reweighting has been performed considering three FONLL kinematics distributions: the central prediction, the prediction corresponding to the upper limit associated to the uncertainty range, and the prediction corresponding to the lower limit associated to the uncertainty range; in this way, we can compare up to four hypotheses for the input of the open charm and beauty processes.

The discussion presented in the following section applies to the open charm process as well as to the open beauty one; similarly, each figure will include two panels, the "a" one dedicated for the open charm case, the "b" for the beauty case.

4.2.1 PYTHIA– FONLL Comparison

To estimate the difference between the available hypotheses on the input parton kinematics, the ratio of the FONLL partonic p_T distributions (corresponding to the central value and the upper-lower limits of the uncertainty range) to the PYTHIA one is shown in Figure 4.10. In this figure, the ratio corresponding to FONLL central value is represented in solid curve and the ratios corresponding to the upper and lower limits of FONLL uncertainty range are represented as an uncertainty band. As can one see, the ratio of the central FONLL value to PYTHIA deviates significantly from unity, the deviation becomes stronger when the upper-lower limits of the FONLL prediction are considered. The PYTHIA-FONLL disagreement is stronger for the charm than for the beauty.

It is now interesting to investigate how the difference between the PYTHIA and FONLL predictions for the input kinematic distributions of the $c\bar{c}$ and $b\bar{b}$ quark pairs affects the shape of the reconstructed dimuon mass spectra, which will be used as ingredients of the fit of the data. To do so, the reconstructed mass spectra corresponding to the four available MC inputs are compared in figure 4.11: PYTHIA, FONLL central value, FONLL upper value, and FONLL lower value. For the sake of comparison, the four distributions are normalized to the same integral. In the case of the open charm process, figure 4.11a, the differences between the models are clearly visible accross the considered mass range, while for the open beauty process, figure 4.11b, there is a remarkable agreement between the curves. A possible way to quantify the uncertainty on reconstructed dimuon mass distributions of open charm and beauty, due to the model assumed for the input partonic distribution, is to evaluate the FONLL over PYTHIA ratios as a function of the dimuon mass, as shown in figure 4.12.

As expected, the ratios for the open beauty process stay significantly closer to unity than the open charm process. By inspecting the graphs, one can estimate the uncertainty on the open charm shape to be of the order of 15% in the LMR, significantly increasing

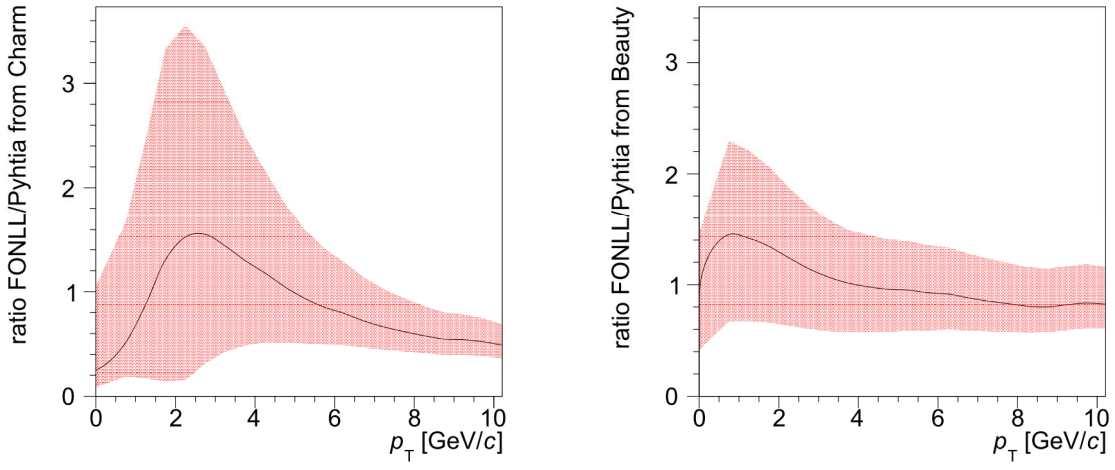

(a) charm (b) beauty

Figure 4.10: Partonic p_T distribution ratio FONLL [87] over PYTHIA: the black curve represents the reference value of the ratio and the red hatching represents the error according to FONLL model.

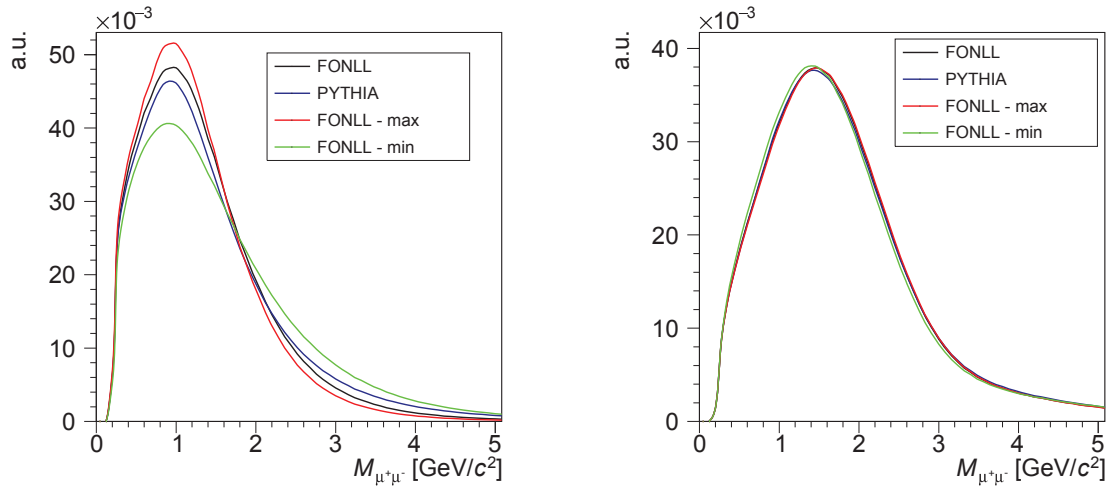

(a) open charm (b) open beauty

Figure 4.11: Reconstructed dimuon mass coming from open heavy flavor semi-leptonic decays.

towards large masses, while from the open beauty shape the uncertainty in the LMR stays within 5%. We will come back to these uncertainties in section 5.2, where the fit routine allowing the signal extraction will be discussed.

4.2.2 Decay Chain Length in the Open Heavy-Flavor Processes

In the open heavy-flavor processes considered in this section, the number of decay steps between the initial parton and the final muon (noted *decay chain* afterwards) can be potentially large, resulting in a weakening of the kinematic correlation between the initial and the final states. If the decay chains associated to the two final muons are sufficiently

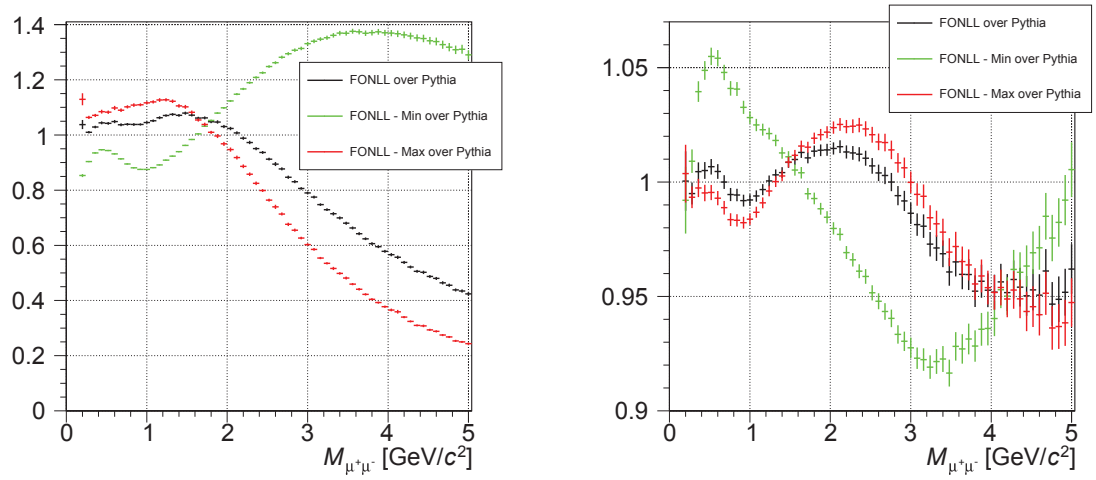

(a) open charm (b) open beauty

Figure 4.12: Dimuon mass spectrum ratio from FONLL (reference, min and max value) over PYTHIA.

long, the initial $q\bar{q}$ correlation could be substantially washed out in the final muon pair. For this reason it is interesting to study the distribution of the decay chain length (λ_μ) in simulated open charm and beauty processes, defined as the number of decay steps between the initial parton and the final muon.

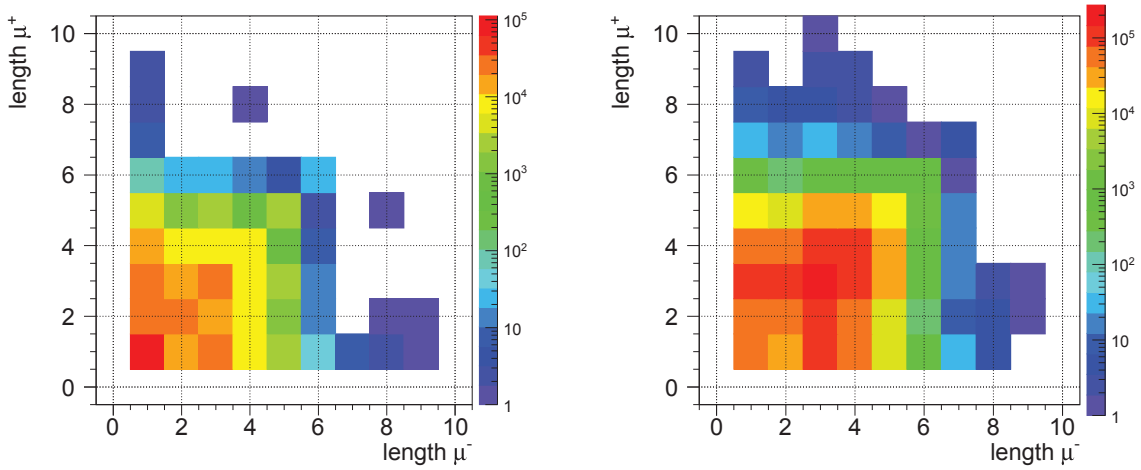

(a) open charm (b) open beauty

Figure 4.13: μ-chain for open heavy flavor at generated level.

In figure 4.13 the correlation between the λ_μ of the positive and negative muons is shown for the dimuons coming from the open charm and beauty simulations. In this figure, on can clearly see that λ_μ can get as large as 10. As expected, the average λ_μ values are larger for the open beauty process than the open charm one, due to the larger phase space available.

Since the λ_μ distributions extend over relatively large ranges, one can wonder which is the impact of having short or long muon decay chains on the shape of the dimuon invariant

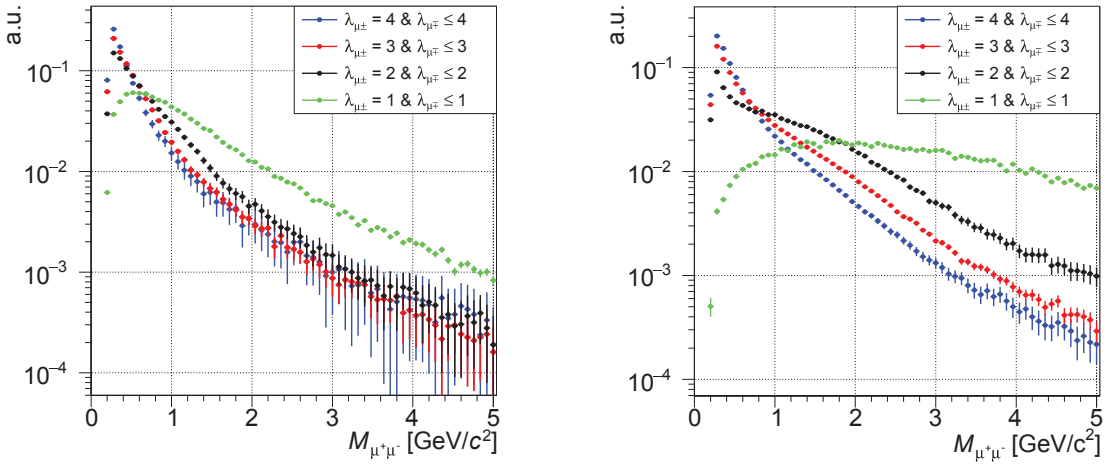

(a) open charm (b) open beauty

Figure 4.14: Generated dimuon mass coming from open heavy flavor semi-leptonic decays with particular λ_μ.

mass distributions. To do so, in figure 4.14 the dimuon mass distributions are shown for four particular $\lambda_{\mu^+}\lambda_{\mu^-}$ combinations. As expected, shorter decay chains correspond to harder mass distributions.

We thus verified that the shape of the invariant mass profile of the open charm and beauty dimuons depends of the length of the decay chains of the two muons. This means that, to properly reproduce the dimuon mass profile of the open charm and beauty components in the data, we have to correctly reproduce the distribution of the decay length chains for the simulated dimuons. Now, this is not a problem as long as any dimuon from an open charm or beauty process is retained, both in the data and in the MC. However, the data considered for the signal extraction are obtained by subtracting the combinatorial background from the raw dimuon spectrum, implying that we should retain in the MC the correlated dimuons only. But the correlation of a muon pair coming from an open charm or beauty process is progressively lost as the length of the decay chains of the two muons increases and it is extremely hard — in terms of analysis strategy and CPU time — to estimate and take such an effect into account in the MC simulations. This introduces a source of uncertainty when describing the correlated continuum in the data with the superposition of the open charm and beauty simulations.

Chapter 5

Signal Extraction

Summary

In this chapter, the main source of background for the dimuon decay channel will be discussed, as well as the strategy considered for the extraction of the signals of interest. From now on, following a convention widely used within the ALICE muon community, rapidity values are given in the positive axis, justified by the symmetry of the pp collision system with respect to $y = 0$.

5.1 Combinatorial Background Evaluation and Subtraction

The present analysis is based on the study of the OS dimuon invariant mass spectrum. Dimuons are built by combining muon pairs coming from the same event (see section 3.1). Since dimuons coming from the light-neutral meson decays of interest for this work cannot be disentangled from the other dimuon sources, any pair of muons must be considered when building the dimuon invariant mass spectrum. This implies that a fraction of the considered dimuons actually comes from randomly paired uncorrelated muons: this fraction of dimuons is conventionally named "combinatorial background". The ratio between the correlated and uncorrelated dimuon components varies significantly according to the collision system, the considered mass region and the apparatus performance. In the low-mass region, the ALICE muon spectrometer gives correlated over uncorrelated dimuon ratios as large as few units (in pp collisions) and as low as few percents (in the most central Pb-Pb collisions).

5.1.1 The Event Mixing Technique

The combinatorial background for the OS dimuons has been evaluated using an event mixing technique, based on the reasonable assumption that the LS dimuon sample does not contain correlated muon pairs. The mixing event technique implies the creation of a sample of uncorrelated dimuon formed by pairing two muons coming from two different events. In the following, we will identify dimuons built from a same event with the label "dir", and dimuons built from different events with the label "mix". The event mixing technique is illustrated in figure 5.1.

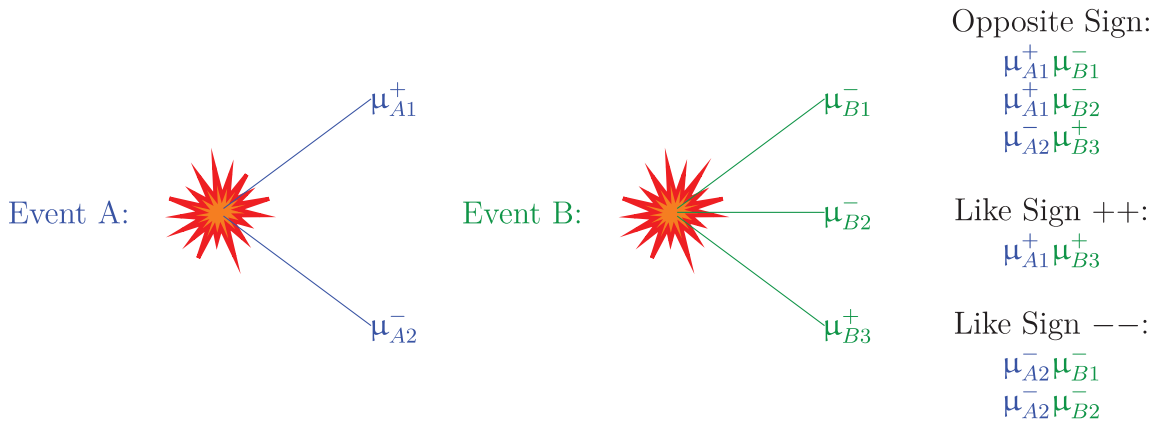

Figure 5.1: Illustration of mixing events with two events, one with two muons and one with three muons

The mixed OS dimuon sample is used, in the event mixing technique, to estimate the OS combinatorial background in the direct OS dimuon sample: for this reason, only events sharing same global properties are considered in the event mixing. Among these global properties, one can cite the z-position of the primary vertex, the charged-particle multiplicity or, in nucleus-nucleus collisions, the orientation of the event plane. In the pp collisions considered in the present analysis, the impact of classifying the events according to the z-position of the primary vertex and the charged-particle multiplicity was tested, resulting in no difference with respect to the case in which the events are mixed regardless of their global properties[1].

The shape of the invariant mass distribution expected for the OS uncorrelated dimuons is taken, for each kinematic range considered in the analysis, directly from the output distribution $N^{\mathrm{mix}}_{+-}(M)$ given by the event mixing technique. The normalization is fixed to the integral of the distribution $2R(M)\sqrt{N^{\mathrm{dir}}_{++}(M)\cdot N^{\mathrm{dir}}_{--}(M)}$ extracted from the data:

$$N^{\mathrm{mix}}_{+-}(M) \longrightarrow N^{\mathrm{mix}}_{+-}(M)\frac{\int 2R(M)\sqrt{N^{\mathrm{dir}}_{++}(M)\cdot N^{\mathrm{dir}}_{--}(M)}\,\mathrm{d}M}{\int N^{\mathrm{mix}}_{+-}(M)\,\mathrm{d}M}. \tag{5.1}$$

The integral of the $2R(M)\sqrt{N^{\mathrm{dir}}_{++}(M)\cdot N^{\mathrm{dir}}_{--}(M)}$ distribution is indeed a good estimation of the total number of the OS dimuons in the data as long as the LS dimuon samples

[1] This is valid as long as the analysis is integrated over the mentioned global properties, in particular the charged-particle multiplicity.

$N^{\rm dir}_{++}$ and $N^{\rm dir}_{--}$ do not contain any correlated muon pair. The R factor accounts for the possible differences between the acceptances of $++$, $--$, and $+-$ muon pairs:

$$R(M) = \frac{A_{+-}(M)}{2\sqrt{A_{++}(M) \cdot A_{--}(M)}}. \tag{5.2}$$

The R factor was estimated as

$$R(M) = \frac{N^{\rm mix}_{+-}(M)}{2\sqrt{N^{\rm mix}_{++}(M) \cdot N^{\rm mix}_{--}(M)}}. \tag{5.3}$$

where $N^{\rm mix}_{++}$ and $N^{\rm mix}_{--}$ is the number of dimuons for the given sign combination. the acceptances are evaluated with the mixing.

5.1.2 Monte Carlo Validation of the Event Mixing Technique

A Monte Carlo approach was considered to check the quality of the combinatorial background estimation, as follows. Events containing two muons were simulated, with the kinematics extracted randomly and independently for the two muons from some $p_{\rm T}$ and y distributions taken from the data. The azimuthal angle of each muon was randomly drawn within flat distribution, and the charges also randomly attributed. In this way, the OS sample of the direct dimuons from this MC event sample could be assumed to be purely combinatorial, by construction. We could thus check if the procedure described above was able to reproduce its mass shape and normalisation. To do this, we applied to this same MC sample the event mixing technique to obtain the mass shape with the correct normalization.

The ratio $R^{\rm MC}_{\rm dir/mix}$ between the true and estimated mass shapes of the combinatorial OS dimuons was thus extracted for each kinematics interval considered in the analysis. Several options are possible, for the trigger class of the events considered in the event mixing procedure. The considered trigger classes are based on the "V0" trigger condition, see section 3.1, to which a specific condition is added, based on the response of the muon trigger:

- "MUL": based on the presence of at least two tracklets in the muon trigger system, of opposite sign, both passing the low-$p_{\rm T}$ single-muon threshold
- "MLL": based on the presence of at least two tracklets in the muon trigger system, of like sign, both passing the low-$p_{\rm T}$ single-muon threshold
- "MSL": based on the presence of at least one tracklet in the muon trigger system, passing the low-$p_{\rm T}$ single-muon threshold
- "MSL-only": it is defined by this logical combination of trigger conditions: `MSL &!MUL &!MLL`, so it is the condition which minimizes the impact of the dimuon trigger condition on the retained events.

The trigger condition of the events considered for the event mixing technique was chosen as the one maximizing the flatness of $R^{\rm MC}_{\rm dir/mix}$. Figures 5.2 and 5.3 show that the

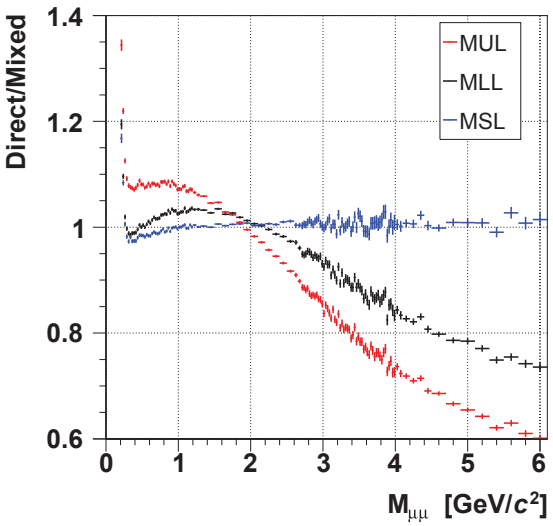

Figure 5.2: Comparison of background evaluation ratio direct over mixed for "MUL", "MLL" and "MSL" conditions.

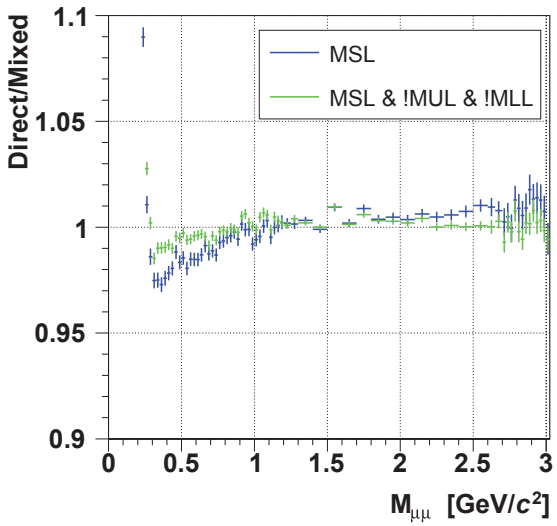

Figure 5.3: Comparison of background evaluation ratio direct over mixed for "MSL" and "MSL-only" conditions.

best results are obtained considering events satisfying the "MSL-only" condition, with "MSL" condition also giving a reasonably small deviation of $R^{\mathrm{MC}}_{\mathrm{dir/mix}}$ from unity. On the contrary, the worst performance is associated to the MLL and MUL trigger conditions.

The combinatorial background mass shape evaluated for the real data was corrected for the $R^{\mathrm{MC}}_{\mathrm{dir/mix}}$ ratio. To get rid of the statistical fluctuations due to the limited available MC sample, this ratio is parametrized by the following function before being used to correct the data:

$$f(M) = A\,\mathrm{e}^{-aM} - B\,\mathrm{e}^{-bM} + C, \tag{5.4}$$

where all the parameters are imposed to be positive except C. This correction is performed independently in each (p_{T}, y) phase space interval considered in the analysis.

5.1.3 The Combinatorial Background Estimation

Having validated the method for the evaluation of the combinatorial background, it is now possible to use it for isolating the dimuon correlated signal in the data. Following the result of the MC validated presented in the previous section, the "MSL-only" events are used as input for the event mixing technique. The typical mass dependence of the R-factor (ratio between the acceptance of LS and OS muon pairs), defined in equation (5.2) and estimated as equation (5.3), is shown in figure 5.4 for the phase space interval $1.0 < p_{\mathrm{T}} < 10.0$ GeV/c and $-4.00 < y < -2.50$. In this same kinematics interval, the comparison between the raw dimuon and the combinatorial background is shown in figure 5.5. The corresponding isolated dimuon correlated signal is shown in figure 5.6 for $M_{\mu\mu} < 10.0$ GeV/c^2, where the peaks of the Υ(1S), ψ(2S) and J/ψ resonances can be observed, and in figure 5.7 for the low-mass region, where the peaks of the ϕ and ρ/ω two-body decays are visible together with the structure of the η Dalitz decay.

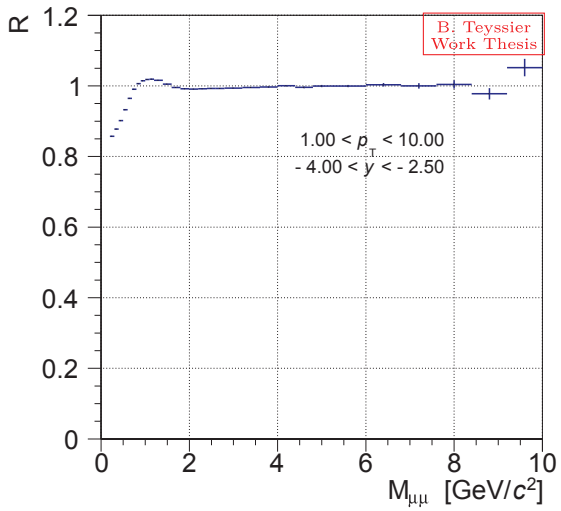

Figure 5.4: The R factor for the data integrated in $1.0 < p_{\mathrm{T}} < 10.0$ GeV/c and $-4.00 < y < -2.50$

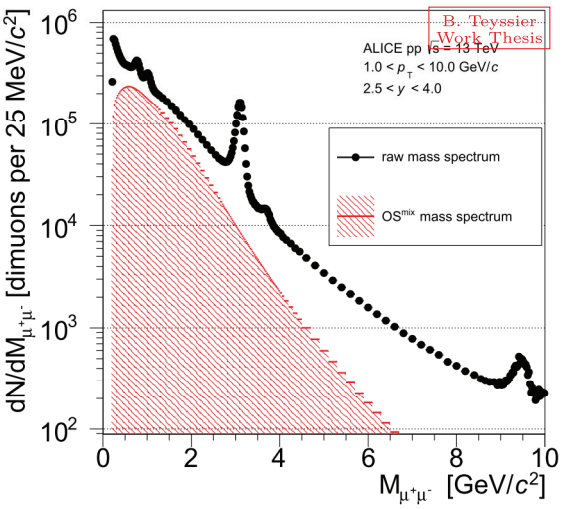

Figure 5.5: Raw data between $2.50 < y < 4.00$ and $1.0 < p_{\mathrm{T}} < 10.0$ GeV/c

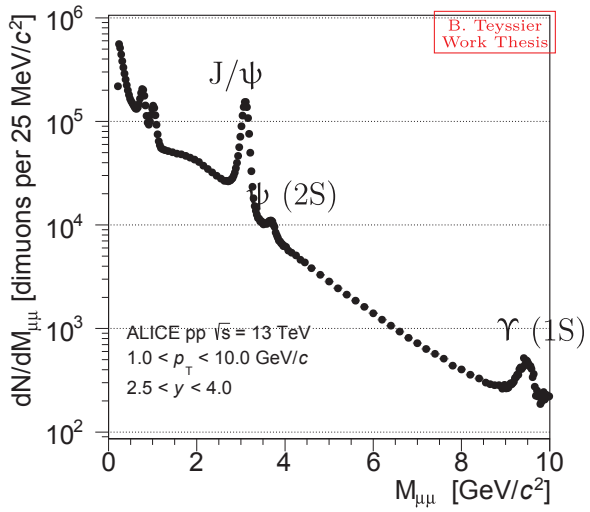

Figure 5.6: Signal after subtraction of combinatorial background in mass range between 0.2 to 10.0 GeV/c^2 .

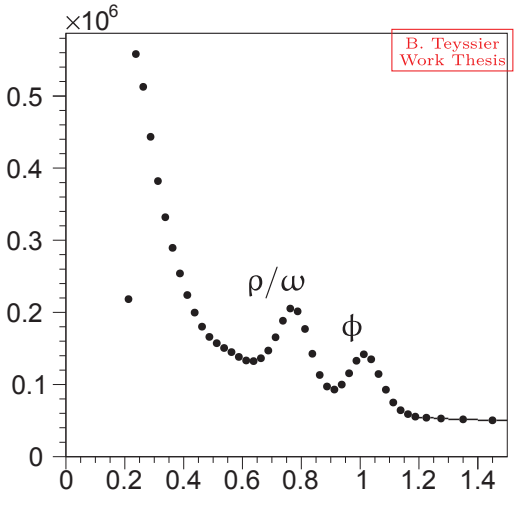

Figure 5.7: Signal after subtraction of combinatorial background in mass range between 0.2 to 1.5 GeV/c^2.

The combinatorial background estimation and subtraction is particularly challenging at very low p_{T}, where the signal-over-background ratio is smaller (as small as ≈ 1 at the ϕ peak). In order to appreciate how the signal can nevertheless be extracted down to very low p_{T}, in figure 5.8 (top panels) the raw data with the associated combinatorial background are shown for $0.0 < p_{\mathrm{T}} < 0.2\ \mathrm{GeV}/c$ in the rapidity intervals where the acceptance is non-negligible (the most forward region, see figures 4.3 and 4.7). The corresponding isolated signal is shown in the same figure (bottom panels).

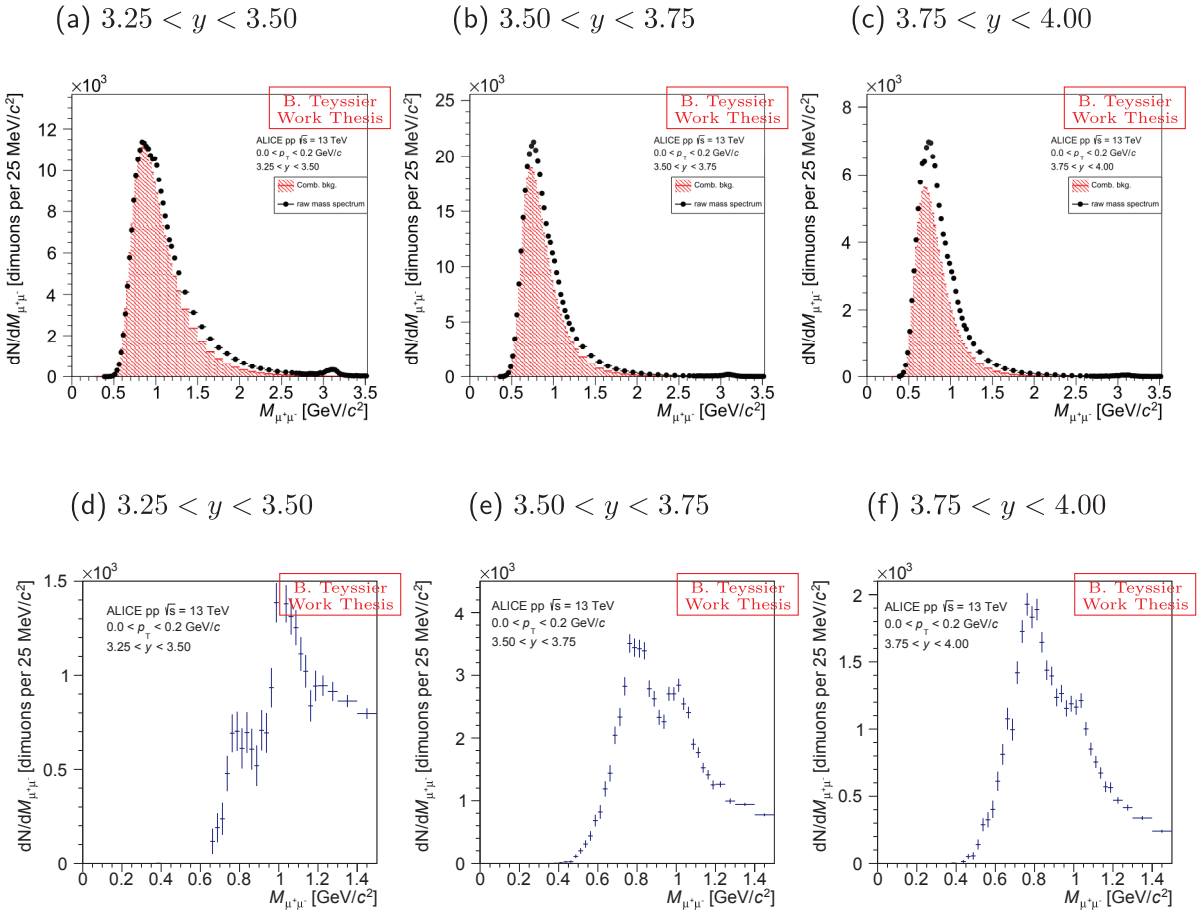

Figure 5.8: Rapidity evolution of signal and combinatorial background shapes for $0.0 < p_{\mathrm{T}} < 0.2\ \mathrm{GeV}/c$

5.2 Invariant Mass Fit Procedure

After subtraction of the uncorrelated background, the next step in the analysis is the extraction of the signals of interest from the dimuon correlated invariant mass spectrum; in this specific case, this means counting how many dimuons from the $\eta \to \mu^+\mu^-\gamma$, $\omega \to \mu^+\mu^-$ and $\phi \to \mu^+\mu^-$ decays can be extracted from the data, for each of the p_{T}-y intervals considered in the analysis. For this step, the dimuon correlated invariant mass spectrum is decomposed into the expected sources composing the hadronic cocktail (two-body and Dalitz decays of light neutral mesons, see section 4.1) via a fit procedure also

including a description of the correlated continuum component.

5.2.1 Specific Constraints on the Hadronic Cocktail Components

In the fit procedure considered in this analysis for the extraction of the signals of interest, specific constraints have been imposed to the components of the hadronic cocktail, in order to reduce the number of degrees of freedom, fixing the minor processes (in terms of reconstructed dimuons) to the major ones. Each considered constraint has been also taken as a contribution in the evaluation of the systematics on the signal extraction, discussed in section 6.1.

Fixing the relative branching ratios of two-body and Dalitz decays for the η and ω meson — The η and ω mesons contribute to the hadronic cocktail with two decay channels: $\eta \to \mu^+\mu^-\gamma$ and $\eta \to \mu^+\mu^-$ for the η and $\omega \to \mu^+\mu^-\pi^0$ and $\omega \to \mu^+\mu^-$ for the ω. Since the branching ratios of each channel is known from the literature, the normalizations of the two-body and Dalitz decay modes can be fixed to each other (as long as the quality of the data does not allow for an independent measurement of the relative branching ratios). This constraint has been technically implemented for the η meson by considering the normalization of the $\eta \to \mu^+\mu^-\gamma$ process has a free parameter, and fixing the $\eta \to \mu^+\mu^-$ contribution to it; for the ω meson, the normalization of the $\omega \to \mu^+\mu^-$ process has been left as a free parameter, the contribution of the $\omega \to \mu^+\mu^-\pi^0$ decay being fixed to it. For each particle, the process associated to the free parameter is the one more clearly identifiable in the invariant mass profile of the data. The relevant branching ratios are listed in tables 4.2 and 4.3.

Fixing the $\sigma_{\eta'}/\sigma_\phi$ cross-section ratio — The contribution of the η' Dalitz decay accounts for a very small fraction of the total reconstructed dimuon mass spectrum; for this reason and because of its continuum shape having no dominant structure apart from the broad peak at ρ mass (due to the contribution of the ρ meson to the η' form factor, see section 4.1.2) the fit procedure is not sensitive to this contribution. Consequently, the normalization of the $\eta' \to \mu^+\mu^-\gamma$ process has been set by fixing the η' cross-section to the cross-section of one of the particles giving a major contribution to the invariant mass spectrum, namely the ϕ meson. The reference value for the $\sigma_{\eta'}/\sigma_\phi$ cross-section ratio has been evaluated with `PHOJET` to be 3.151 in the rapidity window $2.5 < y < 4.0$, integrated over p_T. This ratio has been rescaled in each p_T-y interval considered in the analysis, according to the kinematic distributions of the two particles, also given by `PHOJET`.

Fixing the $\sigma_\rho/\sigma_\omega$ cross-section ratio — Due to the broad line shape of the ρ meson, and the limited mass resolution of the detector for the superimposed $\omega \to \mu^+\mu^-$ peak, the $\rho \to \mu^+\mu^-$ contribution cannot be easily disentangled in the fit procedure. For this reason, the normalization of the $\rho \to \mu^+\mu^-$ contribution has been set to the $\omega \to \mu^+\mu^-$ one by fixing the $\sigma_\rho/\sigma_\omega$ cross-section ratio. The reference value for this ratio has been taken as 1.0, from previous measurements [88–90].

Due to the mass resolution of the ω peak, the distinction of the ω and ρ two-body contribution is not obvious. So it is better to enslave the ρ two-body component to the ω to increase the stability of the fit. The ratio of the production cross-section of ρ/ω is measured to 1.0 in several previous experiments [88–90].

5.2.2 Correlated Continuum Treatment

Several choices can be considered for the description of the correlated continuum, as discussed below. As discussed in section 4.2, the main sources in the correlated dimuon continuum are the open charm and beauty processes. However, as also discussed in section 4.2, the evaluation of the MC template of the invariant mass shape of the open charm and beauty dimuons is affected by potentially non-negligible uncertainties, according to the considered input for the $c\bar{c}$ and $b\bar{b}$ kinematics and the real degree of correlation of the final state muons. Moreover, one as to consider the possibility of having some residual uncertainty from the combinatorial background subtraction and a possible dimuon component from correlated light-flavor hadron decays. On the basis of these considerations, two approaches have been tested, for the description of the correlated continuum.

In the fit process, for treating the underlying physics continuum, we assume that the main source of this continuum is based on the open heavy-flavor where the way to obtain the shapes of open charm and beauty are described in section 4.2. Two possible ways for using these shapes in the fit process, one based on the full description of all processes, the other based on a phenomenological approach for the correlated continuum and realistic description of processes are considered.

The "charm+beauty" approach — This approach is based on three assumptions:

1. The correlated continuum has only two components, open charm and beauty;

2. The shapes of the dimuon invariant mass templates for the open charm and beauty processes are known with negligible uncertainties (with the same precision as the templates for the hadronic cocktail processes);

3. The ratio between the open beauty and the open charm dimuon components is known (together with its p_{T} and y dependence, at the specific energy considered in the analysis), either from measurements or from tuned models like `FONLL` or `PYTHIA`.

In this approach, the correlated continuum description is associated to one free parameter. The only available measurements for the $c\bar{c}$ and $b\bar{b}$ cross-section at forward rapidity come from LHCb [38,91–93]: the ratio $\sigma_{b\bar{b}}/\sigma_{c\bar{c}}$, is $(5.94 \pm 0.55) \cdot 10^{-2}$, in good agreement with the central value of the `FONLL` prediction $(6.45 \cdot 10^{-2})$ [86,87].

When considering this approach in the description of the correlated continuum, non-negligible tensions between data and MC can be found according to the specific phase space interval considered. These tensions increase towards mid-rapidity while are almost negligible for the most forward rapidity intervals. An example is given in the left-column plots of figures 5.9 and 5.10, where the data-MC comparison is shown for the six y intervals

considered for the analysis, in the p_T interval $2.0 < p_T < 2.2$ GeV/c. The same trend is observed in almost all the considered p_T intervals.

As a matter of fact, these tensions induce an indirect bias on the extraction of the signals of interest for the analysis, particularly important for the extraction of the $\omega \to \mu^+\mu^-$ signal. For this reason, this approach is probably not well-fitted for this specific analysis, aiming to simultaneously extract the $\eta \to \mu^+\mu^-\gamma$, $\omega \to \mu^+\mu^-$ and $\phi \to \mu^+\mu^-$ signals.

The semi-empirical approach — This new approach has been developed after considering the major limitations of the "charm+beauty" approach in describing the data over the full rapidity interval available. The main difference with respect to the previous approach, is the fact that we abandon any strict physical interpretation of the correlated continuum, describing it with an empirical profile, flexible enough to saturate the tension between data and MC, ensuring a robust extraction of the signals of interest for the analysis. This is achieved by describing the correlated continuum by means of two (or more) free parameters, each controlling the normalization of an independent empirical shape. The specific shape of these independent components is not really important: still, one has to use sufficiently different mass shapes, to ensure enough freedom on the total profile of the continuum.

Two variants of this semi-empirical approach have been tested in this analysis:

- A 2-component description of the correlated continuum. In this case, an obvious choice is to take the two components as the invariant mass distributions of OS dimuons from open charm and open beauty simulations[2]. This choice allows one to combine the required smoothness of the continuum invariant mass shape with the kinematical constraints typical of a reconstructed dimuon mass distribution close to the low-mass threshold: this would not have been (easily) achievable with any trivial combination of analytical parametric functions.

- A 3-component description of the correlated continuum. In this variant, we add a third component to the two components already considered in the previous case: a reasonable choice is to take this third component to have the profile of the combinatorial background evaluated in each p_T and y interval considered in the analysis.

The results of the data description with these two variants of the semi-empirical approach are shown in figures 5.9 and 5.10, in the center and right panels respectively for the 2- and the 3-component description of the correlated continuum. As one can see, the 2-component description already fixes the tension between data and MC, found with the "charm+beauty" approach, in the full y range. Nevertheless, the addition of the third degree of freedom allowed by the 3-component description of the correlated continuum still improves the extraction of the signal in some specific cases, see for instance the extraction of the $\phi \to \mu^+\mu^-$ signal in figures 5.9b and 5.9c. For this reason, the 3-component variant of the semi-empirical approach has been retained as the reference method for the signal extraction for the present analysis.

[2] It should be clear that, in this semi-empirical approach, the physical interpretation of any of the two components taken separately is meaningless and must be avoided.

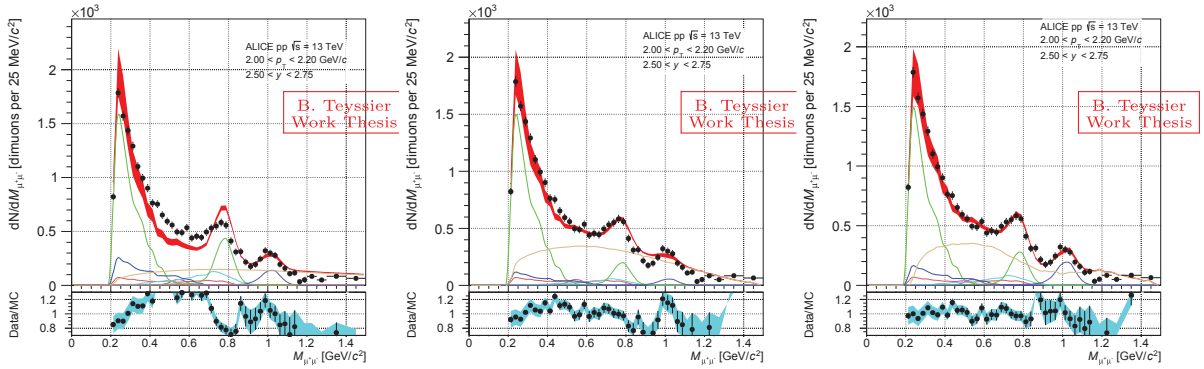

(a) $2.50 < y < 2.75$ (b) $2.50 < y < 2.75$ (c) $2.50 < y < 2.75$

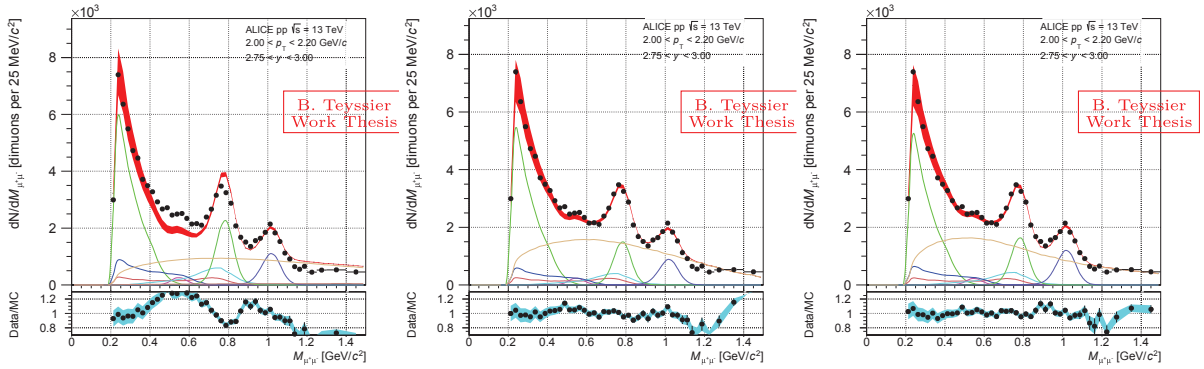

(d) $2.75 < y < 3.00$ (e) $2.75 < y < 3.00$ (f) $2.75 < y < 3.00$

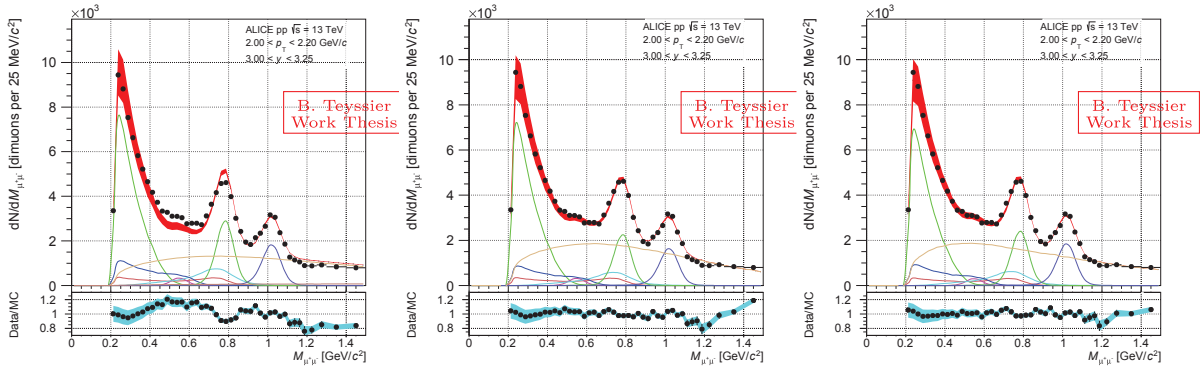

(g) $3.00 < y < 3.25$ (h) $3.00 < y < 3.25$ (i) $3.00 < y < 3.25$

Figure 5.9: Signal fit for $2.0 < p_{\mathrm{T}} < 2.2$ GeV/c and various y intervals. The first figure of each line corresponding to the method with the full description of processes, the second and third figures of each line corresponding to the hybrid method with two or three components respectively

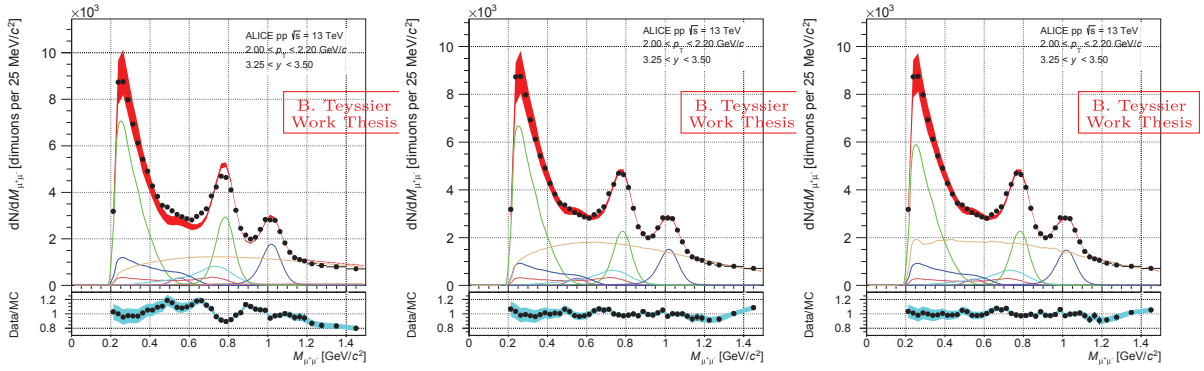

(a) $3.25 < y < 3.50$ (b) $3.25 < y < 3.50$ (c) $3.25 < y < 3.50$

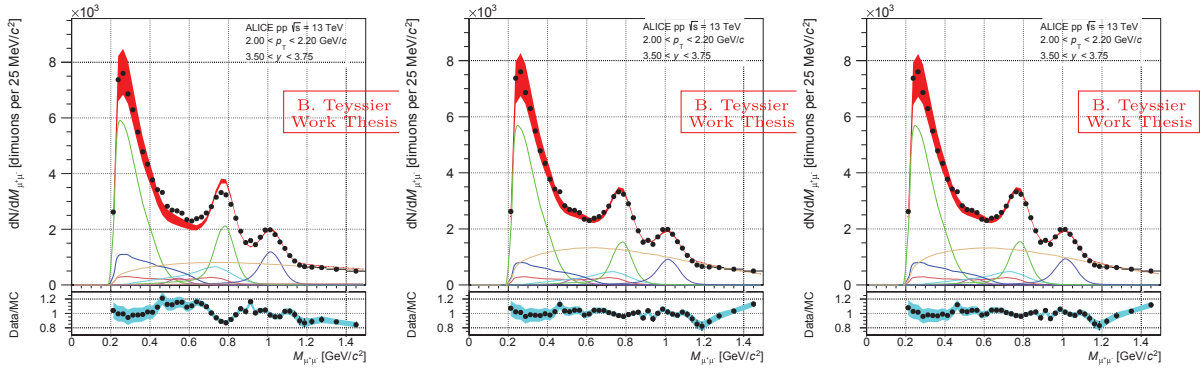

(d) $3.50 < y < 3.75$ (e) $3.50 < y < 3.75$ (f) $3.50 < y < 3.75$

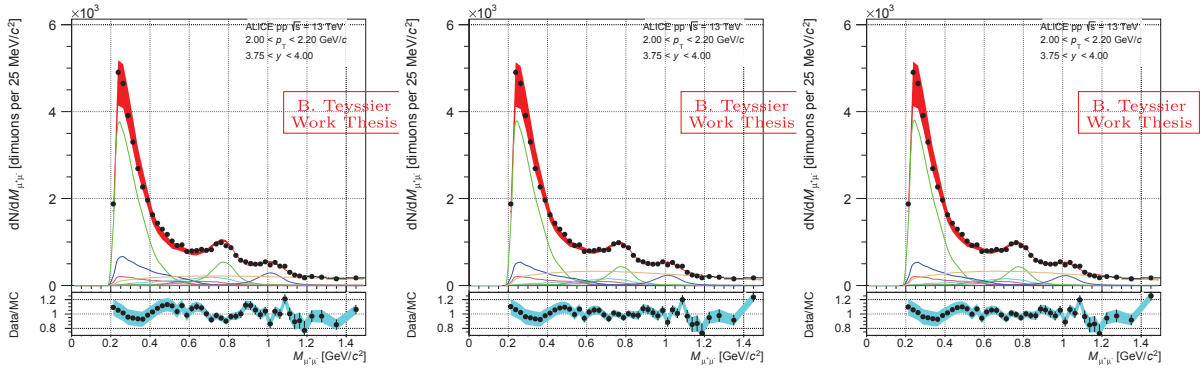

(g) $3.75 < y < 4.00$ (h) $3.75 < y < 4.00$ (i) $3.75 < y < 4.00$

Figure 5.10: Signal fit for $2.0 < p_{\mathrm{T}} < 2.2\ \mathrm{GeV}/c$ and various y intervals. The first figure of each line corresponding to the method with the full description of processes, the second and third figures of each line corresponding to the hybrid method with two or three components respectively.

5.2.3 A Few Examples of Hadronic Cocktail Fits

The detailed breakdown of the MC sources involved in the fit procedure is shown in figure 5.11 where the data sample considered in the present analysis is integrated over $2.50 < y < 4.00$ and $1.0 < p_{\mathrm{T}} < 10.0\,\mathrm{GeV}/c$. The structures of the $\eta \to \mu^+\mu^-\gamma$, $\omega \to \mu^+\mu^-$ and $\phi \to \mu^+\mu^-$ processes, considered for the estimation of the η, ω and ϕ yields, are observed to shine out over the underlying continuum. Here, as well as in the fits presented in the rest of the document, the red profile is the sum of the MC sources. The uncertainty on the total MC profile is evaluated by combining the uncertainties on the normalization of each considered source. For the processes whose normalization is left free in the fit, this uncertainty is the statistical one resulting from the fit procedure itself; for the other processes, we propagate the systematic uncertainty on the parameters (branching ratios or cross section ratios) which fix their normalizations to those of the free processes.

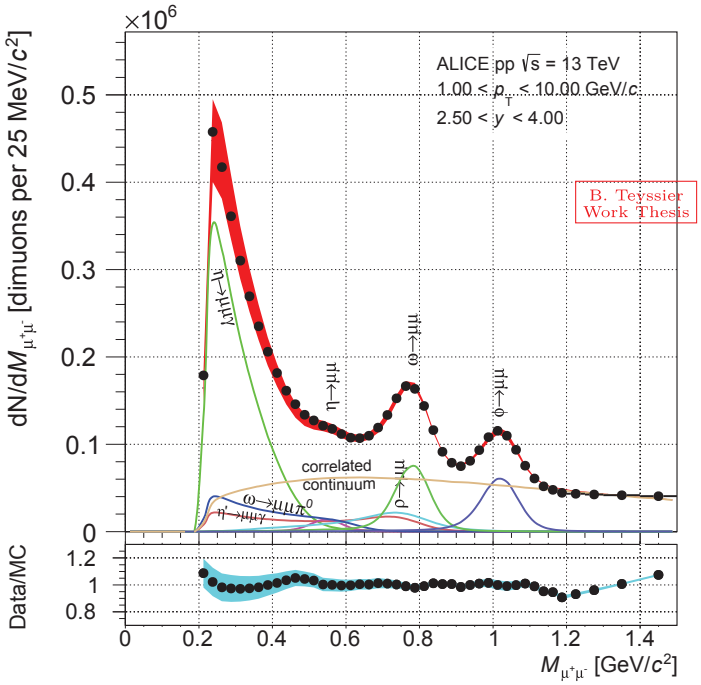

Figure 5.11: Example of hadronic fit in $2.50 < y < 4.00$ and $1.0 < p_{\mathrm{T}} < 10.0\,\mathrm{GeV}/c$

The shape of the dimuon invariant mass spectrum changes significantly according to the considered p_{T}-y interval. In particular, at very low-p_{T} and towards central rapidity, the acceptance constraints imposed by the detector deplete the mass spectrum near the kinematic threshold. For this reason, some of the processes are not measurable in specific regions of the phase space, as it could be expected by inspecting the p_{T}-y profiles of the $(A \times \varepsilon)$ reported in figures 4.3 and 4.7. In addition, at high-p_{T} one observes a decrease of the ratio of the hadronic cocktail over the correlated continuum, which could be attributed to the decrease of the ratio of the light flavor sources (composing the hadronic cocktail) over the heavy flavor ones (contributing to the correlated continuum). The full evolution of the dimuon invariant mass spectrum profile as a function of p_{T} and y can be appreciated

by considering the plots in appendix C. In figure 5.12 we report a few examples, illustrating the discussed point.

(a) $0.0 < p_{\mathrm{T}} < 0.2$ GeV/c and $3.75 < y < 4.00$

(b) $0.4 < p_{\mathrm{T}} < 0.5$ GeV/c and $3.50 < y < 3.75$

(c) $2.0 < p_{\mathrm{T}} < 2.2$ GeV/c and $3.00 < y < 3.25$

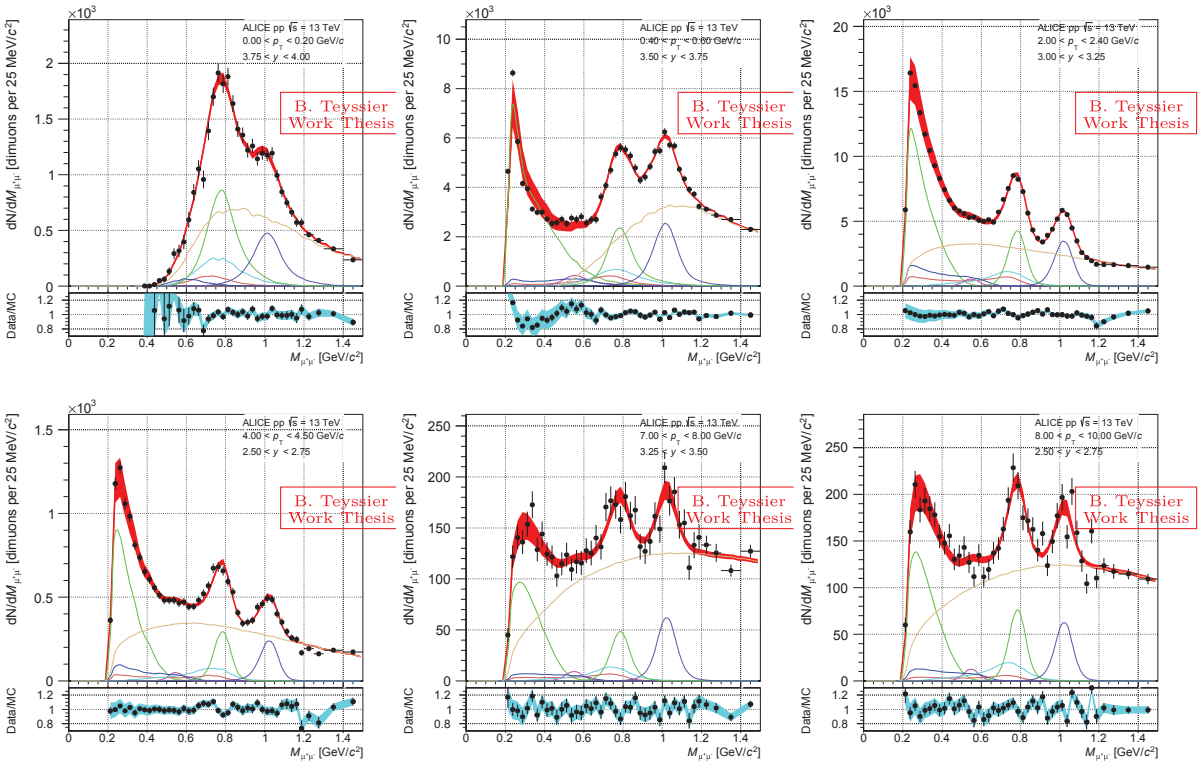

(d) $4.0 < p_{\mathrm{T}} < 4.5$ GeV/c and $2.50 < y < 2.75$

(e) $7.0 < p_{\mathrm{T}} < 8.0$ GeV/c and $3.25 < y < 3.50$

(f) $8.0 < p_{\mathrm{T}} < 10.0$ GeV/c and $2.50 < y < 2.75$

Figure 5.12: A few examples of hadronic fit in several p_{T} and y intervals.

Chapter 6

Systematics Evaluation

Summary

In this chapter, all the systematics sources of the present analysis are presented. Two main groups of systematics uncertainties have been studied:

- the sources contributing to the systematics uncertainty on the signal extraction;
- the sources contributing to the systematics on the $(A \times \varepsilon)$ evaluation.

In the first group, we include the uncertainties on the parameters involved in the fit procedure (see section 5.2): relative branching ratios, cross-section ratios, correlated continuum shape, fit range. In the second group, we include the uncertainties on the kinematic input of the MC simulations, on the tracking efficiency and the trigger response.

6.1 Systematics on the Signal Extraction

In order to define the systematics tests on the signal extraction, a reference scenario has been defined based on the reference values of the parameters involved in the fit procedure. For each parameter, one or more alternative values have been considered; each systematic test is defined by the variation of one parameter only, while the others are kept fixed to their reference value. In total, 10 systematic tests have been considered: the total systematic uncertainty on the number of $\eta \to \mu^+\mu^-\gamma$, $\omega \to \mu^+\mu^-$ and $\phi \to \mu^+\mu^-$ dimuons was taken as the standard deviation of the values resulting from these tests.

Syst. test	**reference value**	**alternative value(s)**	
BR $\eta \to \mu^+\mu^-$	PDG	PDG -1σ	PDG $+1\sigma$
BR $\omega \to \mu^+\mu^-\pi^0$	PDG	PDG -1σ	PDG $+1\sigma$
Ratio $\sigma_{\eta'}/\sigma_\eta$	0.295	-50%	$+50\%$
Ratio $\sigma_\rho/\sigma_\omega$	1.0	-10%	$+10\%$
Upper fit limits	1.5 GeV/c^2	2.0 GeV/c^2	
Templates for the correlated continuum components	$c\bar{c} \to \mu\mu$ from PYTHIA $b\bar{b} \to \mu\mu$ from PYTHIA OS from evt. mix. (data)	$c\bar{c} \to \mu\mu$ from FONLL $b\bar{b} \to \mu\mu$ from FONLL OS from combinatorial bkg. (MC)	

Table 6.1: Summary of systematics tests

6.1.1 Relative Branching Ratio of two-body and Dalitz Decays for the η and ω Mesons

This systematics test reflects the uncertainty on the ratio between the branching ratio of the two-body and Dalitz decay channel of the η and ω mesons. In this analysis, this test was implemented by varying the branching ratio of the $\eta \to \mu^+\mu^-$ and $\omega \to \mu^+\mu^-\pi^0$ processes by $\pm 1\sigma$, where σ is the uncertainty on the measurement reported by the PDG (shown in tables 4.2 and 4.3), resulting in four independent, alternative fits on the data.

The variation of the $\eta \to \mu^+\mu^-$ branching ratio was found to have a negligible impact on the extraction of $\eta \to \mu^+\mu^-\gamma$ and $\phi \to \mu^+\mu^-$ signals and a limited impact on the extraction of the $\omega \to \mu^+\mu^-$ signal, of the order of 1%. On the contrary, the variation of the $\omega \to \mu^+\mu^-\pi^0$ branching ratio by $\pm 1\sigma$ has an average impact of $\pm 3\%$ for the extraction of $\eta \to \mu^+\mu^-\gamma$ and $\omega \to \mu^+\mu^-$ signals and negligible for the $\phi \to \mu^+\mu^-$ signals.

6.1.2 $\sigma_{\eta'}/\sigma_\phi$ Cross-Section Ratio

The ratio $\sigma_{\eta'}/\sigma_\phi$ was varied by $\pm 50\%$ to take into account the general lack of measurements for this ratio, and the differences between the predictions from the available phenomenological models PYTHIA6 and PHOJET. The impact of the considered $\pm 50\%$ variation has been observed to be, in average, $\mp 2\%$ for the $\omega \to \mu^+\mu^-$ signal, and negligible for the $\phi \to \mu^+\mu^-$ and $\eta \to \mu^+\mu^-\gamma$ signal.

6.1.3 $\sigma_\rho/\sigma_\omega$ Cross-Section Ratio

The uncertainty on the $\sigma_\rho/\sigma_\omega$ ratio has been taken from the existing measurements at lower energy [88–90]. The absence of any strong theoretical argument in favor of an important energy dependence of this ratio, allowed us to take a $\pm 10\%$ for the associated uncertainty. As expected, the impact of this $\pm 10\%$ variation is non-negligible only for the extraction of the $\omega \to \mu^+\mu^-$ signal, which is affected by a corresponding $\mp 2\%$ uncertainty.

6.1.4 Upper limit of the fit

The lower limit of the invariant mass fit range has been set to the $2m_\mu$ kinematic threshold, in order to be sensitive to the full structure of the $\eta \to \mu^+\mu^-\gamma$ decay. For the upper limit, a reference value has been set at 1.5 GeV/c^2: this value is a trade-off between being sensitive to the full width of the $\phi \to \mu^+\mu^-$ peak, and limiting the impact of the continuum region between the ϕ and J/ψ resonance, where no signal of interest for the light-neutral mesons can be extracted. To study the systematic uncertainty linked to the choice of the upper limit of the fit range, an alternative value has also been defined at 2.0 GeV/c^2. The corresponding average impact on the extraction of the signals of interest is -3%, -12% and -4%, respectively for the $\eta \to \mu^+\mu^-\gamma$, $\omega \to \mu^+\mu^-$ and $\phi \to \mu^+\mu^-$ signals.

6.1.5 The correlated continuum shape

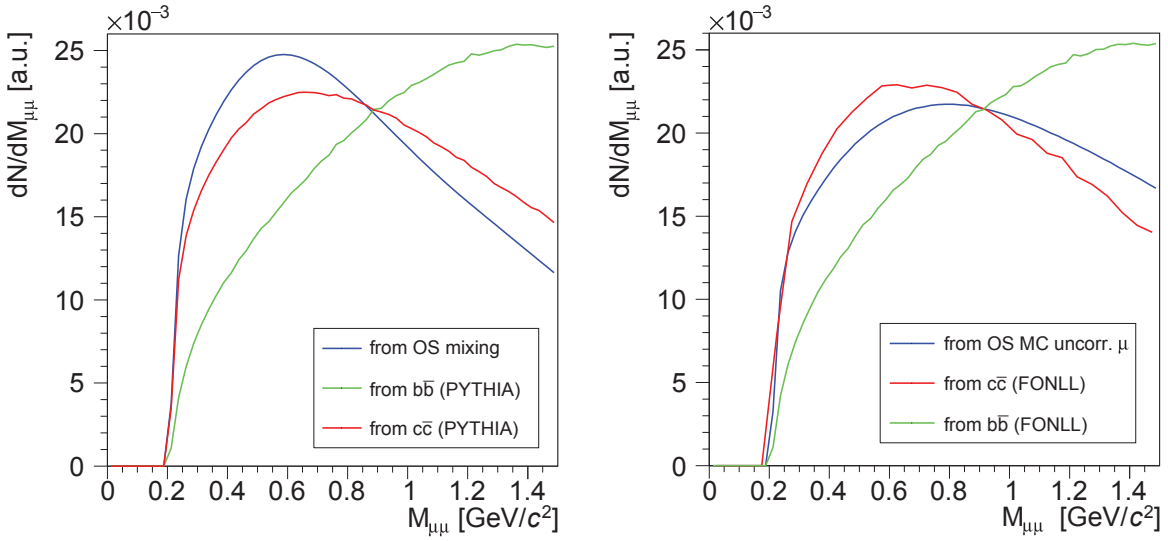

(a) Reference (b) Alternative

Figure 6.1: Normalized shape of continuum templates.

The shape of the correlated continuum is determined by the fit by optimizing the relative weight of three invariant mass templates, as explained in section 5.2.2. To evaluate the systematic uncertainty associated to the choice of this set of templates, an alternative set of templates have been considered. The alternative templates correspond

to the reconstructed open charm/beauty dimuons generated with the lower limit of the FONLL prediction range (offering the largest deviation from the corresponding reference templates, see figure 4.12), and to the OS dimuons from the MC simulations of uncorrelated muons, already considered for the validation of the event mixing technique (see section 5.1.2). Considering the alternative set of templates has an average impact of −1% for the $\eta \to \mu^+\mu^-\gamma$, 2% for the $\omega \to \mu^+\mu^-$ and 9% for the $\phi \to \mu^+\mu^-$ signals.

6.1.6 Systematic Uncertainty Computation

As already mentioned, the systematic uncertainty on the signal extraction is computed, separately for the $\eta \to \mu^+\mu^-\gamma$, $\omega \to \mu^+\mu^-$ and $\phi \to \mu^+\mu^-$ processes, as the standard deviation of the distribution of value obtained from the systematic tests described above:

$$\sigma^2 = \frac{1}{N} \sum_{i}^{\text{tests}} (x_i - \langle x \rangle)^2 , \tag{6.1}$$

where x_i is the outcome of the i-th systematic test, out of the N available tests, and the expectation value $\langle x \rangle$ is taken as the outcome of the reference fit. This approach is justified by the assumption that for each source of systematics, the associated uncertainty can be assumed to be Gaussian. This evaluation is done for each p_T-y interval considered in this analysis.

The global uncertainty on the signal extraction is reported in table 6.2 for the three signals extracted with the fit procedure: since its value depends on the p_T and y interval, the minimum and maximum values are quoted. The average uncertainties corresponding to the considered systematic tests on the signal extraction are also reported in the table.

Syst. test	$\eta \to \mu^+\mu^-\gamma$	$\omega \to \mu^+\mu^-$	$\phi \to \mu^+\mu^-$
BR $\eta \to \mu^+\mu^-$	< 1 %	2 %	2 %
BR $\omega \to \mu^+\mu^-\pi^0$	3 %	3 %	2 %
Ratio $\sigma_{\eta'}/\sigma_\phi$	< 1 %	3 %	2 %
Ratio $\sigma_\rho/\sigma_\omega$	1 %	2 %	2 %
Upper fit limit	5 %	6 %	8 %
Templates for the correlated continuum	6 %	4 %	5 %
Standard deviation from (6.1)	1 - 22 %	2 - 12 %	1 - 16 %

Table 6.2: Summary of the systematic tests considered on the signal extraction procedure.

6.2 Systematics from the MC input

The first source of systematic uncertainty considered for the $(A \times \varepsilon)$ evaluation is the choice of the input kinematic distributions assumed in MC simulations, for the generated η, ρ, ω, η' and ϕ mesons, see section 4.1.1. The reference choice being the correlated

p_T-y input from PHOJET, the alternative MC input has been based on parametrized non-correlated p_T and y distributions form PYTHIA6. The corresponding systematic uncertainty has been evaluated for each p_T and y interval considered in this analysis, by taking the difference of the $(A \times \varepsilon)$ value estimated with the reference and the alternative MC inputs. The corresponding, average impact on the extraction of the signals of interest is 5%, 5.5% and 1%, respectively for the $\eta \to \mu^+\mu^-\gamma$, $\omega \to \mu^+\mu^-$ and $\phi \to \mu^+\mu^-$ signals.

6.3 Systematics on Trigger Efficiency

The systematics on the trigger efficiency has been determined by comparing the probability of reconstructing dimuons of a given kinematics, with two different trigger response functions, one obtained from the data and the other from MC simulations. The standard procedure to estimate the systematic uncertainty from the trigger response function can be summarized as follows:

- Fit the ratio low-p_T/A-p_T obtained dividing the p_T distribution of single muons matching the low-p_T trigger condition, by the p_T distribution of single muons matching the A-p_T condition (see paragraph [e] on section 2.2.3). This ratio is evaluated both in data and in realistic MC simulations, and the corresponding fits define the trigger response function.

- Select muons matching the A-p_T trigger condition in the MC simulation of a specific dimuon signal, and weigh each of them (according to their p_T) by either the data or the MC trigger response function.

- Extract the number of reconstructed dimuons under the two assumptions of the trigger response function. The difference is the systematics uncertainty of the trigger efficiency.

6.3.1 Evaluation of the Trigger Response Function

The definition of the trigger response function given above cannot be used in the present analysis, because in the considered data set the low-p_T and the A-p_T trigger matching conditions coincide. Therefore, an alternative definition of the trigger response function is adopted here, namely the ratio low-p_T/*All* where the denominator is the p_T distribution of *All* reconstructed muons, imposing no trigger matching condition.

Unfortunately, this new definition of the trigger response function cannot be safely applied to the data, because the *All* muon sample is contaminated by a non-negligible hadronic component. In this case, one can still estimate the low-p_T/*All* for the data starting from the ratio of the corresponding MC ratio, through a data/MC conversion factor. This conversion factor is defined as the ratio between the trigger response functions low-p_T/A-p_T of data and MC, estimated in a dataset ($\mathcal{B}$) as close as possible to the one ($\mathcal{A}$) considered in the present analysis, and characterized by different thresholds for the

low-p_{T} and A-p_{T} trigger matching conditions:

$$\left.\frac{\text{low-}p_{\mathrm{T}}}{All}\right|_{\mathcal{A}}^{\text{data}}(p_{\mathrm{T}}) = \left.\frac{\text{low-}p_{\mathrm{T}}}{All}\right|_{\mathcal{A}}^{\text{MC}}(p_{\mathrm{T}}) \times \frac{\left.\frac{\text{low-}p_{\mathrm{T}}}{\text{A-}p_{\mathrm{T}}}\right|_{\mathcal{B}}^{\text{data}}(s \times p_{\mathrm{T}})}{\left.\frac{\text{low-}p_{\mathrm{T}}}{\text{A-}p_{\mathrm{T}}}\right|_{\mathcal{B}}^{\text{MC}}(s \times p_{\mathrm{T}})} \tag{6.2}$$

with the p_{T} dependence of the trigger response functions in the reference dataset $\mathcal{B}$ being "stretched" by the s factor:

$$s = \frac{p_{\mathrm{T}}^{\mathrm{cut}}(\mathrm{MC},\, \mathcal{B})}{p_{\mathrm{T}}^{\mathrm{cut}}(\mathrm{MC},\, \mathcal{A})}, \tag{6.3}$$

where ${p_{\mathrm{T}}}^{\mathrm{cut}}(\mathrm{MC},\, \mathrm{x})$ is defined as the p_{T} value for which the trigger response function (low-p_{T}/All or low-p_{T}/A-p_{T}, respectively for the datasets $\mathcal{A}$ and $\mathcal{B}$) reaches half the difference between the maximum and minimum. This approach is correct as long as two assumptions are valid:

- the trigger response per local board does not change with time,
- the relative difference data/MC between the low-p_{T}/A-p_{T} trigger response functions from data and MC, does not change when considering the low-p_{T}/All trigger response functions.

The low-p_{T}/A-p_{T} trigger response functions defining the data/MC conversion factor in equation (6.2) can be replaced by a parametrization given by the function:

$$F(p_{\mathrm{T}}, p_{\mathrm{T}}^{\mathrm{cut}}, \sigma) = 1 + p_0 \times \left(\mathrm{erf}\left(\frac{p_{\mathrm{T}} - \frac{p_{\mathrm{T}}^{\mathrm{cut}}}{s}}{\sqrt{2}\sigma/s} \right) - 1 \right), \tag{6.4}$$

based on the three free parameters p_0, $p_{\mathrm{T}}^{\mathrm{cut}}$ and σ.

In the present analysis, the reference dataset $\mathcal{B}$ has been assumed to be the 2015 Pb-Pb dataset (restricted to the peripheral collisions in the 60-100% centrality class) taken at $\sqrt{s} = 5.02$ TeV; this choice is also used in other dimuon analyses based on the pp dataset at $\sqrt{s} = 5$ TeV and the p-Pb dataset at $\sqrt{s_{\mathrm{NN}}} = 5$ — 8.16 TeV.

6.3.2 Results

The two versions of the trigger re-weighting described above produced two alternative estimations of the $(A \times \varepsilon)$ for the three considered processes. For each p_{T}-y cell considered in the analysis we retained the alternative version giving the largest deviation with respect to the reference value: this deviation is shown, in the form of a ratio, in figure 6.2. The absolute deviation of this ratio is taken as the systematic uncertainty on the trigger efficiency: the average values of this uncertainty are 2%, 0.6% and 1% respectively for the $\eta \to \mu^+\mu^-\gamma$, $\omega \to \mu^+\mu^-$ and $\phi \to \mu^+\mu^-$ processes. In the analysis, this uncertainty has been evaluated for each specific p_{T}-y cell considered for the extraction of the signal. Systematic uncertainty values as large as 30% were tolerated in this analysis: this resulted in the exclusion of the $(-3.50 < y < 3.25,\ 0.4 < p_{\mathrm{T}} < 0.6\ \mathrm{GeV}/c)$ interval for the $\eta \to \mu^+\mu^-\gamma$ signal, affected by a systematic on the trigger efficiency larger than 70%.

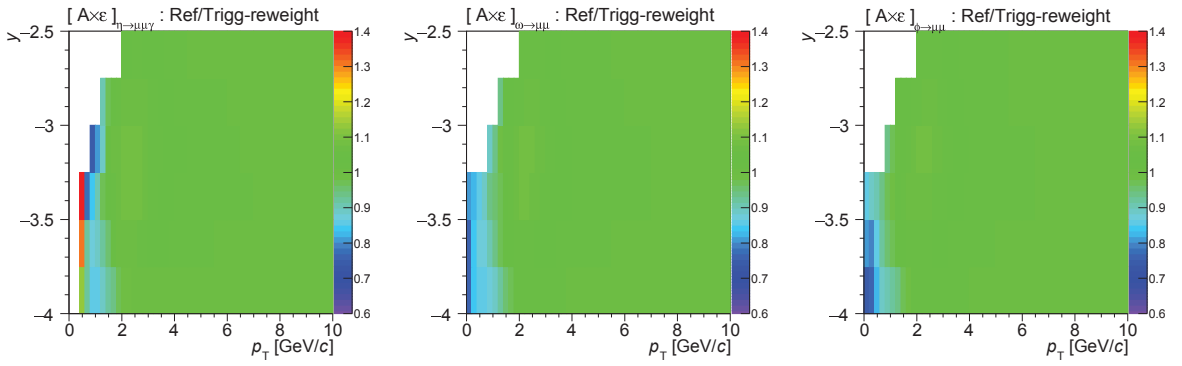

(a) $\eta \to \mu^+\mu^-\gamma$ (b) $\omega \to \mu^+\mu^-$ (c) $\phi \to \mu^+\mu^-$

Figure 6.2: Ratio of $A \times \varepsilon$ for original simulation over the re-weighted simulation for estimating the systematics associated to the trigger efficiency.

6.4 Systematics on Tracking Efficiency

The systematics on tracking efficiency is one of the contributions to the uncertainty on the $(A \times \varepsilon)$ estimation. To compute this uncertainty, one has to evaluate the ratio between the tracking efficiencies of data and MC.

6.4.1 Preliminary Check

Before studying the tracking efficiencies in data and MC, it must be verified that the status of the detector described in the realistic MC simulations is compatible with the status of the detector reflected by the data. This is done by inspecting the cluster maps of the tracking chambers in data and MC: in this way one can verify whether the dead areas in the data are correctly reproduced in the MC, and no additional dead area is introduced. An example of such comparison is shown in figure 6.3.

Another point to be checked is the variation of the high voltage supplied to the tracking chambers, with respect to the value 1.6 kV corresponding to the nominal operating conditions. During Run 2, indeed, some frequent high voltage drops to 1.4 kV were spotted, resulting in a degraded efficiency of the chambers. Since this intermediate behavior, between the full operation and the off status, cannot be easily reproduced in MC, specific detector elements being significantly affected by high voltage drops are added to a "reject list" and excluded from the reconstruction both in data and MC. Alternatively, when this pathological high voltage behavior only affects a limited fraction of the considered data sample, full runs can be excluded: it was the case in the present analysis, where 4 runs of the LHC16n period were rejected to avoid major discrepancies between data and MC.

After checking the agreement between data and MC concerning the detector status, and the behavior of the high voltage, it is possible to launch the evaluation of the tracking efficiency both in data and MC.

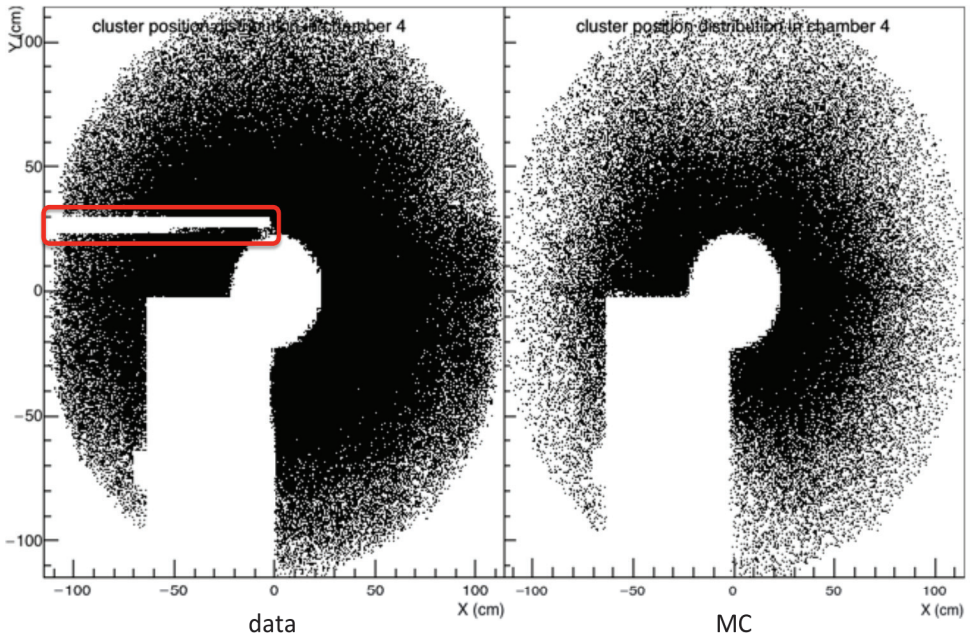

Figure 6.3: Comparison between cluster maps of tracking chamber 4 in data (left) and MC (right).

6.4.2 Tracking Efficiency Evaluation

The tracking efficiency ($\varepsilon_{\text{global}}$) is computed as the product of the efficiency ($\varepsilon_{\text{St}i}$) of each tracking station,

$$\varepsilon_{\text{global}} = \varepsilon_{\text{St1}} \cdot \varepsilon_{\text{St2}} \cdot \varepsilon_{\text{St3}} \cdot \varepsilon_{\text{St45}}. \tag{6.5}$$

The fact the efficiencies of stations 4 and 5 are combined together in the efficiency $\varepsilon_{\text{St45}}$ is due to the logic operating mode implemented in the tracking algorithm [78,94], requiring one cluster per station for stations 1, 2 and 3, and three clusters from the combined stations 4-5.

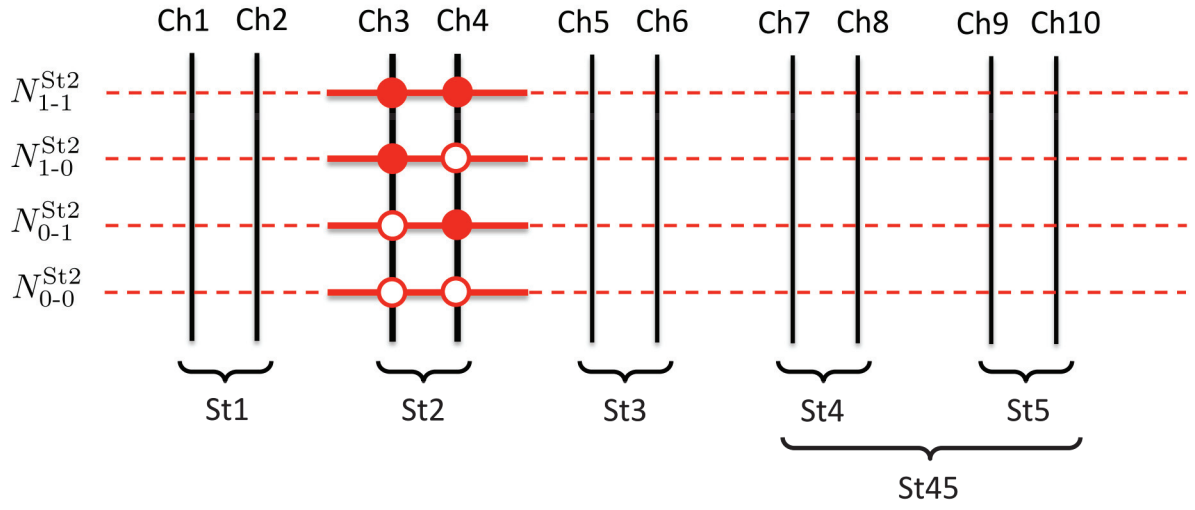

Figure 6.4: Sketch showing the arrangement of the chambers into stations and the possible responses of one station to the passage of a particle.

To evaluate the efficiency of a given station, one has to start considering the efficiency of the chamber composing the station (see section 2.2.3 for a more detailed description of the muon spectrometer structure). To evaluate the efficiency of each tracking chamber, the assumption is done, that its efficiency does not depend on the efficiency of the other chambers: under this assumption, the redundancy of the information given by the two chambers of a specific station, can be used to determine the efficiency of each chamber separately. Figure 6.4 shows the possible responses of station 2 to the passage of a particle. Generalizing to the case of an arbitrary station k, the reconstructed track can have a cluster in both chambers ($N^{\mathrm{St}k}_{\text{1-1}}$), a cluster either in the first or the second of the two stations ($N^{\mathrm{St}k}_{\text{1-0}}$ or $N^{\mathrm{St}k}_{\text{0-1}}$), or the track does not fulfill the tracking conditions so it is not reconstructed ($N^{\mathrm{St}k}_{\text{0-0}}$). Still focusing on station k, composed of chamber i and $j(= i + 1)$, one can express the number of reconstructed tracks (N_{tot}, each of them crossing station k due to the conditions imposed by the tracking algorithm) as:

$$N_{\mathrm{tot}} = N^{\mathrm{St}k}_{\text{1-1}} + N^{\mathrm{St}k}_{\text{0-1}} + N^{\mathrm{St}k}_{\text{1-0}}. \tag{6.6}$$

Under the assumption that the efficiencies of chambers i and j are independent, $N^{\mathrm{St}k}_{\text{1-1}}$, $N^{\mathrm{St}k}_{\text{1-0}}$ and $N^{\mathrm{St}k}_{\text{0-1}}$ can be expressed as a function of N_{tot}:

$$N^{\mathrm{St}k}_{\text{1-1}} = N_{\mathrm{tot}} \cdot \varepsilon_{\mathrm{Ch}i} \cdot \varepsilon_{\mathrm{Ch}j} \tag{6.7}$$

$$N^{\mathrm{St}k}_{\text{1-0}} = N_{\mathrm{tot}} \cdot \varepsilon_{\mathrm{Ch}i} \cdot (1 - \varepsilon_{\mathrm{Ch}j}) \tag{6.8}$$

$$N^{\mathrm{St}k}_{\text{0-1}} = N_{\mathrm{tot}} \cdot (1 - \varepsilon_{\mathrm{Ch}i}) \cdot \varepsilon_{\mathrm{Ch}j} \tag{6.9}$$

By combining the above equations, the efficiencies of chamber i and j are given by

$$\varepsilon_{\mathrm{Ch}i} = \frac{N^{\mathrm{St}k}_{\text{1-1}}}{N^{\mathrm{St}k}_{\text{1-1}} + N^{\mathrm{St}k}_{\text{0-1}}} \qquad \varepsilon_{\mathrm{Ch}j} = \frac{N^{\mathrm{St}k}_{\text{1-1}}}{N^{\mathrm{St}k}_{\text{1-1}} + N^{\mathrm{St}k}_{\text{1-0}}}. \tag{6.10}$$

The individual chamber efficiencies can be combined to compute the efficiency of each station. In the case of the first three stations, the efficiency is defined as the probability for a muon to be detected by at least one of the two chambers:

$$\begin{aligned} \varepsilon_{\mathrm{St1(2,3)}} &= 1 - \Big(1 - \varepsilon_{\mathrm{Ch1(3,5)}}\Big)\Big(1 - \varepsilon_{\mathrm{Ch2(4,6)}}\Big) \\ &= \varepsilon_{\mathrm{Ch1(3,5)}}\,\varepsilon_{\mathrm{Ch2(4,6)}} + \Big(1 - \varepsilon_{\mathrm{Ch1(3,5)}}\Big)\,\varepsilon_{\mathrm{Ch2(4,6)}} + \varepsilon_{\mathrm{Ch1(3,5)}}\,\Big(1 - \varepsilon_{\mathrm{Ch2(4,6)}}\Big) \end{aligned} \tag{6.11}$$

For the last two stations the efficiency has to be calculated as a whole due to the tracking algorithm requirements. This efficiency is the probability that a muon is detected by at least three out of the four chambers in the stations; the corresponding formula is the generalization of equation (6.11):

$$\varepsilon_{\mathrm{St45}} = \prod_{i=7}^{10} \varepsilon_{\mathrm{Ch}i} + \sum_{i=7}^{10} \left((1 - \varepsilon_{\mathrm{Ch}i}) \prod_{\substack{j=7 \\ j\neq i}}^{10} \varepsilon_{\mathrm{Ch}j} \right) \tag{6.12}$$

6.4.3 MC parametrization

In order the tracking efficiency estimation in the MC to be reliable, the considered parametric muon generator must be tuned in order to reproduce the reconstructed kinematics of the single muons measured in pp collisions at $\sqrt{s} = 13$ TeV considered in the present analysis. The tuning is performed by means of a recursive procedure, illustrated in figure 6.5, which includes the following steps:

1. Run MC simulations of single muons with given input p_{T} and y distributions;

2. Compute the $(A \times \varepsilon)$ as a function of p_{T} and y;

3. Use the $(A \times \varepsilon)$ to correct the reconstructed muon distributions from data;

4. Compute the ratio, as a function of both p_{T} and y, between the corrected data distribution and the kinematic distributions considered for the MC input . Should this ratio be compatible with one, convergence is reached and the procedure is stopped;

5. Inject the corrected p_{T} and y data distributions as the new input for MC simulation;

until step 4 is equal to one.

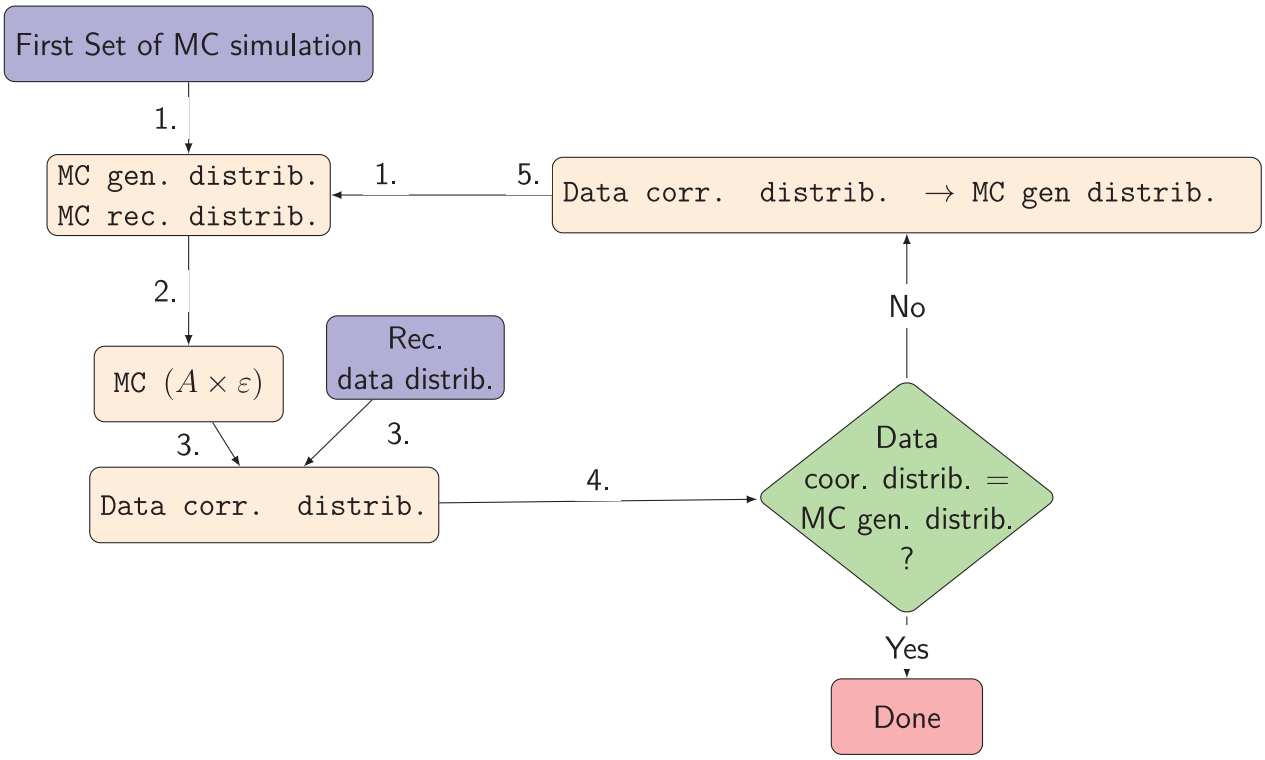

Figure 6.5: Illustration of the data driven method used to tune the input distribution of single muon

6.4.4 Results

Tracking efficiency estimations from the data and from the tuned MC simulation are shown in figure 6.6 as a function of p_T, y, the azimuthal angle φ and the run number. A 2% systematic uncertainty is observed in average for single muon, from the comparison between data and MC. For the dimuon signals, the systematic uncertainty on the tracking efficiency is estimated to be twice the systematics on the single muons: in this case, this results in a 4% systematic uncertainty, independent of p_T and y.

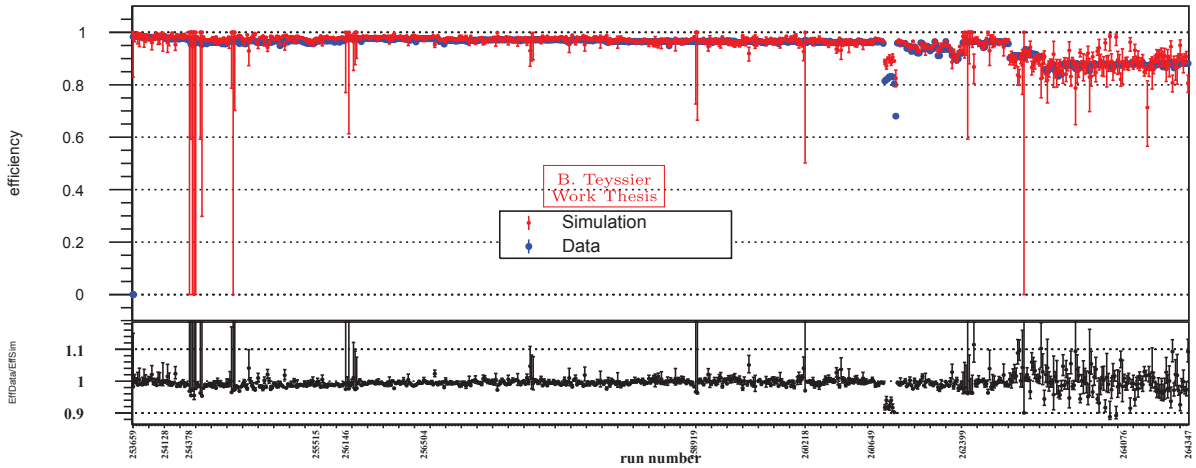

Figure 6.6: Tracking efficiency measured in data and in the tuned MC simulation, as a function of run number.

6.5 Summary of Systematic Uncertainty

In table 6.3 are summarized the various sources of systematic uncertainties discussed in this chapter. For each of these sources, and each signal of interest for this analysis, we report the value of the systematic uncertainty; when the uncertainty values depend on the p_T or the y interval, their maximum and minimum values are quoted.

Syst. source	η	ω	ϕ
Signal extraction	1 - 22 %	2 - 12 %	1 - 15.7 %
MC input	5 %	5.5 %	1 %
Trigger efficiency	1 - 31 %	1 - 24 %	1 - 25 %
Branching ratio	13 %	2 %	1 %
Tracking efficiency	4 %		
Luminosity	5 %		

Table 6.3: Summary of the systematic uncertainty sources contributing to the measurement of the η, ρ/ω and ϕ meson cross-section.

Chapter 7

Light Neutral Meson Production

Summary

This chapter describes the steps followed to convert the reconstructed signal into cross-section for the η, ρ/ω and ϕ mesons. The p_{T} dependence of the production cross-section is extracted in six y intervals, and compared to the predictions of the available models. In the case of the ϕ and ρ/ω mesons, the p_{T} dependence of the rapidity-integrated cross-section is also derived, allowing for the comparison with the results from existing measurements in pp collisions in the same rapidity range.

7.1 Estimation of the Number of Generated Mesons

The very first step after signal extraction consists in correcting the number of reconstructed dimuons for the $A \times \varepsilon$ evaluated with the MC simulations discussed in section 4.1. In the case of the two-body decays $\rho/\omega \to \mu^+\mu^-$ and $\phi \to \mu^+\mu^-$, the information on the dimuons can be directly converted into the corresponding information on the parent mesons by correcting for the branching ratios of the involved decays. In the case of the Dalitz decay $\eta \to \mu^+\mu^-\gamma$, an additional step is required, to convert the dimuon kinematics to the η meson one, before correcting for the branching ratio.

7.1.1 The Two-Body Decay Case

As far as the two-body decays of the ρ/ω and ϕ mesons are concerned, the corrected number of mesons ($N_{\rho/\omega}$ and N_{ϕ}, respectively) corresponding to the reconstructed dimuons $N^{\mathrm{rec}}_{\mu\mu}$ is given, for each p_{T}-y interval considered in this analysis, by the following formula:

$$N_{\rho/\omega,\,\phi}(p_{\mathrm{T}}, y) = \frac{N^{\mathrm{rec}}_{\mu\mu}(p_{\mathrm{T}}, y)}{[A \times \varepsilon]_{\mu\mu}(p_{\mathrm{T}}, y) \cdot BR \cdot \Delta p_{\mathrm{T}} \cdot \Delta y}, \tag{7.1}$$

where $[A \times \varepsilon]_{\mu\mu}(p_T, y)$ is the product of the acceptance and the dimuon reconstruction efficiency evaluated in the specific p_T-y cell, BR is the branching ratio of the considered decay channel (see table 4.3), and $\Delta p_T \cdot \Delta y$ are the widths of the p_T-y cell. For the estimation relative to the ρ/ω mesons, $N^{rec}_{\mu\mu}(p_T, y)$, $[A \times \varepsilon]_{\mu\mu}(p_T, y)$ and the BR are referred to the $\omega \to \mu^+\mu^-$ decay.

7.1.2 The Dalitz Decay Case

When dealing with the Dalitz decay of the η, we start by correcting the number of reconstructed dimuons for the $A \times \varepsilon$ and the widths of the considered p_T-y cell:

$$N^{gen}_{\mu\mu}(p_T, y) = \frac{N^{rec}_{\mu\mu}(p_T, y)}{[A \times \varepsilon]_{\mu\mu}(p_T, y) \cdot \Delta p_T \cdot \Delta y}. \tag{7.2}$$

Contrary to the two-body case, the corrected kinematics distribution of the dimuon does not coincide with the one of the parent meson, due to the Dalitz decay kinematics implying a third body.

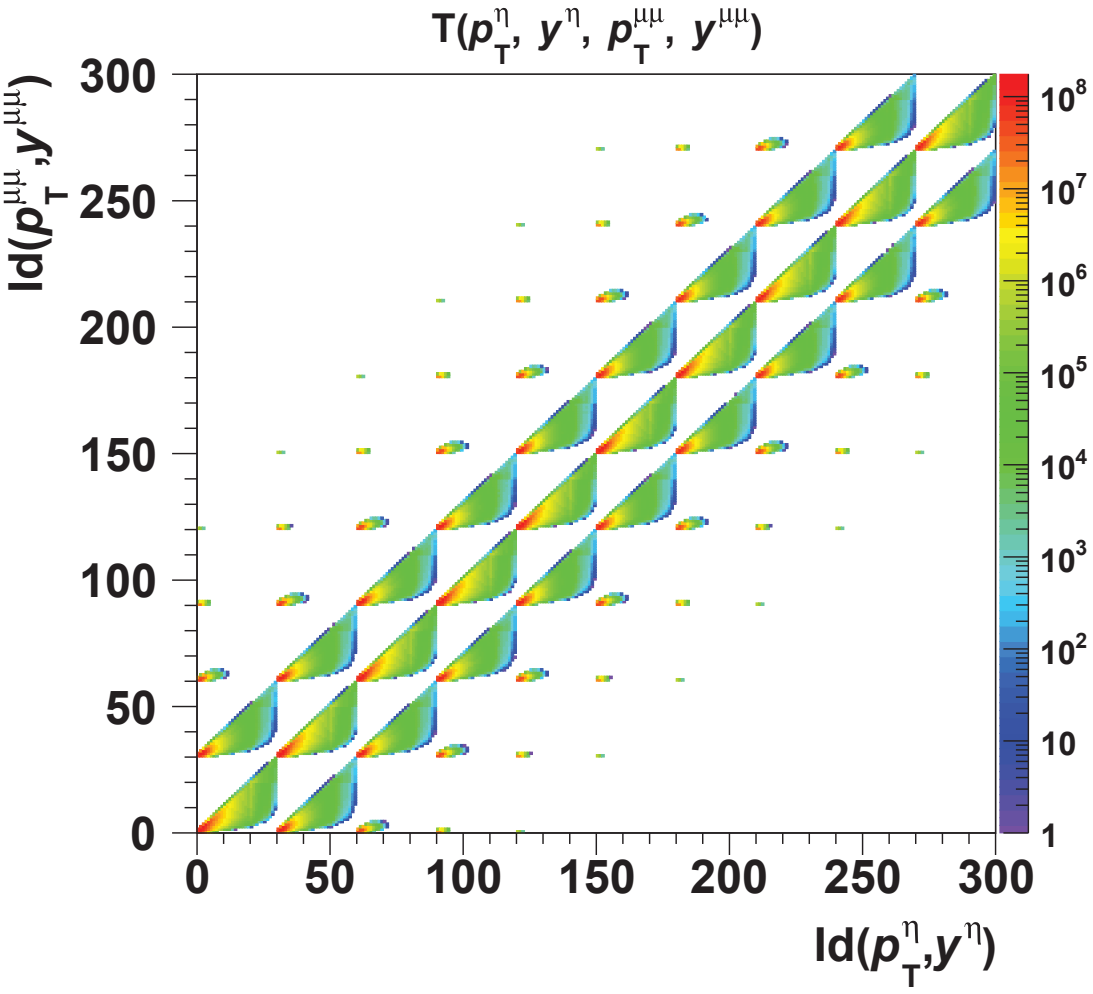

Figure 7.1: Correlation matrix $T(p_T^\eta, y^\eta; p_T^{\mu\mu}, y^{\mu\mu})$ represented in cell coordinates.

So, to obtain the correct kinematic distributions of the parent η meson, an additional transformation is needed:

$$N_{\eta\to\mu\mu\gamma}(p_T, y) = T^{-1} \cdot N^{gen}_{\mu\mu}(p_T, y) \ , \tag{7.3}$$

where T^{-1} is the inverse of the matrix encoding the correlation between the kinematics of the parent η meson and the one of the dimuon, both expressed in terms of p_T and y. The $T(p_T^\eta, y^\eta; p_T^{\mu\mu}, y^{\mu\mu})$ is shown in figure 7.1: each $T(p_T^\eta, y^\eta; p_T^{\mu\mu}, y^{\mu\mu})$ element of the matrix is defined as the probability of an η meson with a given (p_T^η, y^η) kinematics to produce a dimuon with a given $(p_T^{\mu\mu}, y^{\mu\mu})$ kinematics, so that one can write:

$$N^{gen}_{\mu\mu}(p_T, y) = T \cdot N_{\eta\to\mu\mu\gamma}(p_T, y) \tag{7.4}$$

from which equation (7.3) is derived. The row-column indexes of the elements of the Tmatrix identify a specific p_T^η, y^η and $p_T^{\mu\mu}, y^{\mu\mu}$ cell, respectively. In this specific analysis, the phase space limits considered for both the η and the dimuon are $2.0 < y < 4.5$ and $0.0 < p_T < 15.0\,\mathrm{GeV}/c$: in this way, any possible edge effect affecting the numerical problem will have a limited impact on the phase space covered by the available data.

Once the correction expressed by equation (7.3) is performed, the resulting kinematic distribution is further scaled for the $\eta \to \mu^+\mu^-\gamma$ branching ratio, in order to obtain the correct normalization for the $N_\eta(p_T, y)$ distribution.

7.2 Cross-Section Production for Light Neutral Mesons

The $N_{\eta,\rho/\omega,\phi}(p_T, y)$ distributions obtained after correcting for the $A \times \varepsilon$ and the branching ratio (and for the meson-dimuon kinematic correlation in the case of the η) must be further normalized to the integrated luminosity L_{int} corresponding to the analyzed data sample (the evaluation of the integrated luminosity is discussed in section 3.2). This normalization allows one to obtain the cross-section for the three mesons:

$$\frac{d^2\sigma(p_T, y)}{dp_T dy} = N_{\eta,\rho/\omega,\phi}(p_T, y) \times \frac{1}{L_{int}}. \tag{7.5}$$

7.2.1 Double-Differential η Meson Production

In figure 7.2 the p_T distributions of the dimuon coming from the $\eta \to \mu^+\mu^-\gamma$ decay are shown, for the six y interval considered in this analysis. These distributions represent the $N^{gen}_{\mu\mu}(p_T, y)$ input from which the kinematic distribution of the parent meson can be extracted via equation (7.3). The implementation in the current analysis of the kinematic correction based on equation (7.3) is, however, still under way: for this reason, no result on the η meson cross-section is shown in the rest of the chapter.

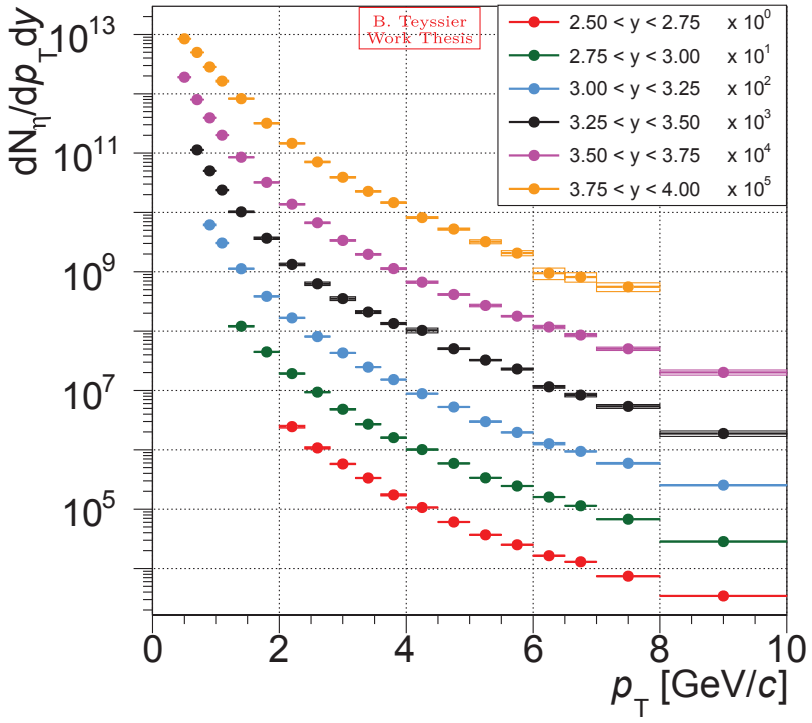

Figure 7.2: Comparison of the p_{T} distribution of η dimuon generated as a function of y.

7.2.2 ρ/ω Meson Production

For the ρ/ω mesons, the double-differential p_{T}-y production cross-section has been evaluated in the available phase space: the results are shown in figure 7.3 as a function of p_{T} in six y intervals. For each y interval, the measured cross-section has been compared to the predictions of PYTHIA8-Monash2013 [95] and PHOJET. The comparison is shown in the panels of figure 7.4: the two models systematically overestimate by a factor ~ 2 the data in the full accessible p_{T} range for each of the considered y intervals.

In figure 7.5 the y dependence of the production cross-section is shown, integrated over the p_{T} range $2.0 < p_{\mathrm{T}} < 6.5$ GeV/c common to the considered y intervals. The comparison with the predictions from PYTHIA8-Monash2013 and PHOJET confirms that the models overestimate the data by a factor ~ 2. Besides the global overestimation, the PHOJET prediction seems to provide a better description than PYTHIA8-Monash2013 of the y dependence of the data.

The ρ/ω production cross-section was also measured in ALICE in pp collisions at $\sqrt{s} = 7$ TeV, integrated over $2.5 < y < 4.0$, as a function of p_{T} in the $1.0 < p_{\mathrm{T}} < 5.0$ GeV/c range. In order to compare our data to the ones at $\sqrt{s} = 7$ TeV, the production cross-section measured in this analysis has been integrated over the full accessible $2.5 < y < 4.0$ range. As it can be seen from figure 7.3, the integration over $2.5 < y < 4.0$ was possible limited to the $2.0 < p_{\mathrm{T}} < 6.5$ GeV/c range. The comparison between the two energies shows that the 13 TeV cross-section is larger than the 7 TeV one by a factor ~ 2 see figure 7.6.

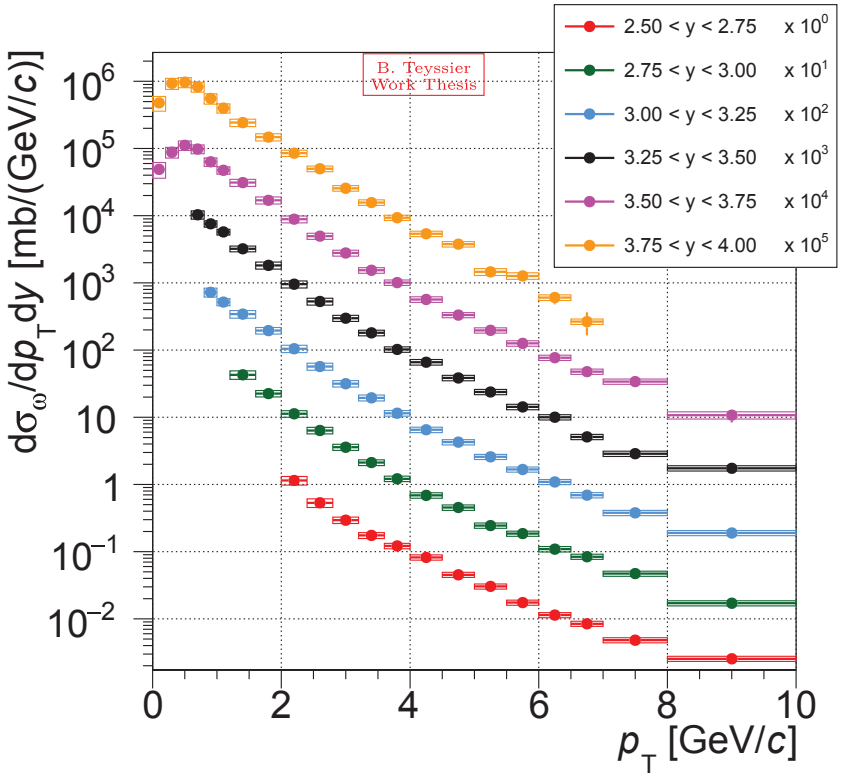

Figure 7.3: Comparison of the p_{T} distribution of ω meson as a function of y.

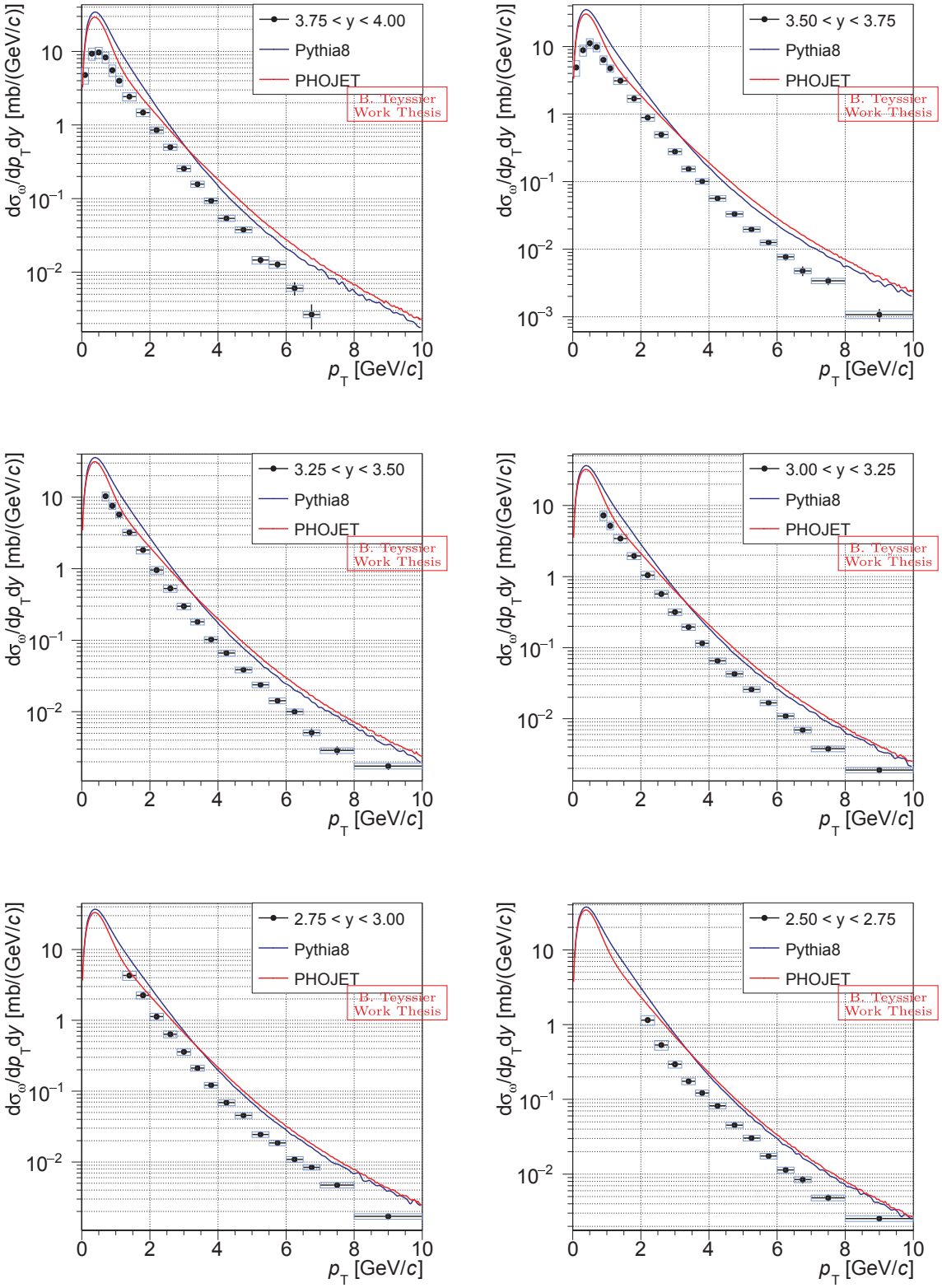

Figure 7.4: p_{T} distributions of ω meson for various y intervals.

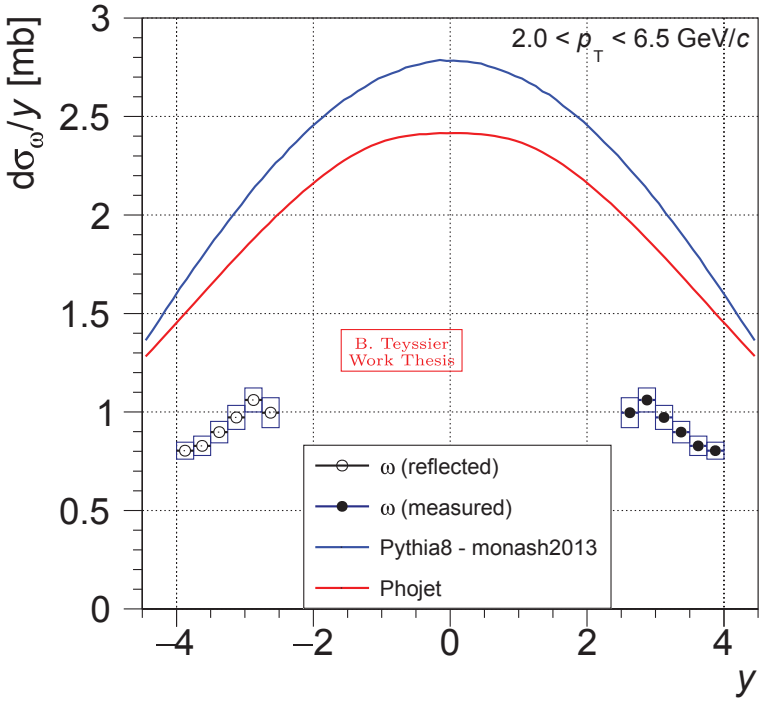

Figure 7.5: y distribution of ω meson integrated in $2.0 < p_{\mathrm{T}} < 6.5$ GeV/c.

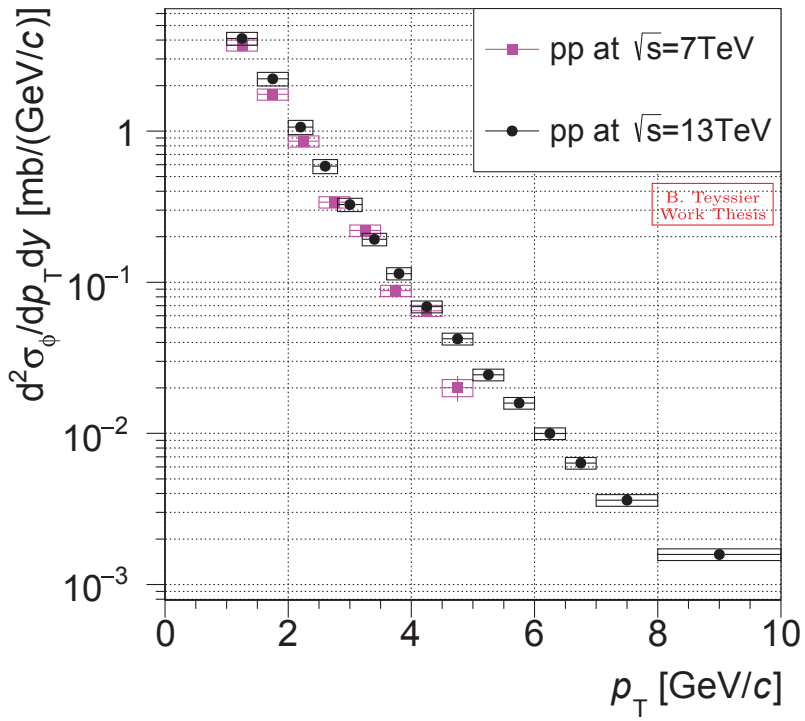

Figure 7.6: p_{T} distribution of ω meson integrated in y and comparison with measurements at 7 TeV [43].

7.2.3 Double-Differential ϕ Meson Production

As for the ρ/ω mesons, the double-differential p_{T}-y production cross-section has been evaluated for the ϕ meson, too, in the available phase space: the results are shown in figure 7.7 as a function of p_{T} in the y intervals considered in the analysis, extended at mid-rapidity with the $\phi \to \mathrm{K}^{+}\mathrm{K}^{-}$ measurements [96]. The comparison of the data with the predictions of the PYTHIA8-Monash2013 and PHOJET models is shown, for each y interval considered in the analysis in the panels of figure 7.8: contrary to what observed for the ω meson, the PYTHIA8-Monash2013 prediction provides a good description of the data. The PHOJET prediction, on the contrary, still slightly fails in estimating the normalization and the shape of the p_{T} dependence of the production cross-section.

The y dependence of the production cross-section is shown in figure 7.9, integrated over the p_{T} range $2.0 < p_{\mathrm{T}} < 6.5$ GeV/c common to the considered y intervals. As one can see, the data points sit between the predictions from PYTHIA8-Monash2013 and PHOJET, which both slightly fail in describing the shape of the y dependence. The results for the ϕ meson production in the dikaon channel provide an additional point at mid-rapidity which could be compared to the forward measurements presented here.

Results for the ϕ meson production cross-section are also available from ALICE measurements in pp collisions at $\sqrt{s} = 2.76$, 5.02, 7 and 8 TeV, integrated over $2.5 < y < 4.0$, as a function of p_{T}, in various p_{T} ranges. In order to compare our data to the ones at lower energies, the ϕ meson production cross-section measured in this analysis has been integrated over the full accessible $2.5 < y < 4.0$ range. As it can be seen from figure 7.7, this integration was possible limited to the $2.0 < p_{\mathrm{T}} < 6.5$ GeV/c range. As expected, the cross-section at 13 TeV is found to be larger than the measurements at lower energies.

The energy dependence of the ϕ meson production cross-section has been studied integrating the present measurement over the y and p_{T} ranges $2.5 < y < 4.0$ and $1.5 < p_{\mathrm{T}} < 5.0$ GeV/c common to the data at the various available energies. The results are shown in figure 7.11, compared with the PYTHIA8-Monash2013 and PHOJET prediction: the trend as a function of $\sqrt{s}$ is found to be approximately linear in the considered energy range, with the PHOJET model in good agreement with the data and the PYTHIA8-Monash2013 prediction systematically underestimating the results. The analysis strategy at 13 TeV is being slightly revised in order to reduce the systematic uncertainty associated to the integrated cross-section by optimizing the integration procedure, namely integrating over the rapidity before signal extraction.

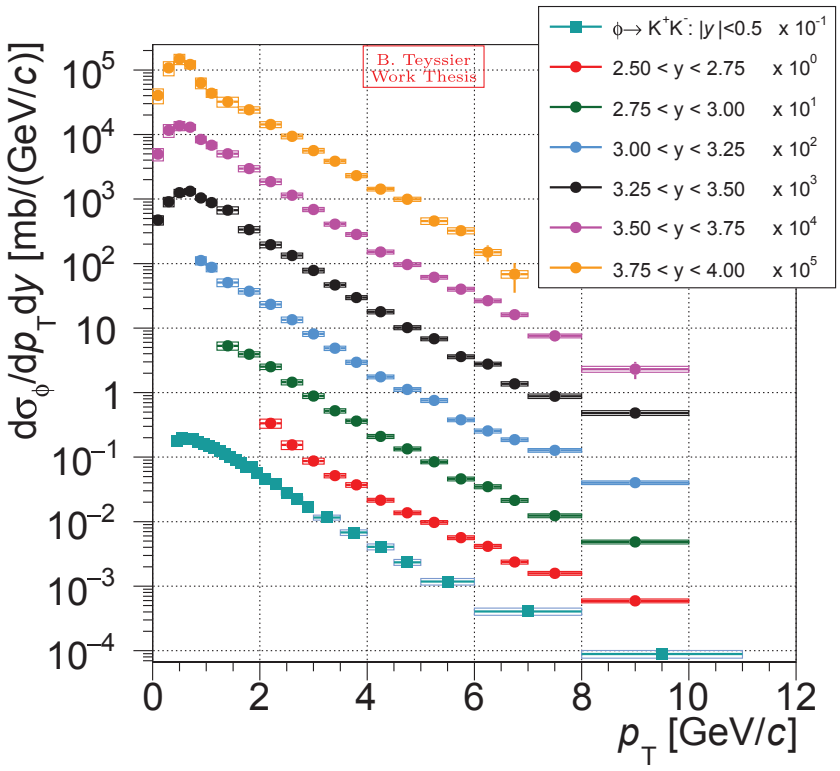

Figure 7.7: Comparison of the p_{T} distribution of ϕ meson as a function of y extended at mid-rapidity by the $\phi \rightarrow \mathrm{K}^{+}\mathrm{K}^{-}$ measurements [96].

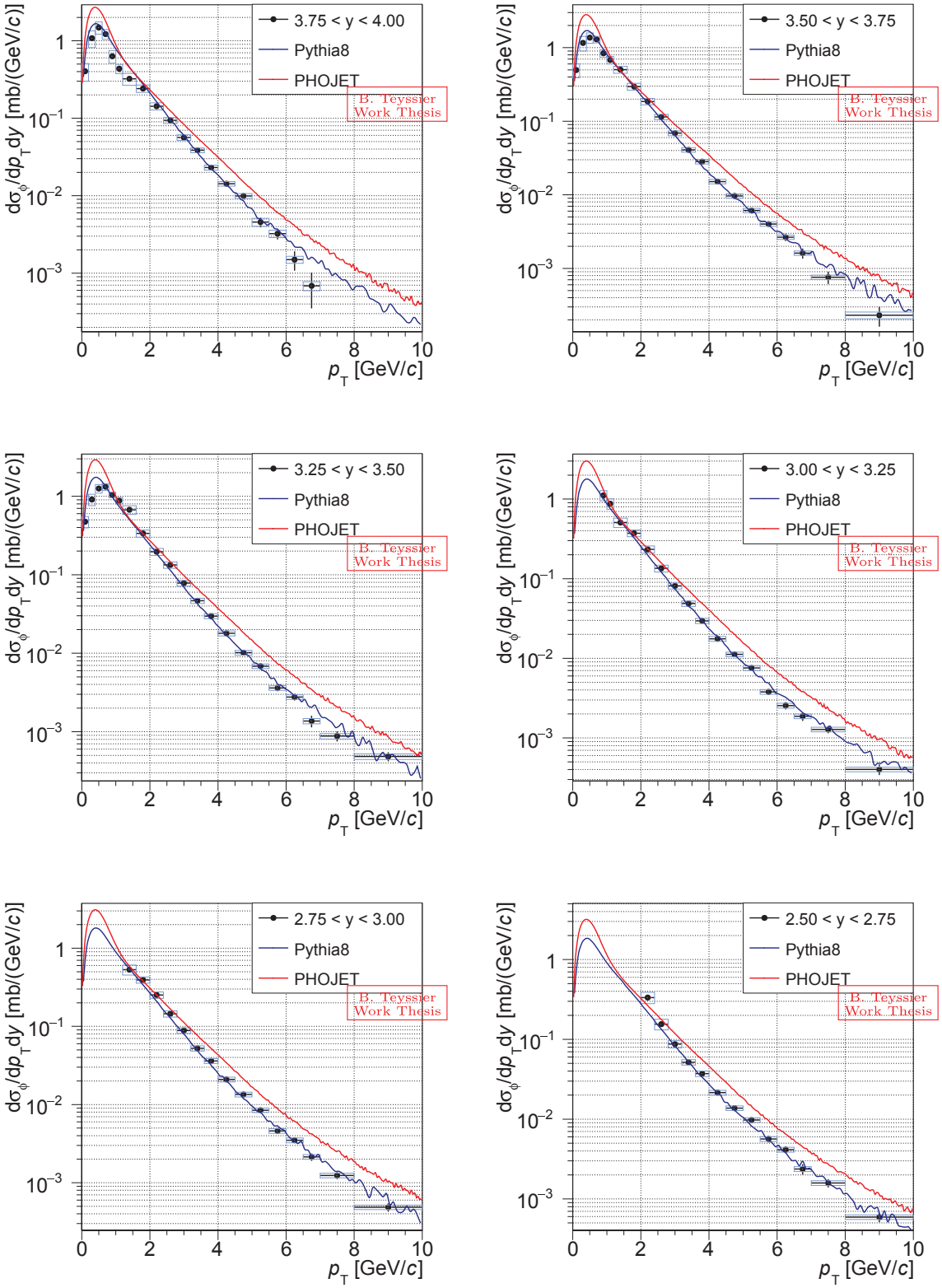

Figure 7.8: p_{T} distribution of ϕ meson for various y intervals.

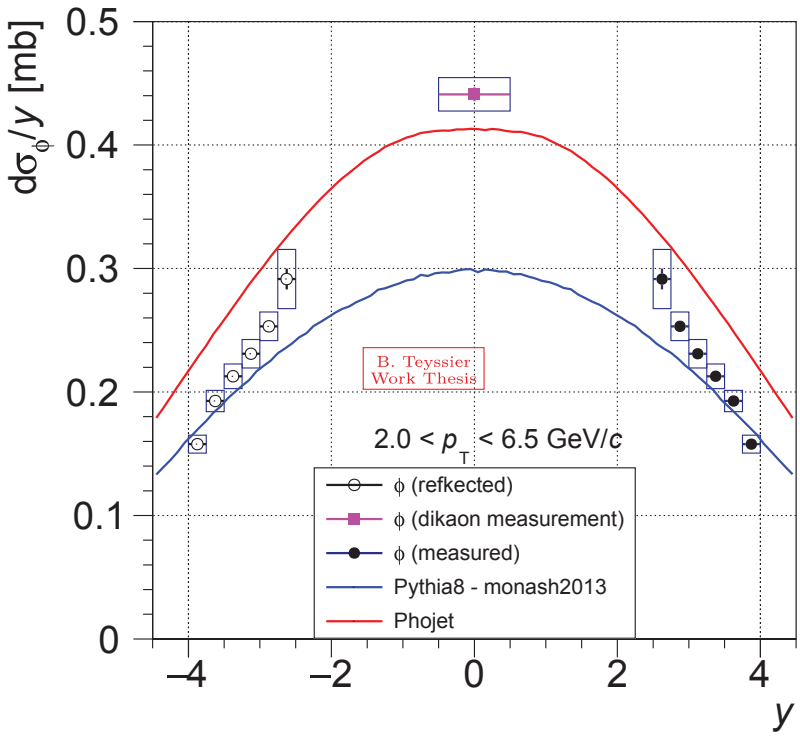

Figure 7.9: y distribution of ϕ meson integrated in $2.0 < p_{\mathrm{T}} < 6.5$ GeV/c, extended at mid-rapidity by the $\phi \to \mathrm{K}^{+}\mathrm{K}^{-}$ measurements [96].

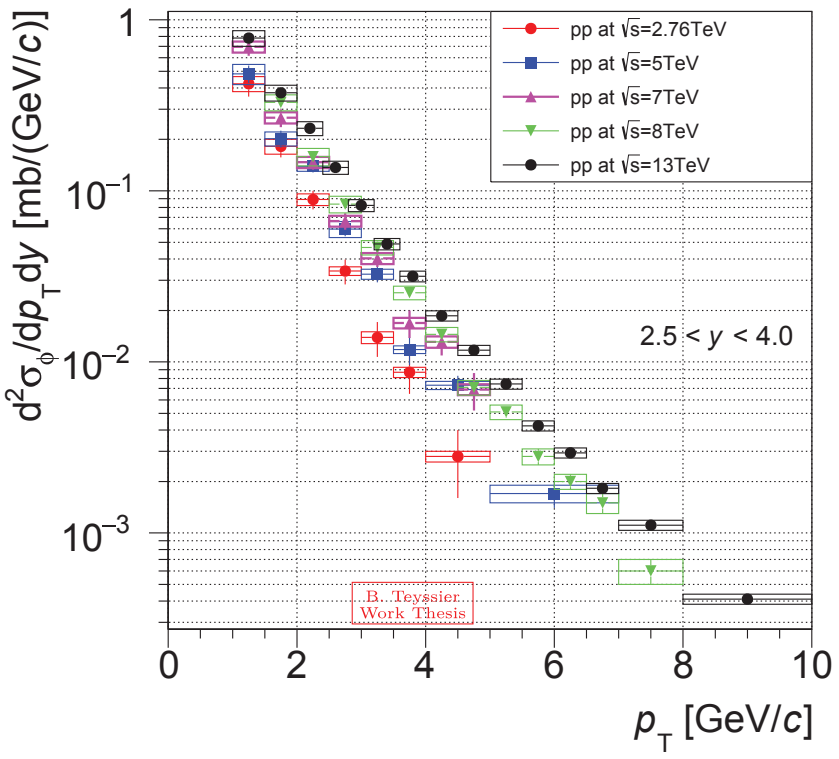

Figure 7.10: ϕ meson p_{T} distribution, integrated over $2.5 < y < 4.0$, in pp collisions at $\sqrt{s} = 13$ TeV (this analysis), compared to previous measurements at lower energies.

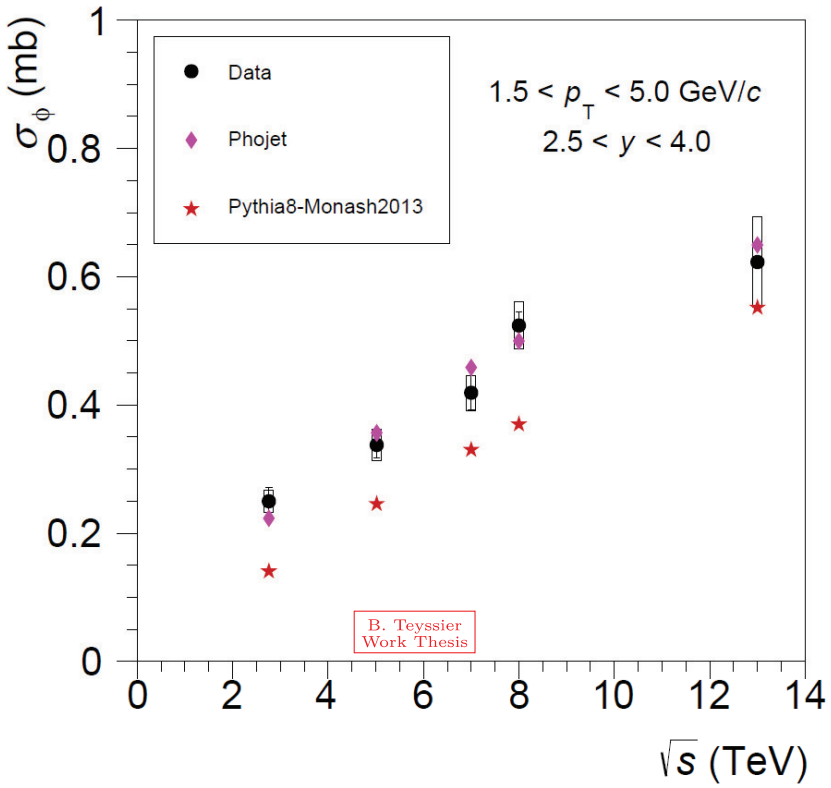

Figure 7.11: Energy dependence of the ϕ meson production cross-section in $2.5 < y < 4.0$ and $1.5 < p_{\mathrm{T}} < 5.0$ GeV/c.

Conclusions and Perspectives

This work focused on the study of the production cross-section of the η, ρ/ω and ϕ mesons. This study has been achieved by performing a double-differential p_{T}-y analysis in the phase space available for each meson. Results have been compared to the available theoretical predictions from the PYTHIA8 and PHOJET models: this comparison resulted in a better data/model agreement for the ϕ meson than for the ρ/ω meson. Moreover, existing results at several, lower collision energies in the same y interval allowed to investigate the energy evolution of the production cross-section for the ϕ meson and, limited to the comparison with the $\sqrt{s} = 7$ TeV results, for the ρ/ω mesons. For the ϕ meson, the energy evolution of the production cross-section integrated over $2.5 < y < 4.0$ and $1.5 < p_{\mathrm{T}} < 5.0$ GeV/c was found to be approximately linear, with the PHOJET model in good agreement with the data and the PYTHIA8-Monash2013 prediction systematically underestimating the results. In a next future, the results for the ϕ meson from the present analysis could also be compared to the mid-rapidity measurement performed in ALICE in the dikaon channel.

The present analysis did not exploit the full potential of the large data sample available in pp collisions at $\sqrt{s} = 13$ TeV, which could possibly profit from the combination of the 2016 and 2017 data taking. Among the measurements which could still be performed, based on the analysis of the low-mass dimuon region, one can cite:

- the study of the multiplicity dependence of the light-neutral meson production;
- the search for strangeness enhancement, collective phenomena and azimuthal anisotropies in light-neutral meson production in high-multiplicity pp events;
- the study of the light-neutral meson polarization.

Finally, beyond the standard dimuon analyses, the large pp data sample at $\sqrt{s} = 13$ TeV could also be exploited for the search of the first evidence of the $\eta \to 2\mu^+2\mu^-$ decay, for which only an upper limit is currently available from literature [4]. The proximity of the η meson mass to the $4m_{\mu}$ threshold makes the observation of this decay particularly challenging and sensitive to the description to the combinatorial background.

Appendix A
List of Runs

000253659	000253680	000253682	000253748	000253751	000253755	000253756	000253757
000253813	000253819	000253825	000253826	000253832	000253834	000253951	000253956
000253957	000253958	000253961	000253978				

Table A.1: Run list for period LHC16f

000254128	000254147	000254148	000254149	000254174	000254175	000254178	000254193
000254199	000254204	000254205	000254293	000254302	000254304	000254331	000254332

Table A.2: Run list for period LHC16g

000254378	000254381	000254394	000254395	000254396	000254419	000254422	000254476
000254479	000254604	000254606	000254608	000254621	000254629	000254630	000254632
000254640	000254644	000254646	000254648	000254649	000254651	000254652	000254653
000254654	000254983	000254984	000255008	000255009	000255010	000255042	000255068
000255071	000255073	000255074	000255075	000255076	000255079	000255082	000255085
000255086	000255091	000255111	000255154	000255159	000255162	000255167	000255171
000255173	000255176	000255177	000255180	000255182	000255240	000255242	000255247
000255248	000255249	000255251	000255252	000255253	000255255	000255256	000255275
000255276	000255280	000255283	000255350	000255351	000255352	000255398	000255402
000255415	000255440	000255442	000255447	000255463	000255465	000255466	000255467
000255469							

Table A.3: Run list for period LHC16h

000255515	000255533	000255534	000255535	000255537	000255538	000255539	000255540
000255542	000255543	000255577	000255583	000255591	000255592	000255614	000255615
000255616	000255617	000255618					

Table A.4: Run list for period LHC16i

000256146	000256147	000256148	000256149	000256156	000256157	000256158	000256161
000256169	000256204	000256207	000256210	000256212	000256213	000256215	000256219
000256222	000256223	000256227	000256228	000256231	000256281	000256282	000256283
000256284	000256287	000256289	000256290	000256292	000256295	000256297	000256298
000256302	000256307	000256311	000256356	000256357	000256361	000256362	000256363
000256364	000256365	000256366	000256368	000256372	000256373	000256415	000256417
000256418	000256420						

Table A.5: Run list for period LHC16j

000256504	000256506	000256510	000256512	000256552	000256554	000256556	000256557
000256560	000256561	000256564	000256565	000256567	000256589	000256591	000256592
000256619	000256620	000256658	000256676	000256677	000256681	000256684	000256691
000256694	000256695	000256697	000256941	000256942	000256944	000257011	000257012
000257021	000257026	000257028	000257071	000257077	000257080	000257082	000257083
000257084	000257086	000257092	000257095	000257224	000257260	000257318	000257320
000257322	000257330	000257358	000257364	000257433	000257457	000257468	000257474
000257487	000257488	000257490	000257491	000257492	000257530	000257531	000257540
000257541	000257560	000257561	000257562	000257563	000257564	000257565	000257566
000257587	000257588	000257590	000257592	000257594	000257595	000257601	000257604
000257605	000257606	000257630	000257632	000257635	000257636	000257642	000257644
000257682	000257684	000257685	000257687	000257688	000257694	000257697	000257724
000257725	000257727	000257733	000257734	000257735	000257737	000257892	000257893
000257901	000257912	000257932	000257936	000257937	000257939	000257957	000257958
000257960	000257963	000257979	000257986	000257989	000258008	000258012	000258014
000258017	000258019	000258039	000258041	000258042	000258045	000258048	000258049
000258059	000258060	000258062	000258063	000258107	000258108	000258109	000258113
000258114	000258117	000258178	000258197	000258202	000258203	000258204	000258256
000258257	000258258	000258270	000258271	000258273	000258274	000258278	000258280
000258299	000258301	000258302	000258303	000258306	000258307	000258332	000258336
000258359	000258387	000258388	~~000258391~~	000258393	000258399	000258426	000258452
000258454	000258456	000258477	000258498	000258499	000258537		

Table A.6: Run list for period LHC16k

000258919	000258920	000258921	000258923	000258931	000258962	000258964	000259086
000259099	000259117	000259118	000259162	000259164	000259204	000259261	000259263
000259264	000259269	000259270	000259271	000259272	000259273	000259274	000259302
000259303	000259305	000259307	000259334	000259339	000259340	000259341	000259342
000259378	000259379	000259381	000259382	000259394	000259395	000259396	000259469
000259471	000259477	000259649	000259650	000259668	000259697	000259700	000259703
000259704	000259705	000259711	000259713	000259750	000259751	000259756	000259788
000259789	000259822	000259841	000259842	000259860	000259866	000259867	000259868
000259888	000259954	000259961	000259979	000260010	000260011	000260014	

Table A.7: Run list for period LHC16l

000260218	000260240	000260310	000260312	000260313	000260338	000260340	000260351
000260354	000260357	000260379	000260411	000260432	000260435	000260437	000260440
000260441	000260447	000260471	000260472	000260475	000260476	000260481	000260482
000260487	000260490	000260495	000260496	000260497	000260537	000260539	000260540
000260541	000260542	000260564	000260586	000260611	000260613	000260614	000260615
000260616	000260647						

Table A.8: Run list for period LHC16m

000260649	000260650	000260657	000260667	000260671	000260672	000260689	000260691
000260693	~~000260695~~	000260700	000260704	000260710	000260713	000260722	000260723
000260727	000260728	000260740	000260741	000260749	000260750	~~000260751~~	~~000260752~~
000260763	000260770	000260777	~~000260782~~	000260784	000260786	000260788	000260804
000260808	000260809	000260810	000260815	000260913	000260914	000260920	000260934
000260935	000260936	000260938	000260960	000260963	000260992	000260993	000261020
000261022	000261025	000261026	000261027	000261052	000261055	000261065	000261076
000261083	000261088	000261093	000261094	000261095	000261099	000261100	

Table A.9: Run list for period LHC16n

000262399	000262418	000262419	000262422	000262423	000262424	000262428	000262430
000262451	000262487	000262492	000262528	000262532	000262533	000262537	000262563
000262567	000262568	000262569	000262570	000262571	000262572	000262574	000262578
000262583	000262593	000262594	000262628	000262632	000262635	000262705	000262706
000262713	000262717	000262719	000262723	000262725	000262727	000262760	000262768
000262776	000262777	000262778	000262841	000262842	000262844	000262847	000262849
000262853	000262855	000262858	000263332	000263487	000263490	000263496	000263497
000263647	000263652	000263653	000263654	000263657	000263662	000263663	000263682
000263689	000263690	000263691	000263737	000263738	000263739	000263741	000263743
000263744	000263784	000263785	000263786	000263787	000263790	000263792	000263793
000263803	000263810	000263813	000263823	000263824	000263829	000263830	000263861
000263863	000263866	000263905	000263916	000263917	000263920	000263923	000263977
000263978	000263979	000263981	000263984	000263985	000264033	000264035	

Table A.10: Run list for period LHC16o

000264076	000264078	000264082	000264085	000264086	000264109	000264110	000264129
000264137	000264138	000264139	000264164	000264168	000264188	000264190	000264194
000264197	000264198	000264232	000264233	000264235	000264238	000264259	000264260
000264261	000264262	000264264	000264265	000264266	000264267	000264273	000264277
000264279	000264281	000264305	000264306	000264312	000264336	000264341	000264345
000264346	000264347						

Table A.11: Run list for period LHC16p

Appendix B

Raw-Background Comparison — figures

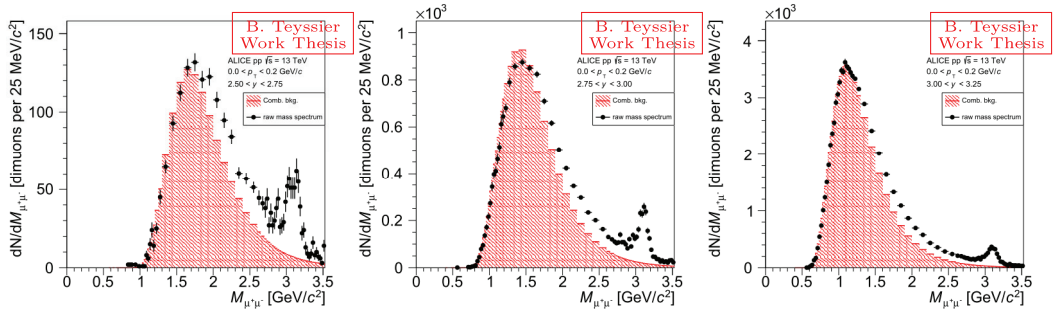

(a) $2.50 < y < 2.75$ (b) $2.75 < y < 3.00$ (c) $3.00 < y < 3.25$

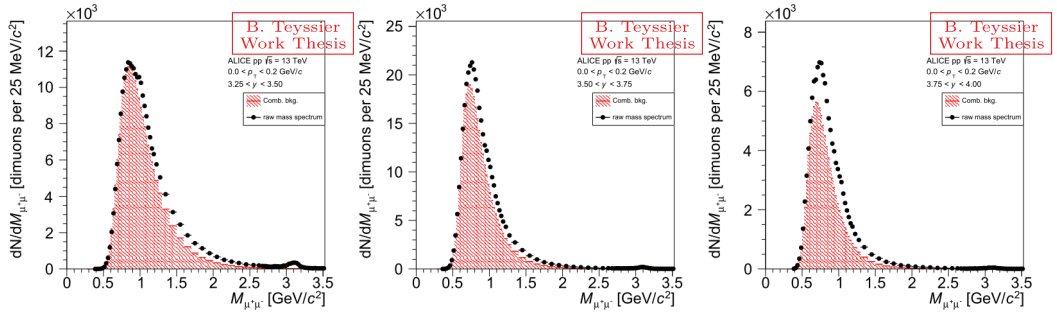

(d) $3.25 < y < 3.50$ (e) $3.50 < y < 3.75$ (f) $3.75 < y < 4.00$

Figure B.1: Evolution of signal and combinatorial background shapes for $0.00 < p_{\mathrm{T}} < 0.20$ GeV/c

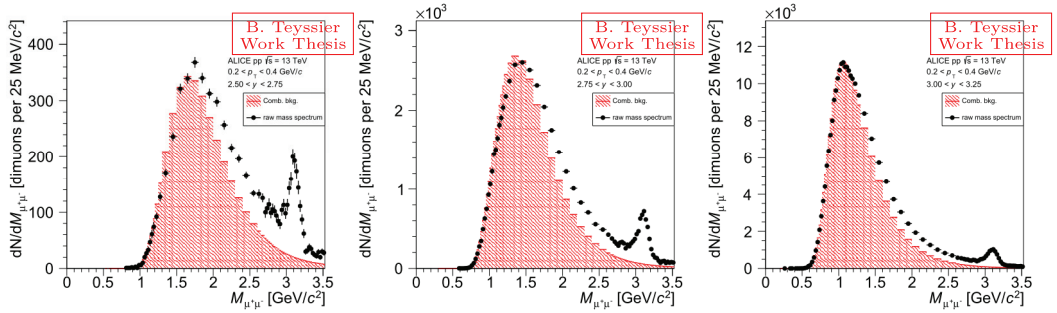

(a) $2.50 < y < 2.75$ (b) $2.75 < y < 3.00$ (c) $3.00 < y < 3.25$

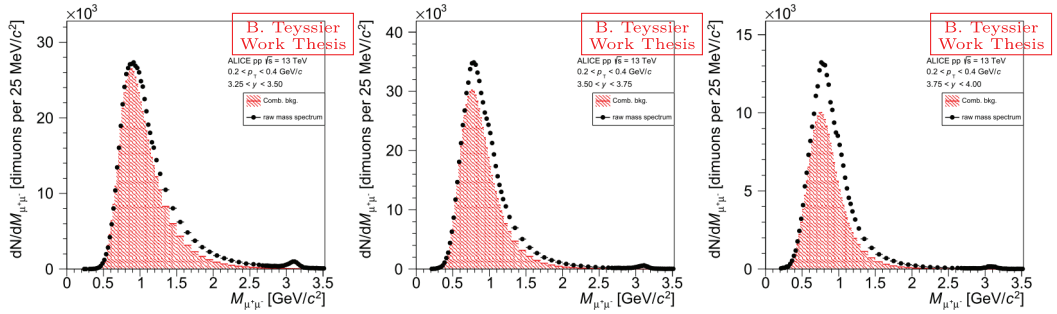

(d) $3.25 < y < 3.50$ (e) $3.50 < y < 3.75$ (f) $3.75 < y < 4.00$

Figure B.2: Evolution of signal and combinatorial background shapes for $0.20 < p_{\mathrm{T}} < 0.40$ GeV/c

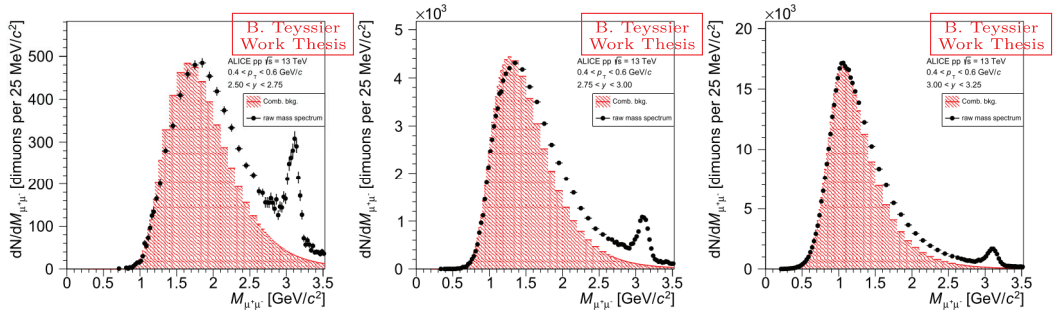

(a) $2.50 < y < 2.75$ (b) $2.75 < y < 3.00$ (c) $3.00 < y < 3.25$

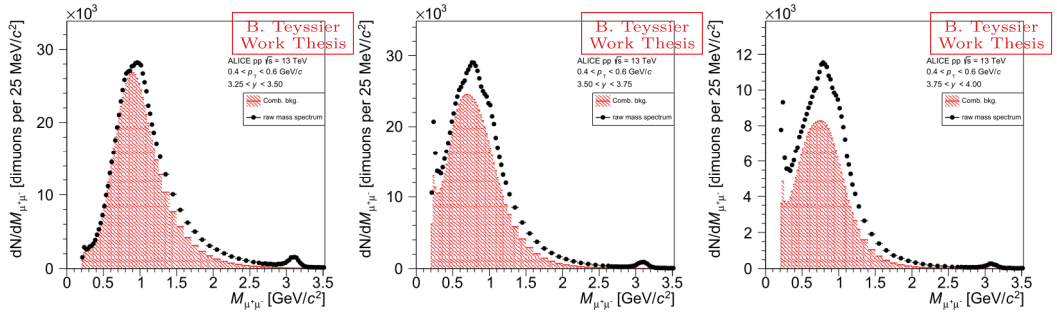

(d) $3.25 < y < 3.50$ (e) $3.50 < y < 3.75$ (f) $3.75 < y < 4.00$

Figure B.3: Evolution of signal and combinatorial background shapes for $0.40 < p_{\mathrm{T}} < 0.60$ GeV/c

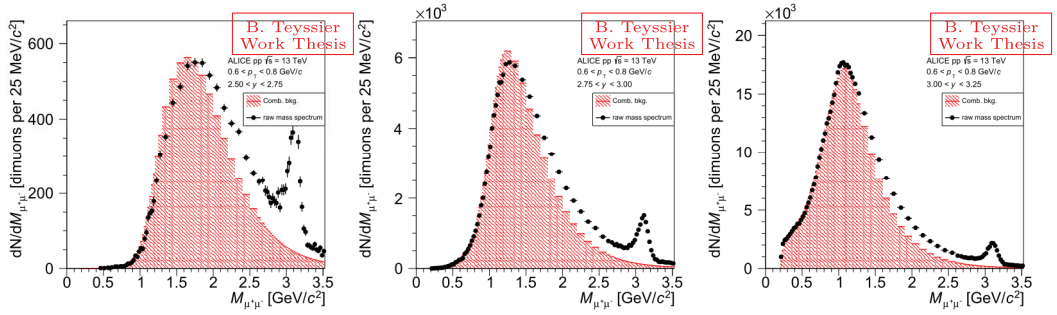

(a) $2.50 < y < 2.75$ (b) $2.75 < y < 3.00$ (c) $3.00 < y < 3.25$

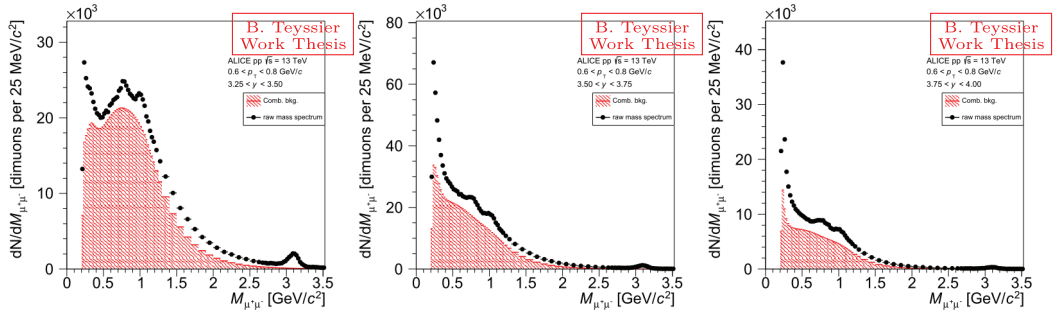

(d) $3.25 < y < 3.50$ (e) $3.50 < y < 3.75$ (f) $3.75 < y < 4.00$

Figure B.4: Evolution of signal and combinatorial background shapes for $0.60 < p_{\mathrm{T}} < 0.80$ GeV/c

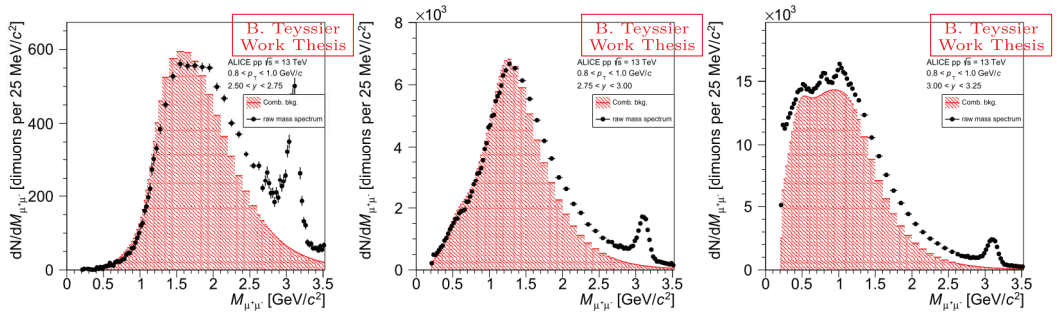

(a) $2.50 < y < 2.75$ (b) $2.75 < y < 3.00$ (c) $3.00 < y < 3.25$

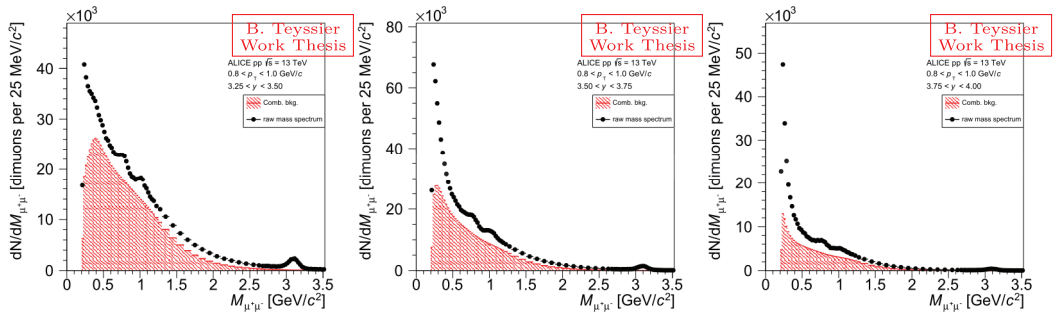

(d) $3.25 < y < 3.50$ (e) $3.50 < y < 3.75$ (f) $3.75 < y < 4.00$

Figure B.5: Evolution of signal and combinatorial background shapes for $0.80 < p_{\mathrm{T}} < 1.00$ GeV/c

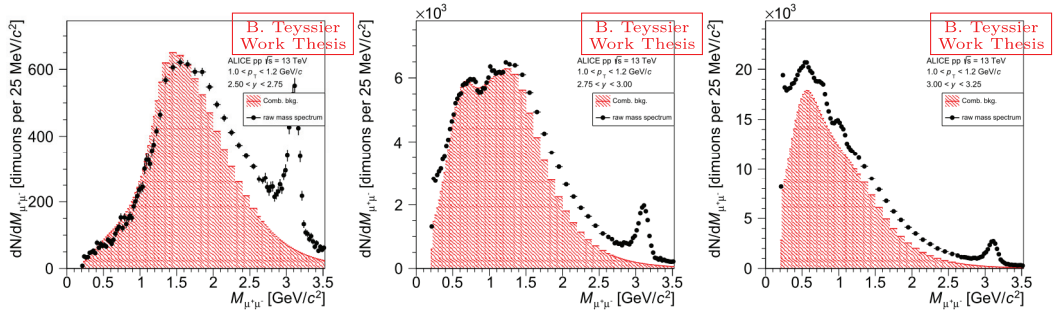

(a) $2.50 < y < 2.75$

(b) $2.75 < y < 3.00$

(c) $3.00 < y < 3.25$

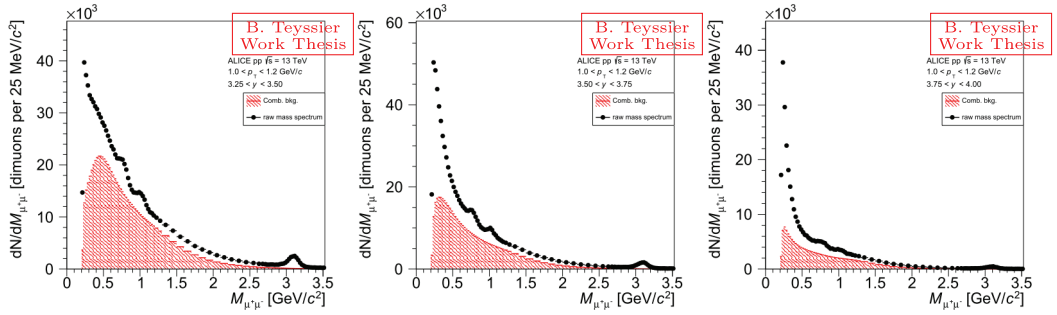

(d) $3.25 < y < 3.50$

(e) $3.50 < y < 3.75$

(f) $3.75 < y < 4.00$

Figure B.6: Evolution of signal and combinatorial background shapes for $1.00 < p_{\mathrm{T}} < 1.20$ GeV/c

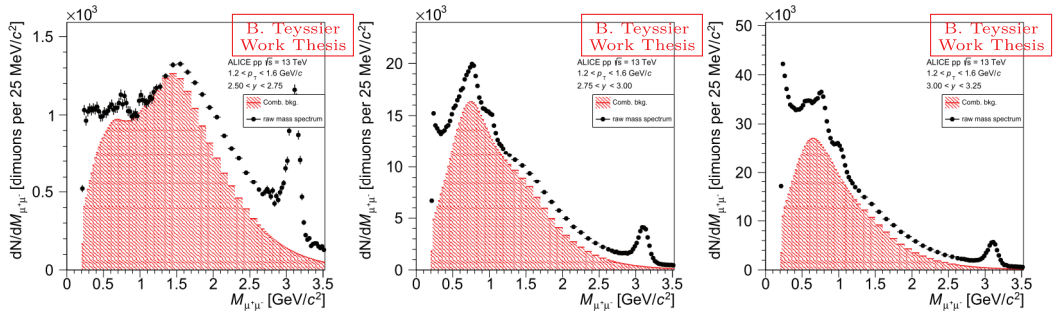

(a) $2.50 < y < 2.75$

(b) $2.75 < y < 3.00$

(c) $3.00 < y < 3.25$

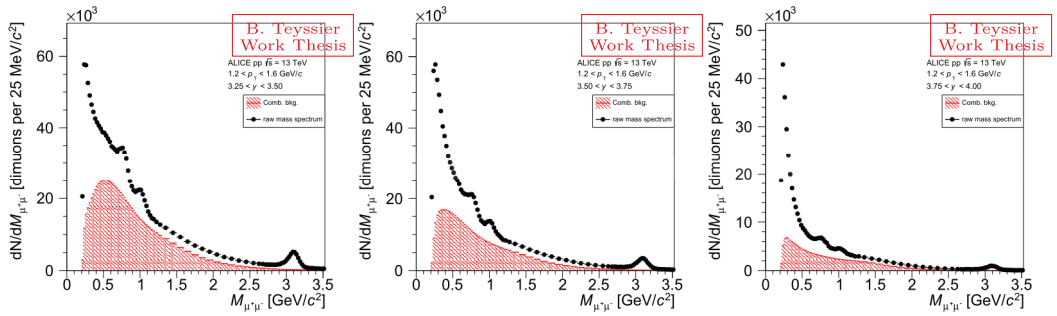

(d) $3.25 < y < 3.50$

(e) $3.50 < y < 3.75$

(f) $3.75 < y < 4.00$

Figure B.7: Evolution of signal and combinatorial background shapes for $1.20 < p_{\mathrm{T}} < 1.60$ GeV/c

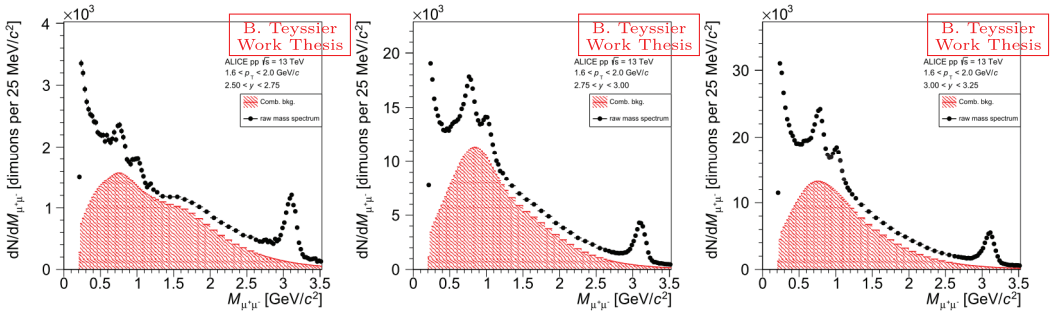

(a) $2.50 < y < 2.75$ (b) $2.75 < y < 3.00$ (c) $3.00 < y < 3.25$

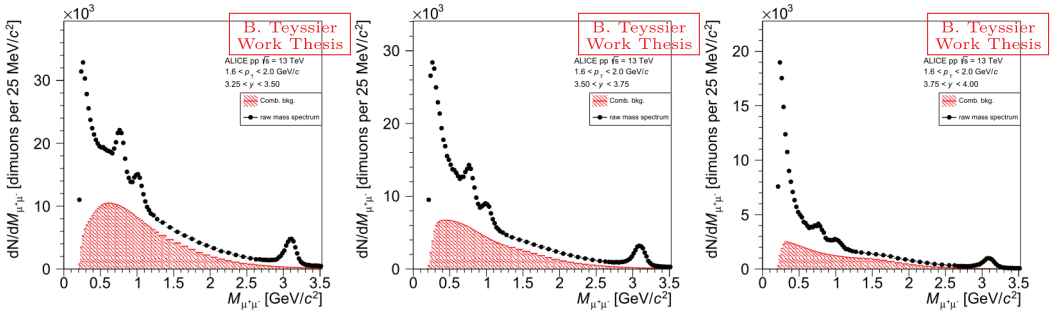

(d) $3.25 < y < 3.50$ (e) $3.50 < y < 3.75$ (f) $3.75 < y < 4.00$

Figure B.8: Evolution of signal and combinatorial background shapes for $1.60 < p_{\mathrm{T}} < 2.00$ GeV/c

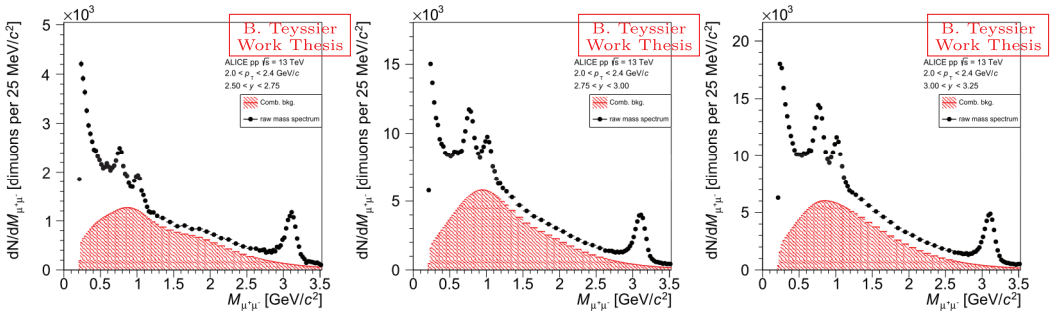

(a) $2.50 < y < 2.75$ (b) $2.75 < y < 3.00$ (c) $3.00 < y < 3.25$

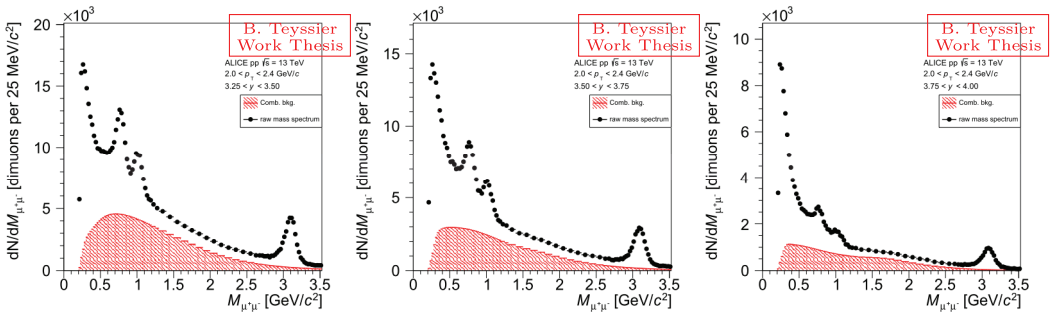

(d) $3.25 < y < 3.50$ (e) $3.50 < y < 3.75$ (f) $3.75 < y < 4.00$

Figure B.9: Evolution of signal and combinatorial background shapes for $2.00 < p_{\mathrm{T}} < 2.40$ GeV/c

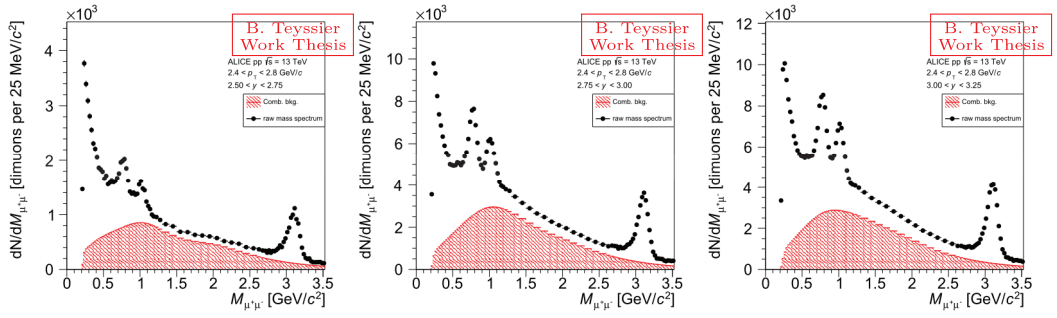

(a) $2.50 < y < 2.75$

(b) $2.75 < y < 3.00$

(c) $3.00 < y < 3.25$

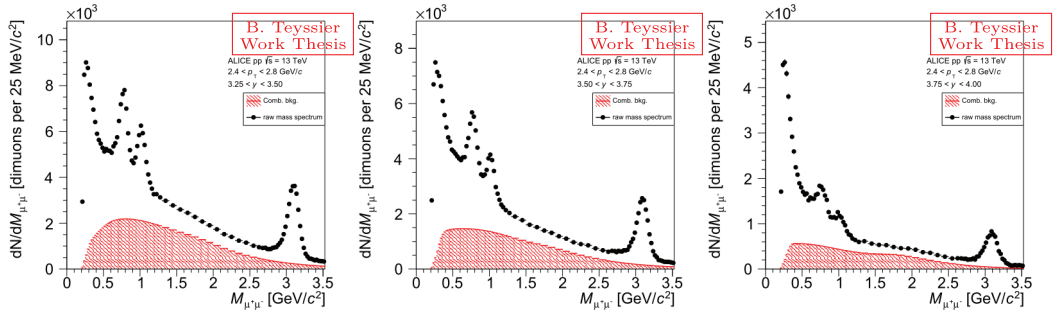

(d) $3.25 < y < 3.50$

(e) $3.50 < y < 3.75$

(f) $3.75 < y < 4.00$

Figure B.10: Evolution of signal and combinatorial background shapes for $2.40 < p_{\mathrm{T}} < 2.80$ GeV/c

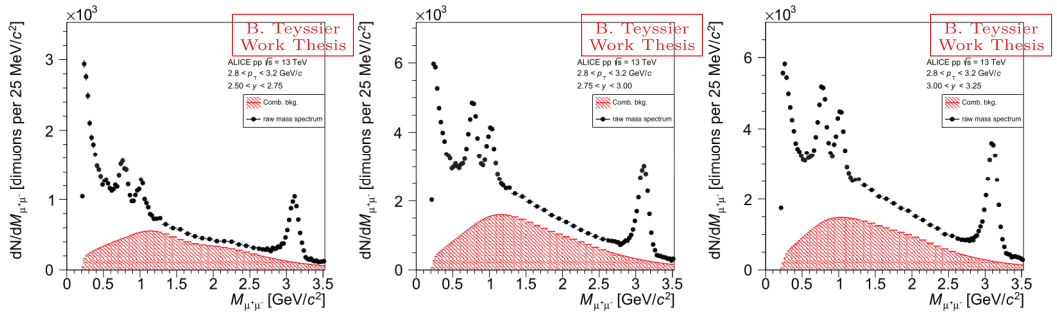

(a) $2.50 < y < 2.75$

(b) $2.75 < y < 3.00$

(c) $3.00 < y < 3.25$

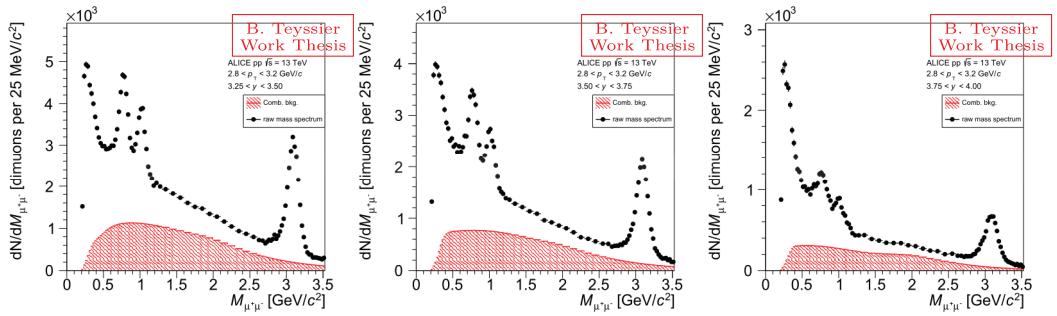

(d) $3.25 < y < 3.50$

(e) $3.50 < y < 3.75$

(f) $3.75 < y < 4.00$

Figure B.11: Evolution of signal and combinatorial background shapes for $2.80 < p_{\mathrm{T}} < 3.20$ GeV/c

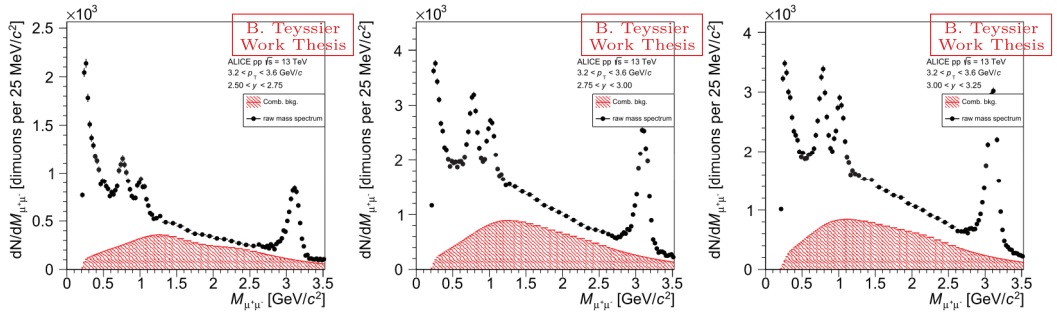

(a) $2.50 < y < 2.75$ (b) $2.75 < y < 3.00$ (c) $3.00 < y < 3.25$

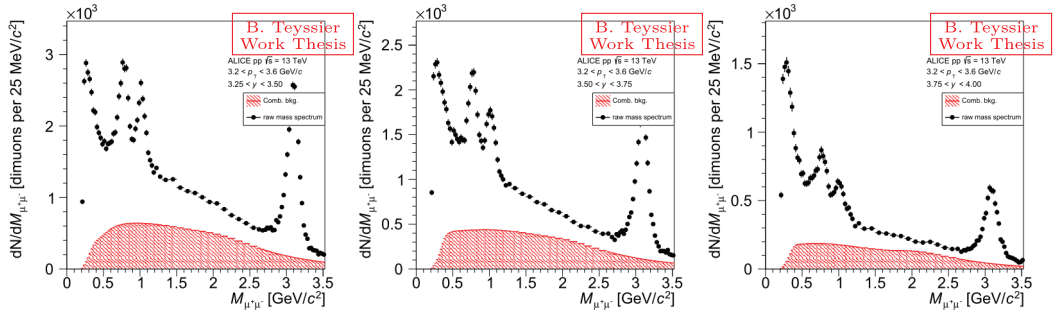

(d) $3.25 < y < 3.50$ (e) $3.50 < y < 3.75$ (f) $3.75 < y < 4.00$

Figure B.12: Evolution of signal and combinatorial background shapes for $3.20 < p_{\mathrm{T}} < 3.60$ GeV/c

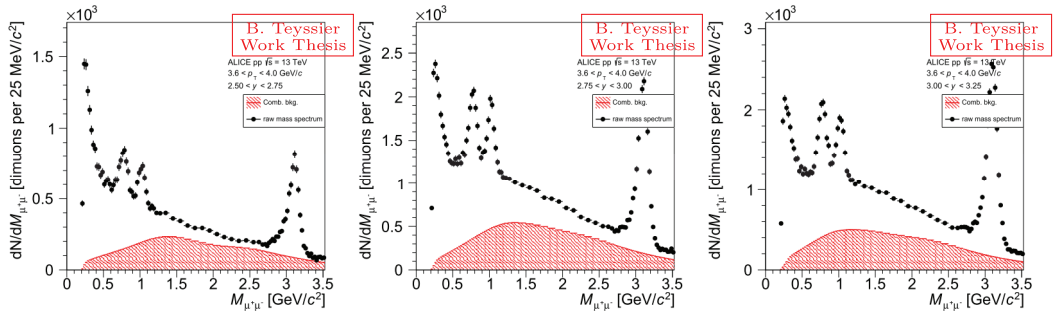

(a) $2.50 < y < 2.75$ (b) $2.75 < y < 3.00$ (c) $3.00 < y < 3.25$

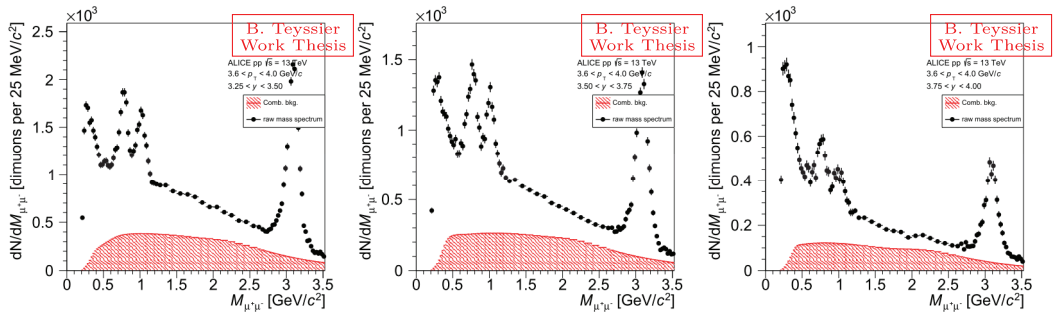

(d) $3.25 < y < 3.50$ (e) $3.50 < y < 3.75$ (f) $3.75 < y < 4.00$

Figure B.13: Evolution of signal and combinatorial background shapes for $3.60 < p_{\mathrm{T}} < 4.00$ GeV/c

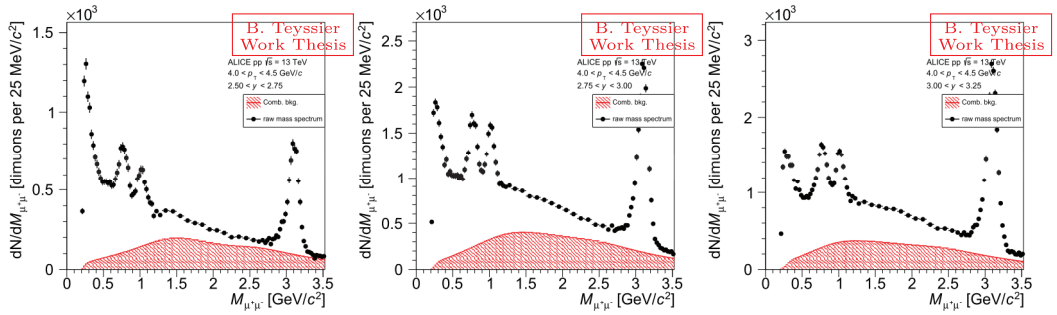

(a) $2.50 < y < 2.75$ (b) $2.75 < y < 3.00$ (c) $3.00 < y < 3.25$

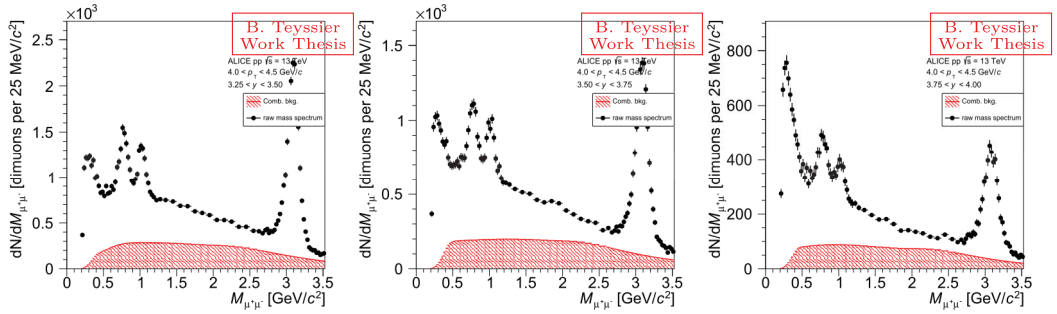

(d) $3.25 < y < 3.50$ (e) $3.50 < y < 3.75$ (f) $3.75 < y < 4.00$

Figure B.14: Evolution of signal and combinatorial background shapes for $4.00 < p_{\mathrm{T}} < 4.50$ GeV/c

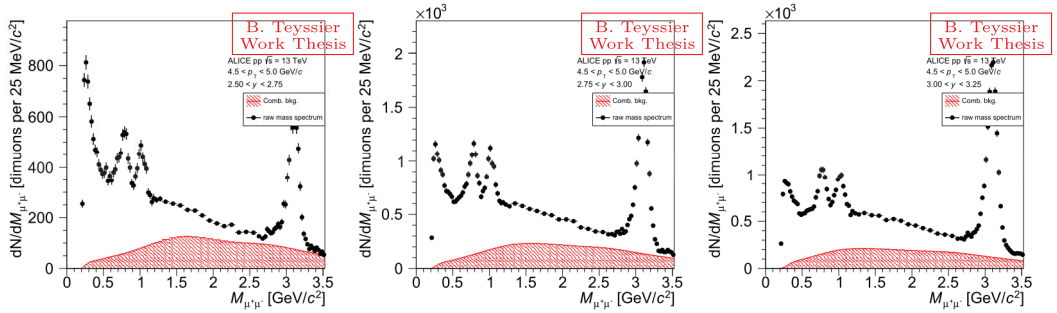

(a) $2.50 < y < 2.75$

(b) $2.75 < y < 3.00$

(c) $3.00 < y < 3.25$

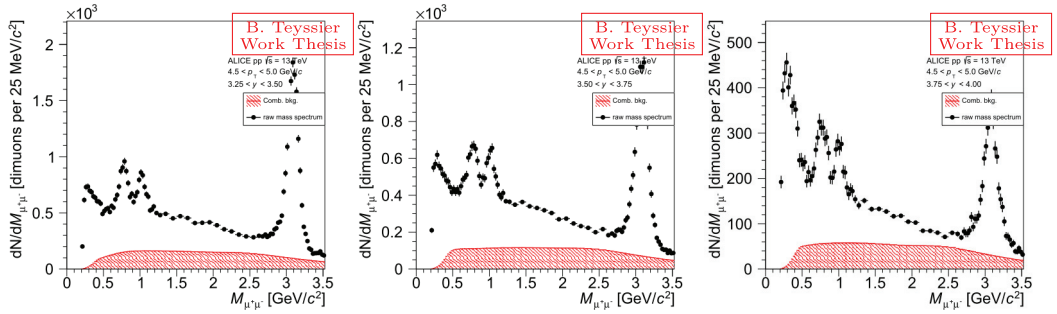

(d) $3.25 < y < 3.50$

(e) $3.50 < y < 3.75$

(f) $3.75 < y < 4.00$

Figure B.15: Evolution of signal and combinatorial background shapes for $4.50 < p_{\mathrm{T}} < 5.00$ GeV/c

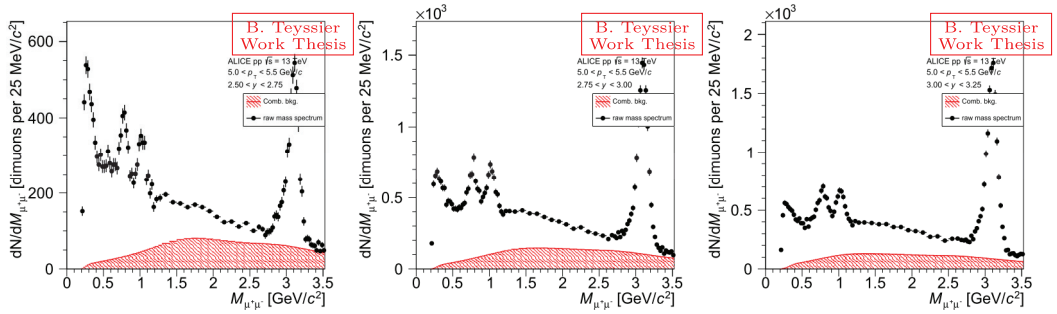

(a) $2.50 < y < 2.75$

(b) $2.75 < y < 3.00$

(c) $3.00 < y < 3.25$

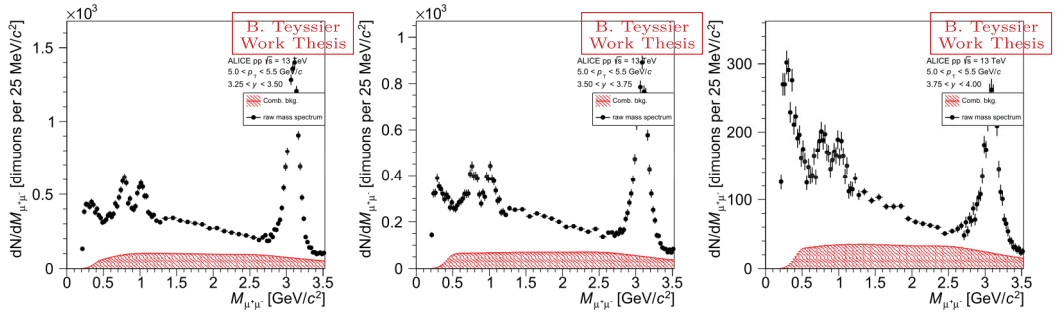

(d) $3.25 < y < 3.50$

(e) $3.50 < y < 3.75$

(f) $3.75 < y < 4.00$

Figure B.16: Evolution of signal and combinatorial background shapes for $5.00 < p_{\mathrm{T}} < 5.50$ GeV/c

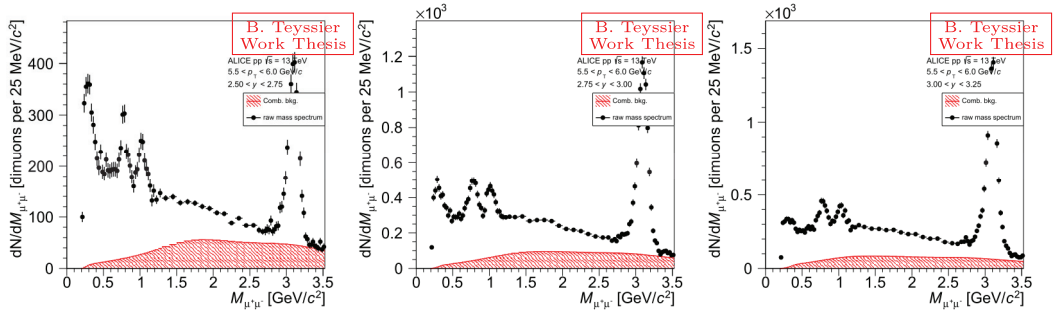

(a) $2.50 < y < 2.75$ (b) $2.75 < y < 3.00$ (c) $3.00 < y < 3.25$

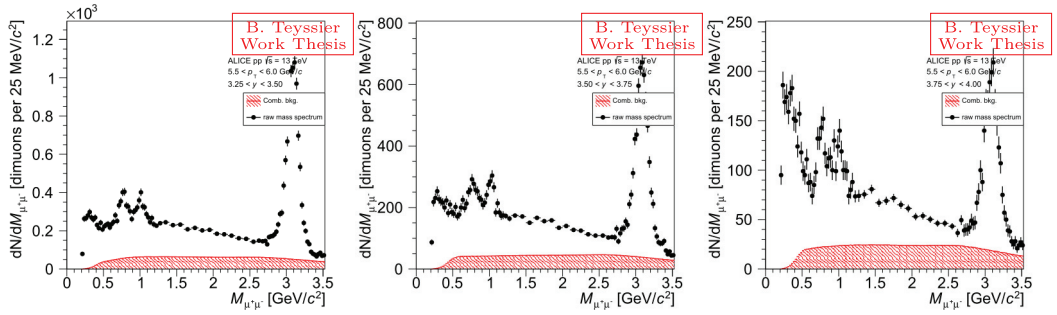

(d) $3.25 < y < 3.50$ (e) $3.50 < y < 3.75$ (f) $3.75 < y < 4.00$

Figure B.17: Evolution of signal and combinatorial background shapes for $5.50 < p_{\mathrm{T}} < 6.00$ GeV/c

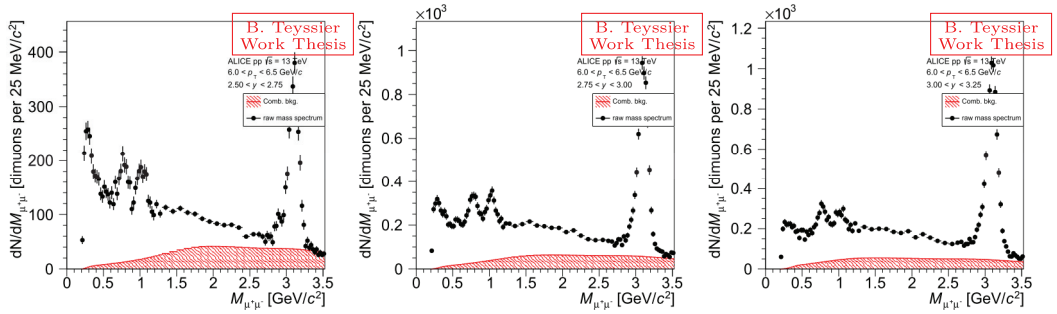

(a) $2.50 < y < 2.75$ (b) $2.75 < y < 3.00$ (c) $3.00 < y < 3.25$

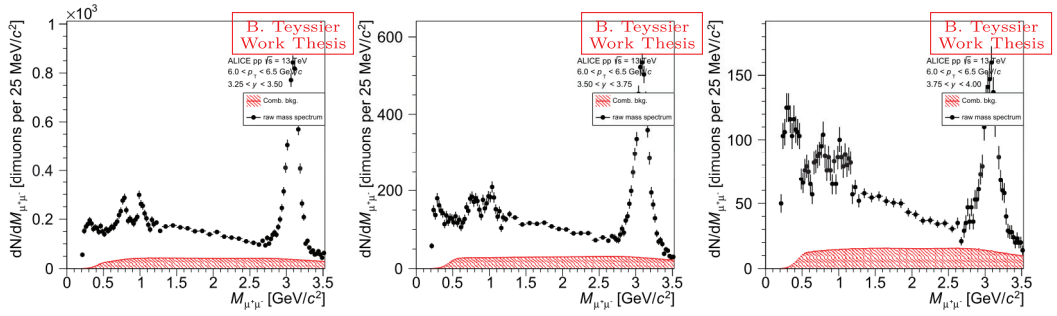

(d) $3.25 < y < 3.50$ (e) $3.50 < y < 3.75$ (f) $3.75 < y < 4.00$

Figure B.18: Evolution of signal and combinatorial background shapes for $6.00 < p_{\mathrm{T}} < 6.50$ GeV/c

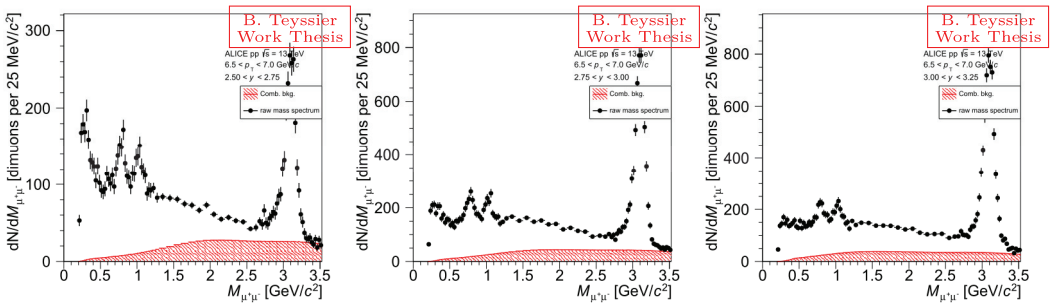

(a) $2.50 < y < 2.75$ (b) $2.75 < y < 3.00$ (c) $3.00 < y < 3.25$

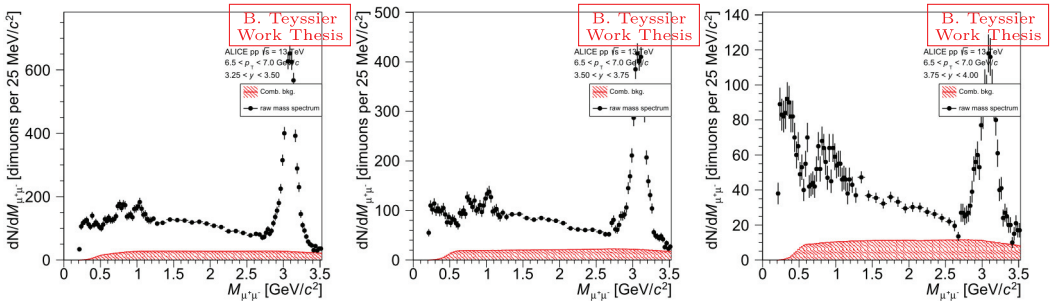

(d) $3.25 < y < 3.50$ (e) $3.50 < y < 3.75$ (f) $3.75 < y < 4.00$

Figure B.19: Evolution of signal and combinatorial background shapes for $6.50 < p_{\mathrm{T}} < 7.00$ GeV/c

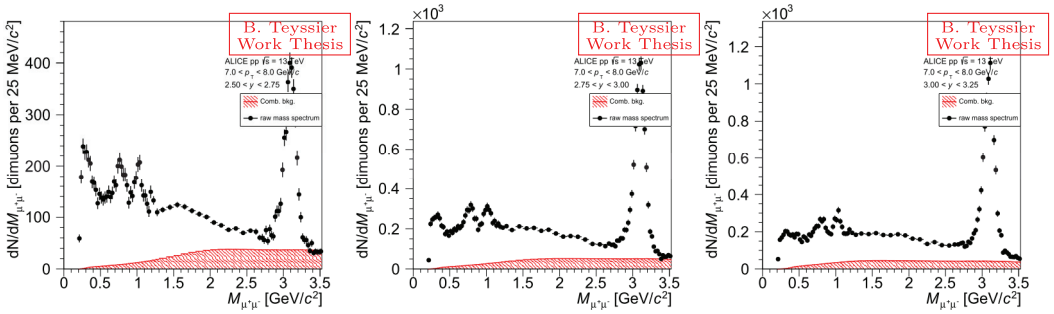

(a) $2.50 < y < 2.75$ (b) $2.75 < y < 3.00$ (c) $3.00 < y < 3.25$

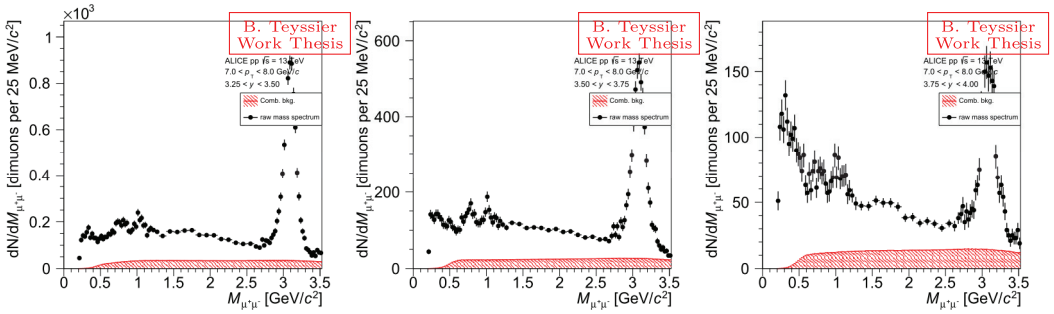

(d) $3.25 < y < 3.50$ (e) $3.50 < y < 3.75$ (f) $3.75 < y < 4.00$

Figure B.20: Evolution of signal and combinatorial background shapes for $7.00 < p_{\mathrm{T}} < 8.00$ GeV/c

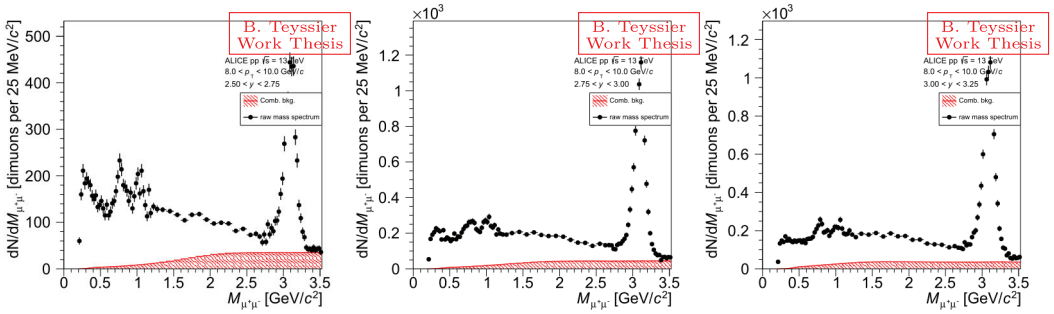

(a) $2.50 < y < 2.75$ (b) $2.75 < y < 3.00$ (c) $3.00 < y < 3.25$

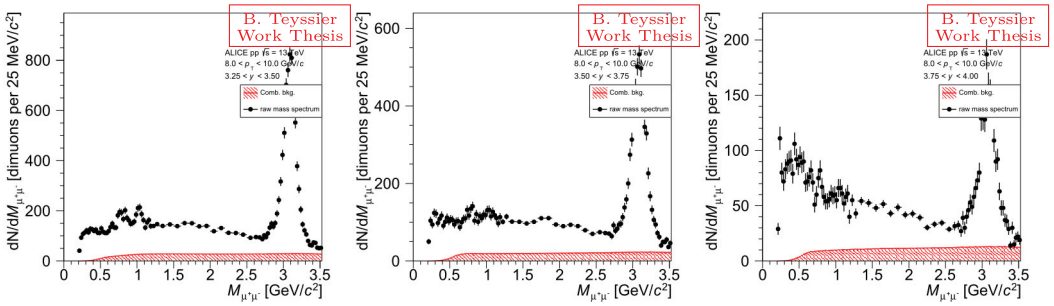

(d) $3.25 < y < 3.50$ (e) $3.50 < y < 3.75$ (f) $3.75 < y < 4.00$

Figure B.21: Evolution of signal and combinatorial background shapes for $8.00 < p_{\mathrm{T}} < 10.00$ GeV/c

Appendix C

Hadronic-Cocktail fits — figures

Not available fit in $2.50 < y < 2.75$

Not available fit in $2.75 < y < 3.00$

Not available fit in $3.00 < y < 3.25$

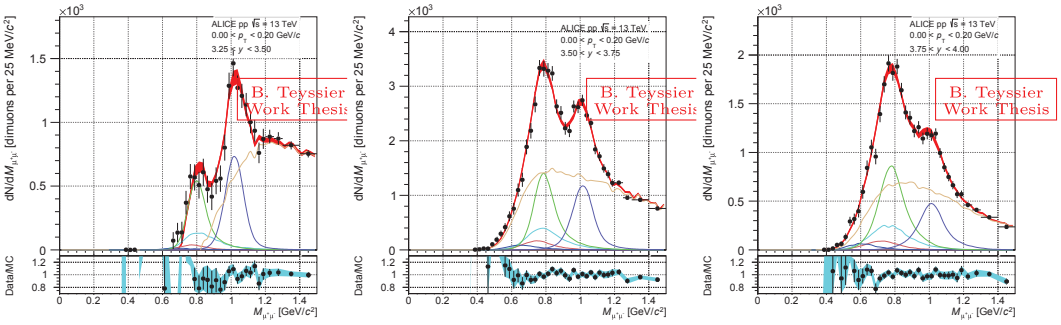

(a) $3.25 < y < 3.50$ (b) $3.50 < y < 3.75$ (c) $3.75 < y < 4.00$

Figure C.1: Hadronic cocktail fits for $0.00 < p_{\mathrm{T}} < 0.20$ GeV/c

Not available fit in $2.50 < y < 2.75$

Not available fit in $2.75 < y < 3.00$

Not available fit in $3.00 < y < 3.25$

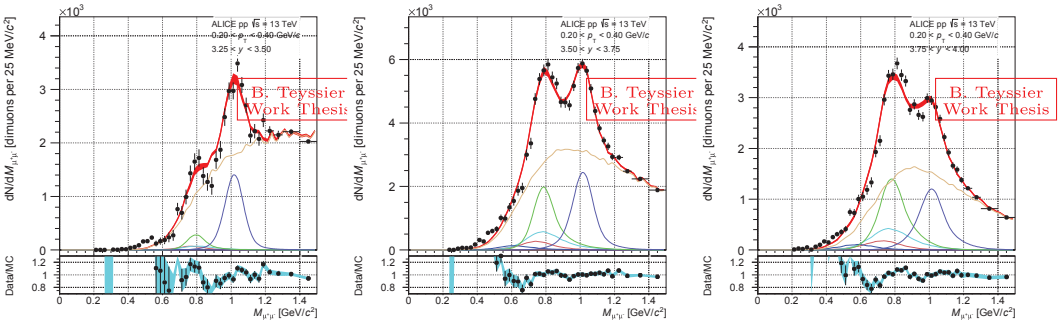

(a) $3.25 < y < 3.50$ (b) $3.50 < y < 3.75$ (c) $3.75 < y < 4.00$

Figure C.2: Hadronic cocktail fits for $0.20 < p_{\mathrm{T}} < 0.40$ GeV/c

Not available fit in $2.50 < y < 2.75$

Not available fit in $2.75 < y < 3.00$

Not available fit in $3.00 < y < 3.25$

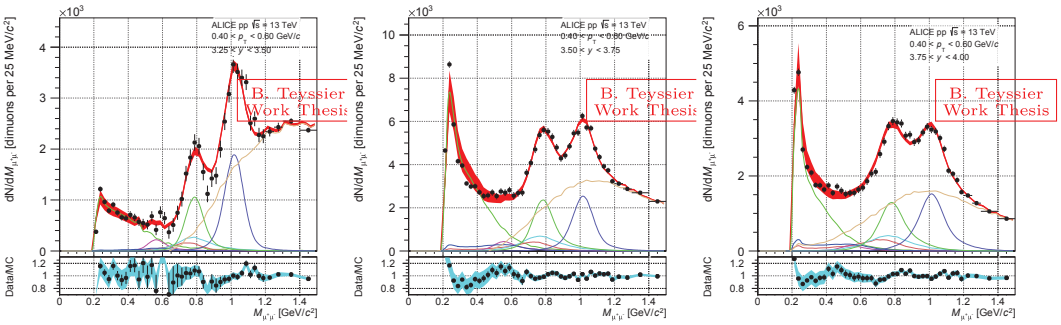

(a) $3.25 < y < 3.50$ (b) $3.50 < y < 3.75$ (c) $3.75 < y < 4.00$

Figure C.3: Hadronic cocktail fits for $0.40 < p_{\mathrm{T}} < 0.60$ GeV/c

Not available fit in $2.50 < y < 2.75$

Not available fit in $2.75 < y < 3.00$

Not available fit in $3.00 < y < 3.25$

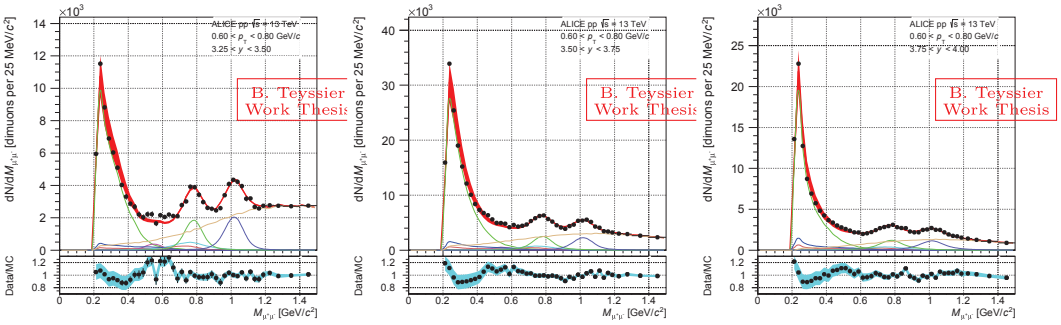

(a) $3.25 < y < 3.50$ (b) $3.50 < y < 3.75$ (c) $3.75 < y < 4.00$

Figure C.4: Hadronic cocktail fits for $0.60 < p_{\mathrm{T}} < 0.80$ GeV/c

Not available fit in $2.50 < y < 2.75$

Not available fit in $2.75 < y < 3.00$

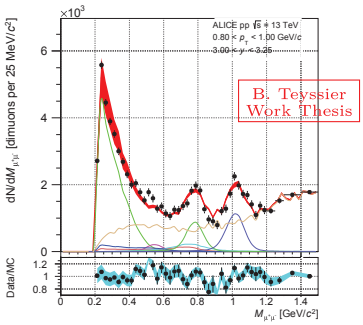

(a) $3.00 < y < 3.25$

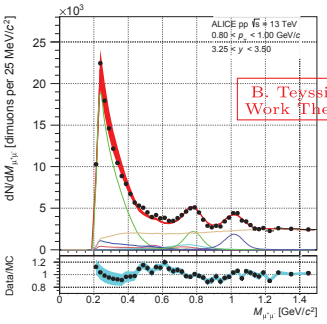

(b) $3.25 < y < 3.50$

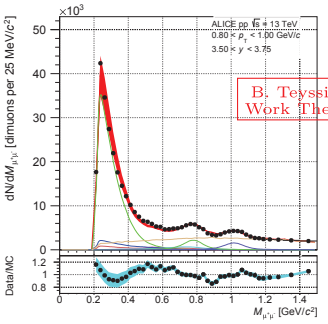

(c) $3.50 < y < 3.75$

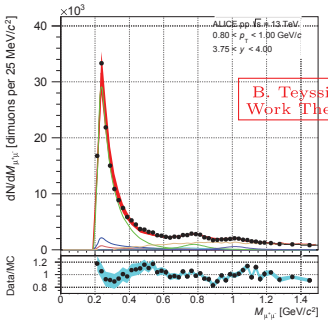

(d) $3.75 < y < 4.00$

Figure C.5: Hadronic cocktail fits for $0.80 < p_{\mathrm{T}} < 1.00$ GeV/c

Not available fit in $2.50 < y < 2.75$

Not available fit in $2.75 < y < 3.00$

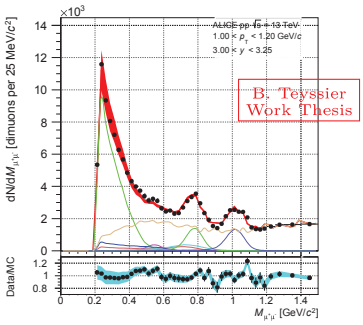

(a) $3.00 < y < 3.25$

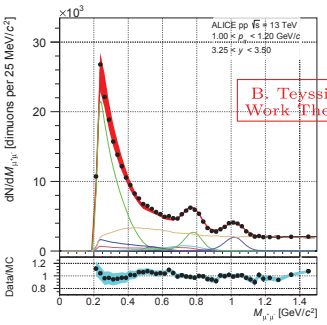

(b) $3.25 < y < 3.50$

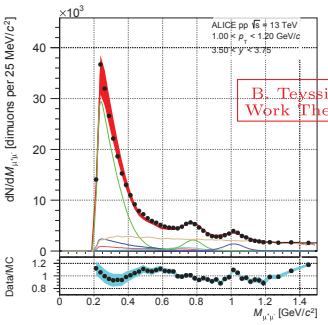

(c) $3.50 < y < 3.75$

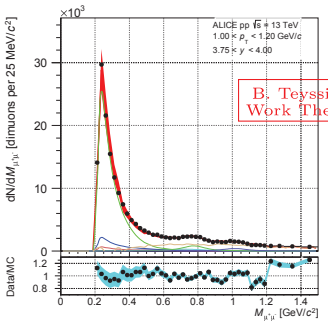

(d) $3.75 < y < 4.00$

Figure C.6: Hadronic cocktail fits for $1.00 < p_{\mathrm{T}} < 1.20$ GeV/c

Not available fit in $2.50 < y < 2.75$

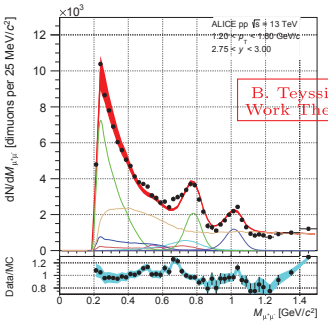

(a) $2.75 < y < 3.00$

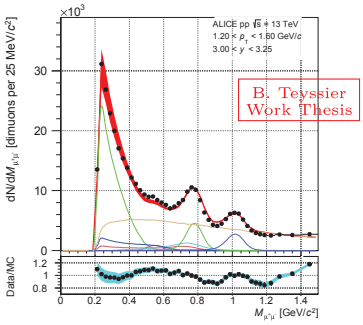

(b) $3.00 < y < 3.25$

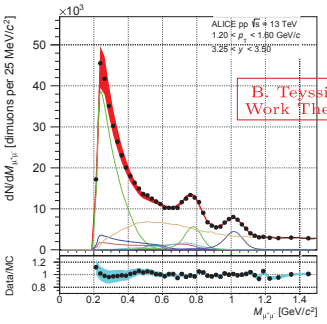

(c) $3.25 < y < 3.50$

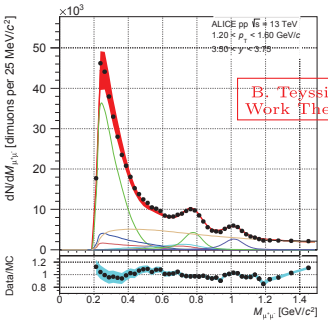

(d) $3.50 < y < 3.75$

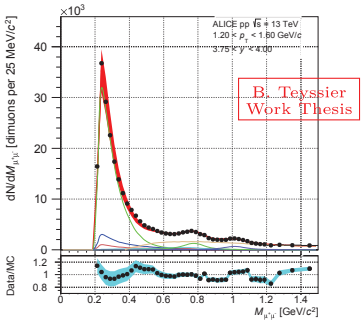

(e) $3.75 < y < 4.00$

Figure C.7: Hadronic cocktail fits for $1.20 < p_{\mathrm{T}} < 1.60$ GeV/c

Not available fit in $2.50 < y < 2.75$

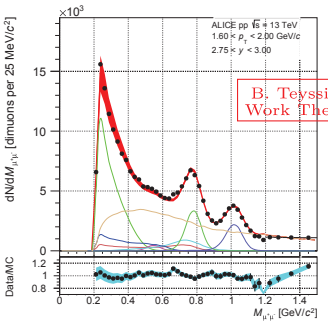

(a) $2.75 < y < 3.00$

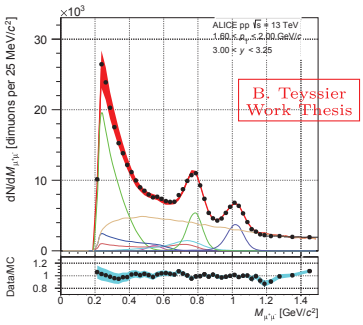

(b) $3.00 < y < 3.25$

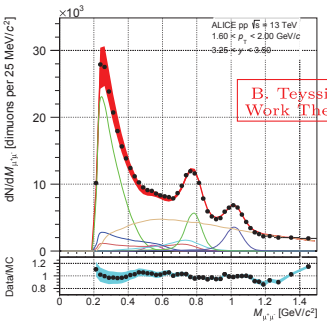

(c) $3.25 < y < 3.50$

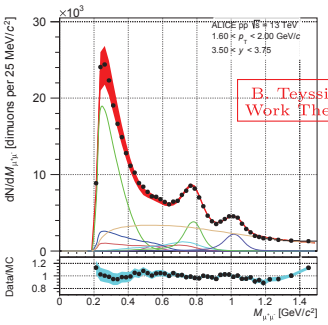

(d) $3.50 < y < 3.75$

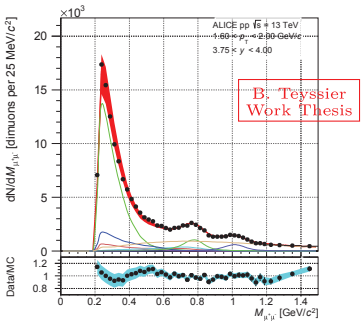

(e) $3.75 < y < 4.00$

Figure C.8: Hadronic cocktail fits for $1.60 < p_{\mathrm{T}} < 2.00$ GeV/c

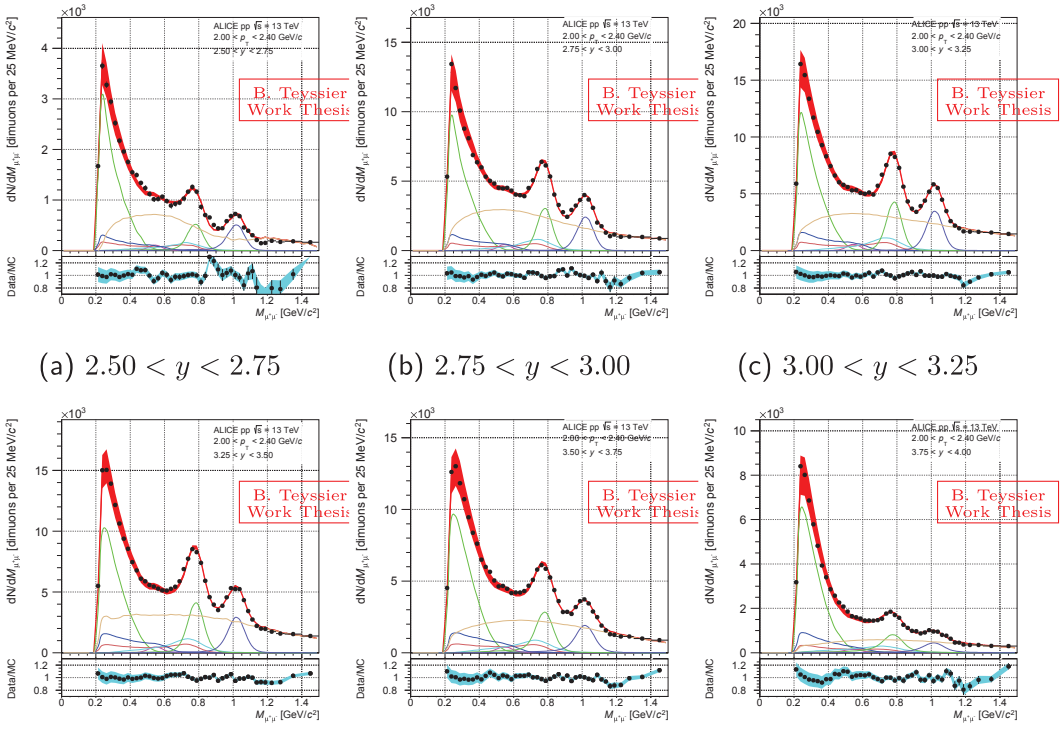

(a) $2.50 < y < 2.75$ (b) $2.75 < y < 3.00$ (c) $3.00 < y < 3.25$

(d) $3.25 < y < 3.50$ (e) $3.50 < y < 3.75$ (f) $3.75 < y < 4.00$

Figure C.9: Hadronic cocktail fits for $2.00 < p_{\mathrm{T}} < 2.40$ GeV/c

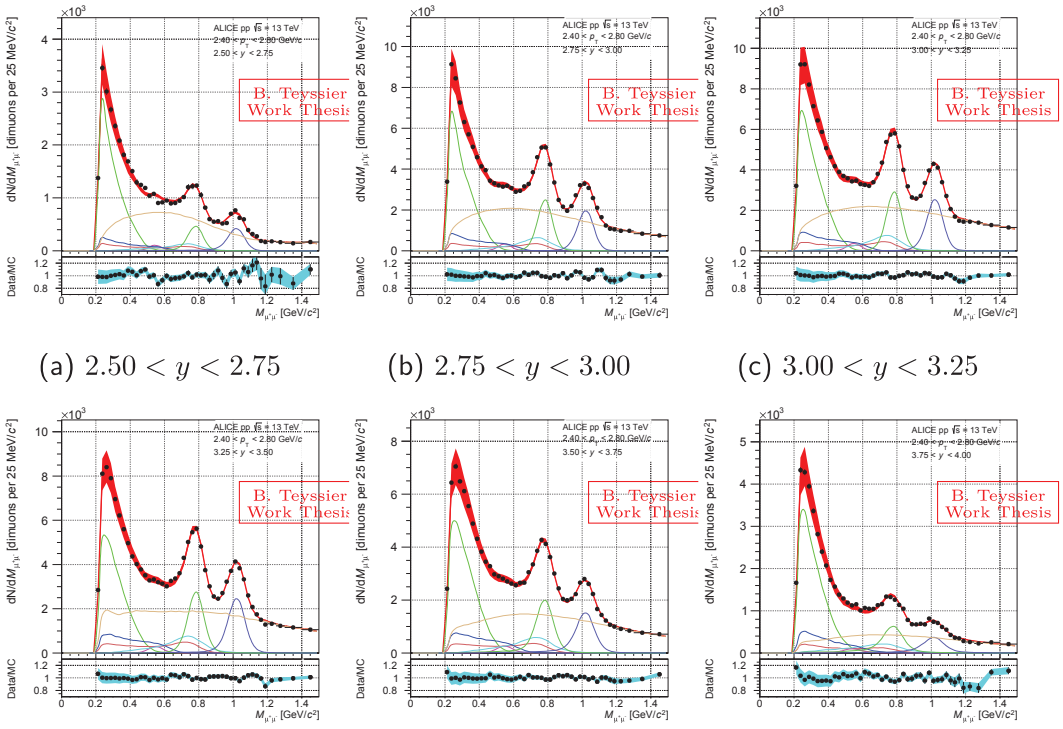

(a) $2.50 < y < 2.75$ (b) $2.75 < y < 3.00$ (c) $3.00 < y < 3.25$

(d) $3.25 < y < 3.50$ (e) $3.50 < y < 3.75$ (f) $3.75 < y < 4.00$

Figure C.10: Hadronic cocktail fits for $2.40 < p_{\mathrm{T}} < 2.80$ GeV/c

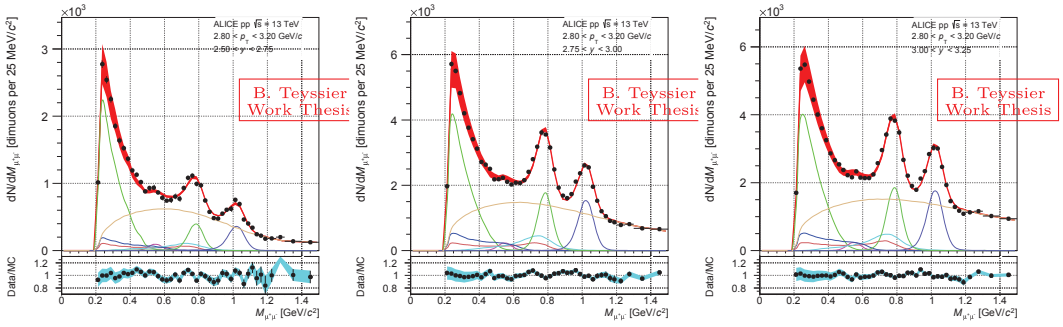

(a) $2.50 < y < 2.75$ (b) $2.75 < y < 3.00$ (c) $3.00 < y < 3.25$

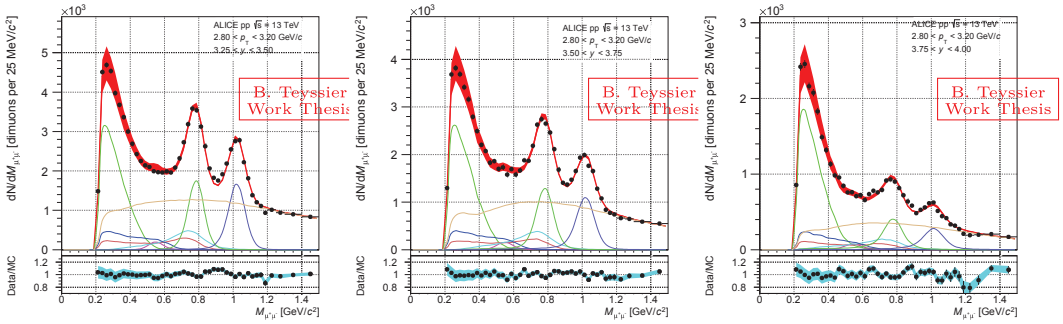

(d) $3.25 < y < 3.50$ (e) $3.50 < y < 3.75$ (f) $3.75 < y < 4.00$

Figure C.11: Hadronic cocktail fits for $2.80 < p_{\mathrm{T}} < 3.20$ GeV/c

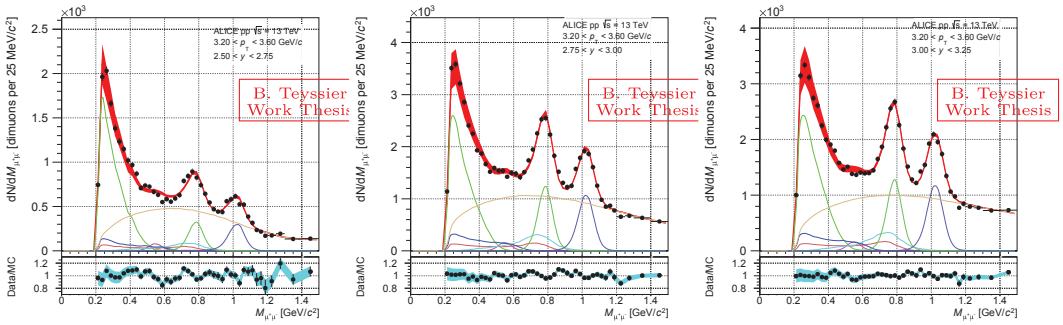

(a) $2.50 < y < 2.75$ (b) $2.75 < y < 3.00$ (c) $3.00 < y < 3.25$

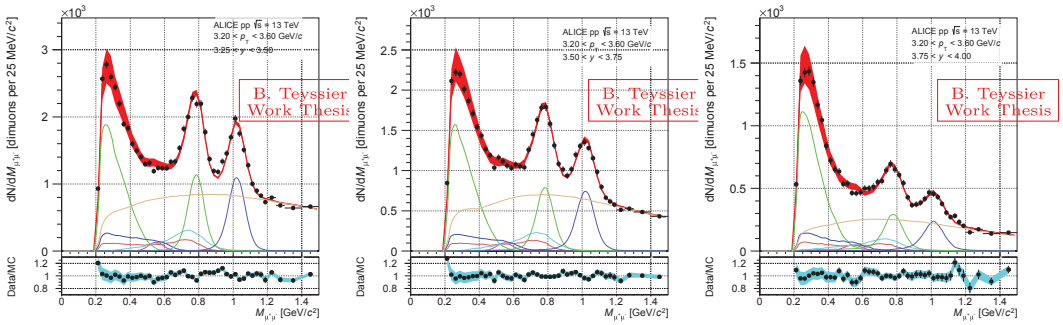

(d) $3.25 < y < 3.50$ (e) $3.50 < y < 3.75$ (f) $3.75 < y < 4.00$

Figure C.12: Hadronic cocktail fits for $3.20 < p_{\mathrm{T}} < 3.60$ GeV/c

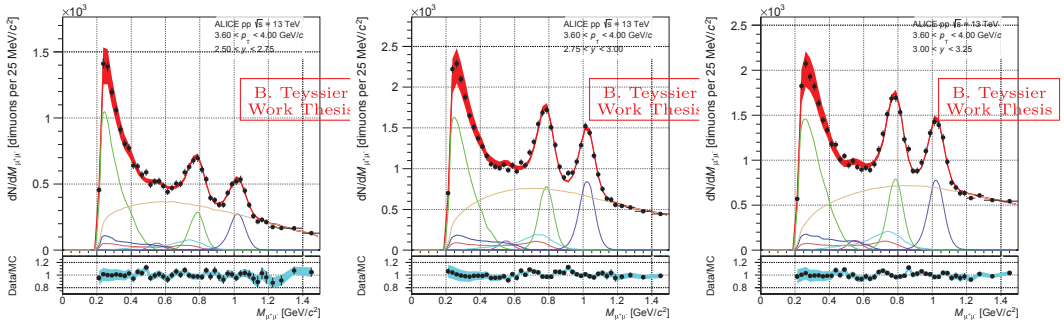

(a) $2.50 < y < 2.75$ (b) $2.75 < y < 3.00$ (c) $3.00 < y < 3.25$

(d) $3.25 < y < 3.50$ (e) $3.50 < y < 3.75$ (f) $3.75 < y < 4.00$

Figure C.13: Hadronic cocktail fits for $3.60 < p_{\mathrm{T}} < 4.00$ GeV/c

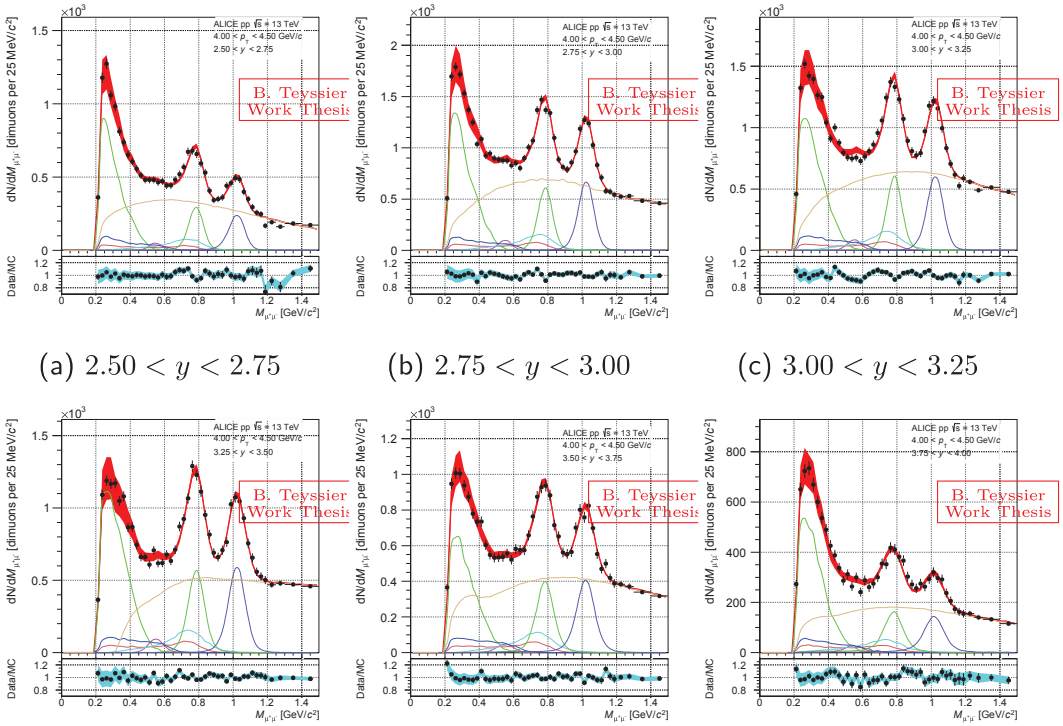

(a) $2.50 < y < 2.75$ (b) $2.75 < y < 3.00$ (c) $3.00 < y < 3.25$

(d) $3.25 < y < 3.50$ (e) $3.50 < y < 3.75$ (f) $3.75 < y < 4.00$

Figure C.14: Hadronic cocktail fits for $4.00 < p_{\mathrm{T}} < 4.50$ GeV/c

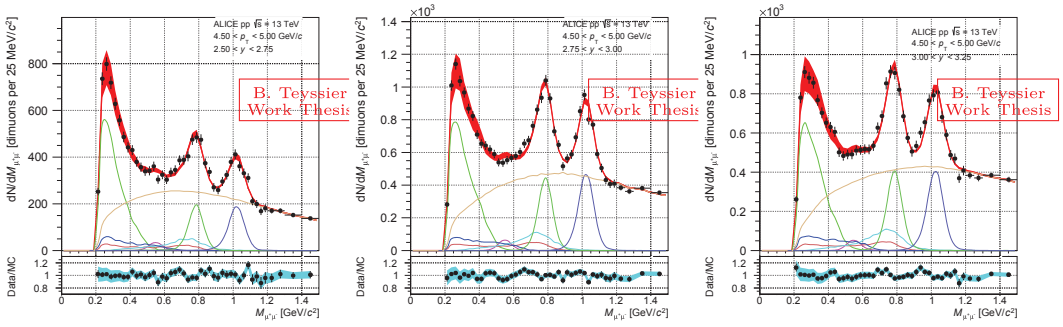

(a) $2.50 < y < 2.75$

(b) $2.75 < y < 3.00$

(c) $3.00 < y < 3.25$

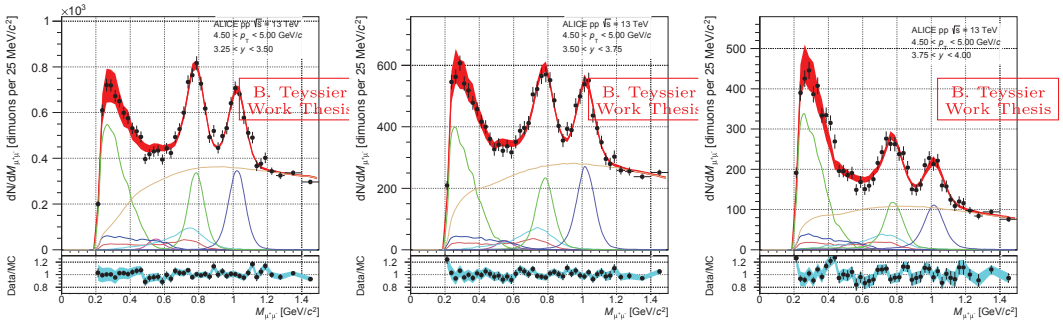

(d) $3.25 < y < 3.50$

(e) $3.50 < y < 3.75$

(f) $3.75 < y < 4.00$

Figure C.15: Hadronic cocktail fits for $4.50 < p_{\mathrm{T}} < 5.00$ GeV/c

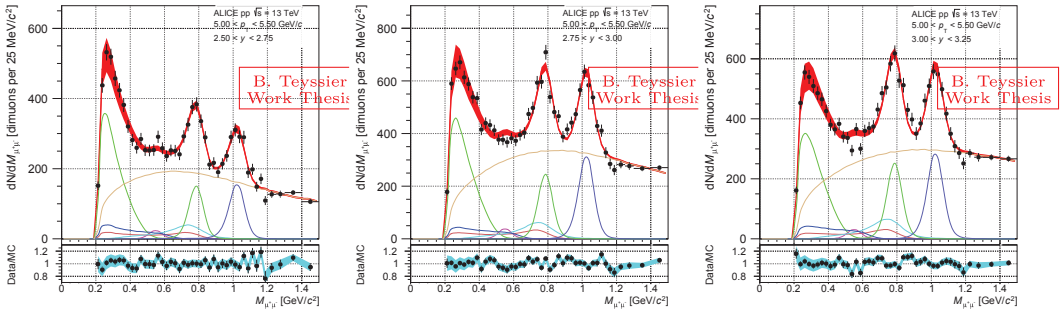

(a) $2.50 < y < 2.75$

(b) $2.75 < y < 3.00$

(c) $3.00 < y < 3.25$

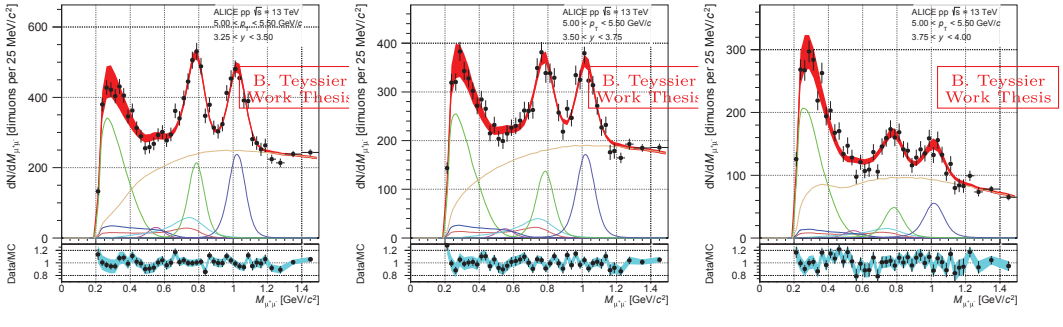

(d) $3.25 < y < 3.50$

(e) $3.50 < y < 3.75$

(f) $3.75 < y < 4.00$

Figure C.16: Hadronic cocktail fits for $5.00 < p_{\mathrm{T}} < 5.50$ GeV/c

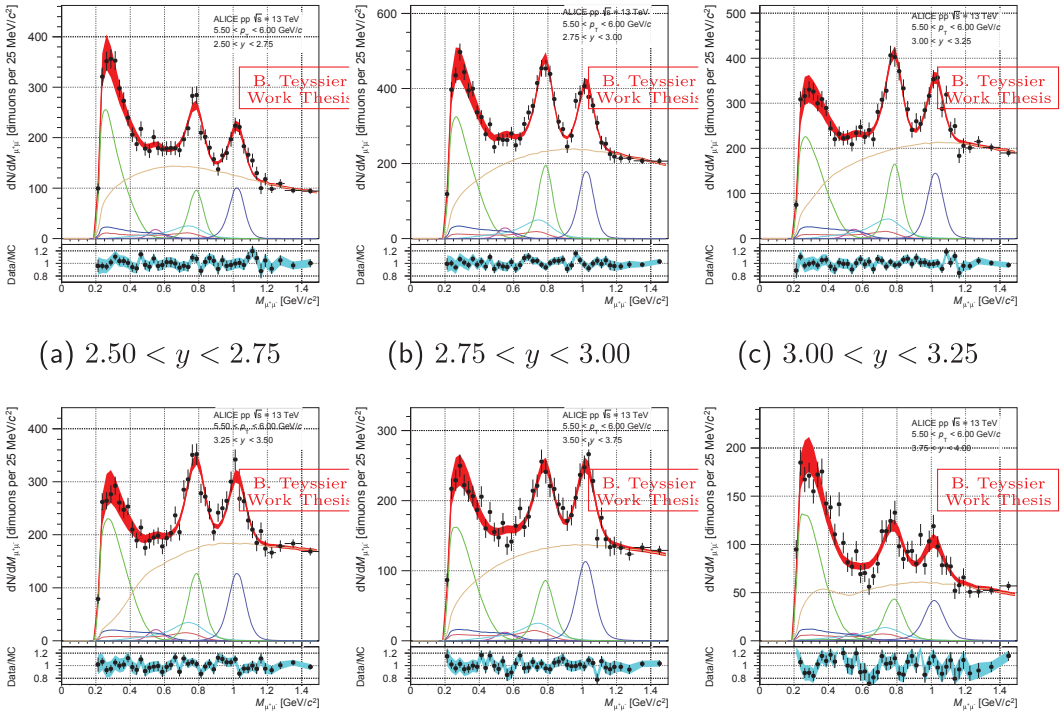

(a) $2.50 < y < 2.75$ (b) $2.75 < y < 3.00$ (c) $3.00 < y < 3.25$

(d) $3.25 < y < 3.50$ (e) $3.50 < y < 3.75$ (f) $3.75 < y < 4.00$

Figure C.17: Hadronic cocktail fits for $5.50 < p_{\mathrm{T}} < 6.00$ GeV/c

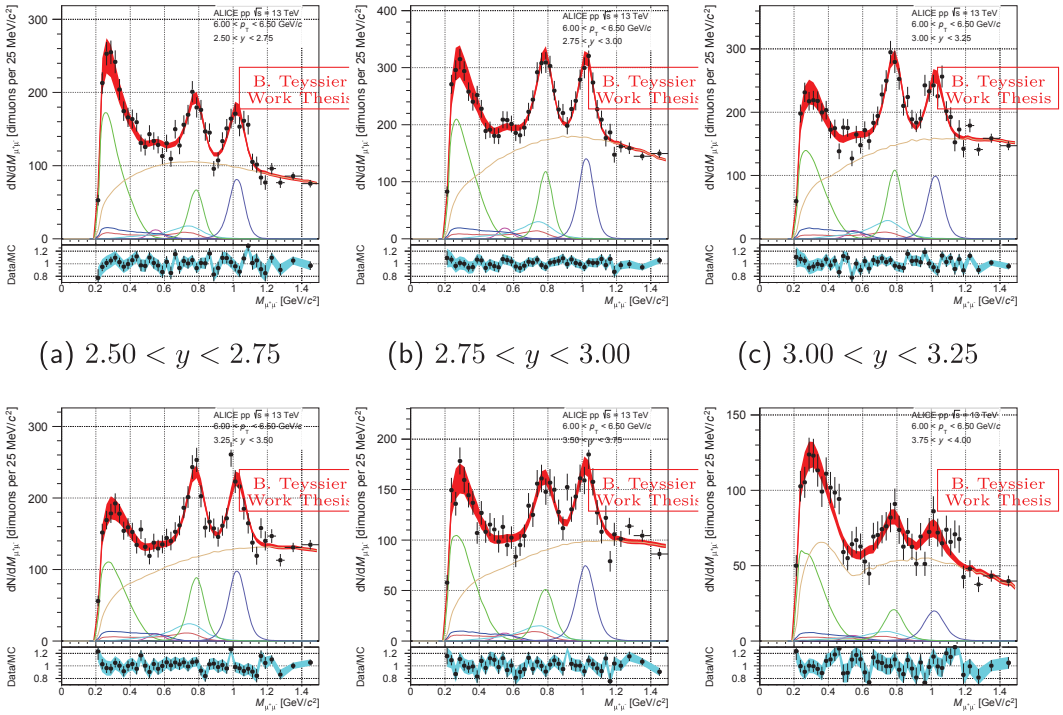

(a) $2.50 < y < 2.75$ (b) $2.75 < y < 3.00$ (c) $3.00 < y < 3.25$

(d) $3.25 < y < 3.50$ (e) $3.50 < y < 3.75$ (f) $3.75 < y < 4.00$

Figure C.18: Hadronic cocktail fits for $6.00 < p_{\mathrm{T}} < 6.50$ GeV/c

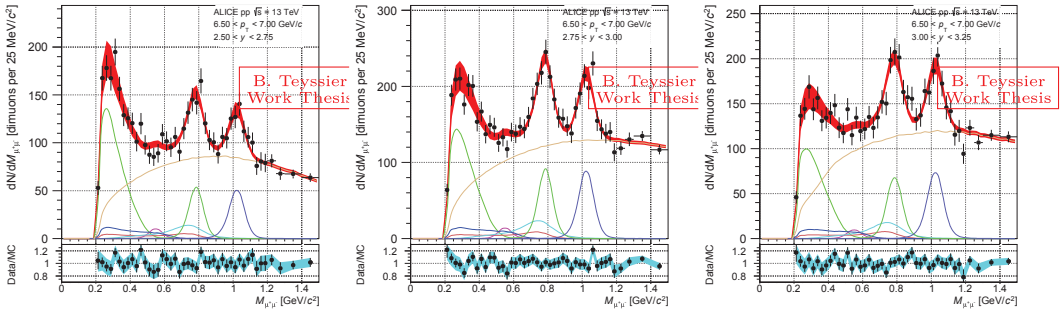

(a) $2.50 < y < 2.75$

(b) $2.75 < y < 3.00$

(c) $3.00 < y < 3.25$

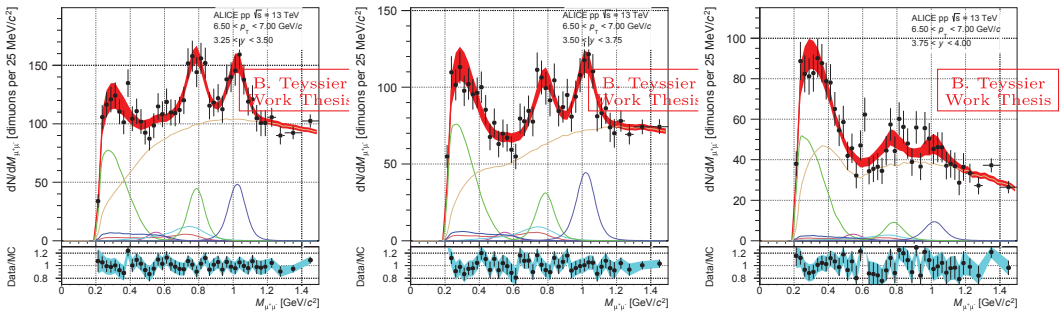

(d) $3.25 < y < 3.50$

(e) $3.50 < y < 3.75$

(f) $3.75 < y < 4.00$

Figure C.19: Hadronic cocktail fits for $6.50 < p_{\mathrm{T}} < 7.00$ GeV/c

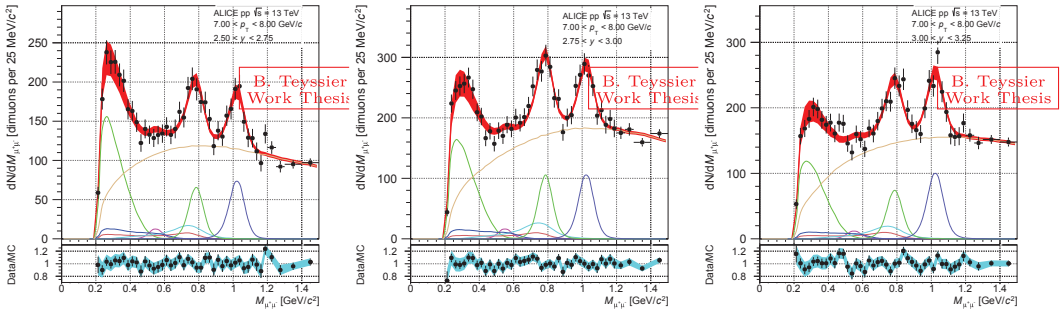

(a) $2.50 < y < 2.75$

(b) $2.75 < y < 3.00$

(c) $3.00 < y < 3.25$

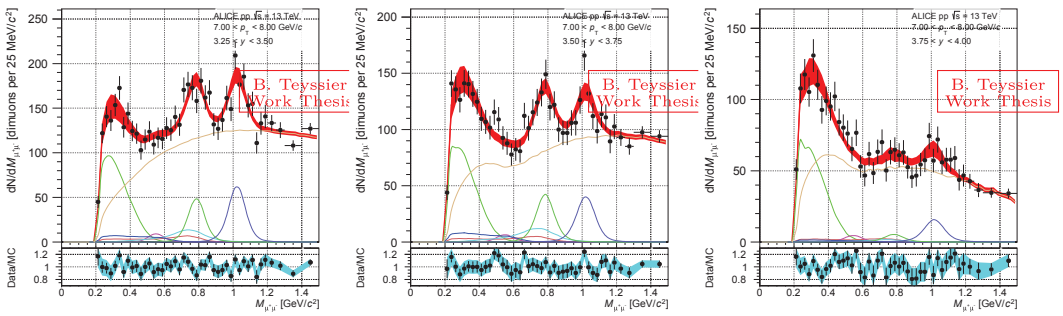

(d) $3.25 < y < 3.50$

(e) $3.50 < y < 3.75$

(f) $3.75 < y < 4.00$

Figure C.20: Hadronic cocktail fits for $7.00 < p_{\mathrm{T}} < 8.00$ GeV/c

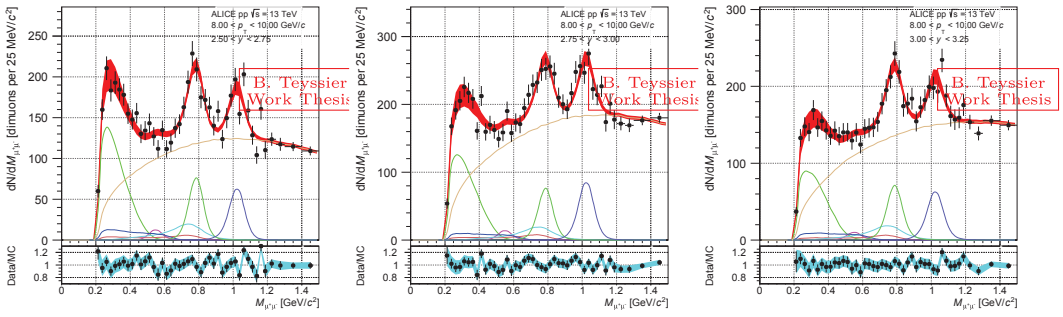

(a) $2.50 < y < 2.75$ (b) $2.75 < y < 3.00$ (c) $3.00 < y < 3.25$

(d) $3.25 < y < 3.50$ (e) $3.50 < y < 3.75$

Not available fit in $3.75 < y < 4.00$

Figure C.21: Hadronic cocktail fits for $8.00 < p_{\mathrm{T}} < 10.00$ GeV/c

Bibliography

[1] Michael E. Peskin and Daniel V. Schroeder. *An Introduction to Quantum Field Theory*. Addison-Wesley, 3 edition, 1951. (Cited pages 1 et 7.)

[2] C. A. Baker, D. D. Doyle, P. Geltenbort, and others. Improved Experimental Limit on the Electric Dipole Moment of the Neutron. *Phys. Rev. Lett.*, 97(13):131801, September 2006. [link]. (Cited page 4.)

[3] S.M. Barr. A review of CP violation in atoms. *International Journal of Modern Physics A*, 08(02):209–236, January 1993. [link]. (Cited page 4.)

[4] C. Patrignani, K. Agashe, G. Aielli, and others. Review of Particle Physics. *Chin.Phys.*, C40:100001, October 2016. [link]. (Cited pages 4, 5, 7, 54, 56, 58 et 105.)

[5] E. Eichten, K. Gottfried, T. Kinoshita, and others. Charmonium: The model. *Phys. Rev. D*, 17(11):3090–3117, June 1978. [link]. (Cited page 6.)

[6] Gerard't Hooft. Symmetry Breaking Through Bell-Jackiw Anomalies. *Phys.Rev.Lett.*, 37:8–11, 1976. (Cited page 10.)

[7] S. P. Klevansky. The Nambu-Jona-Lasinio model of quantum chromodynamics. *Rev. Mod. Phys.*, 64:649–708, 1992. (Cited pages 10 et 12.)

[8] P. Costa, C. A. de Sousa, M. C. Ruivo, and others. The QCD critical end point in the SU(3) Nambu–Jona-Lasinio model. *Physics Letters B*, 647(5):431–435, April 2007. [link]. (Cited page 10.)

[9] J Stachel and G. R. Young. Relativistic Heavy ION Physics at CERN and BNL. *Annu. Rev. Nucl. Part. Sci.*, 42(1):537–597, December 1992. [link]. (Cited page 13.)

[10] H. R. Schmidt and J. Schukraft. The physics of ultra-relativistic heavy-ion collisions. *J. Phys. G: Nucl. Part. Phys.*, 19(11):1705, 1993. [link]. (Cited page 13.)

[11] RHIC. Physics of the Relativistic Heavy Ion Collider, 2017. [https://www.bnl.gov/rhic/physics.asp]. (Cited page 13.)

[12] CERN. Heavy ions and quark-gluon plasma. [https://home.cern/about/physics/heavy-ions-and-quark-gluon-plasma]. (Cited page 13.)

[13] ALICE Collaboration. ϕ-meson production at forward rapidity in p-Pb collisions at $\sqrt{s_{\mathrm{NN}}} = 5.02$ TeV and in pp collisions at $\sqrt{s} = 2.76$ TeV. *Physics Letters B*, 768:203–217, May 2017. [link]. (Cited pages 14, 15 et 26.)

[14] Michael L. Miller, Klaus Reygers, Stephen J. Sanders, and others. Glauber Modeling in High-Energy Nuclear Collisions. *Annu. Rev. Nucl. Part. Sci.*, 57(1):205–243, October 2007. [link]. (Cited page 14.)

[15] J. Stachel, A. Andronic, P. Braun-Munzinger, and others. Confronting LHC data with the statistical hadronization model. *J. Phys.: Conf. Ser.*, 509(1):012019, 2014. [link]. (Cited page 16.)

[16] ALICE Collaboration. Pion, Kaon, and Proton Production in Central Pb-Pb Collisions at $\sqrt{s_{NN}} = 2.76$ TeV. *Phys. Rev. Lett.*, 109(25), December 2012. [link]. (Cited page 17.)

[17] Piotr Bożek. Components of the elliptic flow in Pb–Pb collisions at. *Physics Letters B*, 699(4):283–286, May 2011. [link]. (Cited page 17.)

[18] ALICE Collaboration. Elliptic Flow of Charged Particles in Pb-Pb Collisions at $\sqrt{s_{NN}} = 2.76$ TeV. *Phys. Rev. Lett.*, 105(25):252302, December 2010. [link]. (Cited page 17.)

[19] Johann Rafelski and Berndt Müller. Strangeness Production in the Quark-Gluon Plasma. *Phys. Rev. Lett.*, 48(16):1066–1069, April 1982. [link]. (Cited page 18.)

[20] ALICE Collaboration. Enhanced production of multi-strange hadrons in high-multiplicity proton-proton collisions. *Nat Phys*, 13(6):535–539, June 2017. [link]. (Cited page 18.)

[21] CMS Collaboration. Evidence of b-Jet Quenching in PbPb Collisions at $\sqrt{s_{NN}} = 2.76$ TeV. *Phys. Rev. Lett.*, 113(13):132301, September 2014. [link]. (Cited page 19.)

[22] Jason Glyndwr Ulery. Jet-Medium Interactions in Pb–Pb Collisions. *Nuclear Physics A*, 904-905:744c–747c, May 2013. [link]. (Cited page 19.)

[23] Magdalena Djordjevic. Heavy Flavor Puzzle at LHC: A Serendipitous Interplay of Jet Suppression and Fragmentation. *Phys. Rev. Lett.*, 112(4):042302, January 2014. [link]. (Cited page 19.)

[24] I. Kuznetsova and J. Rafelski. Heavy flavor hadrons in statistical hadronization of strangeness-rich QGP. *Eur. Phys. J. C*, 51(1):113–133, June 2007. [link]. (Cited page 19.)

[25] Min He, Rainer J. Fries, and Ralf Rapp. D_s Mesons as a Quantitative Probe of Difusion and Hadronization in Nuclear Collisions. *Phys. Rev. Lett.*, 110(11):112301, March 2013. [link]. (Cited page 19.)

[26] ALICE Collaboration. Transverse momentum dependence of D-meson production in Pb-Pb collisions at $\sqrt{s_{\mathrm{NN}}} = 2.76$ TeV. *Journal of High Energy Physics*, 2016(3), March 2016. [arXiv:1509.06888]. (Cited page 20.)

[27] Davide Caffarri. Open heavy-flavour and quarkonium production in Pb-Pb and p-Pb collisions measured by the ALICE detector at the LHC — Rencontres de Moriond on QCD and High Energy Interactions Proceedings. March 2016. [link]. (Cited page 20.)

[28] T. Matsui and H. Satz. J/ψ Suppression by Quark-Gluon Plasma Formation,. *Physics Letters B*, page 416, 1986. [link]. (Cited page 20.)

[29] S. Digal, P. Petreczky, and H. Satz. Quarkonium Feed-Down and Sequential Suppression. *Physical Review D*, 64(9), October 2001. [arXiv:0106017]. (Cited page 20.)

[30] Xingbo Zhao and Ralf Rapp. Medium Modifications and Production of Charmonia at LHC. *Nuclear Physics A*, 859(1):114–125, June 2011. [arXiv:1102.2194]. (Cited page 20.)

[31] E. G. Ferreiro. Charmonium dissociation and recombination at LHC: Revisiting comovers. *Physics Letters B*, 731:57–63, April 2014. [arXiv:1210.3209]. (Cited page 20.)

[32] Chad Steven Flores. Bottomonia results from the LHC Run 1 and 2 with CMS - QM17 Presentation, February 2017. [https://indico.cern.ch/event/433345/contributions/2358628/]. (Cited page 20.)

[33] ALICE Collaboration. Direct photon production in Pb–Pb collisions at $\sqrt{s_{\mathrm{NN}}}$ = 2.76TeV. *Physics Letters B*, 754:235–248, March 2016. [link]. (Cited pages 21 et 22.)

[34] R. Rapp. Dilepton Production in Heavy-Ion Collisions. *arXiv:1306.6394 [hep-ph, physics:nucl-ex, physics:nucl-th]*, June 2013. [arXiv:1306.6394]. (Cited pages 21 et 22.)

[35] R. Rapp, J. Wambach, and H. van Hees. The Chiral Restoration Transition of QCD and Low Mass Dileptons. *arXiv:0901.3289 [hep-ph, physics:nucl-ex, physics:nucl-th]*, 23:134–175, 2010. [arXiv:0901.3289]. (Cited page 21.)

[36] CMS Collaboration. Charged-particle nuclear modification factors in PbPb and pPb collisions at $\sqrt{s_{\mathrm{NN}}} = 5.02$ TeV. *JHEP*, 1704:039, April 2017. (Cited page 22.)

[37] LHCb Collaboration. Measurements of prompt charm production cross-sections in pp collisions at $\sqrt{s} = 5$ TeV. *J. High Energ. Phys.*, 2017(6):147, June 2017. [link]. (Cited page 22.)

[38] LHCb Collaboration. Measurement of the b-Quark Production Cross Section in 7 and 13 TeV pp Collisions. *Phys. Rev. Lett.*, 118(5):052002, February 2017. [link]. (Cited pages 22 et 72.)

[39] Kevin Welsh, Jordan Singer, and Ulrich Heinz. Initial-state fluctuations in collisions between light and heavy ions. *Phys. Rev. C*, 94(2):024919, August 2016. [link]. (Cited page 22.)

[40] ALICE Collaboration. ϕ production at forward rapidity in Pb-Pb collisions at $\sqrt{s_{NN}} = 2.76$ TeV. (Cited page 24.)

[41] Alessandro De Falco. ϕ meson production at forward rapidity in pp and Pb–Pb collisions with ALICE at the LHC — SQM17 Proceedings. *EPJ Web Conf.*, 171:13006, 2018. [link]. (Cited pages 24, 27 et 28.)

[42] Constantino Tsallis. Possible generalization of Boltzmann-Gibbs statistics. *J Stat Phys*, 52(1-2):479–487, July 1988. [link]. (Cited page 26.)

[43] ALICE Collaboration. Light vector meson production in pp collisions at $\sqrt{s} = 7$ TeV. *Physics Letters B*, 710(4–5):557–568, April 2012. [link]. (Cited pages 27, 46 et 97.)

[44] CERN. CERN Fac - The LHC guide, 2008. [https://cds.cern.ch/record/1092437/files/CERN-Brochure-2008-001-Eng.pdf]. (Cited page 30.)

[45] CERN. LHC-Commissioning, 2016. [http://lhc-commissioning.web.cern.ch/lhc-commissioning/schedule/LHC%20schedule%20beyond%20LS1%20MTP%202015_Freddy_June2015.pdf]. (Cited page 31.)

[46] Alexander Wu Chao, Karl Hubert Mess, Maury Tigner, and others, editors. *Handbook of accelerator physics and engineering*. World Scientific, second edition, 2013. OCLC: 855827052. (Cited page 31.)

[47] Lyndon Evans and Philip Bryant. LHC Machine. *Journal of Instrumentation*, 3(08):S08001–S08001, August 2008. [link]. (Cited page 31.)

[48] ALICE Collaboration. ALICE luminosity determination for pp collisions at $\sqrt{s} = 13$ TeV. *CERN Document Server / ALICE-PUBLIC-2016-002*, June 2016. [link]. (Cited pages 31 et 45.)

[49] S. van der Meer. Calibration of the Effective Beam Height in the ISR. 1968. [link]. (Cited page 31.)

[50] Yasuyuki Akiba, Aaron Angerami, Helen Caines, and others. The Hot QCD White Paper: Exploring the Phases of QCD at RHIC and the LHC. *arXiv:1502.02730 [hep-ex, physics:hep-lat, physics:hep-ph, physics:nucl-ex, physics:nucl-th]*, February 2015. [arXiv:1502.02730]. (Cited page 32.)

[51] N. Abgrall, O. Andreeva, A. Aduszkiewicz, and others. NA61/SHINE facility at the CERN SPS: beams and detector system. *J. Inst.*, 9(06):P06005, 2014. [link]. (Cited page 32.)

[52] A. Dainese, E. Scomparin, G. Usai, and others. INFN What Next: Ultra-relativistic Heavy-Ion Collisions. *arXiv:1602.04120 [nucl-ex, physics:nucl-th]*, February 2016. [arXiv:1602.04120]. (Cited page 32.)

[53] V. Golovatyuk, M. Kapishin, V. Kekelidze, and others. Prospects for the dense baryonic matter research at NICA. *J. Phys.: Conf. Ser.*, 668(1):012015, 2016. [link]. (Cited page 32.)

[54] GSI. Facility for Antiproton and Ion Research: Fair Home, 2016. [http://www.fair-center.eu/]. (Cited page 32.)

[55] S. J. Brodsky, F. Fleuret, C. Hadjidakis, and others. Physics opportunities of a fixed-target experiment using LHC beams. *Physics Reports*, 522(4):239–255, January 2013. [link]. (Cited page 32.)

[56] Gianluca Usai. Dimuon production in PbPb collisions at 20–160 AGeV at the CERN SPS: Mapping the QCD phase diagram in the transition region with a new NA60-like experiment. *Nuclear Physics A*, 931:729–734, November 2014. [link]. (Cited page 32.)

[57] Gianluca Usai, Sabyasachi Siddhanta, Rosario Turrisi, and others. Physics Beyond Colliders Kickoff Workshop (6-7 septembre 2016), September 2016. [https://indico.cern.ch/event/523655/contributions/2247739/]. (Cited page 32.)

[58] ALICE Collaboration. Performance of the ALICE Experiment at the CERN LHC. *International Journal of Modern Physics A*, 29(24):1430044, September 2014. [arXiv:1402.4476]. (Cited page 33.)

[59] CERN. Statistics, 2017. [https://acc-stats.web.cern.ch/acc-stats/#lhc/]. (Cited pages 33 et 34.)

[60] ALICE Collaboration. Performance of the ALICE VZERO system. *J. Inst.*, 8(10):P10016, 2013. [link]. (Cited page 37.)

[61] Livio Bianchi. *J/ψ polarization in pp collisions at $\sqrt{s} = 7$ TeV with the ALICE muon spectrometer at the LHC*. PhD thesis, Université Paris Sud - Paris XI, Università degli studi di Torino, March 2012. [link]. (Cited page 38.)

[62] M. Guilbaud. *Etude de la densité de particules chargées et des mésons vecteurs de basses masses en collisions Pb-Pb à $\sqrt{s_{NN}} = 2.76$ TeV dans ALICE au LHC*. PhD thesis, Université Claude Bernard - Lyon I, October 2013. [link]. (Cited page 39.)

[63] ALICE Collaboration. ALICE technical design report of the dimuon forward spectrometer. *CERN/LHCC 99-22*, August 1999. [link]. (Cited page 39.)

[64] ALICE Collaboration. AliRoot Core: Main Page. [http://alidoc.cern.ch/AliRoot/master/index.html]. (Cited page 40.)

[65] ALICE Collaboration. AliPhysics Main Page, 2016. [http://alidoc.cern.ch/AliPhysics/master/index.html]. (Cited page 40.)

[66] Brun, R. and Rademakers, F. ROOT - An Object Oriented Data Analysis Framework. *Nucl. Inst. & Meth. in Phys. Res. A*, (389):81–86, 1997. [link]. (Cited page 40.)

[67] Torbjörn Sjöstrand, Stephen Mrenna, and Peter Skands. PYTHIA 6.4 physics and manual. *Journal of High Energy Physics*, 2006(05):026–026, May 2006. [link]. (Cited page 40.)

[68] Wei-Tian Deng, Xin-Nian Wang, and Rong Xu. Hadron production in $p+p$, $p+$Pb, and Pb$+$Pb collisions with the HIJING 2.0 model at energies available at the CERN Large Hadron Collider. *Phys. Rev. C*, 83(1):014915, January 2011. [link]. (Cited page 40.)

[69] René Brun, F. Bruyant, Federico Carminati, and others. GEANT Detector Description and Simulation Tool. 1994. [link]. (Cited page 40.)

[70] S. Agostinelli, J. Allison, K. Amako, and others. Geant4 — A simulation toolkit. *Nucl. Inst. & Meth. in Phys. Res. A*, 506(3):250–303, July 2003. [link]. (Cited page 40.)

[71] A. Ferrari, P.R. Sala, A. Fasso, and others. FLUKA : a multi-particle transport code. *CERN-2005-10 , INFN/TC_05/11, SLAC-R-773*, 2005. [link]. (Cited page 40.)

[72] ALICE Collaboration. Technical Design Report for the Upgrade of the ALICE Inner Tracking System. *J. Phys. G: Nucl. Part. Phys.*, 41(8):087002, 2014. [link]. (Cited page 42.)

[73] ALICE Collaboration. Technical Design Report for the Muon Forward Tracker. Technical Report CERN-LHCC-2015-001. ALICE-TDR-018, January 2015. [link]. (Cited page 42.)

[74] ALICE Collaboration. Upgrade of the ALICE Time Projection Chamber. Technical Report CERN-LHCC-2013-020. ALICE-TDR-016, October 2013. [link]. (Cited page 43.)

[75] ALICE Collaboration. Upgrade of the ALICE Readout & Trigger System. Technical Report CERN-LHCC-2013-019. ALICE-TDR-015, September 2013. [link]. (Cited page 43.)

[76] Ananya, A. Alarcon Do Passo Suaide, C. Alves Garcia Prado, and others. O2 : A novel combined online and offline computing system for the ALICE Experiment after 2018. *J. Phys.: Conf. Ser.*, 513(1):012037, 2014. [link]. (Cited page 44.)

[77] ALICE Collaboration. Numerical Simulations and Offline Reconstruction of the Muon Spectrometer of ALICE. 2009. [link]. (Cited page 46.)

[78] ALICE Collaboration. Development of the Kalman filter for tracking in the forward muon spectrometer of ALICE. 2003. [link]. (Cited pages 46 et 86.)

[79] Evgeny Kryshen. Private comunication. (Cited page 47.)

[80] ALICE Collaboration. ALICE luminosity determination for pp collisions at $\sqrt{s} =$ 13 TeV. *CERN Document Server*, (ALICE-PUBLIC-2016-002), June 2016. [link]. (Cited page 50.)

[81] R. Engel and J. Ranft. Hadronic photon-photon interactions at high energies. *Phys. Rev. D*, 54(7):4244–4262, October 1996. [link]. (Cited page 54.)

[82] S. Roesler, R. Engel, and J. Ranft. The Monte Carlo Event Generator DPMJET-III. In *Advanced Monte Carlo for Radiation Physics, Particle Transport Simulation and Applications*, pages 1033–1038. Springer, Berlin, Heidelberg, 2001. [link]. (Cited page 54.)

[83] R. Arnaldi, K. Banicz, K. Borer, and others. Precision study of the $\eta \to \mu^+\mu^-\gamma$ and $\omega \to \mu^+\mu^-\pi^0$ electromagnetic transition form-factors and of the $\rho \to \mu^+\mu^-$ line shape in NA60. *Physics Letters B*, 757:437–444, June 2016. [link]. (Cited pages 56 et 58.)

[84] L. G. Landsberg. Electromagnetic decays of light mesons. *Physics Reports*, 128(6):301–376, November 1985. [link]. (Cited pages 56 et 57.)

[85] J. Knoll. Transport dynamics of broad resonances. *Progress in Particle and Nuclear Physics*, 42:177–186, January 1999. [link]. (Cited page 58.)

[86] M. Cacciari, M. Greco, and P. Nason. The p_T Spectrum in Heavy-Flavour Hadroproduction. *Journal of High Energy Physics*, 1998(05):007–007, May 1998. [arXiv:9803400]. (Cited pages 61 et 72.)

[87] Matteo Cacciari, Stefano Frixione, Nicolas Houdeau, and others. Theoretical predictions for charm and bottom production at the LHC. *Journal of High Energy Physics*, 2012(10), October 2012. [arXiv:1205.6344]. (Cited pages 62 et 72.)

[88] LEBC-EHS Collaboration, M. Aguilar-Benitez, W. W. W. Allison, and others. Inclusive particle production in 400 GeV/c pp-interactions. *Z. Phys. C - Particles and Fields*, 50(3):405–426, September 1991. [link]. (Cited pages 71, 72 et 81.)

[89] G. Agakichiev, M. Appenheimer, R. Averbeck, and others. Neutral meson production in p-Be and p-Au collisions at 450 GeV beam energy. *Eur. Phys. J. C*, 4(2):249–257, June 1998. [link]. (Cited pages 71, 72 et 81.)

[90] A. Uras for the NA60 Collaboration. Low mass dimuon production in p–A collisions at $\sqrt{s} = 27.5$ GeV with NA60. *J. Phys. G: Nucl. Part. Phys.*, 38(12):124180, 2011. [link]. (Cited pages 71, 72 et 81.)

[91] LHCb Collaboration. Measurements of prompt charm production cross-sections in pp collisions at $\sqrt{s} = 13$ TeV. *J. High Energ. Phys.*, 2016(3):159, March 2016. [link]. (Cited page 72.)

[92] LHCb Collaboration. Erratum to: Measurements of prompt charm production cross-sections in pp collisions at $\sqrt{s} = 13$ TeV. *J. High Energ. Phys.*, 2016(9):13, September 2016. [link]. (Cited page 72.)

[93] LHCb Collaboration. Erratum to: Measurements of prompt charm production cross-sections in pp collisions at $\sqrt{s} = 13$ TeV. *J. High Energ. Phys.*, 2017(5):74, May 2017. [link]. (Cited page 72.)

[94] Javier Martin Blanco. *Study of J/ψ production dependence with the charged particle multiplicity in p-Pb collisions at $\sqrt{s_{NN}} = 5.02$ TeV and pp collisions at $\sqrt{s} = 8$ TeV with the ALICE experiment at the LHC*. PhD thesis, Universite de Nantes, October 2015. [link]. (Cited page 86.)

[95] P. Skands, S. Carrazza, and J. Rojo. Tuning PYTHIA 8.1: the Monash 2013 tune. *Eur. Phys. J. C*, 74(8):3024, August 2014. [link]. (Cited page 94.)

[96] ALICE Collaboration. Measurement of ϕ Mesons at Mid-Rapidity in Minimum-Bias pp Collisions at 13 TeV | Analysis Notes. [https://aliceinfo.cern.ch/Notes/node/466]. (Cited pages 98, 99 et 101.)